國立臺灣大學電機資訊學院光電工程學研究所

博士論文

Graduate Institute of Photonics and Optoelectronics

College of Electrical Engineering and Computer Science

National Taiwan University

Doctoral Dissertation

二維材料在光學元件的應用

2D Materials for Optical Device Applications

黃郁涵

Yu-Han Huang

指導教授：吳肇欣 博士

Advisor：Chao-Hsin Wu, Ph.D.

中華民國 一一四 年 六 月

June 2025

doi:10.6342/NTU202501239

國立臺灣大學博士學位論文
口試委員會審定書
DOCTORAL DISSERTATION ACCEPTANCE CERTIFICATE
NATIONAL TAIWAN UNIVERSITY

二維材料在光學元件的應用
2D Materials for Optical Device Applications

本論文係黃郁涵君（學號 D10941001）在國立臺灣大學光電工程學研究所完成之博士學位論文，於民國 114 年 6 月 16 日承下列考試委員審查通過及口試及格，特此證明

The undersigned, appointed by the Graduate Institute of Photonics and Optoelectronics, on 16 June 2025 have examined a Doctoral Dissertation entitled above presented by HUANG YU HAN (student ID: D10941001) candidate and hereby certify that it is worthy of acceptance.

口試委員 Oral examination committee:

（指導教授 Advisor）

吳肇欣　　陳奕君

張宇庭　　裴靜偉

張子睿　　李柏璁

所長 Director: 吳肇欣

doi:10.6342/NTU202501239

誌謝

在臺灣大學攻讀博士學位的這段日子，是我人生中極為重要且難以忘懷的時光。回顧過去幾年的學術旅程，從初入實驗室時的懵懂與焦慮，到逐漸在研究中找到方向與信心，這一路的成長與蛻變，離不開許多師長、同儕與親友的鼓勵與扶持。在此，謹向所有曾經給予我鼓勵與幫助的人，致上最誠摯的謝意。

首先，衷心感謝我的指導教授吳肇欣博士，以及共同指導教授林時彥研究員。在博士階段的旅程中，兩位老師始終以嚴謹的學術態度與無私的熱忱伴我前行。不僅在研究方法、實驗設計、數據分析與論文撰寫等方面傾囊相授，更在我面臨迷惘、壓力或挫敗時，耐心地引導我調整心態、重新定位方向。老師們傳授的不僅是知識與技術，更是一套面對問題、解決挑戰的態度與方法。兩位老師待我如己出，總是盡心盡力，無論在學術或人生道路上都給予我莫大的支持與鼓勵。在您們的引領下，我學會了如何在困境中堅定前行，也更加體悟作為一名研究者所應肩負的責任與使命。能在求學過程中遇到這樣關懷與專業兼具的導師，是學生的榮幸與福氣。

同時，我也非常感謝臺大與中研院實驗室的所有同儕與夥伴。這些年與大家一同在實驗室工作與生活的點滴，不僅讓我在學術上有諸多成長，也豐富了我的人生經驗。謝謝你們在我實驗失敗時一同找問題、在我情緒低落時給予陪伴，並在壓力之餘一同分享午晚餐、談天說笑，讓這段求學旅程充滿溫度與人情味。

此外，也要感謝口試委員們撥冗審閱本論文，您們所提出的精闢意見不僅協助我發掘研究中的盲點與不足，更激發我從不同角度思考問題。這些回饋讓本論文的內容得以更加嚴謹、具備深度，也成為我未來從事研究的重要養分。

最後，最深的感謝獻給我的家人與長期支持我的摯友。感謝你們在我追尋學術夢想的路上始終如一地支持與理解。當我面臨壓力與瓶頸時，是你們不斷地給我鼓勵與動力，讓我能持續向前。謝謝你們在我人生最關鍵的階段，默默為我付出，讓我得以安心地投入研究，最終順利完成博士論文的撰寫。

這段博士生涯充滿挑戰與收穫，每一位在我生命中出現的你們，都是我不可或缺的重要角色。衷心感謝你們陪伴我走過這段旅程，這份恩情，我將永遠銘記於心。

黃郁涵 謹識

doi:10.6342/NTU202501239

摘要

本研究系統性的探討了二維材料於光學元件可能的應用，其中包括透明電極、垂直與橫向光電偵測器，以及柔性元件等。在透明導電電極的部分，我們使用單層二硫化鉬作為薄金與鈣鈦礦太陽能電池主動層間的介面層，透過二維材料表面的凡德瓦磊晶的幫助，< 10 nm 的薄金展現出良好的導電特性，以薄金/單層二硫化鉬作為透明導電電極，我們成功的製作出雙面鈣鈦礦太陽能電池。利用轉移單層二硫化鉬製備的雙面太陽能電池，在沉積 8 nm 薄金電極後達成 89.6% 的高雙面發電效率，其優異表現可歸因於薄金屬膜的高光學穿透率與良好匹配的二硫化鉬/金界面，有效抑制載子復合。在光偵測器的應用，我們透過高溫硫化非晶二硫化鉬薄膜，成功的成長出晶圓級多層二硫化鉬，其層數可達到 30 層，我們將所成長出的多層二硫化鉬薄膜應用於垂直型光伏與橫向型光導元件中，並探討其在不同結構下的光電特性。垂直元件採用簡單的金屬/半導體/金屬（金/二硫化鉬/鋁）架構，藉由上下電極的功函數差異觸發有效的光伏反應；橫向元件則結合多層二硫化鉬為光吸收層與石墨烯為載子傳輸層，實現高效的載子分離與高響應度，並進一步分析二硫化鉬吸光層的層數對於元件反應時間的影響，我們也透過不同的元件製作流程來最佳化橫向二維材料光偵測器的元件表現。最後，我們也將具不同吸光材料的石墨烯/過渡金屬硫族化物異質結構光電偵測器製作於可撓性基板上，得益於過渡金屬硫族化物層可調變的能隙與石墨烯高的載子遷移率，這些元件展現出偵測波長可調性、高響應度以及高偵測度的優異表現，相較於製作於剛性基板上的元件，製作於可撓性聚對苯二甲酸乙二酯基板上的元件依然維持 10^2-10^3 A/W 的高響應度，並展現出在機械彎曲條件下的穩定光電性能。特別是以二硫化鎢與二硒化鎢為吸光層的元件於不同彎曲狀態下僅顯示出極小的性能衰退，突顯其在柔性與穿戴式光子元件中之機械穩定性與整合潛力。綜合而言，本研究驗證了單層及多層二維材料於透明電極、光伏結構以及高性能光電偵測器等不同的潛在應用。其可擴展的材料堆疊順序及層數、優異的機械柔韌性、波長選擇性以及高光響應度等特性，皆奠定了其於新世代剛性與柔性光電元件應用中的發展潛力。

關鍵字: 二維材料、凡德瓦磊晶、透明電極、晶圓級薄膜、高響應度、光電偵測器、波長選擇性、可撓性元件

doi:10.6342/NTU202501239

Abstract

In this thesis, we have investigated the applications of 2D materials for optical devices including transparent electrodes, vertical and lateral photodetectors and flexible devices. On transparent electrodes, with the assist of van der Waals epitaxy on 2D material surfaces, thin and conductive gold (Au) film can be grown on mono-layer MoS_2 surfaces. By using 8 nm Au/mono-layer MoS_2 as transparent electrodes, bifacial perovskite solar cells with high bifaciality 89.6 % are fabricated. The good light transmittance of the Au/MoS_2 electrode and the minimum carrier recombination in the thin mono-layer MoS_2 layer are the key parameters resulting in the high performances of the device. Through the sulfurization of amorphous MoS_2 films, wafer-scale and multi-layer MoS_2 with layer numbers up to 30 can be grown on sapphire substrates. Based on the multi-layer MoS_2, vertical photodetectors with photovoltaic responses and lateral photodetectors with high responsivities are fabricated. The vertical devices utilized a simple Au/MoS_2/Al configuration, where the work function difference between the electrodes enabled efficient photovoltaic response. The lateral devices adopted a hybrid structure with multi-layer MoS_2 as the light absorption layer and graphene as the carrier transport layer, enabling efficient carrier separation and high responsivities. We have also investigated the influence of MoS_2 layer numbers to response times and optimized the device performances through different device fabrication procedures. By using different transition metal dichalcogenides (TMDs) such as WS_2, MoS_2 and WSe_2, graphene/TMD heterostructure photodetectors are fabricated on PET substrates. The devices exhibit tunable detection wavelengths based on the bandgaps of different TMDs. Compared with the devices fabricated on rigid substrates, the flexible 2D material photodetectors exhibit high responsivities up to 10^2-10^3 A/W, which indicate their high endurance to mechanical deformations. Devices with WS_2 and WSe_2 light absorption layers exhibited minimal performance degradation under various bending conditions, indicating the mechanical robustness and integration potential of these heterostructures for flexible and wearable photonic applications. In conclusion, this study demonstrates the potential of 2D materials for optical device applications. Their scalable synthesis, easy stacking, and wavelength-tunable photo-response make 2D materials promising candidates for next-generation optical device applications on either rigid or flexible substrates.

Key Word: 2D Material, van der Waals epitaxy, transparent electrodes, wafer-scale synthesis, high responsivity, photodetector, wavelength tunability, flexible devices

doi:10.6342/NTU202501239

Table of Contents

doi:10.6342/NTU202501239

doi:10.6342/NTU202501239

doi:10.6342/NTU202501239

doi:10.6342/NTU202501239

doi:10.6342/NTU202501239

List of Figures

doi:10.6342/NTU202501239

doi:10.6342/NTU202501239

doi:10.6342/NTU202501239

doi:10.6342/NTU202501239

doi:10.6342/NTU202501239

doi:10.6342/NTU202501239

doi:10.6342/NTU202501239

doi:10.6342/NTU202501239

doi:10.6342/NTU202501239

doi:10.6342/NTU202501239

doi:10.6342/NTU202501239

doi:10.6342/NTU202501239

doi:10.6342/NTU202501239

List of Tables

doi:10.6342/NTU202501239

Chapter 1 Introduction

1.1 The Rise of 2D Materials in Optics

1.1.1 History and Evolution of 2D Materials

Two-dimensional (2D) materials possess unique physical and chemical properties, making them highly promising for applications in electronics, photonics, and other fields. Since their initial theoretical predictions, they have undergone half a century of development, evolving from an unfamiliar concept to a mature technology. Today, they are widely used in various products and are considered potential candidates for breaking the 1 nm node barrier in future advancements. The concept of 2D materials can be traced back to the mid-20th century. In 1947, Canadian physicist Philip R. Wallace conducted theoretical predictions regarding the electronic behavior of graphite [1]. His research indicated that graphite, a three-dimensional (3D) material, exhibits semiconductor with zero activation energy (E_a), and its electronic structure can be described using the physical properties of a two-dimensional system [1]. Subsequently, other theoretical studies explored the possibility of isolating materials with a two-dimensional atomic structure, such as a single layer of carbon atoms (i.e., graphene). It was not until 2004 that physicists Andre Geim and Konstantin Novoselov at the University of Manchester successfully isolated mono-layer graphene, marking a significant milestone in the development of 2D materials [2]. Although the theoretical study of graphene had been ongoing for many years, its honeycomb lattice structure took decades to be physically realized and presented to the world.

doi:10.6342/NTU202501239

Geim and Novoselov pioneered the mechanical exfoliation method, commonly known as the Scotch tape technique, to isolate mono-layer graphene [2]. Their research revealed that graphene's semi-metallic nature, high carrier concentration (~10^{13} per cm^2) and outstanding mobility (μ~10,000 $cm^2/V{\cdot}s$ at room temperature) positioned it at the forefront of materials science [2]. In 2005, they further reported the successful isolation of various 2D crystals, including mono-layer transition metal dichalcogenides (TMDs, such as $NbSe_2$ and MoS_2), and complex oxides (e.g., $Bi_2Sr_2CaCu_2O_x$) [3]. With the rapid expansion of discoveries in the field of 2D materials, many of these materials have been isolated for the first time using top-down exfoliation methods and have garnered widespread attention, as shown in Figure 1-1 [2-22].

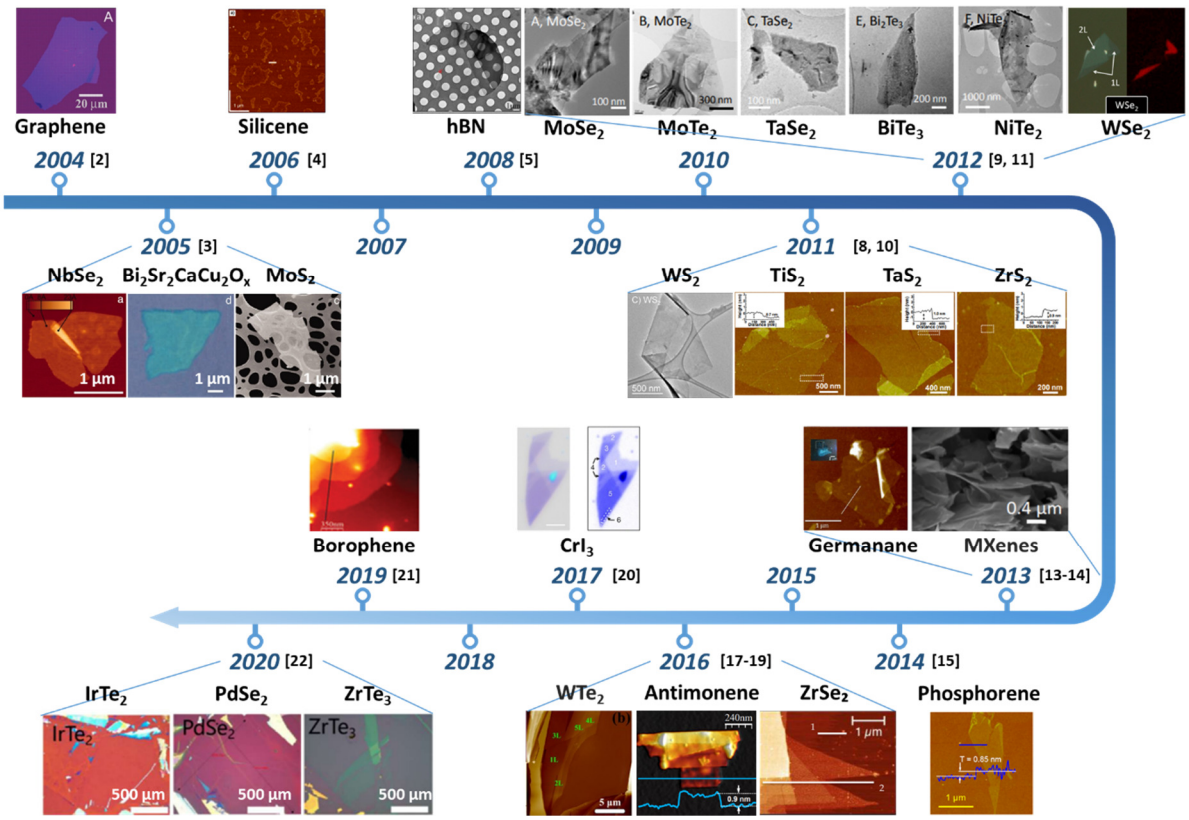

Figure 1-1 Timeline of 2D materials isolated using exfoliation techniques from 2004 to 2020 [2-22].

doi:10.6342/NTU202501239

In 2006 and 2008, Nakano and Pacilé reported the exfoliation of silicene and hexagonal boron nitride (h-BN), respectively, both featuring hexagonal structures but exhibiting distinct electronic properties [4-5]. Compared to graphene, h-BN has a significantly higher bandgap of approximately 4.5-6.0 eV [6]. Following these studies, Bourlinos et al. (2009) investigated the role of solvent selection in material separation [7]. Building on this work, Coleman et al. (2011-2012) successfully exfoliated TMDs, such as WS_2, $MoSe_2$, $MoTe_2$, $TaSe_2$, $BiTe_3$, and $NiTe_2$ for the first time [8, 9]. At the same time, Zeng et al. (2011) also used an electrochemical lithiation process to exfoliate TiS_2, TaS_2, and ZrS_2 from bulk to single layer [10].

In 2012, Zhao et al. demonstrated an indirect-to-direct bandgap transition in mono-layer WSe_2, enhancing photoluminescence (PL) [11]. Around the same time, Fang et al. utilized mono-layer WSe_2 to fabricate high-performance p-type field-effect transistors (FETs), achieving a mobility of approximately 250 $cm^2/V \cdot s$ and an on/off ratio exceeding 10^6 [12]. In 2013, Bianco et al. used mechanical exfoliation to produce germanane films, with predicted direct bandgap and electron mobility values [13]. Concurrently, Mashtalir et al. (2013) introduced a new class of 2D materials—transition metal carbides known as MXenes, such as Ti_3C_2, Ti_3CN, and TiNbC [14]. Functionalized MXenes enabled interlayer chemical reactions, broadening their applicability in catalysis [14].

In 2014, Liu and Li (two independent research groups) both exfoliated black phosphorus (BP) [15-16]. Notably, Li's study mentioned that BP exhibits carrier mobility that varies with thickness, with a BP film approximately 10 nm thick demonstrating a high mobility of ~1,000 $cm^2/V \cdot s$ [16]. Research continued in 2016 when Jiang et al. exfoliated WTe_2 and analyzed its properties using atomic force microscope (AFM) and Raman spectroscopy [17]. That same year, Ares et al. exfoliated and developed a

doi:10.6342/NTU202501239

controlled transfer process for mono-layer antimonene, predicting its band gap to be 1.2-1.3 eV [18]. Meanwhile, Mañas-Valero et al. exfoliated and studied $ZrSe_2$'s Raman spectral dependence on thickness [19]. Next, Huang et al. successfully exfoliated mono-layer CrI_3 and confirmed its Ising ferromagnetism using magneto-optical Kerr microscopy in 2017 [20]. By 2019, Ranjan et al. introduced a scalable sonochemical exfoliation technique for borophene [21]. Recently, Huang et al. (2020) developed a gold-assisted mechanical exfoliation method that enabled the isolation of monolayers from over 40 different layered materials. By pressing bulk crystals onto tape and peeling them off from a gold-coated substrate, this approach significantly improved the exfoliation yield and preserved the structural integrity of the flakes compared to conventional Scotch tape methods [22].

These advancements have not only expanded the catalog of 2D materials but also laid a solid foundation for future optoelectronic technologies. With the continuous innovation of exfoliation techniques and synthesis methods, researchers are now able to precisely control the structure and electronic properties of 2D materials, enabling their integration into various applications. The unique electrical, optical, and mechanical properties of 2D materials, combined with their ease of stacking to form van der Waals heterostructures, allow for the assembly of materials with different properties, showcasing unique physical and chemical characteristics. Nowadays, 2D materials are being used to fabricate high-mobility transistors [23-25], ultra-sensitive or flexible photodetectors [26-28], and light-emitting devices [29-31], showcasing their great potential across various advanced technological fields.

doi:10.6342/NTU202501239

1.1.2 Potential Applications of 2D Materials in Optics

As previously mentioned, 2D materials offer unique advantages over traditional bulk materials. With the continuous progress in the separation and synthesis of new 2D materials, their physical and chemical properties have been widely explored, further promoting their applications in various fields. Among them, optical applications are a key research focus. These materials are well known for their strong light-matter interactions, which stem from their unique band structures, high exciton binding energy, and efficient radiative recombination [32]. As a result, 2D materials can exhibit enhanced photon absorption and emission properties [33]. In addition, their optical response can be further amplified when combined with optical resonators or photonic crystal cavities [34], further expanding their potential in photonic technologies**.**

Beyond their strong light-matter interactions, 2D materials exhibit a diverse range of bandgap energies, allowing them to span a broad spectral range from ultraviolet (UV) and visible (VIS) to infrared (IR). As shown in Figure 1-2 (a), the theoretical absorbance (A) of various mono-layer 2D materials across these spectral ranges is presented [35]. The bandgap properties of 2D materials, especially TMDs, are also strongly affected by the number of layers. For example, a single layer of MoS_2 exhibits a direct band gap, but as the number of layers increases, the band gap gradually shifts from direct to indirect, and the energy gap is reduced from 1.8 eV (689 nm) to 1.2 eV (1033 nm). [36]. To further illustrate this effect, Figure 1-2 (b) depicts the range of photo-responses that different 2D materials can cover [28]. Thus, by selecting appropriate materials and controlling the layer number, one can design customized light absorption and emission devices for specific wavelength ranges.

doi:10.6342/NTU202501239

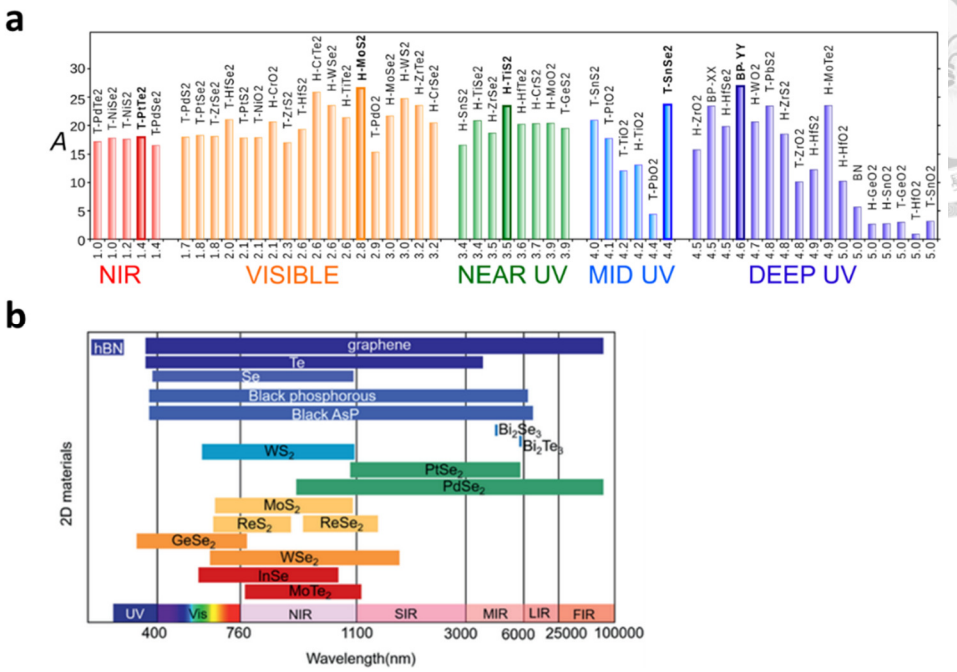

Figure 1-2 (a) Theoretical calculations of the absorbance of various mono-layer 2D materials [35]. (b) Response range covered by different 2D materials [28].

As mentioned earlier, 2D materials exhibit strong light-matter interactions and broadband spectral response capabilities, granting them high tunability and making them ideal for photovoltaics, photodetectors, and light-emitting devices. First, in 2010, Li et al. reported the first graphene-silicon solar cell [37]. They utilized the built-in electric field formed by the graphene-silicon Schottky junction to facilitate charge separation, achieving a solar cell efficiency of approximately 1.5%, as shown in Figure 1-3 (a) [37]. This study also suggested the possibility of using 2D materials, such as graphene, as active layers, channel materials or transparent electrode (TE), leading to a surge in subsequent research on related technologies. For instance, in 2013, Britnell et al. developed a photovoltaic device based on a graphene/WS_2/graphene structure, where WS_2 served as the light-absorbing layer and graphene served as both top and bottom transparent electrodes. This design enabled an external quantum efficiency (EQE) of 30%, as illustrated in Figure 1-3 (b) [32].

doi:10.6342/NTU202501239

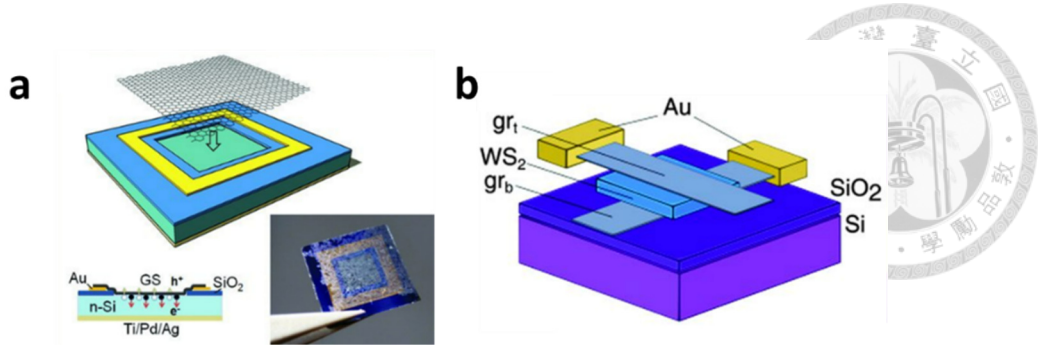

Figure 1-3 Schematic diagrams of device structures: (a) graphene/n-Si Schottky junction solar cell [37] and (b) graphene/WS_2/graphene photovoltaic device [32].

In addition, 2D materials have exhibited great potential in photodetectors, including single-photon detectors (SPDs), imaging sensors, and applications in artificial neural networks (ANNs). SPDs, in particular, can detect individual photons and convert them into electrical signals, making them essential for quantum communication and computing, and ultra-sensitive optical measurements. In 2015, He et al. developed a WSe_2-based SPD, attributing its operation to excitons localized at defects, as illustrated in Figure 1-4 [38].

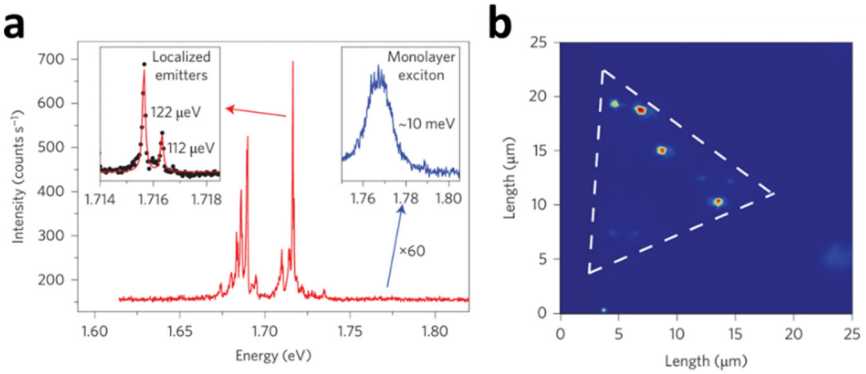

Figure 1-4 (a) PL spectrum of localized emitters at 4.2 K. (b) PL intensity mapping of narrow SPE lines, with the dashed triangle indicating the position of the mono-layer WSe_2 [38].

Beyond SPDs, 2D materials have also been widely explored for image sensor arrays, which are widely used for cameras and biomedical imaging. In 2017, Goossens et al.

doi:10.6342/NTU202501239

introduced a graphene/PbS colloidal quantum dot (CQD) image sensor array with an ultrahigh responsivity exceeding 10^7 A/W, covering an exceptionally broad wavelength range from 300 to 2000 nm, as illustrated in Figure 1-5 [39].

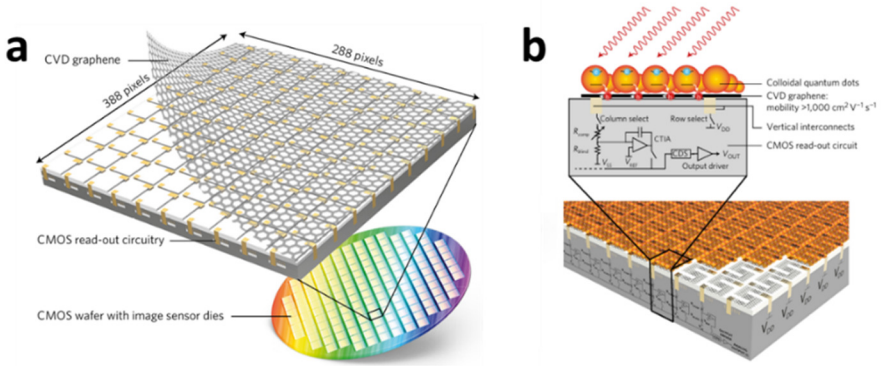

Figure 1-5 Schematic diagrams of (a) the transfer of chemical vapor deposition graphene onto a 388×288 pixel image sensor array, and (b) the image sensor array with PbS CQDs [39].

Recently, the integration of 2D materials with ANNs has opened new possibilities for intelligent sensing. In 2020, Mennel et al. demonstrated a WSe_2-based ANN sensor capable of image classification and encoding, as illustrated in Figure 1-6 [40]. This development enables potential applications of 2D materials in automatic systems, robotic systems, and smart surveillance.

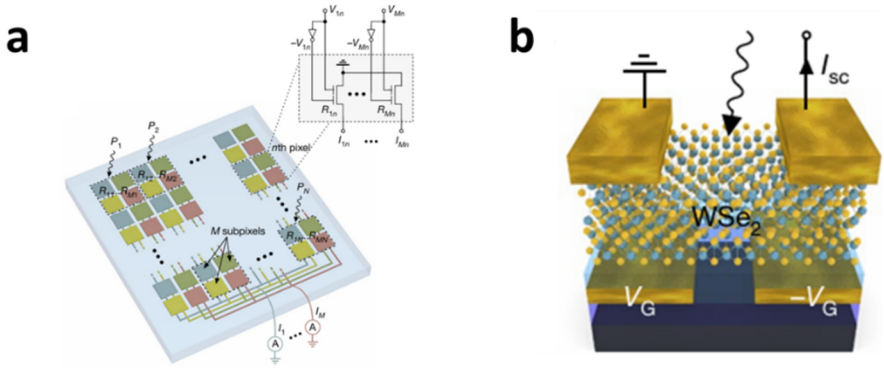

Figure 1-6 Schematic diagram of (a) the ANN photodiode array, with sub-pixels of the same color connected in parallel. And (b) a single WSe_2 photodiode [40].

doi:10.6342/NTU202501239

2D materials also show great promise for light-emitting devices such as LEDs and lasers. Their atomic-scale thickness enables precise control over light-emission properties, making them ideal for the development of more efficient and compact devices, an essential feature for miniaturized and integrated optoelectronic systems. For instance, in 2023, Shin et al. fabricated micro-light-emitting diodes (μLEDs) based on 2D materials, as shown in Figure 1-7 [41]. By integrating 2D materials with semiconductors, they successfully developed vertical RGB μLEDs capable of emitting red, green, blue, yellow, orange, cyan, pink, purple, and white light through RGB color mixing [41]. This breakthrough demonstrates significant potential for applications in display technology, optical communications, and wearable devices.

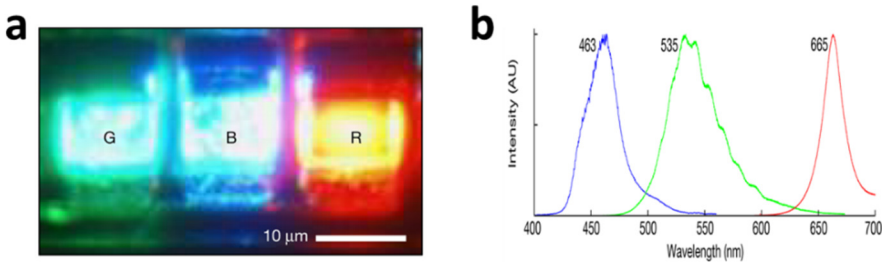

Figure 1-7 (a) EL images and corresponding (b) normalized EL spectra of a vertical RGB μLED device in the dark [41].

In summary, 2D materials have shown outstanding performance and great potential in photovoltaics, photodetection, and light emission, opening new opportunities for high-efficiency optoelectronic devices. Furthermore, researchers are also exploring their applications in plasmonics [42], metamaterials [43], optical modulators [44], and nonlinear optics [45]. The unique structure and exceptional properties of 2D materials make them highly attractive for optical applications, driving rapid progress in the field. While challenges remain, ongoing research and development are expected to facilitate for the commercialization of optoelectronic devices based on 2D materials.

doi:10.6342/NTU202501239

1.2 Fundamental Properties of 2D Materials

1.2.1 Classification of 2D Materials

2D materials exhibit a wide range of electrical, optical, and mechanical properties, making them highly versatile for various technological applications. To date, density functional theory (DFT) calculations have predicted or identified potential layered materials of over 1,800 layered materials [46]. According to their electronic properties, they can be divided into six categories: superconductors, metals, semi-metals, half-metals, semiconductors, and insulators [47]. Each category possesses unique properties that determine its suitability for different applications, as shown in Figure 1-8 [47].

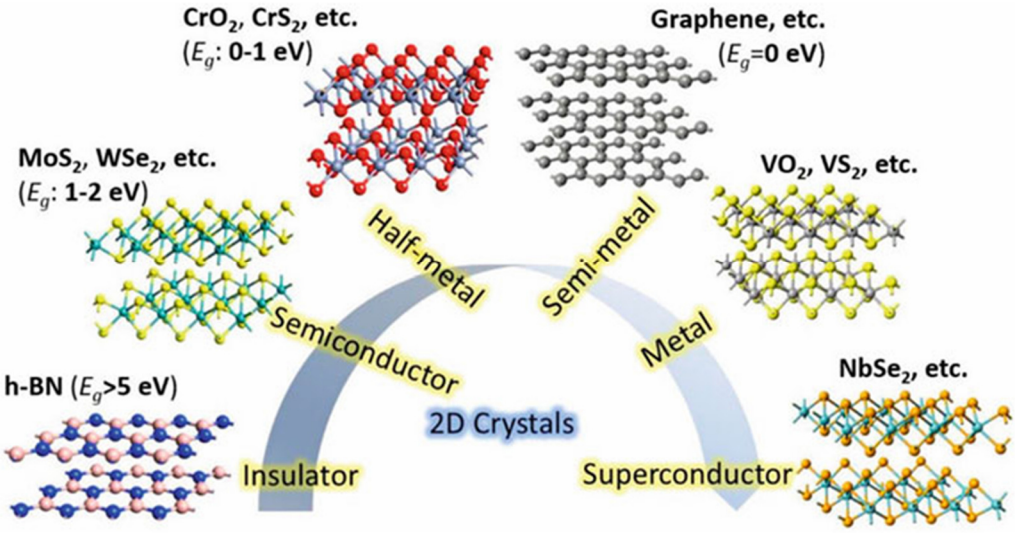

Figure 1-8 2D materials with different properties [47].

First, superconducting 2D materials exhibit zero electrical resistance (R) below a critical temperature (T_C), enabling lossless current flow. Examples include mono-layer $NbSe_2$ (Figure 1-9) [48] and $LaAlO_3/SrTiO_3$ heterostructures [49], both of which show strong potential for use in quantum computing, energy-efficient electronics, and superconducting circuits. Superconducting 2D materials enable ultra-low-power, high-speed devices, making them promising for future electronics and quantum technologies.

doi:10.6342/NTU202501239

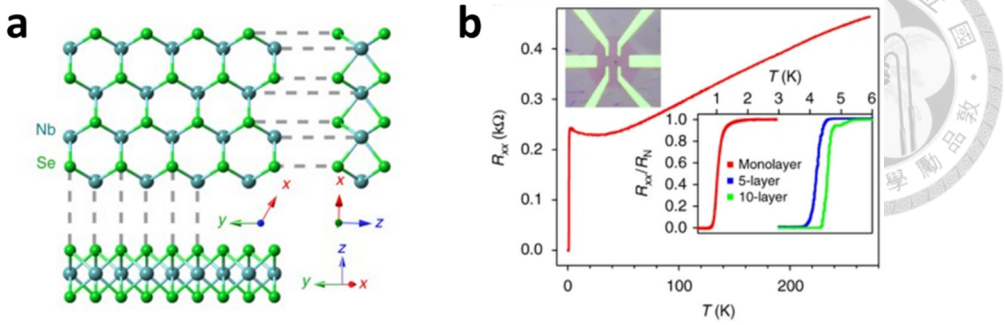

Figure 1-9 (a) Schematic diagram of the atomic structure of $NbSe_2$ crystal and (b) temperature dependence of the longitudinal resistance R_{xx} of $NbSe_2$ devices [48].

Regarding metallic 2D materials, they are well known for their excellent electrical conductivity. This is attributed to their delocalized electrons and high density of states at the Fermi level, which enable efficient charge transport. Examples of such materials include TiS_3 and TaS_2 [50, 51]. Notably, Sipos et al. reported that the resistivity (ρ) of TaS_2 decreases with increasing temperature at ambient pressure, as shown in Figure 1-10 (a) [51]. Furthermore, when subjected to specific temperature and pressure conditions, TaS_2 undergoes a transition from a metallic to a superconducting state, as illustrated in Figure 1-10 (b) [51].

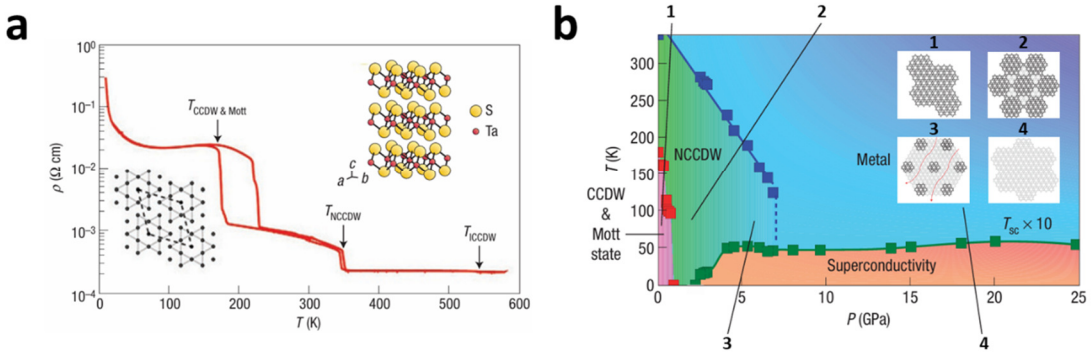

Figure 1-10 (a) Crystal structure of 1T-TaS_2 and resistivity at different temperatures. (b) Temperature-pressure phase diagram of 1T-TaS_2 [51].

doi:10.6342/NTU202501239

Next, graphene, the first experimentally isolated 2D material, can be classified as a semi-metal with properties that fall between those of metals and semiconductors [2]. Owing to the ability of electrons in graphene to travel long distances without significant scattering, it is widely regarded as an ideal channel material for high-speed electronic devices [52]. However, the lack of a band gap prevents graphene-based transistors from achieving proper on/off switching, which restricts its application in conventional electronic switching devices [53]. Even so, its excellent electrical conductivity, high optical transmittance, and outstanding mechanical strength offer significant potential for applications in transparent electrodes, broadband photodetectors, and flexible electronic devices, as shown in Figure 1-11 [54-56].

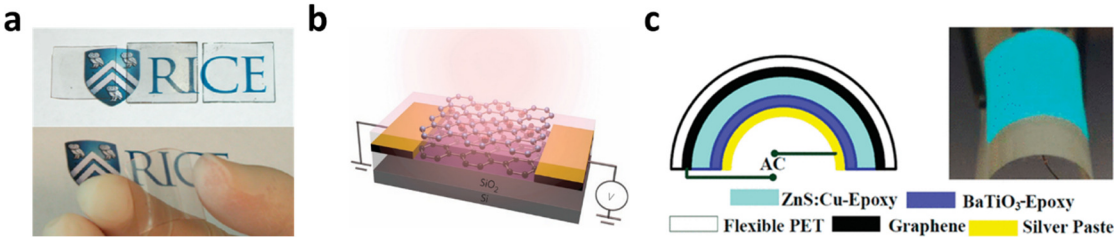

Figure 1-11 (a) Graphene transparent electrodes on glass (top) and PET (bottom) substrates [54]. (b) Schematic of graphene heterostructure photodetector [55]. (c) Schematic and photo of flexible graphene electroluminescent device after bending [56].

Half-metallic 2D materials exhibit a unique electronic property in which electrons with one spin orientation behave metallically while electrons with the opposite spin orientation exhibit insulating behavior [57]. This spin-dependent conduction makes them highly attractive for applications in spin-based logic circuits and spintronics [58]. For example, Ashton et al. conducted theoretical calculations on three 2D iron halides, $FeCl_2$, $FeBr_2$, and FeI_2 , with their structures shown in Figure 1-12 (a) [59]. Due to quantum confinement effects, these materials exhibit exceptionally large spin gaps, suggesting

doi:10.6342/NTU202501239

their potential use in 2D spin valves and other advanced spintronic devices, as shown in Figure 1-12 (b) [59].

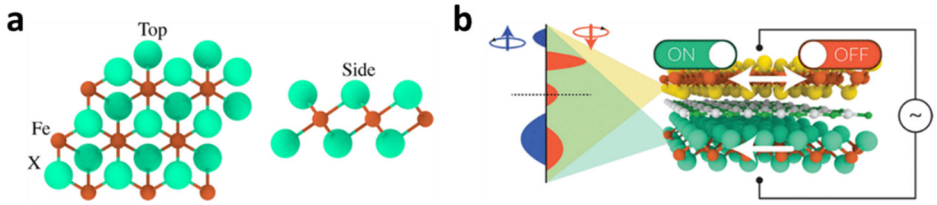

Figure 1-12 (a) Top and side views of the 1T structure of 2D iron dichalcogenides and (b) schematic diagram of their possible applications [59].

When discussing semiconducting 2D materials, TMDs (MoS_2, WS_2, and WSe_2) stand out due to their wide range of band gaps, which enable a variety of applications, including devices such as transistors, photodetectors, and solar cells [24, 37, 40]. Although their mobility is lower than that of metallic 2D materials, their high tunability makes them essential for next-generation optoelectronic technologies. Many researchers have suggested that integrating two-dimensional materials with silicon could help overcome the limitations of Moore's Law, as illustrated in Figure 1-13 [60].

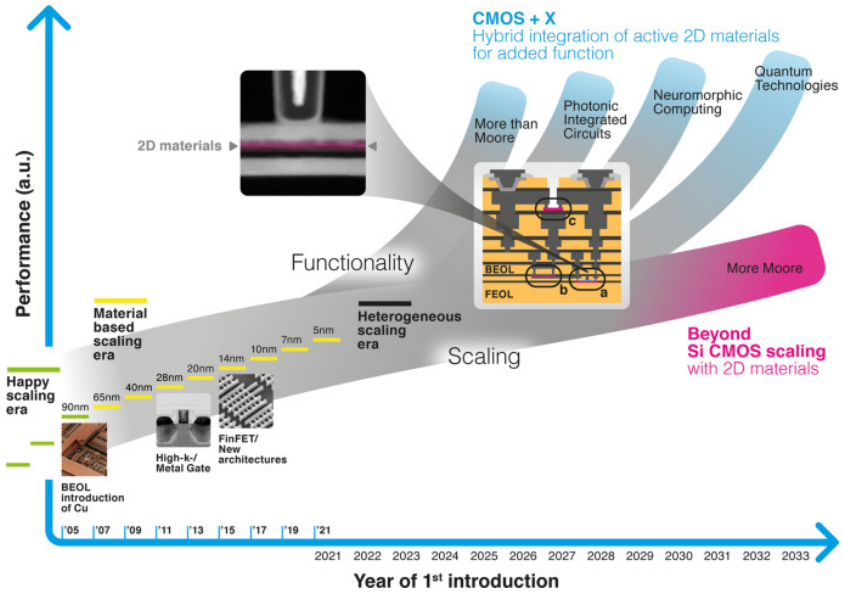

Figure 1-13 The evolution of silicon technology miniaturization and its feasibility in merging with 2D materials [60].

doi:10.6342/NTU202501239

Finally, insulating 2D materials also play an important role in electronic devices. Materials such as boron nitride are known for their high resistivity, relatively low dielectric constant (κ), and ability to sustain a high breakdown field, which allows devices to withstand high voltages without failure, as shown in Figure 1-14 (a-b) [61]. These properties can prevent unwanted leakage currents and improve overall device reliability. By controlling charge carrier behavior and enhancing device stability, insulating 2D materials enable more precise control of electronic functions, which is essential for the development of high-performance, low-power electronics. For this reason, they are often used as dielectric layers or tunnel barriers in various devices, including transistors, memristors, and capacitors, as shown in Figure 1-14 (c) [62-64].

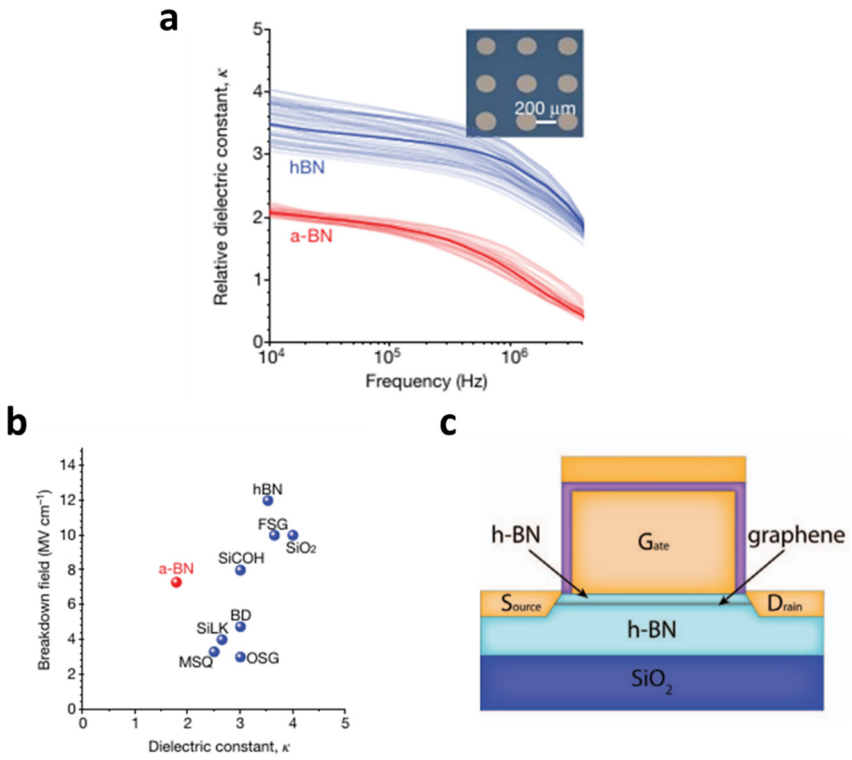

Figure 1-14 The relationship between (a) the relative dielectric constant and frequency of amorphous-BN and hexagonal-BN, as well as (b) the relationship between breakdown field and dielectric constant [61]. (c) Schematic diagram of graphene FET structure with h-BN dielectric layer [62].

doi:10.6342/NTU202501239

1.2.2 Crystal Structure of 2D Materials

2D materials feature strong in-plane covalent bonds and weak interlayer van der Waals forces, allowing them to be easily exfoliated and exhibit properties distinct from their bulk forms [9, 22]. Based on the atomic arrangement within a single layer, these materials can be roughly divided into three categories: planar honeycomb, sandwich-like, and puckered (or wrinkled) configurations, as shown in Figure 1-15 [65]. These distinct morphologies influence the electronic, optical, and mechanical properties of the materials.

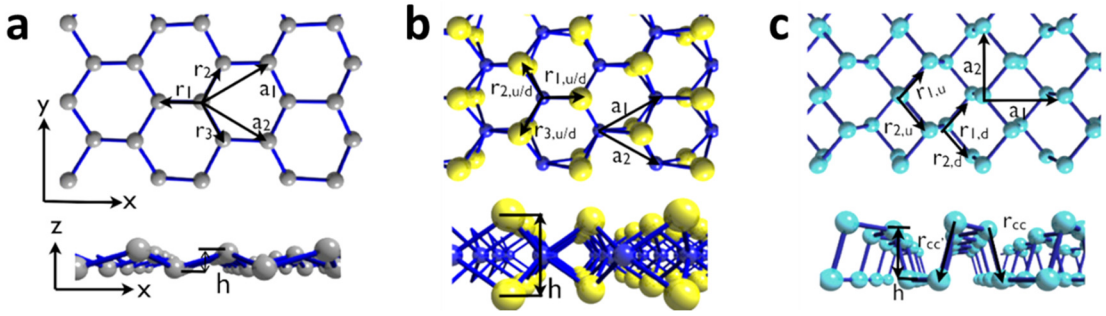

Figure 1-15 The lattice configurations of the three types of 2D materials [65].

The first category includes graphene, the first 2D material successfully exfoliated [2], as well as other graphene-like materials such as hexagonal boron nitride (h-BN), hexagonal boron phosphide (h-BP), and elemental 2D materials like silicene, germanene, and stanene. These materials exhibit highly symmetrical honeycomb (hexagonal) lattice structures, as shown in Figure 1-16 [65-74]. Among them, graphene, h-BN, and h-BP exhibit planar structures, whereas silicene, germanene, and stanene display slight buckling, with height differences along the Z-axis of 0.46, 0.64, and 0.83 Å, respectively [65, 72–74]. According to Figure 1-16, graphene features a hexagonal lattice composed of sp^2-hybridized carbon atoms, which imparts exceptional electrical conductivity. Similarly, h-BN and h-BP adopt graphene-like lattice structures, consisting of alternating hexagonal arrangements of boron and nitrogen (in h-BN) or boron and phosphorus atoms

doi:10.6342/NTU202501239

(in h-BP). Despite their structural similarities, these three materials exhibit distinctly different properties. h-BN possesses a wide bandgap of 4.67 eV, along with excellent thermal stability and electrical insulation capabilities [73]. In contrast, h-BP has a similar honeycomb structure but with a narrower bandgap ranging from 0.9 to 1.37 eV. As a relatively new material under active investigation, h-BP is expected to offer tunable bandgap characteristics and promising potential for semiconductor applications [68]. As for elemental 2D materials such as silicene, germanene, and stanene, the chemical bond strength between the nearest neighboring atoms is insufficient to maintain a perfectly planar hexagonal structure. Therefore, these materials are not sp^2 hybridized but instead have mixed sp^2/sp^3 hybridization, exhibiting slightly curved structures rather than flat planes [71, 72]. The band gaps of mono-layer graphene, silicene, germanene, and stanene are approximately 0, 0.15, 0.23, and 0.10 eV, respectively [71, 72, 75]. Moreover, these materials possess high carrier mobility, making them highly suitable for transistor fabrication [76].

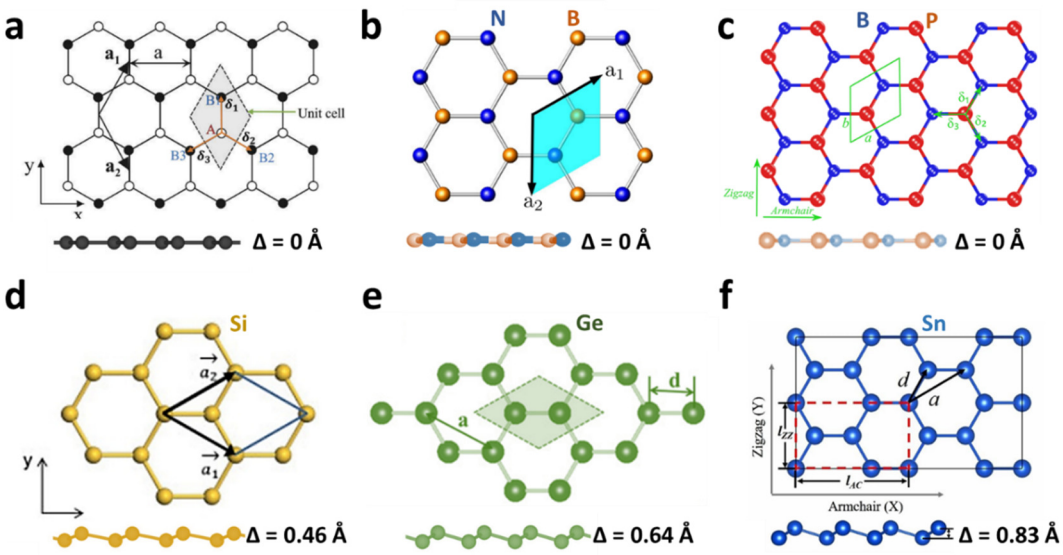

Figure 1-16 The geometric structures of graphene, h-BN, h-BP, silicene, germanene and stanene [65-74].

doi:10.6342/NTU202501239

Beyond the graphene family, another important class of 2D materials is TMDs, generally represented by the formula M_nX_m, where M is a transition metal (such as Ti, Nb, Ta, Mo, W, Pt, or Pd) and X is a chalcogen element (S, Se, or Te). Depending on the ratio of n to m, TMDs can be categorized into the well-known MX_2 structures (such as MoS_2, $MoSe_2$, WS_2, and WSe_2) and the MX structures (such as InS, InSe, GaS, and GaSe), both exhibiting layered architectures with atomic thickness and strong in-plane covalent bonding [77, 78]. In MX_2 compounds, a single layer of metal atoms is sandwiched between two layers of chalcogen atoms (X–M–X), typically forming trigonal prismatic (2H phase) or octahedral (1T phase) coordination geometries, as shown in Figure 1-17 (a-b) [77]. Compared to the 1T phase, the 2H phase features higher crystal symmetry and ABAB stacking [77]. As for MX compounds, they exhibit various lattice symmetries, which often lead to anisotropic behavior and exotic electronic properties, making them promising for applications in nonlinear optics, solar cells, and mid- to far-infrared (FIR) photodetectors, as shown in Figure 1-17 (c) [78]. Notably, many TMDs exhibit a significant bandgap transition between their bulk and mono-layer forms. For example, MoS_2 changes from an indirect to a direct bandgap semiconductor at the mono-layer limit [36]. Additionally, the lack of surface dangling bonds allows seamless stacking with other 2D materials, enabling high-quality heterostructures for optoelectronic devices [28].

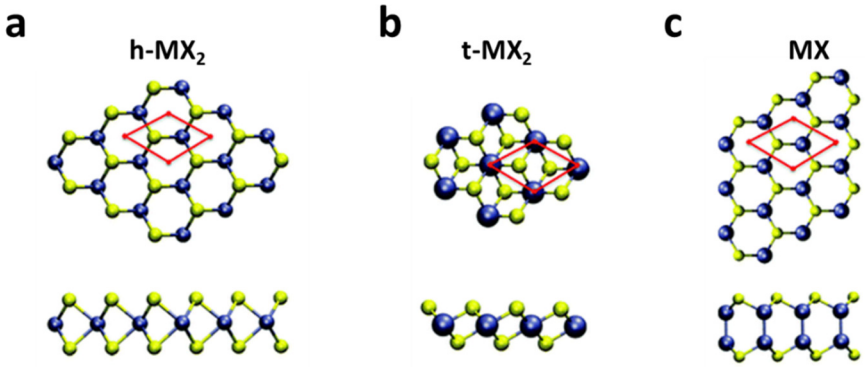

Figure 1-17 The geometric structures of transition metal dichalcogenides (M_nX_m) [77].

doi:10.6342/NTU202501239

The third category of 2D materials features puckered structures, typically composed of group V or IV–V elements with orthorhombic symmetry. Each unit cell consists of four atoms, each of which is bonded to three neighboring atoms in a pyramidal arrangement [79]. Examples include black phosphorus, arsenene, and tin sulfide (SnS), as shown in Figure 1-18 [79]. Phosphorene, a mono-layer form of black phosphorus, has a thickness-dependent bandgap (direct in mono-layer, indirect in bulk [16]) and strong in-plane anisotropy, enabling high carrier mobility for optoelectronic devices like avalanche photodetectors [80]. Black arsenic, similar to phosphorene, has a ~0.3 eV bandgap and anisotropic properties [81]. SnS adopts a puckered structure, offering enhanced piezoelectric and anisotropic properties [79]. These materials are promising for thermoelectric and optoelectronic applications due to their unique anisotropies [79].

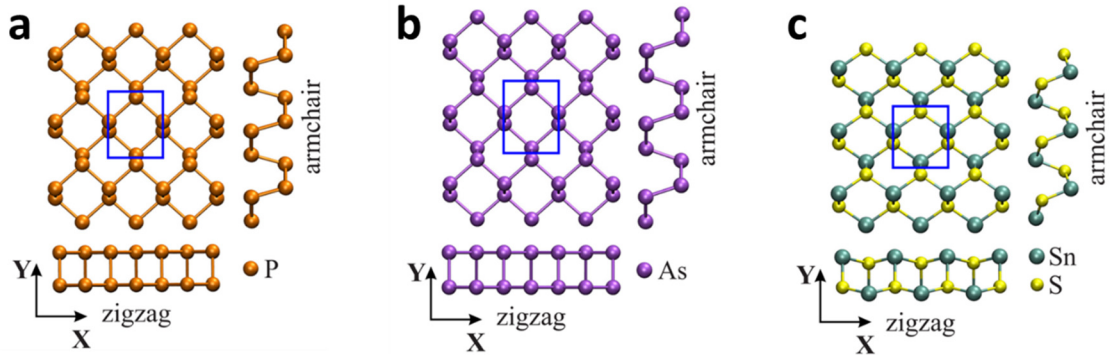

Figure 1-18 The geometric structures of (a) phosphorene, (b) arsenene, and (c) SnS [79].

In summary, planar materials typically feature stable lattice structures and are among the most representative forms of 2D materials [82]. Sandwich-like structures exhibit well-defined stacking and tunable bandgaps, while puckered materials show strong in-plane anisotropy [79, 83]. Due to the van der Waals forces between layers, these three types can be freely stacked without lattice matching, enabling new possibilities for high-quality heterostructures and multifunctional composites in optoelectronic applications [84, 85].

doi:10.6342/NTU202501239

1.2.3 Combinations of 2D Materials and Their Applications

As mentioned earlier, 2D materials exhibit diverse structural forms and a wide range of electronic, optical, and mechanical properties, making them ideal for next-generation nano-optoelectronic devices. Beyond mono-layers, growing interest has been directed toward few-layer homostructures, stacked heterostructures, and mixed-dimensional (heterodimensional) architectures [86]. As shown in Figure 1-19, these can be broadly categorized into eight types: (1) thickness-based junctions, (2) electrostatically doped junctions, (3) lateral and (4) vertical doped homojunctions, (5) lateral and (6) vertical heterostructures, and (7) 2D-0D/2D-1D and (8) 2D-3D mixed-dimensional junctions. These configurations offer greater tunability than mono-layers, enabling new opportunities in material and device design [87].

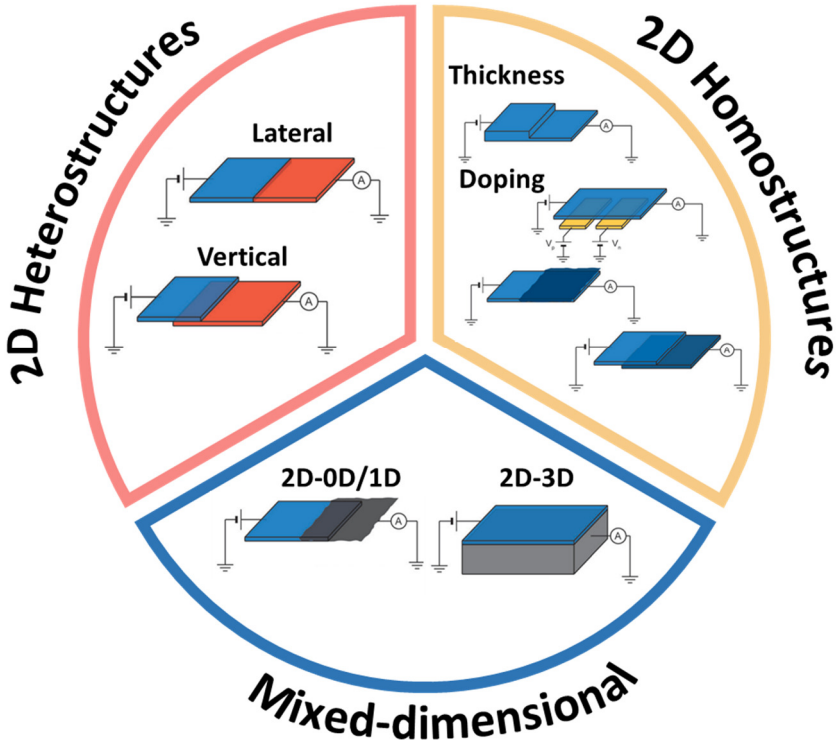

Figure 1-19 Overview of eight structural configurations based on 2D materials found in published studies [86].

doi:10.6342/NTU202501239

From an electronics perspective, both multi-layer and heterostructured 2D materials offer key advantages. Adding layers introduces interlayer coupling and modifies exciton behavior, directly impacting electron transport and device performance [88]. For instance, multi-layer MoS_2 provides higher carrier density and longer data retention in memory devices due to increased charge concentration (Figure 1-20 (a)) [89]. Thicker materials also serve as passivation layers, enhancing stability and mobility (Figure 1-20 (b)) [90]. In addition, thicker TMDs often show lower contact resistance due to better Fermi level alignment and a reduced Schottky barrier, improving FET performance (Figure 1-20 (c); blue and red indicate gold and aluminum electrodes) [91]. Heterostructures further extend these benefits by enabling tunneling mechanisms [92] and built-in electric fields, supporting multifunctional, energy-efficient nanoelectronic devices.

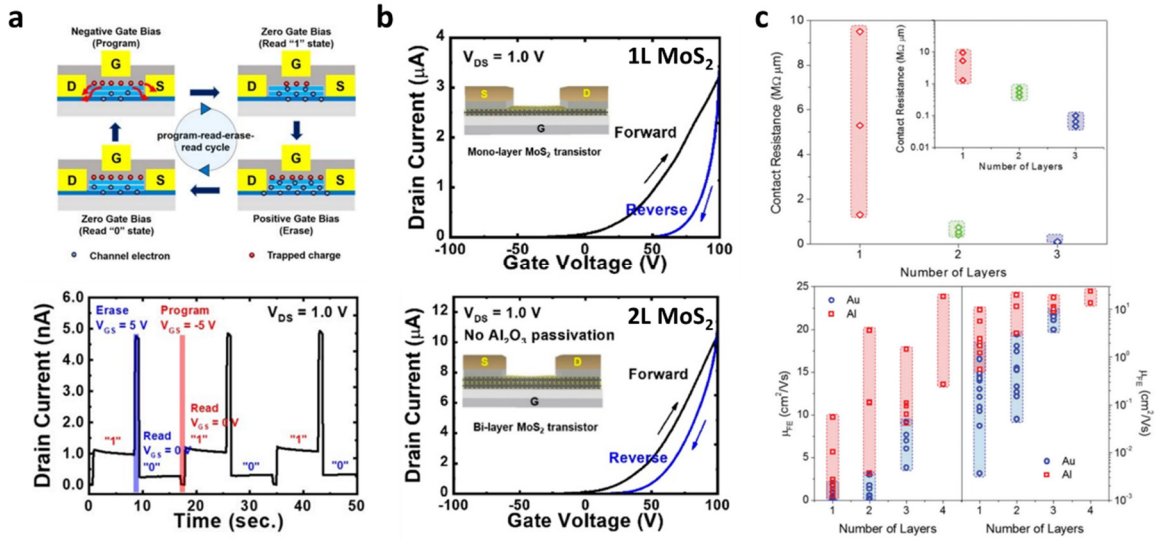

Figure 1-20 (a) Schematic of electron storage and depletion at the interface throughout different stages of the memory cycle, along with device measurements at V_{DS} = 1.0 V [89]. (b) Device transfer curves of MoS_2 transistors with mono-layer and bilayer channels [90]. (c) Contact resistance and field-effect mobility of MoS_2 FETs as a function of layer number and electrode material (gold vs. aluminum) [91].

doi:10.6342/NTU202501239

In photonics, multi-layer 2D materials, especially TMDs, have emerged as promising candidates due to their stronger light-matter interactions , enhanced optical absorption, and more pronounced excitonic effects compared to mono-layers, as shown in Figure 1-21 (a) [28, 35, 93]. At the same time, combining multiple 2D layers improves mechanical robustness, which is essential for ensuring stable device operation under harsh conditions, as shown in Figure 1-21 (b) [94]. Additionally, van der Waals heterostructures provide further tunability through band structure engineering. A representative example is the MoS_2/WSe_2 heterostructure, which exhibits type-II band alignment, enabling efficient charge separation via interlayer exciton formation [95]. As shown in Figure 1-21 (c), the spatial separation of electrons and holes in this structure facilitates effective carrier extraction [95]. These unique advantages make multi-layer and heterostructured 2D materials highly suitable for broadband and wavelength-selective photodetectors [96, 97].

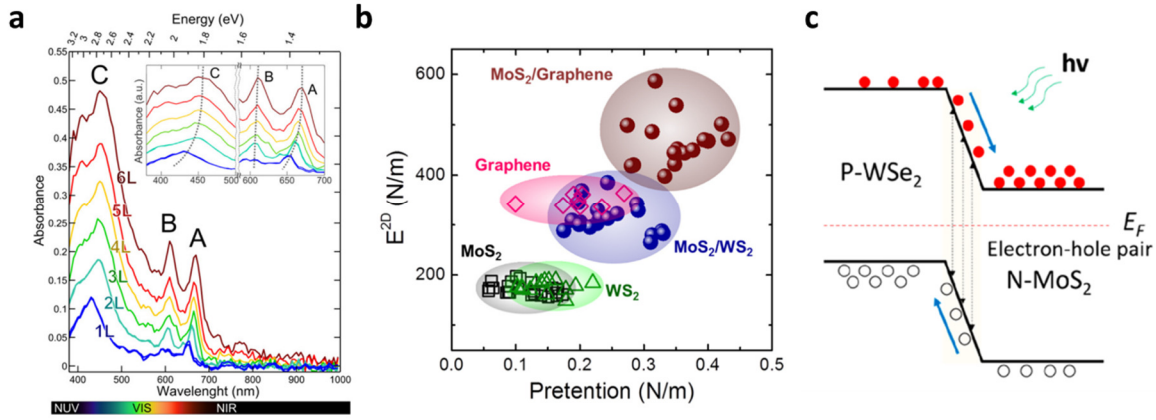

Figure 1-21 (a) Absorption spectra of MoS_2 with varying layer numbers, highlighting the A, B, and C excitonic peaks labeled accordingly [93]. (b) Experimental data on 2D moduli and prestress for various 2D layers and heterostructures [94]. (c) Energy band diagram of the MoS_2/WSe_2 van der Waals P-N heterojunction with photogenerated carriers under illumination conditions [95].

doi:10.6342/NTU202501239

1.3 Challenges and Opportunities of 2D Materials Optical Devices

1.3.1 Challenges in the Synthesis of 2D Materials

Since the first isolation of graphene [2], 2D materials have attracted widespread attention, driving the development of synthesis techniques. These methods are generally classified into top-down and bottom-up approaches [98]. In the early stages, research predominantly employed mechanical exfoliation, a top-down method using adhesive tape (or other techniques) to peel mono-layers from bulk crystals, as shown in Figure 1-1 [2-22]. Although this method produces high-quality flakes suitable for fundamental studies, its low scalability and limited process control pose major challenges for practical and industrial applications [22]. To address these limitations, this section explores alternative 2D material synthesis strategies beyond mechanical exfoliation. These include metal-assisted exfoliation (MAE), liquid-phase exfoliation (LPE), sputtering, chemical vapor deposition (CVD), atomic layer deposition (ALD), and molecular beam epitaxy (MBE), as shown in Figure 1-22.

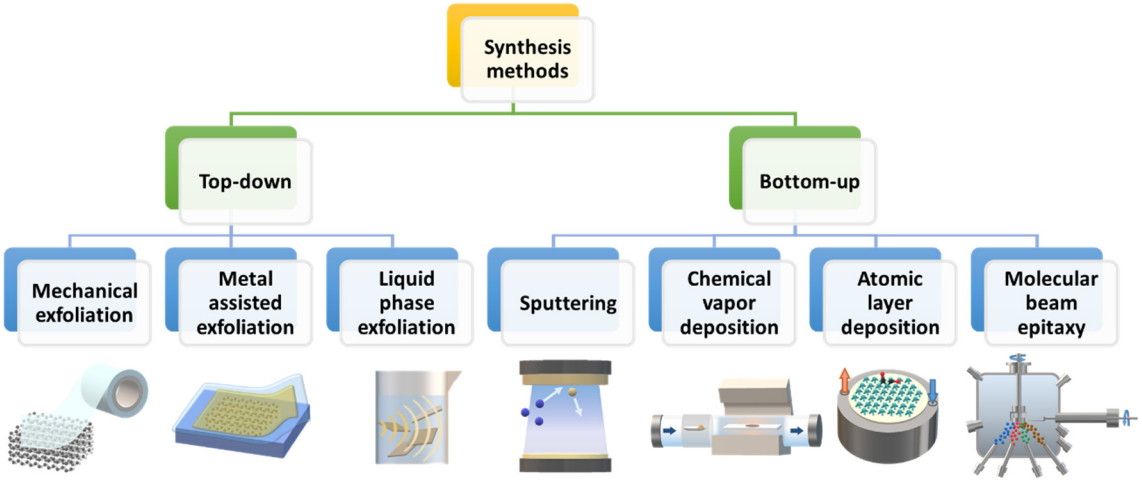

Figure 1-22 Classification of 2D material synthesis methods.

doi:10.6342/NTU202501239

Metal-assisted exfoliation (MAE) utilizes the strong affinity between certain metals (such as Co, Ni, and Au) and layered 2D materials to enable the extraction of large scale mono-layers from bulk crystals [22, 99]. When a metal film is deposited onto the crystal surface, the enhanced adhesion at the interface allows the top layer to be separated, resulting in a scalable exfoliation process. This technique is broadly applicable to various 2D materials. For instance, Huang et al. successfully exfoliated 40 distinct single-crystal mono-layer 2D materials using this method [22].

Another widely used top-down synthesis technique is liquid-phase exfoliation (LPE), which employs ultrasonic to disperse bulk materials into mono- or few-layer nanosheets within a suitable solvent. For example, Coleman et al. exfoliated WS_2, MoS_2, $MoSe_2$, and $MoTe_2$ using 21 different solvents [9]. However, although LPE is applicable to a variety of 2D materials, problems such as poor thickness uniformity, defects, and residual contamination limit its application in high-performance devices.

On the other hand, sputtering is a bottom-up synthesis method that uses high-energy ions to bombard a target material, causing atoms to be ejected and deposited onto a substrate to form a large scale and uniform film [100, 101]. It often provides good consistency and compatibility with traditional semiconductor processes. However, the high-energy particles may damage the atomic structure of 2D materials, and achieving high crystallinity remains challenging [102].

Meanwhile, bottom-up CVD is considered one of the most promising methods for synthesizing large scale, high quality mono-layer films [103]. This method utilizes the vaporization of precursors at high temperatures to nucleate and grow a two-dimensional crystal layer on a substrate [103-104]. By fine-tuning parameters such as precursor

doi:10.6342/NTU202501239

concentration, temperature, pressure, and substrate selection, the quality and uniformity of the resulting films can be significantly improved [104].

As for ALD, although it has traditionally been used for oxides and dielectrics, recent advances have expanded its application to the growth of 2D materials, particularly TMDs [105-106]. ALD is a relatively new technique that enables atomic scale thickness control through sequential, self-limiting surface reactions [107]. Because precursors and reactants are introduced in separate steps and isolated by purge cycles, the chemical reactions occur exclusively on the surface, making them highly dependent on the properties of the underlying substrate and requiring precise tuning of precursor chemistry and reaction conditions [106-107].

In addition, molecular beam epitaxy (MBE) also represents a promising method for the synthesis of 2D materials. In this technique, an elemental source is thermally evaporated to produce a molecular beam that deposits atoms layer by layer onto a heated substrate [108]. Although the use of high-purity elemental sources and ultra-high vacuum conditions facilitates the production of high-purity 2D materials, stringent control over the vacuum and temperature environment, as well as precise adjustment of growth parameters, is required—posing challenges for large scale production [108].

In conclusion, various methods have been developed for synthesizing 2D materials. Exfoliation is simple and low-cost but lacks thickness control and scalability. CVD enables large scale growth, ALD provides atomic-level precision, and MBE ensures high purity and crystallinity. However, all require complex conditions and higher costs [109]. An ideal synthesis method has yet to be established, and challenges remain in achieving controlled, scalable fabrication.

doi:10.6342/NTU202501239

1.3.2 Stability and Endurance of 2D Materials

2D materials feature strong in-plane covalent bonds and weak interlayer van der Waals forces, making them easy to exfoliate and giving them properties distinct from their bulk counterparts. However, their atomic-scale thickness makes stability and durability critical for practical applications. This section will address three key aspects: environmental stability, mechanical property, and thermal stability.

Environmental stability is a major concern for 2D materials. According to Geim et al., they can be classified into three groups: graphene-like materials, 2D chalcogenides, and 2D oxides [82]. Their stability under environmental conditions is summarized in Figure 1-23, showing a step-like distribution [82]. Some materials are highly sensitive to moisture, oxygen, and UV light, which can lead to performance degradation over time. For example, TMDs oxidize when exposed to air, while black phosphorus degrades rapidly upon air exposure due to its moisture sensitivity, limiting its practical use [110-112]. To address these issues, researchers are developing strategies such as surface passivation, encapsulation, and protective coatings to enhance environmental resistance [90, 112].

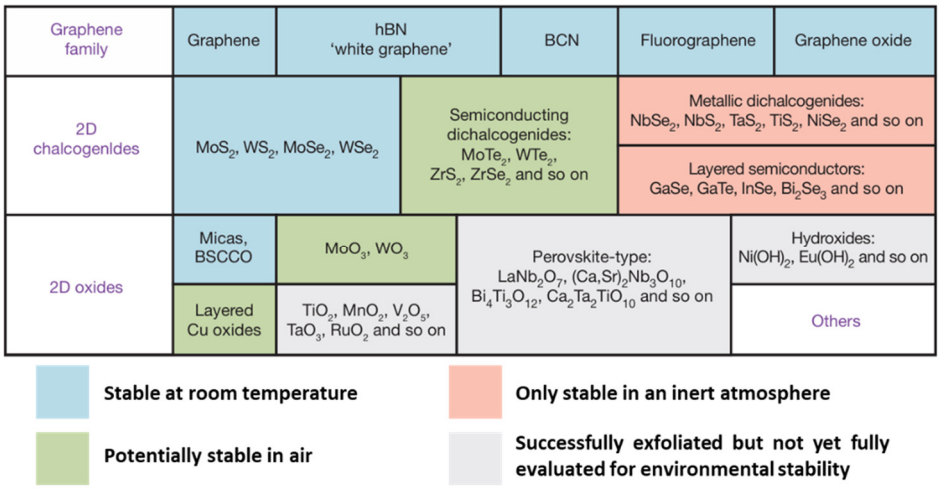

Figure 1-23 Stability distribution map of 2D materials [82].

doi:10.6342/NTU202501239

In addition to environmental considerations, the mechanical properties of 2D materials are also important. As shown in Figure 1-24, the Young's modulus of various 2D materials is presented [113]. Graphene and h-BN, in particular, exhibit exceptionally high Young's modulus values, indicating their high stiffness and resistance to deformation [113]. However, Young's modulus only reflects the material's response to a single deformation and does not capture its performance under repeated mechanical stress, such as bending or stretching. According to the study by Cui [114], and Liu [115] et al. on the fatigue life of graphene and MoS_2, the results indicate that the level of applied stress has a significant impact on the fatigue behavior of these materials [115]. Under identical stress conditions, MoS_2 exhibits a fatigue life that is 6-7 orders of magnitude shorter than that of the more flexible graphene. In this case, evaluating the mechanical characteristics of 2D materials based on specific application requirements is essential.

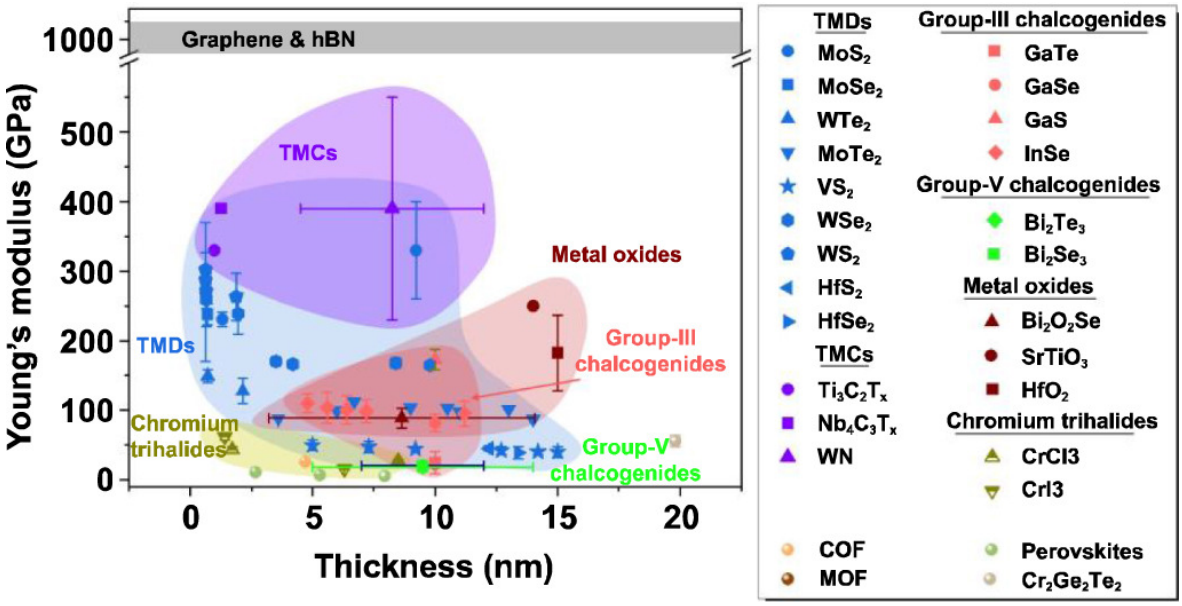

Figure 1-24 An overview of thickness-dependent in-plane elasticity in emerging 2D materials, determined through AFM-based deflection measurements [113].

doi:10.6342/NTU202501239

The stability of 2D materials under high temperature conditions is also a critical concern, as heating caused by factors such as current flow and light absorption is usually unavoidable [116]. Due to their atomically thin nature, 2D materials are highly susceptible to thermal disturbances at elevated temperatures, which may lead to structural reorganization or even decomposition. Different material systems exhibit fully different thermal stabilities. For example, although single-layer graphene possesses strong covalent C-C bonds and demonstrates excellent thermal stability, Raman spectroscopy measurements by Nan et al. indicate that it begins to degrade at approximately 520 °C, as shown in Figure 1-25 (a) [117]. Beyond graphene, the high temperature stability of other 2D materials has also been investigated. According to Wang et al.'s analysis of the thermal stability of MoS_2, the choice of substrate has a direct impact on the material's thermal behavior, as shown in Figure 1-25 (b) [118]. Overall, ensuring the thermal stability of 2D materials is crucial for their reliable integration into practical applications.

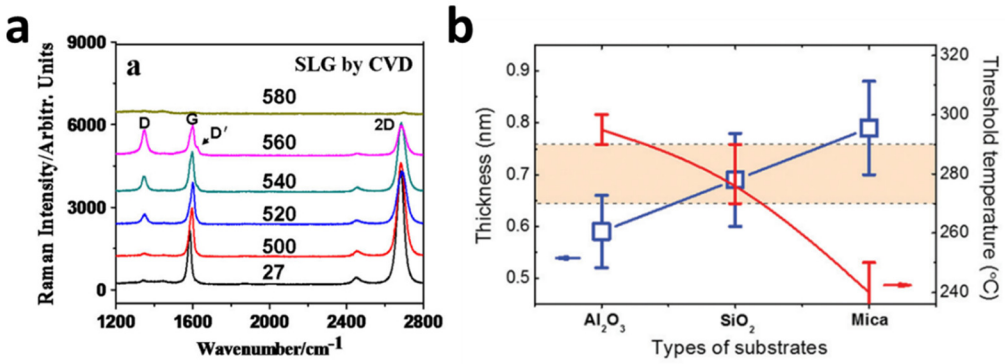

Figure 1-25 (a) Confirmation of graphene defect formation via Raman spectroscopy [117]. (b) Thickness of mono-layer MoS_2 on different substrates and the corresponding threshold temperature for initiating thermal etching [118].

In summary, although 2D materials exhibit excellent properties, their stability under diverse conditions remains a challenge. How to assemble them and enhance device stability is an important issue.

doi:10.6342/NTU202501239

1.3.3 Integration of 2D Materials in Device Architecture

Due to their unique thin body nature and excellent electrical and optical characteristics, 2D materials are promising candidates for next-generation optoelectronic devices. By van der Waals stacking, they can be integrated into various device architectures without being restricted by lattice matching, thus providing significant design flexibility [84, 85]. To further explore their potential, beyond devices based solely on 2D materials, extensive research has focused on combining them with photonic structures (such as microcavities [119], microresonators [120], metamaterials [121], antennas [122], photonic crystals [123], and waveguides [124]) to enhance light-matter interactions, thereby enabling high-performance optoelectronic systems, as shown in Figure 1-26 [119-124].

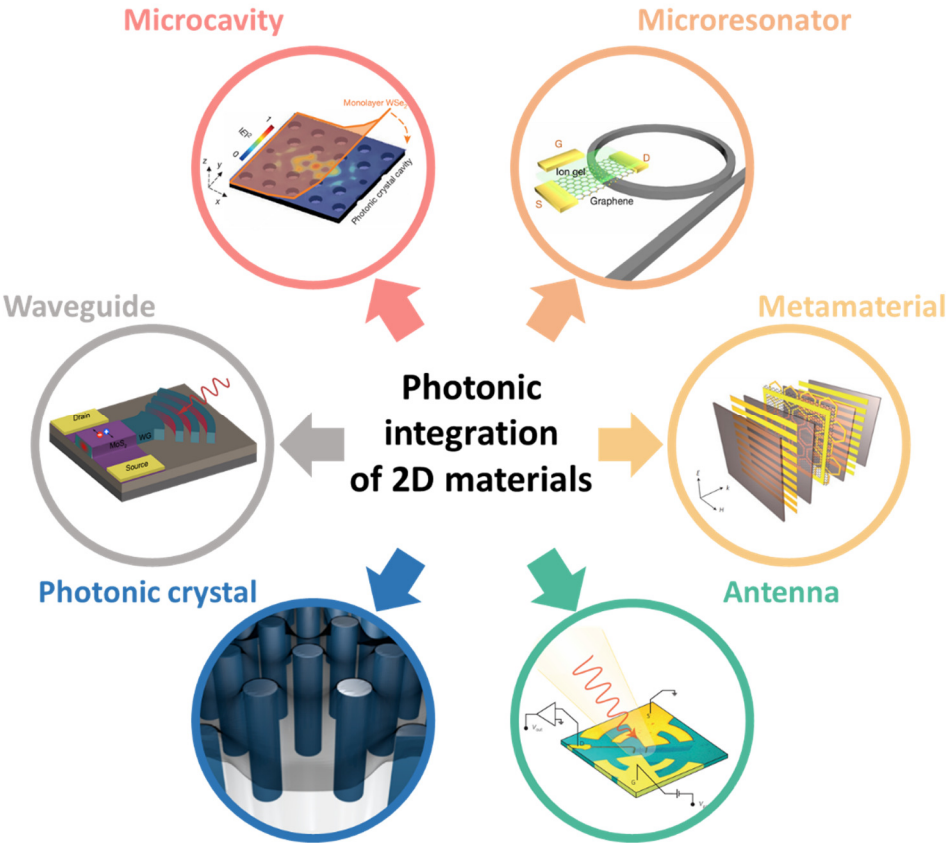

Figure 1-26 Applications of photonic integration of 2D materials [119-124].

doi:10.6342/NTU202501239

Although tuning the layer number or stacking different 2D materials via van der Waals interactions offers flexibility in engineering band structures, constructing p-n junctions, and forming tunnel junctions, major challenges remain in their practical integration and application. The following section introduces three key issues: (1) large-area synthesis and mass transfer, (2) high Schottky barriers and contact resistance, and (3) long-term stability and reliable packaging.

As mentioned earlier (Section 1.3.1), achieving large scale, highly uniform synthesis of 2D materials remains a major challenge. Although current mainstream methods, such as CVD synthesis, have optimized material properties at the laboratory, precise control of defect density, grain boundary management, and layer uniformity is still required. In particular, minimizing defect states at material interfaces is critical for optimizing device performance [109]. Regarding material transfer, in addition to achieving large-area transfer, reducing residual contaminants on the films is equally important [125]. Overall, large-area synthesis and semiconductor-compatible transfer techniques are important to commercialization [109].

Second, interface engineering and high contact resistance are also bottlenecks that limit the performance of 2D material-based devices The lack of dangling bonds on 2D material surfaces, while beneficial for creating clean stacked interfaces, often results in the formation of high Schottky barriers and contact resistance when interfacing with metal electrodes [90, 126-127]. This in turn reduces carrier injection efficiency and adversely affects device switching ratios and response speeds. To address this problem, several strategies have been developed, including heavy doping of the semiconductor and the introduction of semi-metallic materials (such as Sb and Bi) as inter layers, which can effectively reduce the contact resistance, as illustrated in Figure 1-27 [90, 126, 127].

doi:10.6342/NTU202501239

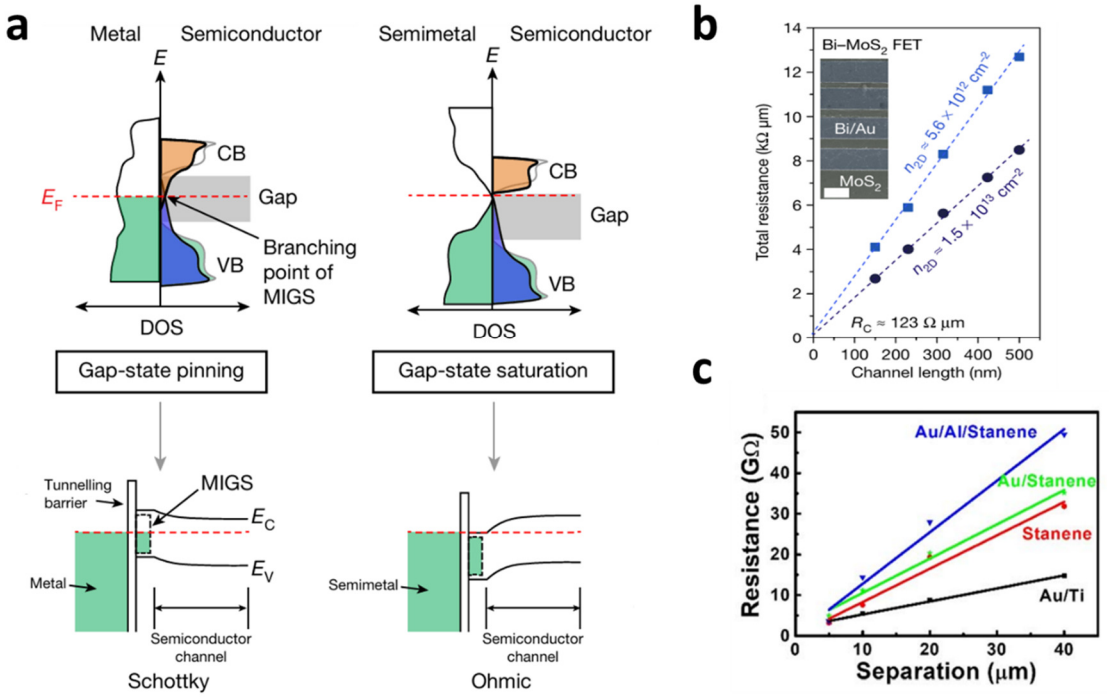

Figure 1-27 (a) Density of states (DOS) of metal-semiconductor and semimetal-semiconductor contacts, along with the corresponding band structure diagrams [126]. Resistance values versus electrode separation for (b) Bi-MoS_2 FETs [126] and (c) four samples with Au/Ti, stanene, Au/stanene, and Au/Al/stanene electrodes [127].

Third, the long-term stability and reliable packaging of 2D material devices are also critical issues that must be addressed, as detailed in Section 1.3.2. Due to their atomically thin nature, 2D materials are highly sensitive to environmental factors such as oxygen, moisture, and light, leading to degradation, performance deterioration, or even device failure [82]. Consequently, effective encapsulation techniques have been developed, including ALD of ultrathin oxide layers such as Al_2O_3, HfO_2, h-BN, and the implementation of multi-layer encapsulation structures such as double graphene encapsulation, to protect devices from environmental attacks and improve their operational lifetime and stability, as shown in Figure 1-28 [128-131].

doi:10.6342/NTU202501239

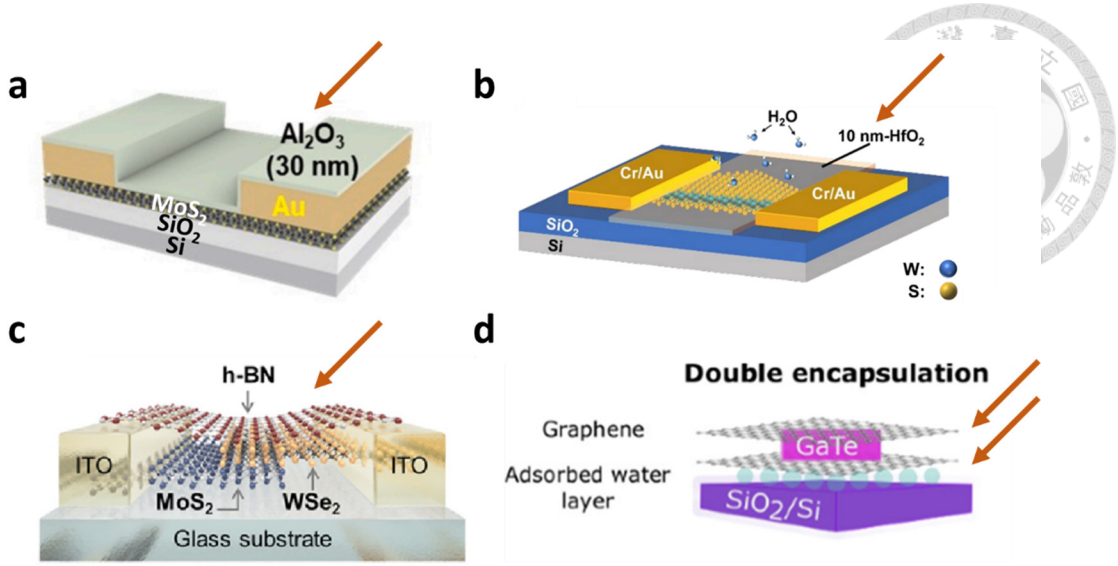

Figure 1-28 Schematic diagram of (a) a polycrystalline MoS_2 transistor with Al_2O_3 passivation [128], (b) a WS_2 nanosheets photodetector passivated with HfO_2 [129], a MoS_2/WSe_2 solar cell with h-BN passivation [130], and (d) GaTe passivated by double graphene encapsulation [131].

With the continuous advancement of manufacturing technology, the large-area synthesis and mass transfer technology of two-dimensional materials have also been steadily improved. The problems of high Schottky barriers and contact resistance have gradually been overcome, and the long-term stability can also be significantly improved by adding a passivation layer. This enables 2D materials to be applied to various fields, and even combined with traditional semiconductor technology to move towards large scale commercial production. All these developments demonstrate the great potential of 2D material-based optoelectronic devices. Accordingly, this work explores the application of 2D materials in various optical devices, including the use as transparent conductive electrodes in perovskite solar cells (Chapter 3), light-absorbing layers in vertical photovoltaic devices, carrier transport and light-absorbing layers in planar heterostructured photoconductive devices (Chapter 4), and transmission layers in heterodimensional structured photodetectors (Chapter 5).

doi:10.6342/NTU202501239

1.4 Applications of 2D Materials in Next-Generation Optical Technologies

1.4.1 Transparent Electrode

Transparent electrodes (TEs) are critical components in numerous optoelectronic devices, including displays, touch screens, solar cells, and LEDs [132, 133]. Traditional materials such as indium tin oxide (ITO) have been widely used as TEs due to their high transparency (over 90% in the visible range) and excellent conductivity [134]. However, ITO also has several drawbacks: it is brittle, expensive, and typically requires high temperature deposition (~400 °C) [135]. Moreover, when ITO TEs are fabricated via sputtering processes, plasma-induced damage may occur, compromising underlying layers or light-absorbing materials, further limiting device performance and scalability [136]. Therefore, in addition to ITO, people are also exploring a variety of different transparent conductive electrodes, as shown in Table 1-1 [134, 137-141].

Table 1-1 Comparison of various transparent electrode [134, 137-141].

Material Name	Type	Conductivity (S/cm)	Transmittance (%)	Advantages	Disadvantages
ITO (Indium Tin Oxide)	Oxide	~10^3	80–90	High transparency and conductivity	High-temperature deposition
FTO (F-doped SnO_2)	Oxide	~10^3	80–85	Good thermal stability; cheaper than ITO	Lower conductivity
AZO (Al-doped ZnO)	Oxide	~10^4	~80	Low-temperature deposition; low cost	Less stable
Graphene	Carbon (2D)	~10^4	>97	Transparency, and mechanical strength	Limited conductivity vs. metals; challenging fabrication
CNT (Carbon Nanotubes)	Carbon	10^2–10^4	85–90	Lightweight, and flexible	Variable conductivity
PEDOT:PSS	Conductive Polymer	~10^2–10^3	>80	Simple solution processing	Moisture/oxygen-sensitive
Ag Nanowires (Ag NWs)	Metallic Nanostructure	>10^4	>90	Flexibility; high transparency	Moisture/oxygen-sensitive
Metal Mesh	Metal Structure	>10^4	70-90	Flexible; tunable architectures	Limited resolution; high cost

doi:10.6342/NTU202501239

As shown in the table above, carbon nanotubes (CNTs), nanowires (NWs), and metal meshes all offer good transmittance and high conductivity. However, a major challenge for carbon nanotubes lies in the difficulty of obtaining large quantities of material with sufficient purity, which makes it difficult to precisely control their conductivity [140]. Nanowires are highly susceptible to moisture, oxygen, and high temperature environments [140]. Metal meshes tend to reduce overall transparency and photocurrent collection efficiency [140]. On the other hand, solution-processed TEs, such as PEDOT:PSS, can be fabricated using scalable techniques like spin coating and inkjet printing and offer advantages such as mechanical flexibility [142, 143]. However, issues related to interface quality and material degradation often lead to poor long-term stability [140].

In this case, the large scale synthesis of 2D materials has been steadily developed (Section 1.3.1), and the materials are generally stable under ambient conditions (Section 1.3.2). Their excellent transparency, combined with van der Waals forces that enable easy stacking onto various structures or devices (Section 1.3.3), make them promising candidates for next-generation TEs. Mono-layer graphene, for instance, absorbs only ~2.3% of visible light, while offering efficient charge transport and excellent mechanical flexibility, making it ideal for TEs in wearable devices [144]. Although its sheet resistance is higher compared to that of ITO, there is room for improvement [145,146]. Nonetheless, graphene has already been employed as a transparent electrode in type-II superlattice IR photodetectors, enabling top-side infrared illumination [147]. You et al. have also utilized CVD-grown graphene as a TE in perovskite solar cells (PSCs) [148]. Furthermore, modern roll-to-roll printing techniques have been applied to the large scale production of 2D materials [149,150], highlighting graphene's strong potential as a TE.

doi:10.6342/NTU202501239

1.4.2 Energy Harvesting Systems

With the growing urgency for renewable energy to mitigate dependence on fossil fuels, energy harvesting systems have emerged as a central solution to the global energy crisis [151]. Among these, solar energy, an abundant and sustainable resource, has positioned photovoltaic (PV) technologies at the forefront of development efforts. As shown in Table 1-2 [152-158], silicon-based solar cells currently dominate the commercial market due to their relatively high power conversion efficiency (PCE) [152]. In addition to silicon, alternative thin-film technologies such as cadmium telluride (CdTe), copper indium gallium selenide (CIGS) [153, 154], and emerging perovskite solar cells, and dye-sensitized solar cells [155, 156] have been introduced to diversify solar energy collection approaches. However, conventional single-junction solar cells are fundamentally limited by the Shockley–Queisser (SQ) limit, which caps their theoretical maximum efficiency at around 30% [151, 157]. To overcome this limitation, tandem and multi-junction solar cells have been developed as a strategic solution. By integrating multiple absorbers with complementary bandgaps, these architectures broaden the usable solar spectrum and enhance overall device efficiency [159, 160]. According to the U.S. National Renewable Energy Laboratory (NREL), a record-breaking four-junction solar cell developed by the Fraunhofer Institute has achieved a power conversion efficiency of 47.4% [161, 162], while perovskite/silicon tandem solar cells have surpassed the 33% efficiency threshold [163].

As shown in Table 1-2 [152-158], although current 2D material solar cells still exhibit relatively low efficiencies in laboratories, they offer broad optical absorption across the entire solar spectrum [28, 158]. Furthermore, their multi-layer structures can significantly enhance light absorption [164]. Even at nanometer-scale thicknesses, two-

doi:10.6342/NTU202501239

dimensional TMDs are capable of absorbing approximately 10% of incident solar radiation and can generate photocurrent through band structure engineering [165]. Since 2013, the PCE of 2D material-based photovoltaic devices has increased rapidly, rising from around 1% to nearly 5% in 2014 [166]. Additionally, thanks to van der Waals forces, these materials can be easily assembled into heterostructures without lattice matching requirements, enhancing charge separation and minimizing recombination to improve solar cell efficiency [84, 85]. Other material combinations exhibiting type-II band alignment, such as MoS_2/WS_2 [167], MoS_2/BP [168], $MoSe_2/WSe_2$ [169], GaTe/MoS_2 [170], and $MoTe_2/MoS_2$ [171], have also demonstrated enhanced photovoltaic effects, and various 2D materials have been successfully implemented in high-performance photovoltaic devices. Moreover, 2D materials can be conveniently transferred onto various interfaces and integrated into hybrid solar cells, offering extended absorption beyond that of conventional photovoltaic materials. For instance, in 2015, Song et al. reported a graphene/silicon Schottky barrier solar cell that achieved a record PCE of 15.6% [172]. In 2017, Dai et al. reported a hybrid solar cell combining 2D materials with perovskites, reaching a PCE of 16.47% [173]. Although their efficiency has not yet surpassed that of traditional photovoltaic technologies, the ultra-thin and light-weight nature of 2D materials makes them highly promising for flexible and wearable photovoltaic applications [158]. Therefore, employing 2D materials alone or incorporating them into hybrid architectures is expected to open new avenues for cost-effective solar energy solutions, especially in applications requiring flexibility and durability.

doi:10.6342/NTU202501239

Table 1-1 Comparison of various solar cells [152-158].

Type	Materials / Structure	Efficiency	Cost	Advantages	Disadvantages
Silicon	Monocrystalline / Polycrystalline Si	12-17.5%	Medium	Mature tech, stable	Rigid, relative high cost
Thin Film	CdTe, CIGS	9-12%	Low–Medium	Flexible, lighter, cheaper than Si	Toxic elements (Cd), lower stability (CIGS)
Perovskite Solar Cells (PSC)	Perovskites (ABX_3)	<30%	Low	High efficiency potential, tunable bandgap	Degradation in air/moisture, and toxicity (Pb)
Dye-Sensitized Solar Cells (DSC)	TiO_2 + dye molecules + liquid electrolyte	<15%	Low	Without the use of toxic materials, design flexibility	Liquid electrolyte leakage, stability issues
Tandem / Multi-junction	Perovskite/Si, III-V stacks	>33% (lab)	High	Breaks single-junction limit, very high efficiency	Complex fabrication, expensive
2D Material Solar Cells	MoS_2, WS_2, graphene, WSe_2, heterostructures	~5–10%	Experimental	Ultra-thin, flexible, transparent	Low efficiency, interface engineering challenges

doi:10.6342/NTU202501239

1.4.3 Sensitive Photodetectors

Another promising application of 2D materials is photodetection, which has become foundational to many modern applications as the field matures. A common example is the photodetector, which converts incident light into measurable electrical signals. Photodetectors are essential in optical communications [174], autonomous driving systems [175], wearable sensors [176], and facial recognition technologies [177].

In general, the working mechanisms of photodetectors include the photovoltaic (PV), photoconductive (PC), photogating (PG), and photothermoelectric (PTE) effects [178]. These mechanisms define the operating modes, performance characteristics, and application scopes of the devices. First, PV-mode photodetectors rely on the built-in electric field within a p-n junction or Schottky junction to efficiently separate photogenerated electron-hole pairs, enabling photocurrent generation without external bias. This self-powered characteristic is highly advantageous in practical applications, such as in solar cells, which are based on this mechanism [179]. In contrast, PC-mode photodetectors typically require an external bias to generate the electric field needed for separating and collecting photocarriers. Nevertheless, they can achieve high photoconductive gain (G) when using materials with either short carrier transit times or long carrier lifetimes [180, 181]. The PG effect, on the other hand, provides an indirect, gate-like control mechanism. Upon illumination, a portion of the photogenerated carriers becomes trapped in localized states, such as surface defects or interface traps, inducing a local electric field. This field modulates the carrier density in the channel region [182], altering its conductivity and enabling ultra-high gain and sensitivity. Lastly, the PTE effect converts light-induced heating into a temperature gradient that drives a

doi:10.6342/NTU202501239

thermoelectric voltage (ΔU), making it ideal for broadband detection from mid-infrared (MIR) to terahertz (THz) wavelengths [183].

For decades, semiconductor photodetectors, particularly silicon-based devices, have maintained a dominant position in the field of optoelectronics, as shown in Table 1-3 [26, 178, 182, 184-191]. Their success is largely attributed to compatibility with mature CMOS fabrication processes, low manufacturing costs, and reliable performance across the visible to near-infrared (NIR) spectrum [184]. Fast response times and ease of integration with modern electronic systems make them ideal for applications such as imaging, optical communication, and consumer electronics [184, 185]. However, silicon photodetectors also face inherent limitations. Their absorption is confined to wavelengths below ~1100 nm, restricting their effectiveness in MIR and broadband detection [180, 185]. Additionally, silicon's rigidity limits its suitability for emerging applications in wearable and flexible electronics [180]. To overcome these challenges, researchers have turned to a range of alternative materials for next-generation photodetection technologies.

Table 1-3 summarizes the internal mechanisms and performance of common photodetector systems, including semiconductors, quantum dots (QDs), topological insulators (TIs), metal oxides/nitrides, perovskites (PVSKs), and 2D materials [26,178,182, 184-191]. Quantum dots, with their size-tunable bandgaps and high absorption coefficients, enable customizable detection across the visible to IR range [186]. Their solution-processability makes them attractive for flexible and large-area devices [186, 187]. Nonetheless, QD devices often suffer from low carrier mobility and instability due to surface traps and environmental sensitivity [186]. Topological insulators, such as Bi_2Se_3, offer unique surface states with high carrier mobility and spin-momentum locking [188, 189]. These properties are advantageous for broadband detection mechanisms, such

doi:10.6342/NTU202501239

as the PTE effect, particularly in the MIR to THz range [188, 189]. However, bulk conduction and material synthesis challenges limit their practical deployment [188]. Metal oxide and nitride-based photodetectors are valued for their UV sensitivity, chemical stability, and thermal robustness, making them suitable for harsh environments [190]. Meanwhile, perovskite photodetectors, renowned for their strong light absorption, long carrier diffusion lengths, and solution-processability, exhibit competitive performance in the visible spectrum [191]. However, their environmental instability, particularly their sensitivity to moisture and ion migration, remains a major challenge to achieving long-term operational reliability [191].

In contrast, 2D materials offer a highly tunable platform with electronic properties ranging from metallic to semiconducting to insulating [47]. This versatility enables the deliberate integration of charge transport and light-absorbing layers, enhancing gain and photo-response. Their atomically thin structure and mechanical flexibility make them well-suited for flexible electronics [26, 178]. Additionally, van der Waals interactions allow for the formation of high-quality heterostructures with diverse materials, circumventing lattice matching requirements [84, 85]. These hybrid systems extend spectral response, improve sensitivity, and enable novel detection mechanisms [26, 178, 182].

As the demand for faster, more sensitive, energy-efficient, and flexible photodetectors grows, traditional semiconductor technologies face inherent limitations [180, 185]. In this context, 2D material-based photodetectors, particularly those integrated with complementary materials, emerge as a promising direction for next-generation, high-performance, and application-specific optoelectronic devices [26, 178, 182].

doi:10.6342/NTU202501239

Table 1-2 Comparison of various photodetectors [26, 178, 182, 184-191].

Type	Materials	Mechanism	Responsivity (R)	Response Time (τ)	Advantages	Disadvantages
Semiconductors	Si, InGaAs etc.	PV (PC)	Commercial Si: ~0.12–0.5 A/W Commercial InGaAs: ~0.22–1.2 A/W	ns – μs	Mature fabrication, high stability	Limited spectral coverage
Quantum Dots (QDs)	PbS, InAs, CdSe QDs etc.	PG, PC (PV)	<20 A/W	μs – ms	Tunable bandgap, solution processable	Toxicity, poor stability
Topological Insulators (TIs)	Bi_2Se_3, Bi_2Te_3, Sb_2Te_3 etc.	PV, PC, PTE	~0.1–10^3 A/W	μs – ms	Low-power and broad-spectrum	Complex synthesis, high noise
Metal Oxides/Nitrides	ZnO, Ga_2O_3, GaN etc.	PC, PV	~0.1–10^3 A/W	ns – μs	Low-cost, capability of bandgap engineering	Poor stability (nanostructured)
Perovskites	$MAPbI_3$, $CH_3NH_3PbI_2$, etc.	PV, PC, PG	~0.1–10^3 A/W	μs – ms	High absorption, large gain, easy to fabricate	Instability, toxicity
2D Materials	MoS_2, WS_2, InSe, BP, Graphene	PV, PC, PG, PTE	~0.1–10^4 A/W	ps – s	Flexible, high gain and bandwidth	Low absorption, demands high crystallinity

doi:10.6342/NTU202501239

Chapter 2 Growth Approaches and Characterizations of 2D Materials

2.1 Synthesis of 2D Materials

2.1.1 Low Pressure Chemical Vapor Deposition System

CVD is widely employed in the semiconductor industry (e.g., for SiO_2 and HfO_2) to produce high-purity, high-quality thin films. It is also a key technique for synthesizing 2D materials. In a typical CVD process, vapor-phase precursors are introduced into a heated chamber, where they react or decompose on the substrate surface to form a thin film. Meanwhile, by-products are continuously removed by the carrier gas to prevent their accumulation. Depending on the operating pressure, CVD can be categorized into atmospheric pressure CVD (APCVD), low-pressure CVD (LPCVD), and ultra-high vacuum CVD (UHVCVD). In this study, to improve the uniformity of the graphene film, deposition was performed under low pressure to suppress undesirable gas-phase reactions. The system setup is illustrated in Figure 2-1 (a). The graphene film was grown on an atomically flat 1.5 × 1.5 cm^2 copper foil by high temperature cracking of C_2H_6, using an LPCVD system consisting of a single-zone tube furnace (model T11-301, SJ High Technology Company), a 1-inch quartz tube, a magnetron quartz sample holder, mass flow controllers (MFC), a pressure control unit (pressure controller and capacitive vacuum gauge), and a mechanical pump, as shown in Figure 2-1.

To grow graphene, it is essential to ensure the cleanliness of both the quartz tube and the copper foil surface; therefore, a high temperature annealing step is performed initially. During the annealing process, the chamber must be evacuated using a mechanical pump.

doi:10.6342/NTU202501239

In this system, the quartz tube is sealed at both ends with O-rings to maintain vacuum conditions and is supported by a water-cooling system to prevent damage and loss of vacuum. A KD1000-1-CH MFC is used to introduce 10 sccm of Ar as the carrier gas, and the pressure is monitored and maintained at 330 mtorr using an MKS-626B12TBE pressure controller. The copper foil, loaded onto the quartz sample holder, is placed at the center of the furnace. The furnace temperature is ramped to 1030 °C at a rate of 20 °C/min and held for 60 minutes to ensure thorough cleaning of the copper surface. After completing the high temperature annealing, graphene is grown at the same temperature. C_2H_6 (15 sccm) and H_2 (7 sccm) are additionally added into the chamber, and the pressure is controlled at 660 mtorr for 30 minutes. At this temperature, C_2H_6 decomposes, facilitating the growth of single-layer graphene on the copper foil. Upon completion of the growth, a magnetic bracket is used to quickly remove the substrate from the hot zone for air cooling, preserving the quality of the synthesized graphene film.

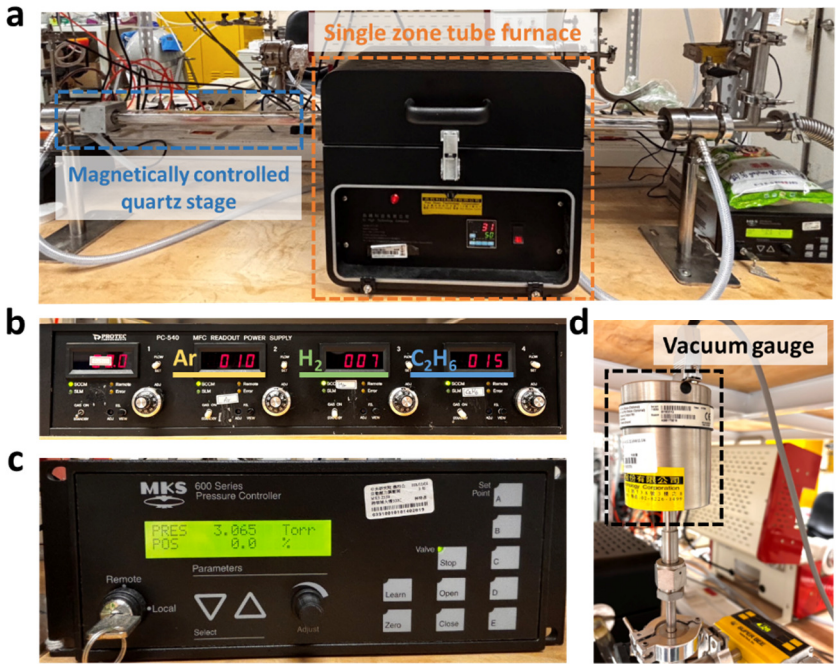

Figure 2-1 (a) Graphene growth system, (b) mass flow controller, (c) pressure controller, and (d) capacitive vacuum gauge.

doi:10.6342/NTU202501239

2.1.2 Sputtering System

Sputtering is a widely used physical vapor deposition (PVD) technique. Unlike CVD, which relies on chemical reactions to form solid films, sputtering produces purer films using simpler and more mature equipment. The process involves introducing an inert gas, typically argon (Ar), into a vacuum chamber and ionizing it using radio frequency (RF) power. These ions are then accelerated toward a cathode target, dislodging atoms from the target material, which subsequently deposit onto the substrate. In this study, an RF magnetron sputtering system was employed to deposit multi-layer MoS_2 films. The process involves two steps: (1) Ar is used to bombard the amorphous MoS_2 target (from Summit-Tech, 99.9%), depositing amorphous MoS_2 onto a single-sided polished C-plane sapphire substrate; (2) high temperature sulfurization is performed in a low-pressure system (the detailed information will be disclosed in Section 2.1.4). This section will focus on the deposition system and methods used for growing amorphous MoS_2. The RF magnetron sputtering system consists of a vacuum chamber (with a stage temperature control panel), a mechanical pump, a diffusion pump, RF signal cable and its control panel, a capacitive vacuum gauge, a pressure controller, and a MFC, as shown in Figure 2-2.

For the pre-deposition of multi-layer MoS_2, the sapphire substrate is initially placed in the sputtering chamber (stage maintain at room temperature), as shown in Figure 2-2 (a). The chamber pressure is initially reduced to approximately 3×10^{-2} torr using a mechanical pump, and then further decreased to below 1×10^{-5} torr with a diffusion pump, as shown in Figure 2-2 (b). The diffusion pump operates as follows: it heats diffusion oil to produce high-speed vapor jets that collide with gas molecules inside the chamber, entraining them and carrying them toward cooled surfaces maintained by liquid nitrogen.

doi:10.6342/NTU202501239

The vapor and captured gas molecules condense on these surfaces, and the resulting liquid is removed by a mechanical pump, allowing the diffusion pump to maintain a high vacuum without moving mechanical parts. Once high vacuum is achieved, the target can then be bombarded with ionized argon gas, initiating deposition. In this step, a KD1000-1-CH MFC regulates the Ar flow rate at 30 sccm, while a high-vacuum valve and a full-range vacuum gauge maintain the pressure at 4×10^{-3} torr, as shown in Figure 2-2 (c-d). As depicted in Figure 2-2 (e-f), after connecting the RF signal cable, the RF power is set to 60 W, and the sputtering time can be controlled between 40-240 seconds by switching the shutter on and off (see Section 4.2.3 for details). These settings ensure a stable high-vacuum environment and precise control over gas flow and pressure, both of which are crucial for the high-quality deposition of MoS_2 films.

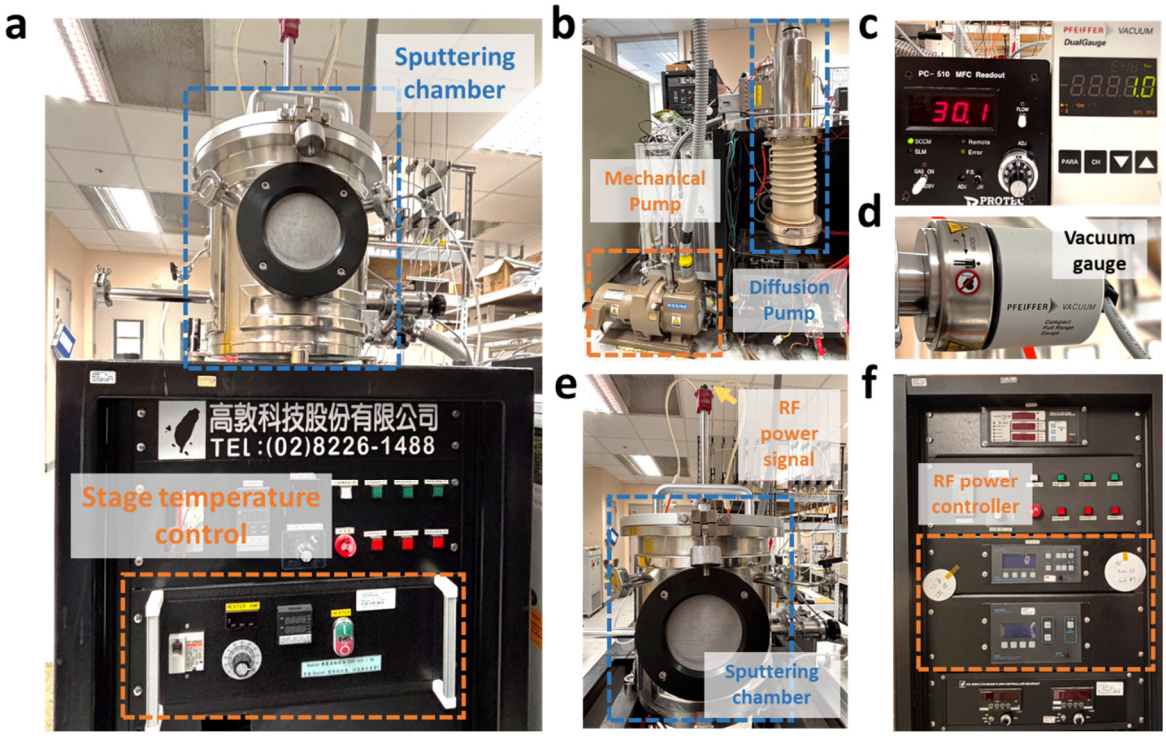

Figure 2-2 (a) Sputtering chamber, (b) mechanical and diffusion pumps, (c) MFC, (d) full-range vacuum gauge, (e) RF signal connector, (f) RF signal control panel.

doi:10.6342/NTU202501239

2.1.3 Atomic Layer Deposition System

ALD is a technique for growing materials one atomic layer at a time, allowing precise control over layer thickness and producing high-quality films with excellent uniformity across large areas. Unlike the previously mentioned CVD and sputtering systems, ALD introduces precursors into the reaction chamber sequentially, where they undergo saturated chemical adsorption and self-limiting surface reactions [107]. This process enables atoms to stack layer by layer, forming a thin film. Although the deposition rate is slower than in the previously mentioned systems, ALD offers atomic-level control over film thickness and uniformity.

The ALD system employed in this study was used to deposit highly crystalline single-layer MoS_2 films. The process mainly involves two steps: (1) pre-deposition of MoO_3 on a single-sided polished C-plane sapphire substrate, and (2) high temperature sulfurization in a low-pressure system (detailed information will be provided in Section 2.1.4). This section focuses on the systems and methods used for the pre-deposition of MoO_3. The ALD equipment was purchased from Syskey Technology Co.，Ltd., as shown in Figure 2-3 (a). It consists of a reaction chamber, an ozone generator, a precursor supply system, a gas flow control system, a temperature control system, and a mechanical pump, as depicted in Figure 2-3 (b-d).

For the pre-deposition of MoO_3, a sapphire substrate was placed in the reaction chamber, and the chamber pressure was reduced to below 1×10^{-2} torr using a mechanical pump. The temperature of the chamber was carefully controlled at 180 °C to optimize the deposition conditions. The ALD deposition process of MoS_2 generally involves four fundamental steps:

doi:10.6342/NTU202501239

(1) Pulse:

The precursor $Mo(CO)_6$ and ozone (O_3) from the ozone generator are introduced into the reaction chamber. The precursor and O_3 molecules adsorb onto the substrate surface, where they undergo chemical reactions.

(2) Soak:

After the precursor and ozone pulse, the chamber is maintained at stable pressure and temperature for a set time to allow the precursors to fully adsorb and react on the sapphire substrate, ensuring surface reactions reach a self-limiting point with no excess material deposited.

(3) Purge:

An inert gas (N_2) is introduced to flush out remaining precursor molecules and reaction products, ensuring only the desired material remains on the substrate.

(4) Pump:

The chamber pressure is reduced by a vacuum system to eliminate residual gases and by-products, preparing the system for the next ALD cycle.

These steps are repeated cyclically to precisely control the MoO_3 layer thickness before high temperature sulfurization.

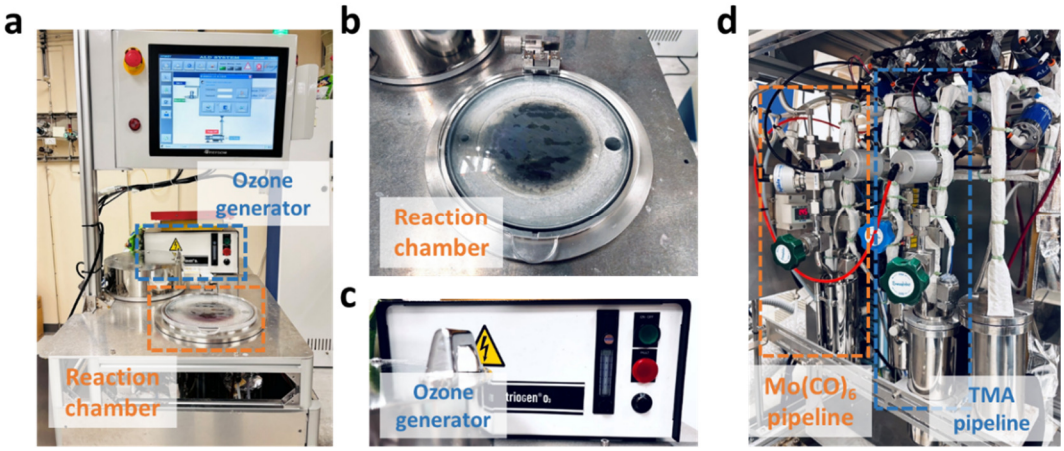

Figure 2-3 (a) ALD deposition system, (b) reaction chamber, (c) ozone generator and (d) precursor pipeline.

doi:10.6342/NTU202501239

This study also used the same ALD system to deposit Al_2O_3, as shown in Figure 2-3. For the deposition of Al_2O_3, the sapphire substrate was placed in the reaction chamber, and the chamber pressure was reduced to below 1×10^{-2} torr using a mechanical pump. The chamber temperature was carefully controlled at 180 °C to optimize deposition conditions. The ALD deposition process of Al_2O_3 generally involves four basic steps:

(1) Pulse:

The precursors trimethylaluminum (TMA) and H_2O were introduced into the reaction chamber. The precursors and H_2O molecules adsorb onto the substrate surface, where chemical reactions take place.

(2) Soak:

After the precursor and H_2O pulse, the chamber is held at stable pressure and temperature to ensure complete surface reactions and self-limiting growth on the sapphire substrate.

(3) Purge:

Inert gas (N_2) is introduced to flush out any remaining precursor molecules and reaction products, ensuring that only the desired materials remain on the substrate.

(4) Pump:

The vacuum system depressurizes the chamber to remove residual gases and by-products, preparing the system for the next ALD cycle.

These steps are repeated cyclically to precisely control the thickness of the Al_2O_3 layer.

doi:10.6342/NTU202501239

2.1.4 Low Pressure Sulfurization System

As described in Sections 2.1.2 and 2.1.3, both single and multi-layer MoS_2 films are grown using a two-step precursor conversion process. Therefore, after the pre-deposition of amorphous MoS_2 (Sputtering system) and Mo oxide (ALD system), high temperature sulfurization is required to improve crystallinity or convert Mo oxide into MoS_2 film. The high temperature sulfurization system described in this section closely resembles the LPCVD system outlined in Section 2.1.1. As shown in Figure 2-4 (a), the setup consists of a single-zone tube furnace (model T11-301, SJ High Technology Company), a 3-inch quartz tube, a quartz stage, a heating belt system, a MFC, a pressure control unit (comprising a pressure controller and a capacitive pressure gauge), and a mechanical pump. To create an independent temperature control zone, the heating belt is wrapped around the quartz tube at a position 23.5 cm from the entrance. This configuration effectively isolates the sulfurization zone from the main heating area of the furnace, enabling precise control over both temperature and reaction duration.

For high temperature sulfurization of MoS_2, the process begins with an annealing step to clean the quartz tube and stage. The quartz stage is placed at the center of the furnace, and the chamber is evacuated using a mechanical pump, as shown in Figure 2-4 (b-c). Then, 200 sccm of Ar is introduced through the KD1000-1-CH MFC. The furnace is heated to 500 °C at a rate of 20 °C/min and held briefly at that temperature to ensure sufficient thermal cleaning. Afterward, the system is allowed to cool naturally to room temperature. This annealing process effectively removes residual contaminants and ensures the cleanliness of both the quartz stage and tube, providing a clean environment for the subsequent high temperature sulfurization. After that, the high temperature sulfurization reaction can be started. The pre-deposited sapphire substrate (either

doi:10.6342/NTU202501239

amorphous MoS_2/sapphire or MoO_3/sapphire grown by ALD) is placed on the quartz stage and positioned at the center of the furnace. Simultaneously, an alumina crucible containing 0.25 grams of sulfur powder, serving as the sulfur source, is placed in an independently temperature-controlled zone established by a heating belt. This zone is regulated by a separate temperature controller (HT-720), as shown in Figure 2-4 (d-f). After setup, the chamber is evacuated to 10^{-3} torr using the mechanical pump. Then, 200 sccm of Ar is introduced through the KD1000-1-CH MFC, as illustrated in Figure 2-4 (g). The chamber pressure is maintained at 50 torr using the MKS-626B12TBE pressure controller and vacuum gauge, as shown in Figure 2-4 (h-i). The furnace is subsequently heated to 850 °C at a rate of 20 °C/min, while the independent temperature controlled zone is maintained at 90 °C. This dual-zone temperature control ensures that when the furnace center reaches 600 °C, the independent zone stabilizes at 160 °C, allowing sulfur to begin sublimating and initiating the sulfurization process. The sulfur vapor, carried by the Ar flow, enters the high temperature zone and reacts with the pre-deposited molybdenum precursor, resulting in the large scale and uniform MoS_2 film. Note that the sputter-deposited amorphous MoS_2/sapphire sample, being a multi-layer, undergoes 20 minutes of sulfurization at 850°C, while the MoO_3/sapphire sample grown by ALD requires only 5-minute at the same temperature.

In this way, the LPCVD high temperature sulfurization system effectively transforms the pre-deposited molybdenum samples into high-quality, large scale MoS_2 films. By precisely controlling the temperature, pressure, and sulfurization time, the system ensures that the molybdenum precursors undergo a controlled sulfurization process, resulting in MoS_2 films with enhanced crystallinity and uniformity, suitable for a range of optoelectronic and electronic applications.

doi:10.6342/NTU202501239

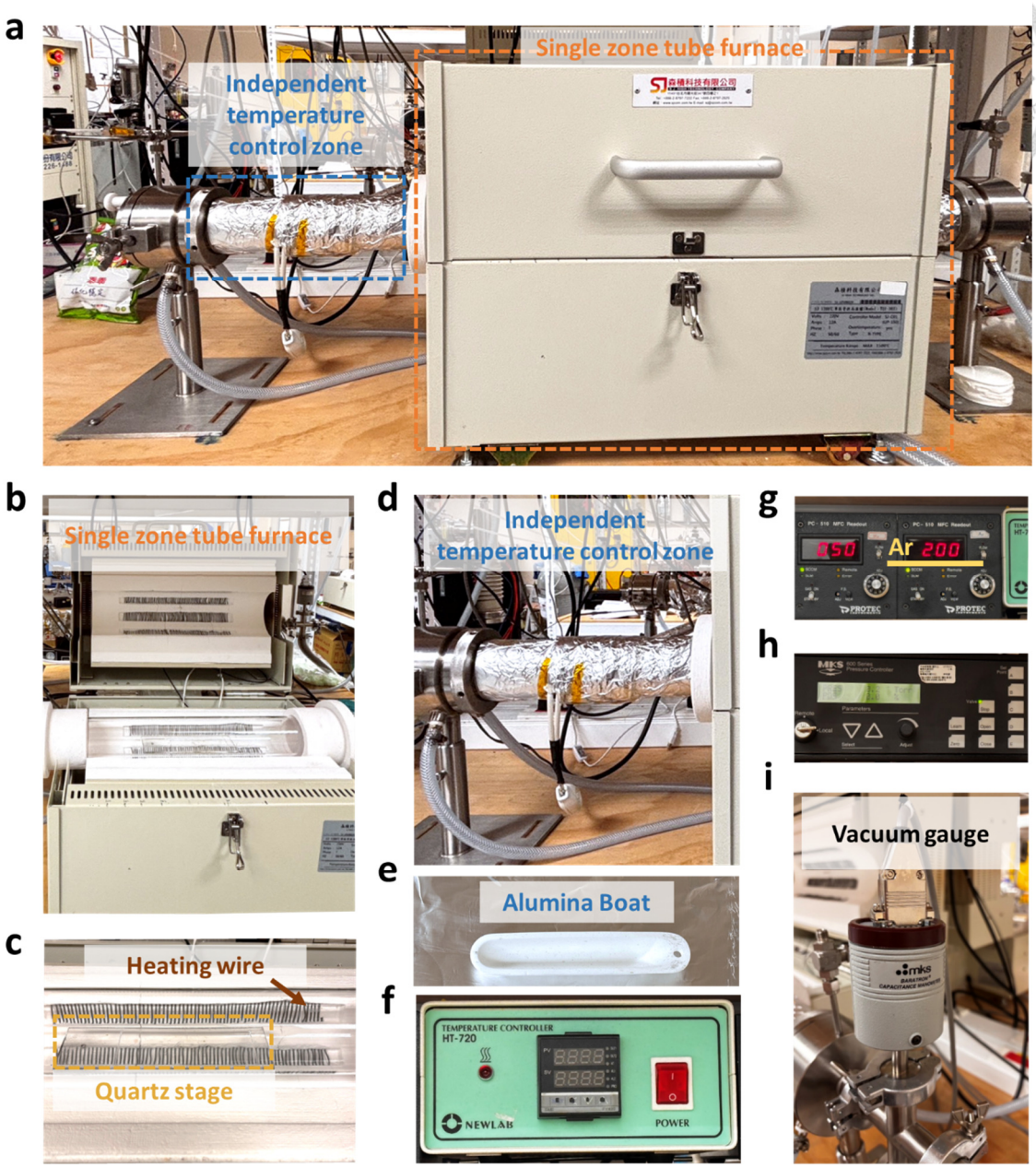

Figure 2-4 (a) LPCVD sulfurization system, (b) 3-inch single zone tube furnace, (c) heating wire and quartz stage of furnace, (d) independent temperature control zone with heating belt, (e) alumina crucible, (f) temperature controller for heating belt, (g) mass flow controller, (h) pressure controller, and (i) capacitive vacuum gauge.

doi:10.6342/NTU202501239

2.2 2D Material Transferring Techniques

2.2.1 PDMS Stamp Transferring

As mentioned earlier, while the synthesis of 2D materials has been successfully addressed, the next challenge lies in achieving their large scale transfer. Currently, polydimethylsiloxane (PDMS) is widely used as a transfer medium for 2D materials due to its high flexibility, transparency, and ability to effectively adhere to their surface, facilitating mechanical delamination [125]. As a result, researchers frequently use PDMS to transfer mono-layer 2D materials grown on sapphire or SiO_2/Si substrates onto target substrates for further device fabrication or material characterization [94].

This work also employs PDMS stamp transfer technology to transfer mono-layer 2D materials, such as MoS_2 and graphene. The following outlines the transfer methods for MoS_2 grown on a sapphire substrate and graphene grown on copper foil. To separate MoS_2 from the sapphire substrate, PDMS is first cut to the required size and carefully attached to the MoS_2 film, ensuring strong adhesion. The PDMS/ MoS_2 stack is then immersed in a 3M potassium hydroxide (KOH) aqueous solution, which gradually penetrates the edges of the film, facilitating the delamination of MoS_2 from the sapphire substrate. Once sufficient separation is achieved, the two can be gently separated using fine-tipped tweezers, leaving a thin film of MoS_2 attached to the PDMS. The PDMS/ MoS_2 membrane was then thoroughly rinsed with deionized (DI) water to remove any residual KOH and heated on a hot plate at 80°C for 5 minute to eliminate moisture. The dried 2D material on PDMS is then aligned and placed onto the target substrate, followed by heat treatment at 80°C for 5 minute to enhance adhesion. Finally, the PDMS layer is gently peeled off with tweezers to complete the transfer process, as shown in Figure 2-5.

doi:10.6342/NTU202501239

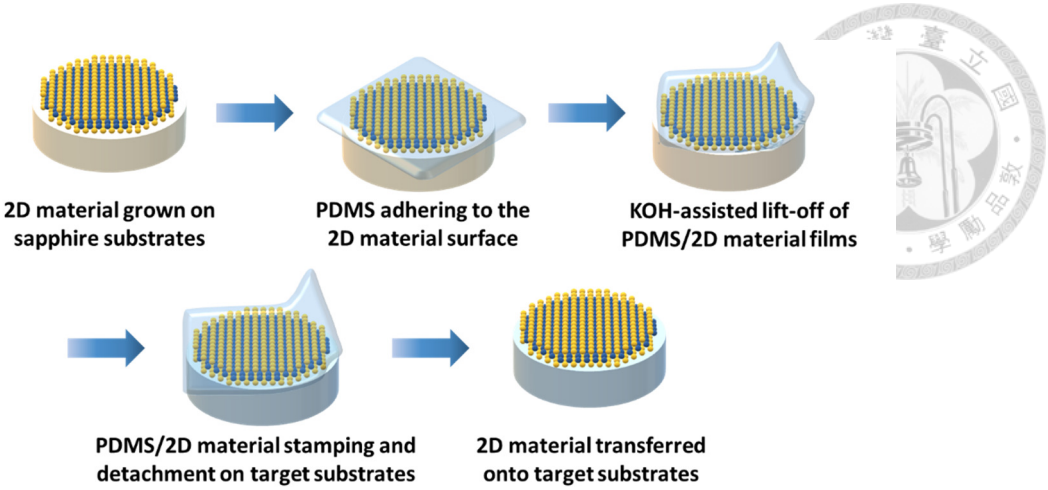

Figure 2-5 Schematic diagram of the PDMS stamping transfer process.

However, the PDMS transfer technique still faces several practical challenges [192]. First, the adhesion between PDMS and 2D materials can vary significantly. Excessive adhesion may cause difficulty in peeling off the PDMS after transfer, while insufficient adhesion can lead to bubbles or wrinkles during the transfer process [90]. Second, PDMS may leave behind polymer residues on the surface of the 2D materials during peeling, which can degrade their material properties. Additionally, PDMS has relatively low stability and a high thermal expansion coefficient, which can lead to stress concentration or film deformation during high temperature processing, thereby affecting the overall transfer quality. To avoid the issues, PDMS with suitable adhesion is specially selected from PF film by Hakuto Company. To prevent bubbles or wrinkles from the transfer process and remove polymer residues and stress concentration, the PDMS is heated in an Ar and H_2 atmosphere at 120°C for 1.5 hours. Ar serves as the carrier gas, while H_2 helps eliminate residual polymer residues. The high temperature also aids in reducing any bubbles or wrinkles remaining after transferring the 2D material [90]. By employing these methods, successful transfer of high-quality 2D materials can be achieved, facilitating their application in various device fabrication processes.

doi:10.6342/NTU202501239

Although various graphene transfer technologies exist, they each present different technical challenges in practical applications [193]. Figure 2-6 illustrates current graphene transfer methods, including wet/dry transfer, roll-to-roll transfer, electrochemical and non-electrochemical bubble transfer, and support layer-free transfer. The main difference from MoS_2 transfer lies in the copper foil substrate. Unlike sapphire substrate, copper foil is soft and prone to deformation. Additionally, separating graphene from copper typically involves chemical etchants like ferric nitrate ($Fe(NO_3)_3$), which can contaminate and damage the graphene film. For example, wet transfer typically uses polymers (such as poly(methyl methacrylate), PMMA) as a support layer and removes the copper foil with an etchant [194]. However, these polymers are difficult to remove completely, and the insufficient support can cause wrinkles and leave residual polymer on the graphene surface, affecting the performance of the device, as shown in Figure 2-6 (a). Dry transfer, as depicted in Figure 2-6 (b), avoids wet etching but is prone to cracking during the peeling process, reducing graphene's structural integrity [195]. Roll-to-roll transfer [149] is suitable for large scale processes but requires high-specification equipment and still faces issues such as contamination and indentation during continuous etching, as seen in Figure 2-6 (c). Bubble transfer technologies, including electrochemical and non-electrochemical methods, generate bubbles to separate graphene from the substrate (Figure 2-6 (d-e)) [196, 197]. However, bubble instability can cause wrinkles and stress accumulation in the film. Finally, support-free transfer eliminates the need for a polymer support layer, improving surface cleanliness [198]. However, the high temperature and pressure conditions may damage the crystal quality and electrical properties of graphene, as shown in Figure 2-6 (f). In summary, graphene transfer still faces challenges, and all transfer technologies must strike a balance between three aspects: "cleanliness," "integrity," and "large scale processability."

doi:10.6342/NTU202501239

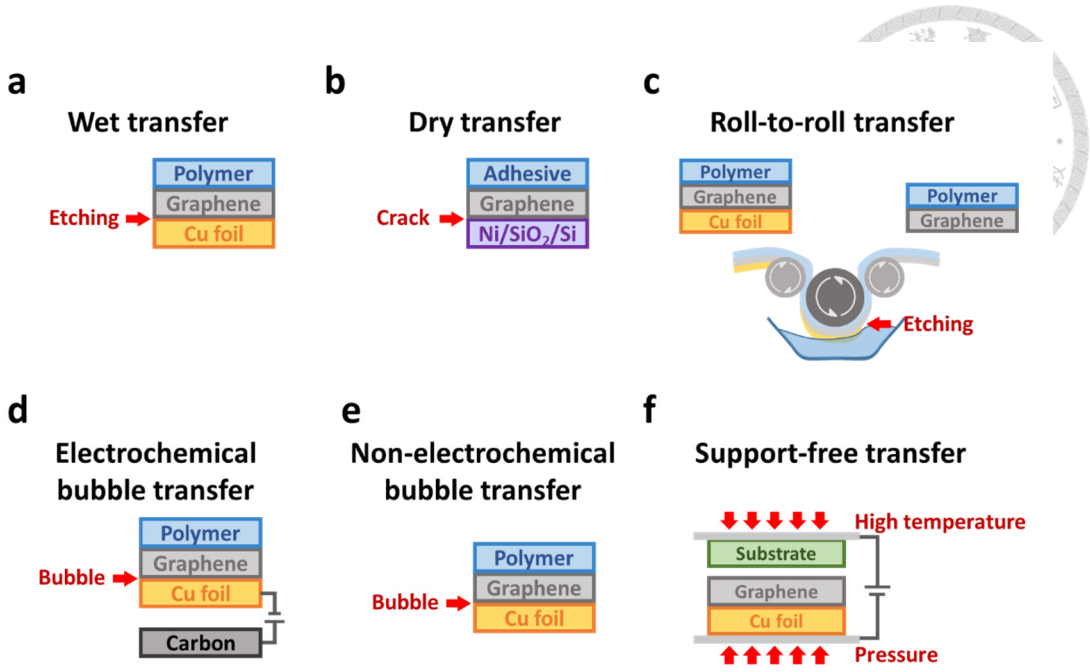

Figure 2-6 Schematic diagrams of various graphene transfer techniques, including (a) wet transfer, (b) dry transfer, (c) roll-to-roll transfer, (d) electrochemical bubble transfer, (e) non-electrochemical bubble transfer, and (f) support-free transfer [149, 194-198].

In this study, the graphene transfer technique was improved, and mono-layer graphene was successfully transferred using a modified PDMS stamping method. To separate the graphene from the copper foil substrate, PDMS was first cut to the desired size and carefully laminated onto the graphene film to ensure strong adhesion. The PDMS/graphene stack was then immersed in a 1 M $Fe(NO_3)_3$ solution to etch away the copper substrate, leaving only the PDMS/graphene stack. After etching, the stack was thoroughly rinsed with DI water to remove any residual etchant, then dried on a hotplate at 80 °C for 5 minute to eliminate moisture. The dried PDMS/graphene film was subsequently aligned and transferred onto the target substrate, followed by heat treatment at 120 °C for 1.5 hours to enhance adhesion. Finally, the PDMS layer was gently peeled off using tweezers to complete the transfer process, as illustrated in Figure 2-7.

doi:10.6342/NTU202501239

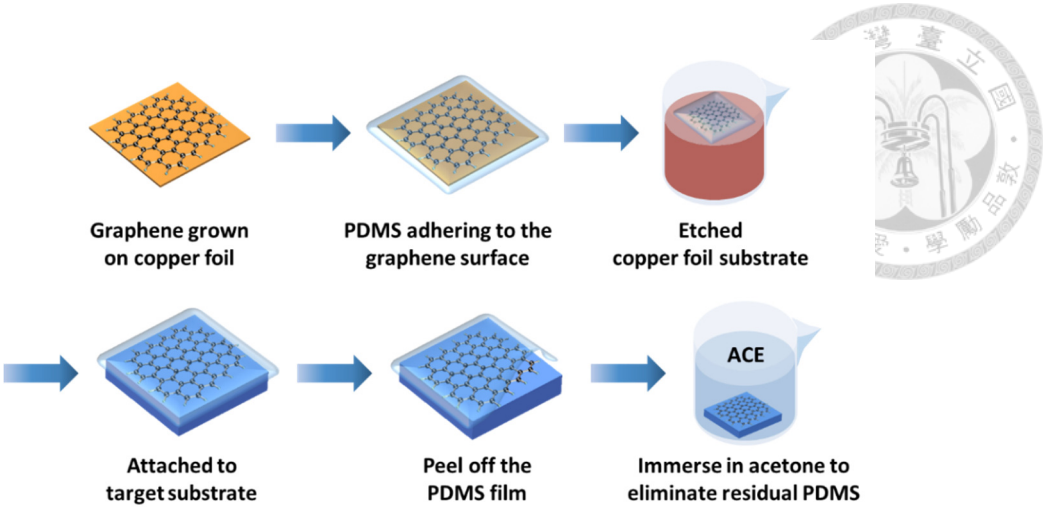

Figure 2-7 Schematic diagram of mono-layer graphene transfer process using PDMS film.

As shown in Figure 2-8, compared to the heavily contaminated graphene transferred by the spin coating method using PMMA [194], the PDMS stamping transfer yields a much cleaner material surface, as illustrated in Figure 2-8 (a, b). However, the PDMS transfer technique also presents some challenges. Due to the longer heat treatment required to ensure good adhesion between the graphene and the target substrate, more PDMS residue remains compared to the transfer of MoS_2 using the same method, thereby degrading the material's properties. To address this issue, an additional 5-minute acetone soaking step is necessary to remove the residual PDMS, as indicated in the final step of Figure 2-7. After acetone treatment, as shown in Figure 2-8 (c), most of the contaminants are effectively removed, resulting in a high-quality 2D material after successful transfer.

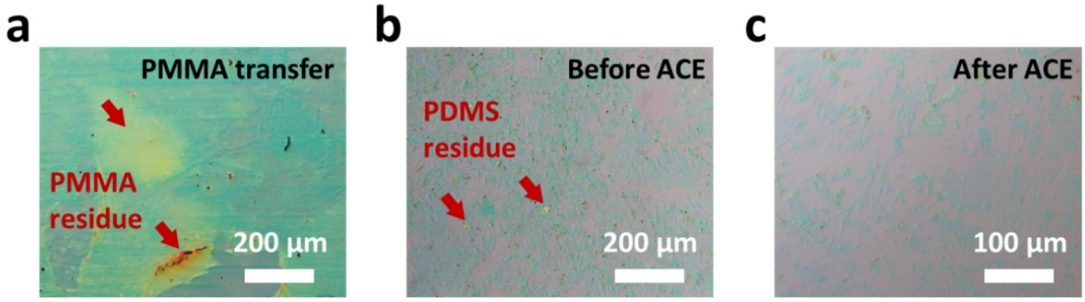

Figure 2-8 Optical microscopy (OM) images of graphene transferred onto a SiO_2/Si substrate by (a) PMMA assistance, (b) PDMS stamping without acetone soaking, and (c) PDMS stamping with acetone soaking.

doi:10.6342/NTU202501239

2.2.2 PMMA Assisted Transferring

The difficulty of transferring multi-layer 2D materials compared to mono-layers arises from stronger interlayer interactions and adhesion forces [199]. In multi-layer structures, the van der Waals forces between layers produce stronger internal bonding (MoS_2-MoS_2 interlayer bonding) than single-layer materials, making the separation of 2D materials from substrates during the transfer process more challenging. Moreover, these interlayer forces compromise structural integrity, often resulting in damage or wrinkling during the transfer process.

Therefore, to address these challenges, multi-layer MoS_2 requires a PMMA assisted transfer process instead of the PDMS stamping method used for mono-layer MoS_2. This process involves several steps to ensure successful transfer to the target substrate, as shown in Figure 2-9. First, the multi-layer MoS_2/sapphire sample was secured onto a spin coater using a vacuum pump. PMMA A4 was then dispensed onto the surface and spin coated at 500 rpm for 10 seconds, followed by 800 rpm for 20 seconds. The sample was subsequently baked on a hot plate at 120 °C for 5 minute to cure the PMMA layer.

After baking, the sample was cut to the desired size using a utility knife and then immersed in a 3 M KOH solution, allowing the KOH to penetrate along the edges and separate the MoS_2 film from the sapphire substrate. The detached film was transferred into DI water for rinsing, and the process was repeated twice to ensure complete removal of residual KOH. Next, the PMMA coated MoS_2 film was scooped onto the target substrate and baked at 80 °C for 5 minute to remove moisture. A roller press was then applied at 80 °C to flatten the sample and enhance adhesion. This step was followed by an additional 10-minute bake on a hot plate at 80 °C to further strengthen the bonding.

doi:10.6342/NTU202501239

To further enhance the adhesion of the multi-layer MoS_2 to the target substrate, an additional layer of PMMA A4 was applied using the same spin coating parameters (500 rpm for 10 seconds, then 800 rpm for 20 seconds). The samples were then left to rest for 1 hour to ensure complete adhesion. Finally, they were immersed in acetone for 20 minutes to dissolve the PMMA layer and complete the PMMA assisted transfer process.

Although this method still has room for improvement, the clean bottom layer MoS_2 surface can still effectively attach with other 2D materials or substrate without trapping carriers or degrading device performance. At this stage, it is still regarded as an effective and reliable technique for large scale transfer of multi-layer 2D materials.

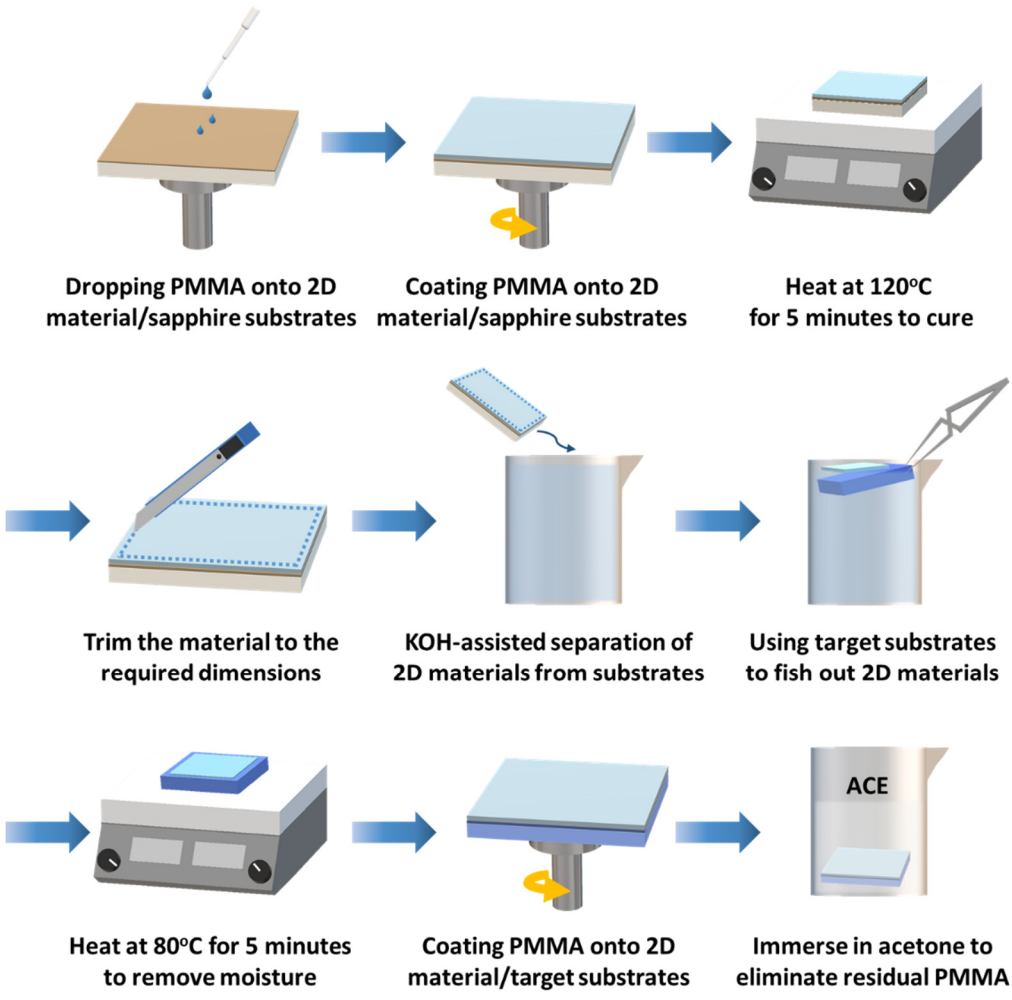

Figure 2-9 The PMMA assisted transfer process of multi-layer MoS_2.

doi:10.6342/NTU202501239

2.3 Characterization of 2D Materials

2.3.1 Micro-Raman Spectrum

Micro-Raman spectroscopy is based on the Raman effect, first discovered by Sir Chandrasekhara Venkata Raman in 1928 [200]. This phenomenon occurs when incident photons interact inelastically with molecular vibrations, resulting in scattered light with a frequency shift, known as the Raman shift [200]. To better understand the origin of Raman signals, it is essential to examine how photons interact with matter during scattering events. When photons encounter molecules or atoms, energy exchange may occur, altering the material's energy level structure and giving rise to different types of scattering phenomena. Depending on whether energy is transferred between the photon and the molecule, Raman scattering can be classified into three types: Rayleigh scattering, Stokes scattering, and anti-Stokes scattering, as shown in Figure 2-10 [201]. First, Rayleigh scattering is the most common and involves no energy exchange between the photon and the molecule ($\Delta E = 0$), resulting in scattered light with the same frequency as the incident light. It is considered elastic scattering and usually appears as background noise in Raman spectra. Second, Stokes scattering occurs when the incident photon transfers energy to a molecule in its ground state, causing a red-shift ($\Delta E < 0$) in the scattered light. Since most molecules are in the ground state at room temperature, Stokes scattering is the dominant Raman signal. As the third type of scattering, anti-Stokes scattering occurs when a molecule is already in an excited vibrational state and transfers energy to the photon, producing scattered light with a higher energy ($\Delta E > 0$, blue-shifted). While this process is less common at room temperature, it becomes more prominent at elevated temperatures or under specific excitation conditions, making it useful for temperature sensing applications [202].

doi:10.6342/NTU202501239

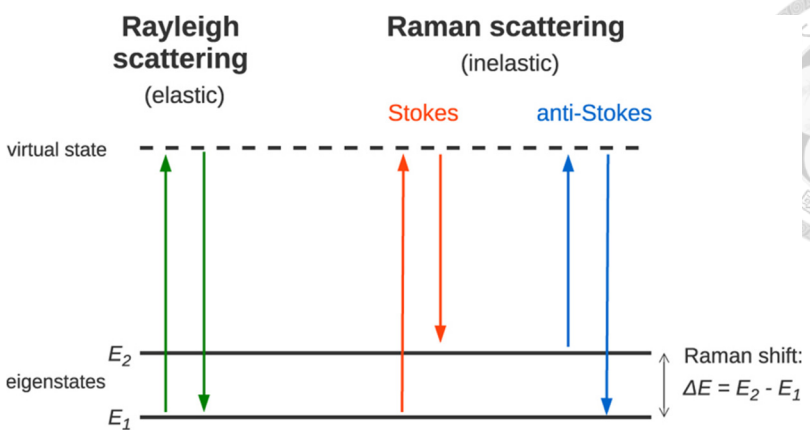

Figure 2-10 Schematic diagram of the three categories of Raman scattering [201].

Raman spectroscopy, based on three types of scattering, provides a non-destructive method for analyzing material structure, molecular bonding, and lattice vibrations. It is widely used to study phonons, electron-phonon coupling, band structures, and interlayer interactions, especially in 2D materials [203, 204]. In this study, a Raman system was used to characterize the synthesized 2D materials. The system includes a 532 nm green semiconductor laser as the excitation source, optical path components, a HORIBA Jobin Yvon HR800 spectrometer, a charge-coupled device (CCD), and analysis software, as shown in Figure 2-11. To ensure measurement accuracy, a single-crystal silicon wafer was used to calibrate the Raman peak at 520 cm^{-1}. A 100× objective lens focused the laser to a spot size of ~2-3 μm, enabling localized Raman analysis and revealing detailed structural and compositional information.

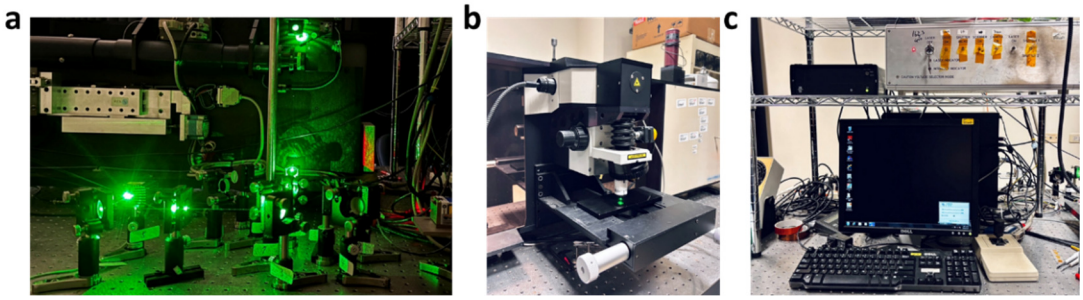

Figure 2-11 Components of the Raman system: (a) semiconductor laser and optical components, (b) spectrometer and CCD, and (c) control and analysis software.

doi:10.6342/NTU202501239

2.3.2 Photoluminescence Spectrum

Photoluminescence (PL) is a non-destructive technique used to investigate the optical properties and band structure of materials through light excitation [204, 205]. The principle of PL involves promoting electrons from the valence band (VB) to the conduction band (CB) when a material is illuminated with light of an appropriate wavelength [205]. As electrons recombine with holes and return to the VB, they primarily release energy in the form of photons, generating photoluminescence. Phonon emission can also occur in non-radiative processes; however, such processes do not generate PL signals [205]. In direct bandgap semiconductors, PL is typically strong due to the high efficiency of radiative recombination. In contrast, in indirect bandgap semiconductors, when electrons return from the CB to the VB, the energy is primarily released via phonon emission, leading to weaker PL signals.

In this study, PL measurements were conducted using the same system as the Raman spectroscopy setup, employing a 532 nm green laser as the excitation source, as shown in Figure 2-11. Despite using the same hardware, the two measurements differ in grating settings, affecting the spectral range and resolution. These adjustments allow precise analysis of the material's optical response, providing insights into its electronic structure and bandgap. PL spectroscopy has currently been widely used for band structure analysis, material quality evaluation, and surface state characterization. Analyzing peak positions and intensity variations in the PL spectrum determines bandgap energy and structural features. Comparing the PL spectra of different samples can also be used to assess the crystallinity and defect characteristics of the material. This makes PL spectroscopy an invaluable tool for understanding the optical properties and structural integrity of materials, particularly in the study of semiconductors and 2D materials.

doi:10.6342/NTU202501239

2.3.3 Atomic Force Microscopy

Atomic force microscopy (AFM) was first developed in 1986 by Gerd Binnig and Calvin F. Quate [206]. Its fundamental principle relies on the interaction between a nanoscale probe and the sample surface, causing vertical displacement detected through light deflection. Then, the optical signal is converted into an electrical signal, and a piezoelectric scanner with three-axis control adjusts the probe's position to maintain constant interaction force during scanning. The resulting data is used to reconstruct the surface topography of the sample. To accommodate various material types and measurement requirements, AFM systems operate in three primary modes: contact, non-contact, and tapping mode, as shown in Figure 2-12 [207]. These modes correspond to different regions on the force-distance curve, which describes the interaction forces between the probe and the sample as the tip approaches the surface. First, in contact mode, the probe is in direct contact with the sample surface, operating in the repulsive force region of the curve, as shown in Figure 2-12 (a, d) [207]. This mode enables high-resolution imaging by detecting atomic repulsion but can apply high pressure, possibly damaging soft materials or wearing the probe tip. Next, in non-contact mode, the probe stays several nanometers above the surface, sensing weak attractive van der Waals forces in the true non-contact region (Figure 2-12 (b, d)). While this avoids physical contact and reduces damage, it is highly sensitive to vibrations or contamination and usually requires vacuum conditions to maintain accuracy. In tapping mode, it operates between the two modes. The probe oscillates and gently touches the surface at the point where attractive and repulsive forces transition, known as the pseudo-contact region (Figure 2-12 (c, d)). This minimizes lateral forces and sample damage, offering high-resolution imaging without the need for vacuum, and is especially suitable for soft or fragile materials.

doi:10.6342/NTU202501239

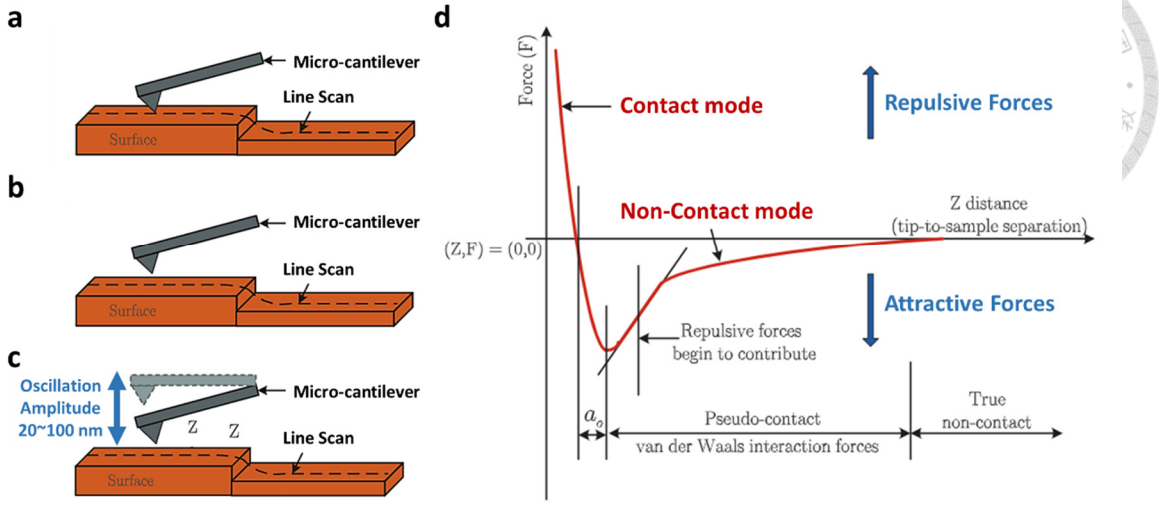

Figure 2-12 Operating modes of AFM: (a) contact mode, (b) non-contact mode, and (c) tapping mode. And (d) force-distance curves corresponding to different AFM operating modes [207].

In this study, the AFM system used was the BRUKER CellHesion® 200, as shown in Figure 2-13. It operated in tapping mode using the POINTPROBE® Plus Tapping Mode – Al-coated probe from NANOSENSORS, ensuring high-resolution imaging and stable measurement results.

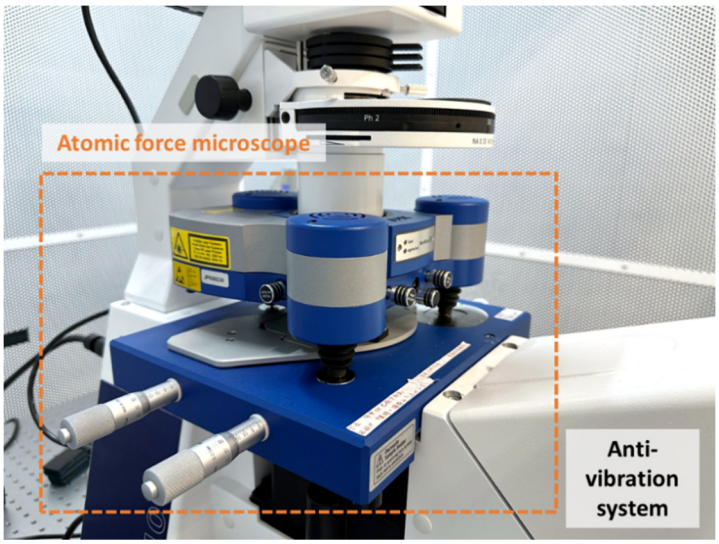

Figure 2-13 AFM system integrated with an anti-vibration system.

doi:10.6342/NTU202501239

2.3.4 High Resolution Transmission Electron Microscope

The invention of TEM dates back to 1931, when German scientists Ernst Ruska and Max Knoll invented the first transmission electron microscope [208]. The basic principle of TEM involves accelerating and focusing the electron beam onto the sample. When electrons collide with atoms in the sample, their direction changes, producing scattering at specific angles. The magnitude of these scattering angles is related to the sample's density and thickness, creating images with varying brightness. These images are further magnified, focused, and displayed on imaging components. Since TEM requires the electron beam to pass through the sample, the sample must be extremely thin, usually requiring thinning through focused ion beam (FIB) treatment to reduce the sample thickness to around 100 nm. During imaging, three main factors influence image contrast: thickness, atomic number, and crystal diffraction effect [209]. First, the thickness effect is observed when a thicker sample causes the electron beam to undergo more high-angle scattering during its passage, which reduces the transmitted intensity and darkens the image. In comparison, thinner samples allow more electrons to pass through, resulting in a brighter image. Second, the atomic number effect, where elements with higher atomic numbers produce more high-angle scattering, reduces the intensity of the transmitted electron beam and results in a darker image. In contrast, lighter elements scatter fewer electrons, allowing more electrons to pass through, thereby producing brighter images. Third, the crystal diffraction effect occurs when the atomic arrangement in the sample is parallel to the direction of the electron beam, leading to increased scattering, which reduces the number of transmitted electrons and darkens the image. Conversely, when the incident direction is not parallel to the atomic arrangement, scattering is reduced, allowing more electrons to pass through and resulting in a brighter image.

doi:10.6342/NTU202501239

The aforementioned effects are key factors in TEM imaging, which not only provides high-resolution images but also enables the analysis of a material's crystal structure. Furthermore, it can be combined with techniques such as selected area diffraction pattern (SADP), energy dispersive X-ray spectroscopy (EDS), and electron energy loss spectroscopy (EELS) to identify even small structural changes. The resolution of electron microscopes has improved with advancements in equipment technology. Today, high-resolution transmission electron microscopy (HRTEM) achieves atomic-scale resolution, allowing for the observation of individual atoms and the detailed analysis of crystal structures. This progress has greatly enhanced our understanding of material properties at the atomic level. As a result, this work utilizes the HRTEM to identify the properties of 2D materials, using the JEOL JEM-2800F model, provided by YIT Technology Co., Ltd., as shown in Figure 2-14.

Figure 2-14 High-resolution transmission electron microscopy.

doi:10.6342/NTU202501239

2.3.5 Ultraviolet-Visible Spectroscopy

Ultraviolet-Visible (UV-VIS) spectroscopy is a widely used analytical technique for characterizing the optical properties of materials by measuring their absorption or transmission of light in the ultraviolet and visible regions of the electromagnetic spectrum. This technique provides valuable information about the electronic structure, bandgap energy, and molecular composition of a sample [210]. When a material is exposed to ultraviolet or visible light, photons with specific energies can excite electrons from lower-energy states to higher-energy states, typically from the VB to the CB in semiconductors. The absorption of light at particular wavelengths corresponds to these electronic transitions, producing a characteristic absorption spectrum [210]. By analyzing the absorption spectrum, fundamental properties such as the optical bandgap, defect states, and molecular structure can be determined.

In this study, UV-Vis spectroscopy was employed to investigate the optical properties of 2D materials. The measurements were carried out using a JASCO V-670 UV-Vis spectrophotometer, which is equipped with both a deuterium lamp for the ultraviolet region and a halogen lamp for the visible region, as shown in Figure 2-15. This setup ensures a broad spectral coverage and reliable measurement accuracy.

Figure 2-15 UV-Vis spectroscopy system.

doi:10.6342/NTU202501239

2.3.6 Four-Point Probe

For 2D materials, sheet resistance measurement plays a crucial role in evaluating conductivity and material uniformity. In addition to indicating material quality, it also serves as an indicator of the material's suitability for optoelectronic applications. Sheet resistance (R_s), also known as square resistance, is expressed in ohms per square (Ω/□). It can be derived from the concept of electrical resistivity in three-dimensional systems. Considering a conventional 3D conductor, its resistance (R) is given by:

$$R = \rho \frac{L}{A} \qquad \text{(Equation } 2-1\text{)}$$

Where ρ is the resistivity, L is the length of the conductor, and A is the cross-sectional area [211]. Since A equals the product of conductor width and film thickness, the resistance equation becomes:

$$R = \frac{\rho}{t} \frac{L}{W} = R_s \frac{L}{W} \qquad \text{(Equation } 2-2\text{)}$$

Where R_s is the sheet resistance. As it is derived by dividing resistivity by thickness, its unit remains Ω. The unit Ω/□ reflects that when L=W, the measured resistance equals R_s across a square section of the film [211].

Among various methods, the four-point probe technique, one of the most widely used for measuring sheet resistance, was first proposed by Valdes in 1954 [212]. The measurement setup consists of four equally spaced, collinear probes. A constant current is applied through the outer probes, while the voltage is measured across the inner probes. This voltage is then used to accurately calculate the film's sheet resistance. A schematic of the measurement setup is shown in Figure 2-16 [213].

doi:10.6342/NTU202501239

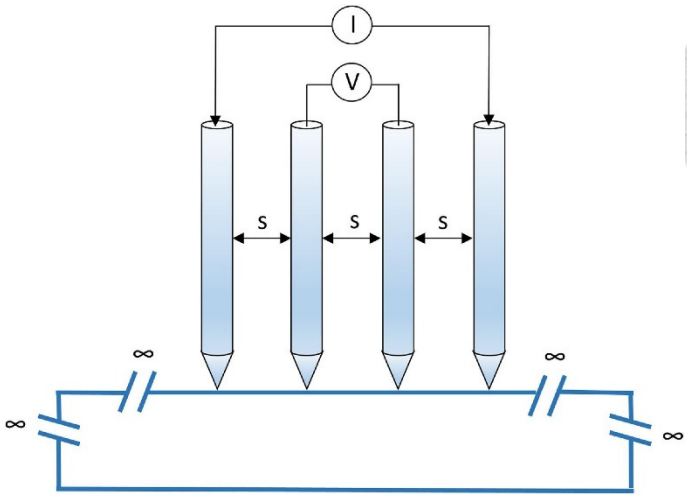

Figure 2-16 Schematic diagram of four-point probe measurement [213].

In this study, the sheet resistance was measured using a Keithley 2400 SourceMeter, as shown in Figure 2-17. The measurement process involves four probes that lightly contact the film surface, with an equal spacing of 1 mm between adjacent probes. A current I is applied through the outer probes, while the voltage V is measured between the inner probes, allowing the resistance to be determined as V/I. For an infinitely large thin film, the sheet resistance is calculated using [211]:

$$R_s = 4.532 \times \frac{V}{I} \qquad \text{(Equation } 2-3\text{)}$$

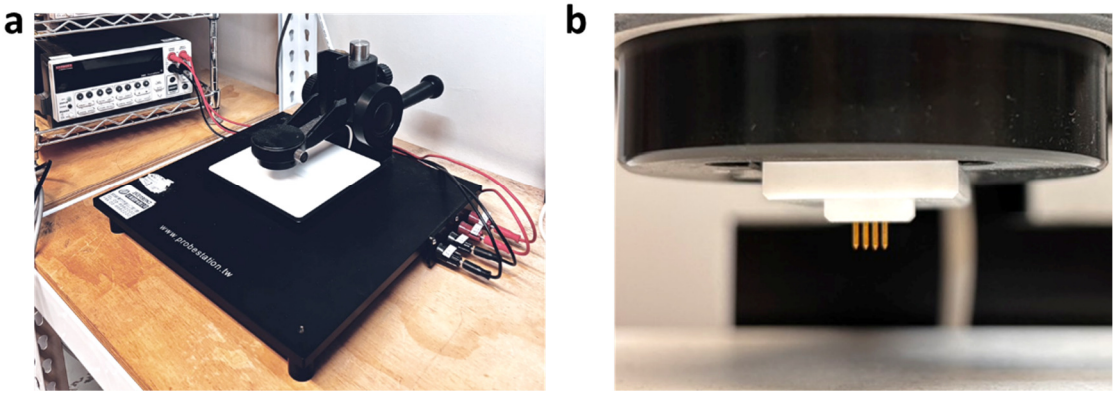

Figure 2-17 (a) Four-point probe measurement system. (b) Close-up view of the four equidistant, collinear probes.

doi:10.6342/NTU202501239

2.4 Fabrication Systems for Optical Devices

2.4.1 Spin Coater

A spin coater is a device that uses centrifugal force to evenly coat a thin film on a flat surface. It is widely used in various fields, including semiconductor processing for wafer surface treatment and photoresist coating, as well as for the application of coatings on optical discs, lens primers, and dimming liquids.

The spin coater used in this study consists of a rotary motor, a rotating wheel, and a mechanical pump, as shown in Figure 2-18. The sample is held at the center of the rotating wheel by the mechanical pump, and the coating material is then dispensed onto the surface of the sample. Subsequently, the sample is spun at high speed to achieve a uniform thin film. This method effectively controls both the uniformity and thickness of the coating. During the device fabrication process in this study, a photoresist (PR) layer was required to be coated on the substrate. The photoresist was then exposed to UV light for pattern development. The use of a spin coater enables the formation of a uniform photoresist layer, which enhances the precision of subsequent pattern transfer during photolithography.

Figure 2-18 Photograph of the spin coater system.

doi:10.6342/NTU202501239

2.4.2 Mask Aligner

The mask aligner is an essential device in semiconductor processing, especially for fabricating very large scale integration (VLSI) circuits. It uses UV light to expose patterns through a chrome mask, and a developer solution to remove the photoresist (PR) from the wafer surface, forming the desired circuit patterns.

The system used in this study includes a UV light source (mercury lamp), adjustable sample and mask stages, and a mechanical pump to ensure that the sample and the mask are firmly fixed, as shown in Figure 2-19. For positive photoresist (+PR), UV exposure softens the resist via a photochemical reaction. In contrast, negative photoresist (-PR) undergoes polymerization under UV light, making it more resistant to the developer. In this study, the mask aligner was used to define the source, drain, and channel regions of the device. The photolithography process involves coating the sample with photoresist, aligning the mask, exposure, and development. After exposure, the developer removes the softened areas, effectively transferring the mask pattern onto the substrate.

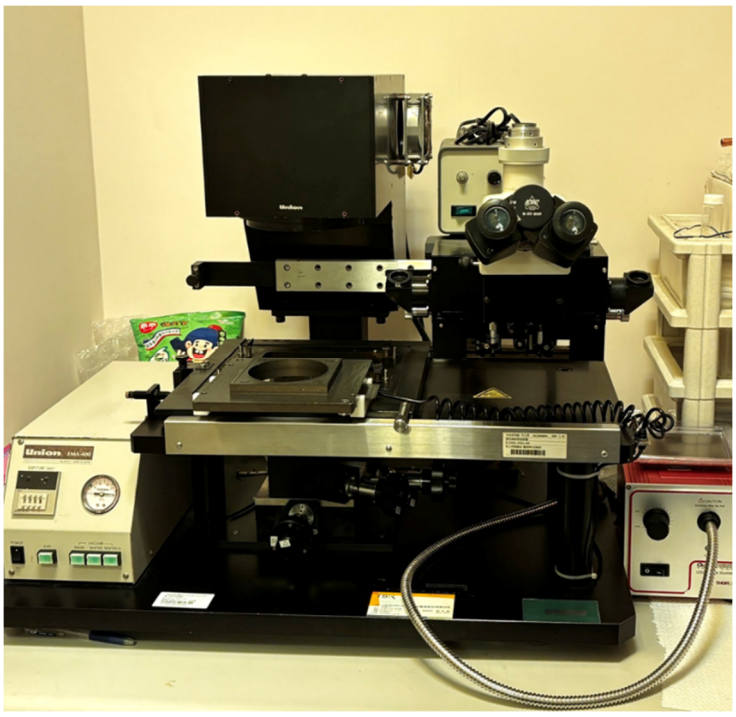

Figure 2-19 Photograph of the mask aligner.

doi:10.6342/NTU202501239

2.4.3 Electron Beam Evaporator

The electron beam evaporation system is a PVD technique that uses a high-energy electron beam to bombard a target material, causing it to heat, melt, and evaporate. The evaporated material deposits onto the substrate surface, forming a thin film. The system used in this study is shown in Figure 2-20.

Since electron beam evaporation requires a high-vacuum environment, the system employs a two-stage pumping mechanism to achieve the necessary vacuum conditions. In the first stage, an oil rotary pump reduces the chamber pressure from atmospheric pressure to approximately 3×10^{-2} torr. In the second stage, a cryo pump further lowers the pressure to 1×10^{-6} torr, ensuring a highly pure and stable deposition environment. Once the chamber reaches high vacuum conditions, the metal thin-film deposition process can proceed, enabling the fabrication of high-quality thin films. This system employs a magnetic field to precisely control the trajectory of the electron beam, focusing it on specific regions of the target material inside a crucible. This localized heating enhances deposition efficiency while ensuring high material purity. Furthermore, since the crucible is not exposed to the high-energy electron beam, contamination and thermal loss are minimized. During the deposition process, the substrate is fixed onto a stage and can also be heated through direct contact with a backside heater, which improves film adhesion and quality. A shutter located under the stage controls the deposition time. On the other hand, quartz crystal oscillator and thickness monitor are used to monitor film growth in real time to ensure uniformity and accuracy. Overall, this electron beam evaporation system enables precise control over the deposition process, ensuring the production of high-quality thin films with minimal contamination and high material integrity.

doi:10.6342/NTU202501239

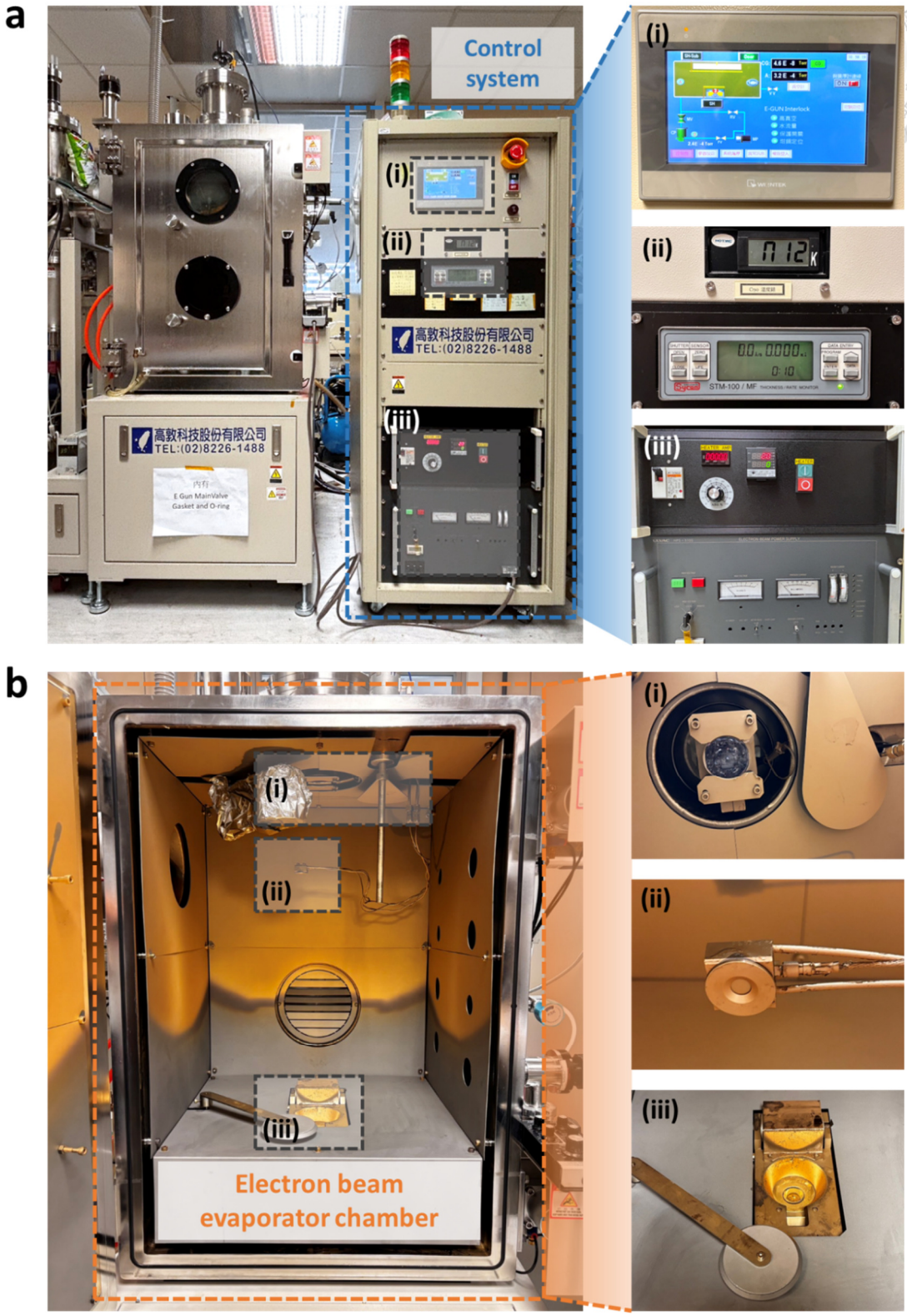

Figure 2-20 (a) The electron beam evaporation system includes a control panel, a coating rate display, and a stage heating temperature controller. (b) The internal configuration of the chamber includes stage and shutter, a quartz crystal oscillator, and a crucible.

doi:10.6342/NTU202501239

2.4.4 Thermal Evaporator

Thermal evaporation is also a PVD technique in which a resistive heating element heats a boat containing the deposition material. When the material reaches its melting or sublimation point, it evaporates and deposits onto the substrate surface. Figure 2-21 shows the thermal evaporation system used in this study. Substrates to be deposited are placed on a sample holder above a shutter that controls the deposition time. To achieve high-quality films, the thermal evaporation process must be carried out in a high-vacuum environment. Initially, a scroll pump evacuates the chamber from atmospheric pressure to about 4×10^{-2} torr. A turbo molecular pump then reduces the pressure to an ultra-high vacuum level of approximately 5×10^{-6} torr or lower. Once the desired vacuum level is reached, the deposition material can begin to evaporate and deposit onto the substrate. To ensure precise control over the deposition process, especially in terms of film uniformity and thickness, additional monitoring tools are required. For example, film thickness is monitored in real-time using a quartz crystal oscillator and thickness monitor. Since each material has a unique density and impedance, these parameters must be calibrated and set correctly in the thickness monitor before deposition to ensure accurate measurements.

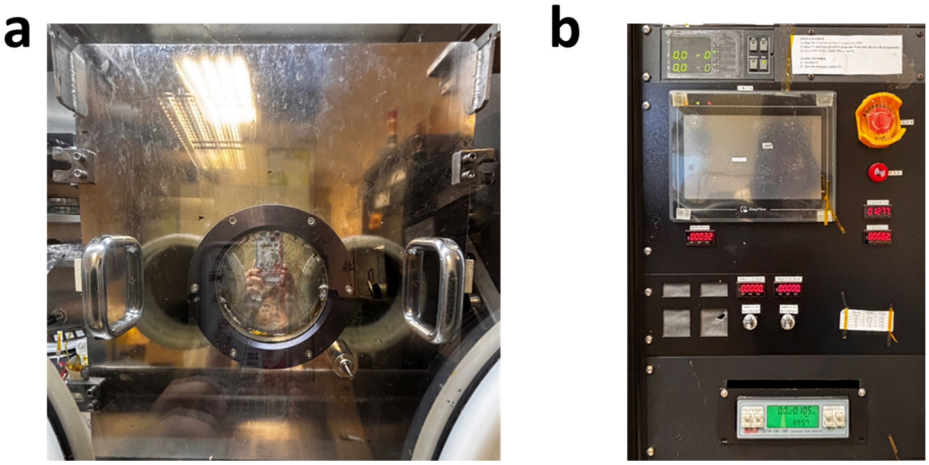

Figure 2-21 Photo of the thermal vapor deposition machine and its control panel.

doi:10.6342/NTU202501239

2.4.5 Reactive-Ion Etching

Reactive ion etching (RIE), also known as plasma etching, is a technique that removes material from a substrate by combining chemical reactions with ion-induced physical bombardment. It operates through two main mechanisms: chemical etching and ion bombardment-assisted etching. In the chemical process, plasma generates charged ions and reactive species that interact with the film surface to form volatile byproducts, which are then evacuated by a vacuum pump. This provides high selectivity and enables precise removal of specific materials. Meanwhile, a high voltage applied between parallel electrodes creates an electric field that accelerates ions toward the substrate. These ions bombard the surface, breaking atomic bonds and dislodging material. This physical interaction helps remove byproducts or polymer residues and enhances gas-surface reactions, thereby improving etch anisotropy and uniformity. In this study, a custom RIE system developed by Syskey Technology Co., Ltd. was used, as shown in Figure 2-22. The process gases, CF_4 and O_2, are selected to achieve the optimal balance of chemical reactivity and ion energy, enabling precise etching control.

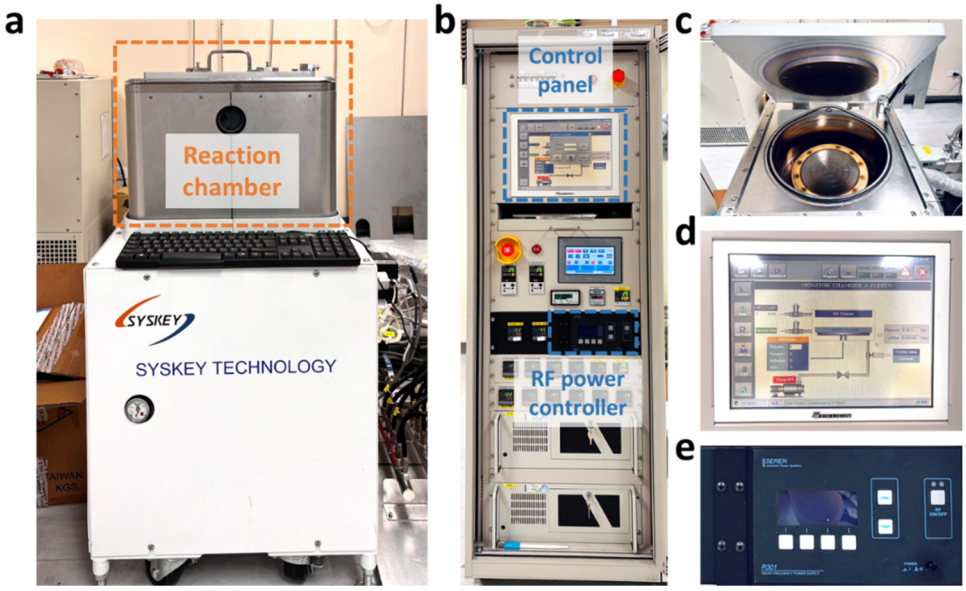

Figure 2-22 (a) Reactive ion etching system, (b) operating interface, and the corresponding (c) etching chamber, (d) control panel, and (e) RF power controller.

doi:10.6342/NTU202501239

2.5 Measurement Systems for Optical Devices

2.5.1 Solar Cell Measurement System

The solar cell measurement system consists of several components that work together to accurately measure the solar cell performance. First, the power supply provides a stable DC voltage or current to ensure the solar cell operates under constant conditions during testing. Second, the solar simulator, equipped with an AM1.5G filter (100 mW/cm^2), mimics sunlight under standard conditions, ensuring test results reflect real-world performance. It also has a shutter to adjust light intensity and measure the device's performance under different conditions. The incident light intensity is calibrated using a silicon photodiode with a KG-5 color filter (Hamamatsu) before testing. Third, a control PC manages all equipment, sets test parameters, and handles data collection and analysis through specialized software. Fourth, the Keithley 2400 source meter, a high-precision instrument, receives control signals from the PC and functions as a voltage or current source to measure the I-V characteristics of solar cells. Finally, the source meter is connected to the four-quadrant source meter and IC test socket. It provides both positive and negative voltages and currents to measure the solar cell's behavior under different operating modes. This system simulates real conditions by precisely controlling light, voltage, and current, enabling accurate assessment of solar cell performance and stability.

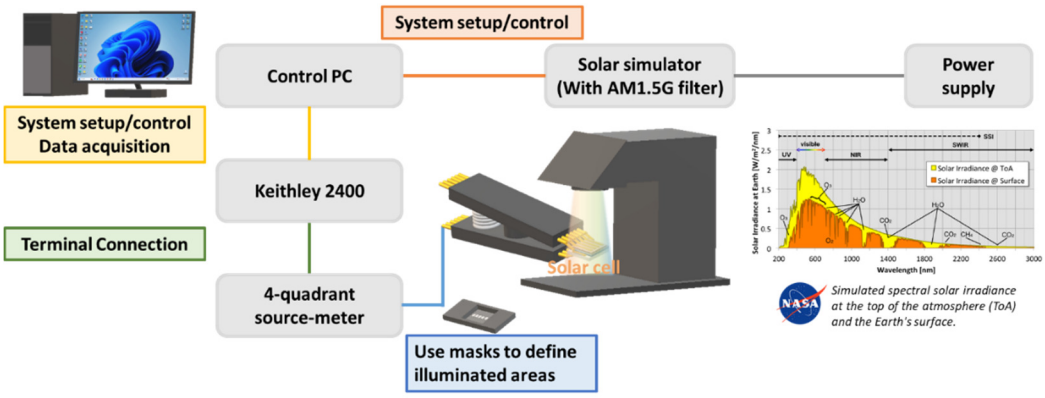

Figure 2-23 The configuration of the solar cell measurement system.

doi:10.6342/NTU202501239

2.5.2 Three-Terminal Measurement System

The three-terminal measurement system measures the electrical performance of 2D material based devices in this study, as shown in Figure 2-24. It includes the Keithley 2636B source meter, a probe station, and a control PC.

The Keithley 2636B source meter can simultaneously source and measure voltage and current. It supports up to 3 A of DC current, 10.5 A of pulse current, and 200 V, and offers a measurement resolution of approximately 10 fA, making it suitable for various low-current device measurements.

As for the probe station, provided by Sadhudesign Co., Ltd., is used for direct contact with devices and precise electrical measurements. It is equipped with tungsten probe needles with tips as small as 1 μm, making it suitable for both two-terminal and three-terminal device characterization. The main application of this system is to obtain the I_D-V_G and I_D-V_D curves of 2D material based devices, which are important for analyzing their static electrical performance.

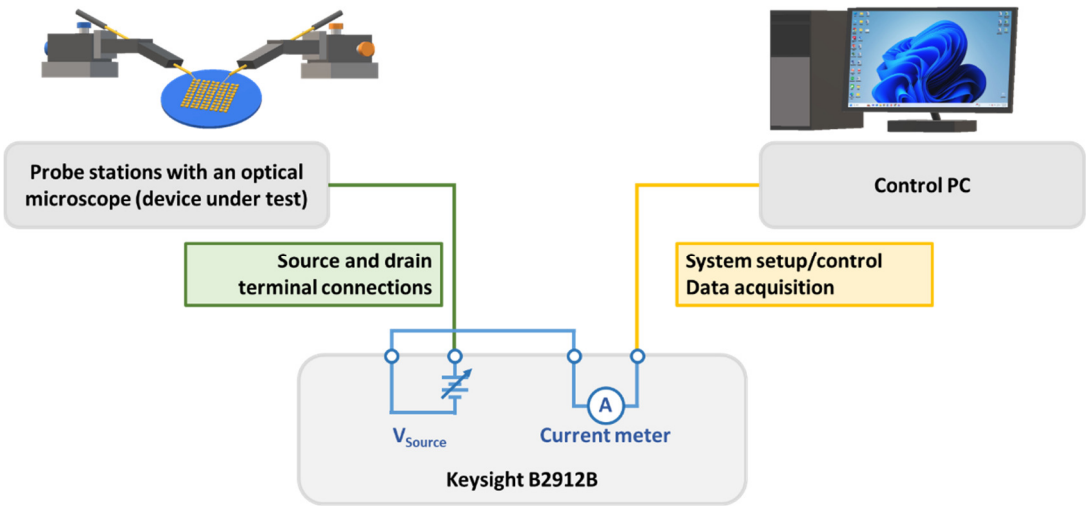

Figure 2-24 The configuration of the three-terminal measurement system.

doi:10.6342/NTU202501239

2.5.3 Photo-Response Measurement System

The photo-response measurement system used in this study, shown in Figure 2-25, consists of light sources (W and Xe lamps), an optical chopper, a spectral system, a lock-in amplifier, a source meter, a probe station, and a control PC. The principle of this system is that light from the sources is transmitted through optical fibers to the sample. When light is incident on the device, it generates a photocurrent, which is measured by the source meter and sent to the lock-in amplifier. The lock-in amplifier demodulates the AC signal and converts it into a DC signal, allowing for accurate photocurrent measurement.

The probe station, provided by Sadhudesign Co., Ltd., is used for direct contact with the device and precise electrical measurements. It is equipped with tungsten probe needles with 1 μm tips. Along with the Keithley 2400 source meter and the Keithley 6487 picoammeter/voltage source, the system provides stable power and measures the device's current. The measured signals are then transmitted to the lock-in amplifier for further processing. The SR830 lock-in amplifier, from Titan Electro-Optics Co., Ltd., performs signal detection at the optical chopper's frequency. It converts the AC photocurrent into a DC signal while amplifying weak signals and suppressing noise, enabling high-precision measurements.

On the other hand, in the optical system, the dual light source configuration expands the measurable wavelength range from visible light (Xe lamp) to the near-infrared region (W lamp). The light first passes through an optical chopper (300CD rotating optical chopper, provided by AST Instruments Co., Ltd.), which modulates the light intensity into an alternating signal and synchronizes it with the lock-in amplifier to ensure a stable signal frequency. After modulation, the light enters the lens group and diffraction grating of the spectroscopy system (model iHR320, provided by AST Instruments Co., Ltd.), which selects the desired wavelength and transmits it to the probe station via optical fiber.

doi:10.6342/NTU202501239

Finally, the power of the light irradiating the device is measured using a calibrated power meter (PM100D, Thorlabs) to determine the incident light intensity at different wavelengths.

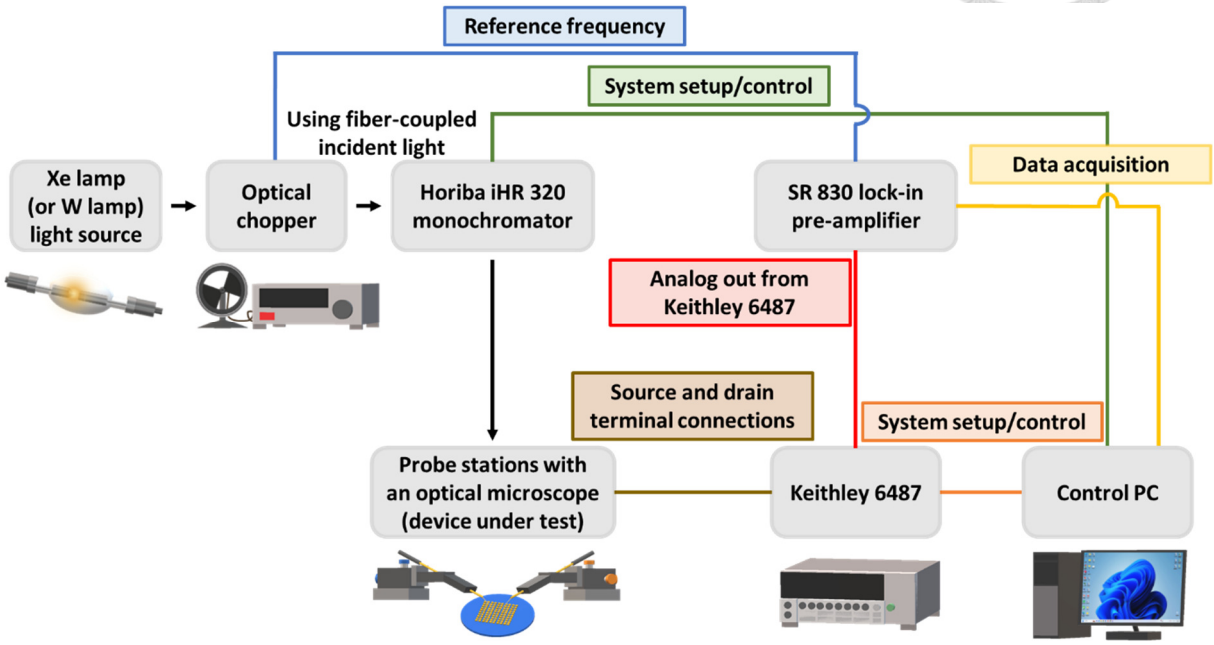

Figure 2-25 The configuration of the spectral response measurement system.

doi:10.6342/NTU202501239

Chapter 3 Bifacial Solar Cells Utilizing Gold Transparent Electrodes Grown on Molybdenum Disulfide

✧ This chapter is adapted from the content published in ACS Applied Energy Materials, vol. 7, issue 14, pp. 5698–5705, June 2024, with partial revisions made by the author.

3.1 Development and Challenges in Transparent Electrodes

3.1.1 Challenges and Bottlenecks of Common Transparent Electrodes

The emergence of highly conductive TEs has ushered in a new generation of tandem solar cells and bifacial photovoltaic technologies. These applications offer higher PCE for solar cell modules. Although light-absorbing materials have been extensively studied, research on TEs remains relatively limited. Fabricating such electrodes requires careful consideration of their interface with the absorber and long-term stability, while also facing strict manufacturing constraints. For instance, processing steps involving strong plasma or elevated thermal conditions should be avoided, and the manufacturing environment may need to be kept free of moisture and oxygen. As described in Section 1.4.1, although current mainstream TEs, namely transparent conductive oxides (TCOs), perfectly fulfill the requirements for high transmittance and high conductivity, they are not suitable for use as top electrodes in vertical structures. High processing temperatures and strong plasma bombardment can damage the underlying active layers, causing irreversible performance degradation [134, 135]. Although various TEs have been developed (Table 1-1 [134, 137–141]), each faces distinct challenges. Achieving both high transmittance and conductivity at low temperatures remains a particularly difficult problem.

doi:10.6342/NTU202501239

3.1.2 Exploring the Potential of Van der Waals Epitaxy for Transparent Electrodes

With the rise of 2D materials, mono-layer graphene was the first to be discovered with both low light absorption and acceptable conductivity (R_s of approximately kΩ/□), making it a promising candidate for use as a TE [2, 144, 148]. However, its sheet resistance remains higher than that of ITO, leaving room for improvement and limiting its applicability in large scale production [145, 146]. To achieve practical commercialization while avoiding stability issues, TCOs and metal mesh electrodes remain more promising alternatives. From a fabrication standpoint, metal-based electrodes also pose fewer processing challenges than TCOs, contributing to their broader adoption.

In addition to the aforementioned structured metal meshes, several studies have explored the use of ultrathin metal films as TEs [141]. When deposited by PVD, these metals typically follow the Volmer–Weber mode on the substrates, forming isolated clusters instead of continuous films [214]. Due to discontinuities, ultrathin films often suffer from high sheet resistance. This issue can be mitigated once the metal thickness exceeds critical thickness (also known as the percolation threshold, usually ~10-20 nm), at which point a continuous conductive path begins to form [141, 215]. While increasing the thickness beyond this threshold improves conductivity, it does so at the expense of optical transmittance. This inherent trade-off between conductivity and transparency has limited the practical use of metal films as TEs in photovoltaics and displays, where both properties are essential.

doi:10.6342/NTU202501239

To address this issue, an effective strategy is to improve the metal-substrate interaction to reduce the percolation threshold [141, 216, 217]. Recent studies have demonstrated that van der Waals epitaxy facilitates the direct deposition of highly conductive metal nano-films, including gold and copper, onto the surfaces of 2D materials such as MoS_2 and WSe_2. Unlike conventional growth on inert substrates, these metals grow laterally in an orderly fashion, forming uniform and continuous films at the nanoscale, rather than aggregating into isolated clusters, as illustrated in Figure 3-1 [218-220]. For example, a 10 nm-thick Au film thermally evaporated on MoS_2 at 100 °C achieved a low sheet resistance of 2.90 Ω/□, indicating that ultrathin, highly conductive films can be obtained under relatively mild fabrication conditions, as shown in Figure 3-1 (a, d) [218]. Similarly, 15 nm Cu films deposited on MoS_2 and WSe_2 at room temperature exhibited sheet resistances of 3.49 Ω/□ and 3.62 Ω/□, respectively [219, 220]. These values are approaching the theoretical sheet resistance of copper in its nature bulk form (1.12 Ω/□), indicating the potential of van der Waals epitaxy to produce low-resistance metal films at relatively low temperatures across various 2D substrates, as shown in Figure 3-1 (b, c, e) [220]. This distinctive growth mechanism not only improves the film's electrical conductivity but also enhances optical transparency when the film is thin enough. Moreover, the ability to transfer 2D materials onto different substrates adds further flexibility for their integration into next-generation optoelectronic devices.

Overall, combining 2D materials with ultrathin metals provides a promising approach for TEs that balance conductivity and transparency. This method not only reduces costs but also offers high compatibility, making it a promising candidate for transparent electrodes in solar cells, flexible electronics, and other optoelectronic devices.

doi:10.6342/NTU202501239

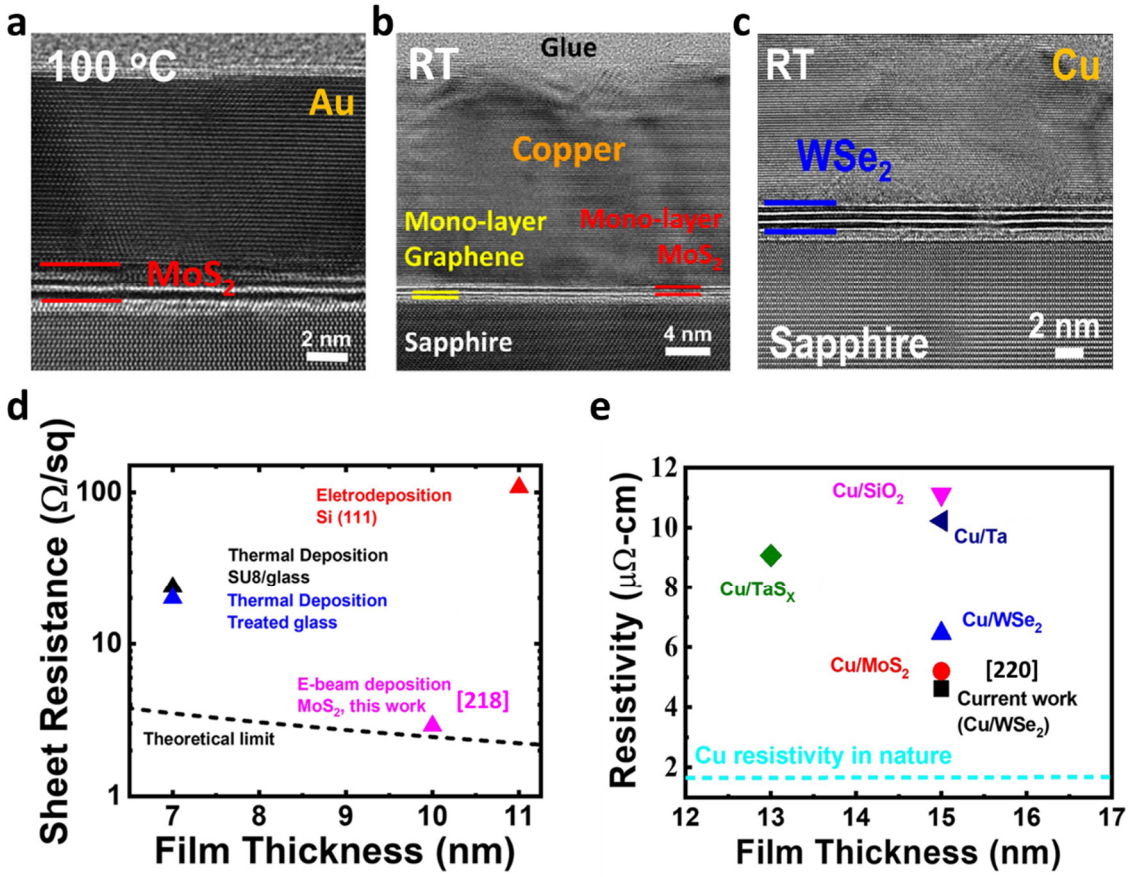

Figure 3-1 The cross-sectional HRTEM images of (a) 10 nm Au/MoS_2, (b) 20 nm Cu/MoS_2/graphene, and (c) 15 nm Cu/WSe_2 samples. Comparison of resistance values of (d) Au and (e) Cu films prepared by different methods [218-220].

doi:10.6342/NTU202501239

3.2 Fabrication and Characterization of Transparent Electrodes

3.2.1 Gold Electrodes Deposited on Mono-layer MoS_2

This section provides a detailed description of the fabrication process for TEs, which can be divided into three main steps: (1) the growth of mono-layer MoS_2, (2) the transfer of mono-layer MoS_2, and (3) the deposition of thin metal films.

(1) Growth of mono-layer MoS_2

In this study, highly crystalline mono-layer MoS_2 films were synthesized using ALD system (Section 2.1.3) followed by low-pressure sulfurization (Section 2.1.4), as illustrated in Figure 3-2.

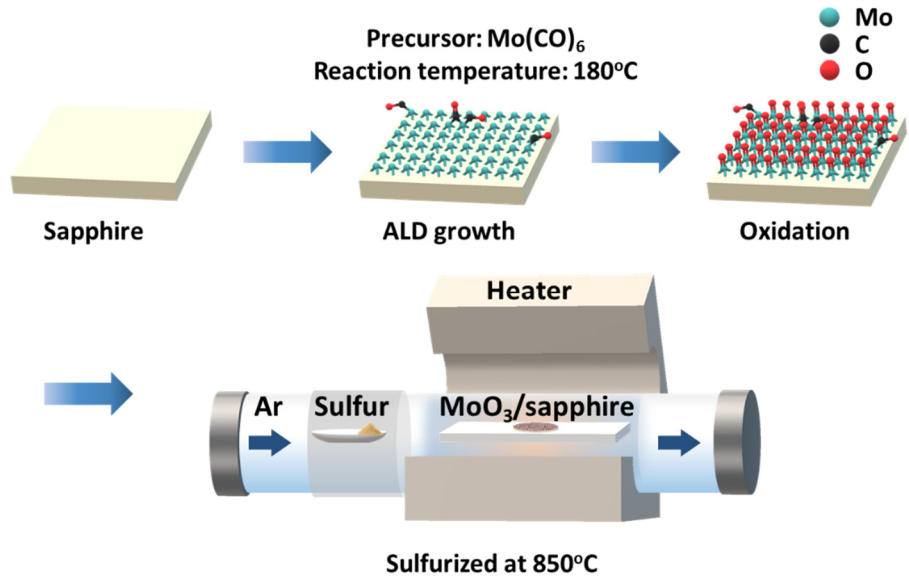

Figure 3-2 The growth procedure of mono-layer MoS_2 through the sulfurization of pre-deposited MoO_3 films prepared by using ALD and the system setup of the hot furnace for the sulfurization procedure at 850 °C.

First of all, MoO_3 was pre-deposited on single-side polished c-plane sapphire substrates via ALD. An ozone generator was activated to purge the chamber with

doi:10.6342/NTU202501239

O_3, ensuring a clean processing environment. After chamber cleaning, N_2 was used to return it to atmospheric pressure, allowing the sapphire substrates to be inserted. The sample was then placed in the chamber and subsequently heated to 180°C. A mechanical pump was employed to reduce the pressure to below 1×10^{-2} torr. The ALD growth parameters and desired number of cycles were set, and the valves for the Mo precursor, molybdenum hexacarbonyl ($Mo(CO)_6$), were opened. The precursor was delivered into the chamber via Ar carrier gas, and the detailed ALD reaction sequence was as follows:

(i) $Mo(CO)_6$ and O_3 were simultaneously introduced into the chamber as the metal and oxidant precursors for the ALD process.

(ii) The substrate was soaked in $Mo(CO)_6$ and O_3 to enable MoO_3 growth.

(iii) N_2 purge to remove residual precursor molecules, ensuring only the desired material remains on the surface;

(iv) Pump-down to remove any residual gases or byproducts, preparing the system for the next ALD cycle.

Repeat the above steps to complete the deposition of MoO_3. Once deposition was complete, N_2 was used to vent the system, and the sample was removed. Subsequently, the sample was transferred to the furnace for high temperature sulfurization. The MoO_3 deposited substrate was placed at the center of the furnace, while sulfur powder was loaded into an alumina crucible located in a separately controlled heating zone equipped with a heating belt. A mechanical pump reduced the chamber pressure from atmospheric pressure to 10^{-3} torr to ensure purity. Ar (200 sccm) was used as the carrier gas, and the system pressure was maintained at 50 torr using a pressure controller. The furnace center was heated to 850 °C at a ramp rate

doi:10.6342/NTU202501239

of 20 °C/min. The sulfur zone was pre-heated to 90 °C and then gradually increased to 160 °C once the center zone reached 500 °C. In this way, when the furnace center reached 600 °C, the sulfur powder began to melt, evaporate, and be carried into the furnace by the Ar flow. The sulfur vapor reacted with the MoO_3 deposited substrate in the center of the furnace, forming MoS_2 within 5 minutes. After the reaction, the furnace was allowed to cool naturally to room temperature. Finally, the chamber was vented with N_2, and the sulfurized MoS_2 sample was retrieved. A photograph of a mono-layer MoS_2 film grown by ALD and low-pressure sulfurization system is shown in Figure 3-3 (a). After the sample growth was completed, Raman spectroscopy was performed to assess the layer number and material quality. As shown in Figure 3-3 (b), the characteristic Raman peaks of MoS_2 were observed with a peak spacing (Δk) of 19.3 cm^{-1}, confirming that the two-step growth process successfully produced mono-layer MoS_2.

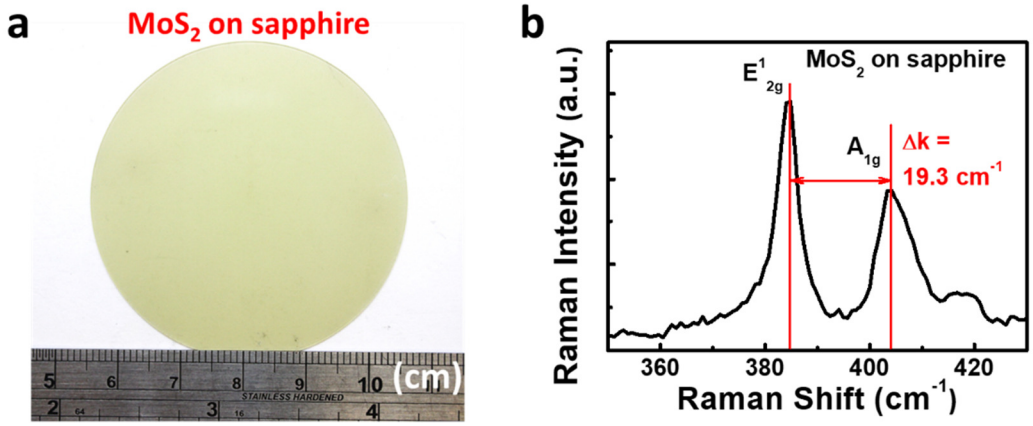

Figure 3-3 (a) The pictures of mono-layer MoS_2 samples grown on 2-inch sapphire substrate; (b) corresponding Raman spectrum confirming mono-layer characteristics.

(2) Transfer of mono-layer MoS_2

Here, the MoS_2 mono-layer was separated using the PDMS stamping transfer technique as described in Section 2.2.1. To separate the mono-layer MoS_2 from the

doi:10.6342/NTU202501239

sapphire substrate, a PDMS sheet was first cut to the desired size and carefully adhered to the MoS_2 film, ensuring strong attachment. The PDMS/MoS_2 stack was then immersed in 3M KOH solution, which gradually penetrated the film edges and facilitated delamination of MoS_2 from the sapphire. Once sufficient separation was achieved, tweezers were used to gently lift off the MoS_2, leaving it attached to the PDMS. The PDMS/MoS_2 film was then thoroughly rinsed with DI water to remove any residual KOH, followed by drying on a hot plate at 80 °C for 5 minute to eliminate moisture. The dried MoS_2 film was then aligned and placed onto the target substrate (glass substrate). A second thermal treatment at 80 °C for 5 minute was performed to enhance adhesion. Finally, the PDMS layer was carefully peeled off using tweezers, completing the transfer process. Photographs of mono-layer MoS_2 transferred onto a glass substrate are shown in Figure 3-4 (a). Next, the mono-layer MoS_2 sample transferred onto a glass substrate was analyzed by Raman spectroscopy, as shown in Figure 3-4 (b). The presence of characteristic MoS_2 Raman peaks with Δk value of 19.3 cm^{-1} confirms that the PDMS stamping process successfully transferred a mono-layer film. This is further confirmed by the uniformity of the transferred film observed in Figure 3-4 (a).

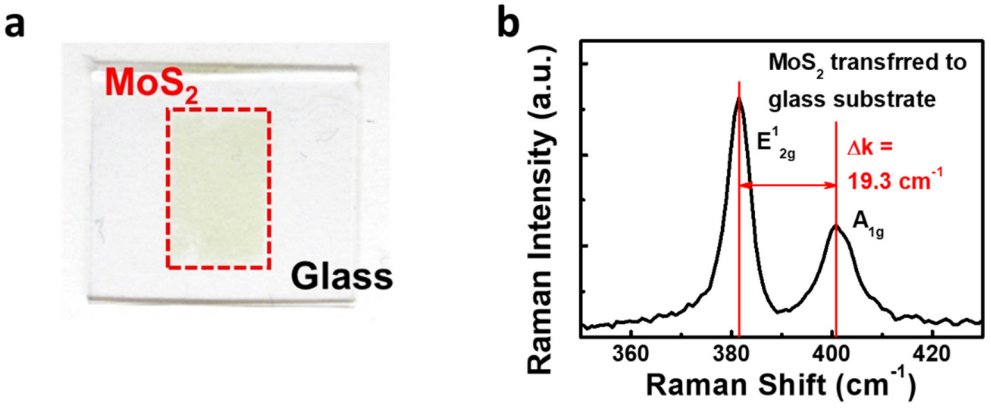

Figure 3-4 (a) The picture and (b) the Raman spectrum of the mono-layer MoS_2 film transferred to the glass substrate.

doi:10.6342/NTU202501239

(3) Deposition of thin metal films

After the successful transfer of mono-layer MoS_2, thin Au films with different thicknesses were deposited on the MoS_2 surface using a thermal evaporator located in a glove box. The deposition process began by placing the sample onto the stage inside the chamber, followed by loading gold into a thermal evaporation boat. The chamber was first evacuated to ~4 × 10^{-2} torr using a scroll pump, then further reduced to ~5 × 10^{-6} torr by a turbo molecular pump. Once the target vacuum was reached, the metal boat was heated, initiating deposition at a rate of 0.05 nm/s. Film thicknesses of 6, 8, and 10 nm were precisely monitored in real time using a calibrated quartz crystal microbalance and thickness monitor. Finally, the vacuum was released using N_2, and the deposited samples were removed. Photographs of 6, 8, and 10 nm Au films deposited on glass, with and without mono-layer MoS_2, are shown in Figure 3-5.

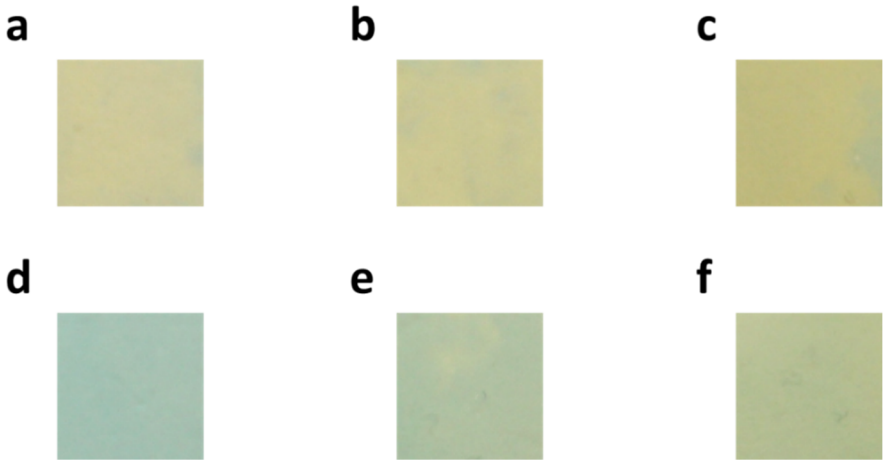

Figure 3-5 Photographs of gold films with varying thicknesses deposited on substrates with and without mono-layer MoS_2. (a–c) 6, 8, and 10 nm Au deposited on mono-layer MoS_2/glass substrates at room temperature. (d–f) 6, 8, and 10 nm Au deposited directly on glass substrates at room temperature.

doi:10.6342/NTU202501239

3.2.2 Characterization and Properties of Au/MoS_2 Transparent Electrodes

To further explore the viability of Au/MoS_2 as a transparent electrode, it is essential to first assess the continuity of the gold film, as this directly influences the electrode's sheet resistance. Discontinuous metal films, which tend to form isolated island-like structures, can cause increased electron scattering and significantly reduce conductivity. Therefore, ensuring the formation of a uniform, low-resistance gold layer is critical for optimizing the performance of transparent electrodes.

Figure 3-6 (a-c) presents 500 × 500 nm^2 AFM images of mono-layer MoS_2 samples with Au films of 6, 8, and 10 nm thickness. Across all samples, the gold film exhibits complete surface coverage without visible cracks, indicating high film continuity. The root mean square (RMS) roughness values decrease with increasing film thickness, 0.76, 0.48, and 0.41 nm, respectively, reflecting enhanced surface uniformity. This atomic-level flatness implies that gold atoms can self-assemble into an orderly configuration on the 2D material surface, as further illustrated in Figure 3-6 (d). As previously reported, nanometer Au films tend to grow along the (111) crystallographic direction, which facilitates the formation of a continuous film [218].

Consistent with previous studies, nanometer-thin Au layers tend to grow preferentially along the (111) crystallographic orientation, promoting continuous film formation [218]. The observed morphology reflects the advantages of van der Waals epitaxy on 2D materials, which facilitates high quality film growth not only at elevated temperatures but also under relatively mild thermal conditions [218, 221]. This is mainly due to the enhanced surface mobility of Au adatoms on MoS_2, allowing even ultra-thin layers (as thin as 6 nm) to form a uniform coating.

doi:10.6342/NTU202501239

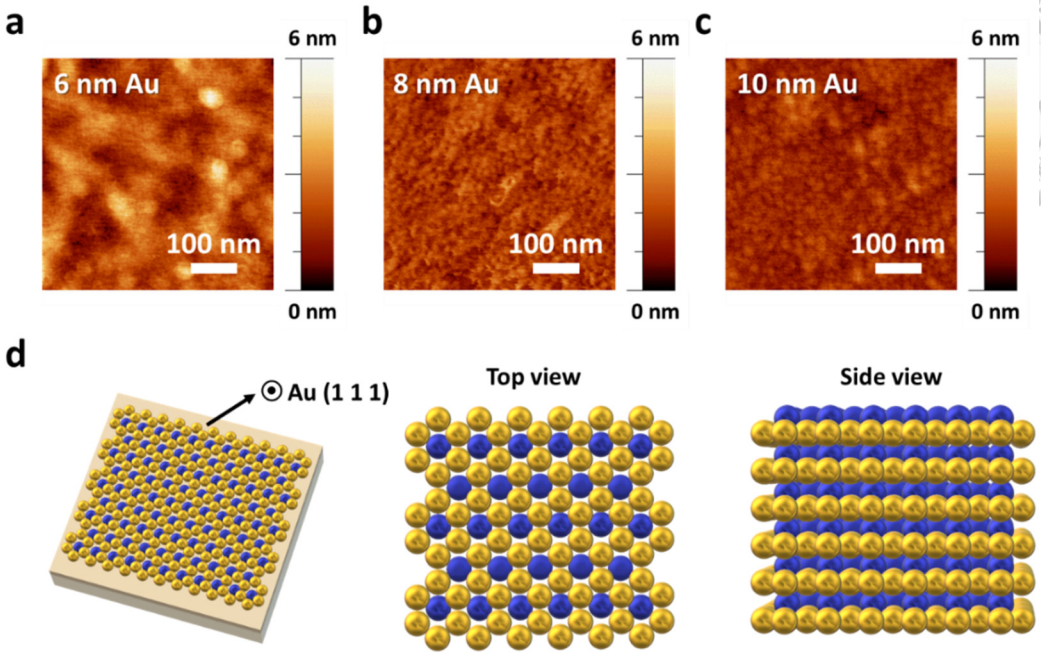

Figure 3-6 The 500 × 500 nm^2 AFM images of the three samples with (a) 6, (b) 8 and (c) 10 nm Au films grown on mono-layer MoS_2 surfaces. (d)Schematic diagram illustrating the orderly deposition of metal atoms on a MoS_2/glass substrate.

To further confirm this growth behavior, cross-sectional HRTEM analysis was conducted on two sets of samples, one with 6 nm Au deposited directly on a glass substrate, and the other on a mono-layer MoS_2/glass substrate. As shown in Figure 3-7 (a, b), only the sample with MoS_2 as a template exhibits a continuous gold film, while the one on bare glass reveals isolated Au clusters. These observations are consistent with the AFM results, confirming that the presence of a 2D template enhances lateral atom migration and promotes seamless film formation. In addition, Figure 3-7 (c, d) reveals differences in film structure: the glass-supported sample transitions from amorphous to polycrystalline phases, whereas the Au film grown on MoS_2/glass demonstrates improved crystallinity, evolving toward a single-crystalline phase. These findings indicate that the use of MoS_2 not only enhances film coverage but also facilitates better structural ordering, even at room temperature. Notably, the glass-supported film also exhibits thicker Au

doi:10.6342/NTU202501239

clusters, likely due to limited atomic mobility on the glass surface, which hinders uniform spreading.

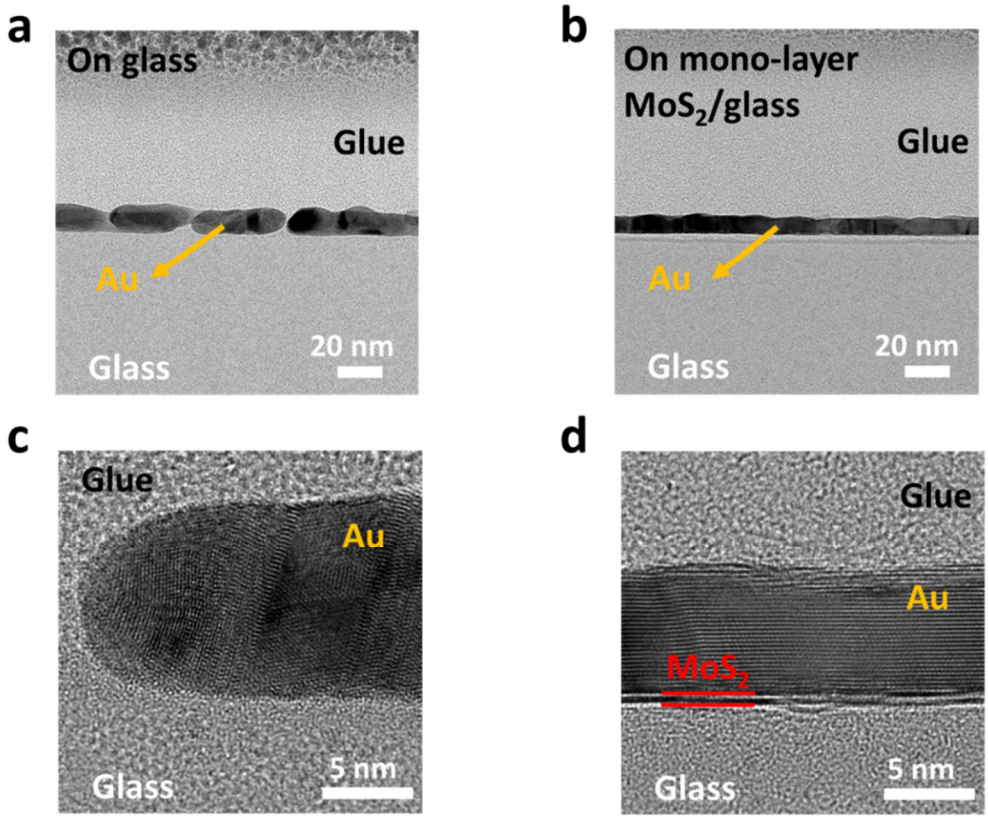

Figure 3-7 The cross-section HRTEM images with × 100 k (upper figures) and × 800 k (lower figures) magnifications of 6 nm Au grown on blank glass and mono-layer MoS_2/glass substrates.

Subsequently, the sheet resistance of Au thin films with thicknesses of 6, 8, and 10 nm, deposited on both MoS_2/glass and bare glass substrates, was measured using a four-point probe system. As summarized in Table 3-1, pre-transferring MoS_2 onto a glass substrate prior to Au deposition significantly lowers the sheet resistance, indicating enhanced electrical continuity. Moreover, as the thickness of the Au film increases, the difference in sheet resistance between the two configurations becomes more pronounced, further confirming that Au deposited on the 2D substrate exhibits superior conductivity.

doi:10.6342/NTU202501239

For example, at a thickness of 10 nm, the sheet resistance values are quite similar: 7.43 Ω/□ for the MoS_2-supported film and 8.11 Ω/□ for the film on bare glass. However, as the Au thickness decreases, the difference becomes more pronounced. At 8 nm, the sheet resistance increases to 11.65 Ω/□ with MoS_2, while it nearly doubles to 21.62 Ω/□ without MoS_2. With further reduction in thickness, the Au film on the bare glass substrate becomes almost non-conductive. In contrast, the MoS_2-supported film still maintains good conductivity (20.35 Ω/□), benefiting from the enhanced atomic mobility facilitated by van der Waals epitaxy.

Table 3-1 Sheet resistance of Au with different thicknesses grown on MoS_2/glass and blank glass substrates.

No.	Substrate	MoS_2	Metal	THK (nm)	R_s (Ω/sq)
1	Glass	No	Au	6	OPEN
2	Glass	Yes	Au	6	20.35
3	Glass	No	Au	8	21.62
4	Glass	Yes	Au	8	11.65
5	Glass	No	Au	10	8.11
6	Glass	Yes	Au	10	7.43

For transparent electrodes, light transmittance is a crucial parameter, as it directly affects the efficiency and functionality of optoelectronic devices. High transparency ensures that a significant amount of light passes through the electrode, which is essential for the device's proper operation, while still maintaining good electrical conductivity. To evaluate this, the transmission spectra of three samples with 6, 8, and 10 nm Au films deposited on mono-layer MoS_2 were measured, as shown in Figure 3-8. For comparison, the transmission spectrum of a commercial 150 nm ITO/glass substrate is also included. As depicted in the figure, all three samples exhibit visible transparency, with transmission

doi:10.6342/NTU202501239

peaks in the 500-600 nm range, which can be attributed to surface plasmons in the gold film [222]. Compared to the 70-80% transmittance of the ITO/glass substrate in the 400-800 nm wavelength range, the sample with a 6 nm gold film achieves a transmittance of 60-80%. As the Au film thickness increases, the transmittance of the 8 nm and 10 nm samples decreases to 50-70% and 40-65%, respectively. These results demonstrate the trade-off between conductivity and transmittance when using thin metal films as transparent electrodes, as the thicker Au films (8 and 10 nm) yield lower sheet resistance values of 11.65 Ω/□ and 7.43 Ω/□, respectively.

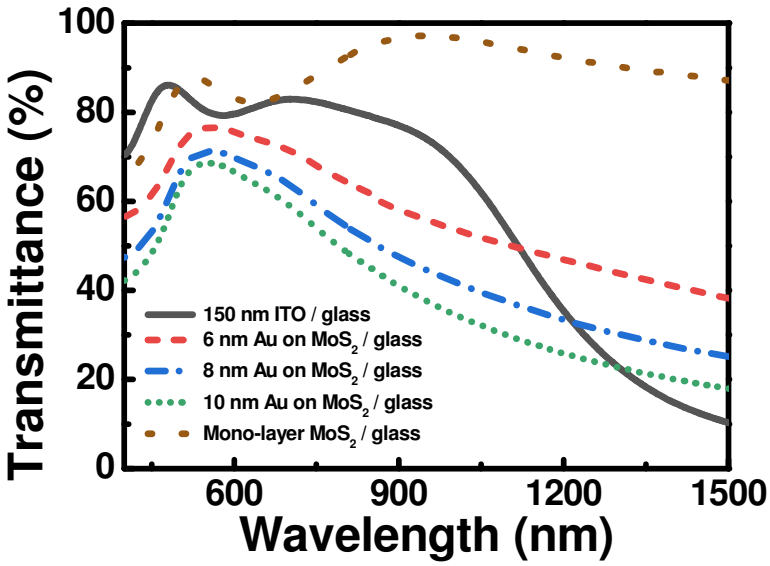

Figure 3-8 The transmission spectra of 150 nm ITO, mono-layer MoS_2, and gold samples of different thicknesses grown on the surface of mono-layer MoS_2.

In general, Au/MoS_2 structures exhibit excellent conductivity along with optical transmittance levels comparable to those of ITO, making them highly suitable for applications as top electrodes in tandem solar cells or bifacial photovoltaic devices. Their favorable balance of transparency and conductivity offers a promising alternative to conventional TCOs, especially in scenarios where flexibility, stability, or compatibility with emerging materials is required.

doi:10.6342/NTU202501239

3.3 Fabrication and Analysis of Bifacial Perovskite Solar Cells

3.3.1 Fabrication of Bifacial Perovskite Solar Cells with Au/MoS_2 Transparent Electrodes

To construct a bifacial perovskite solar cell incorporating a Au/MoS_2 top electrode, the ITO-coated glass substrates first underwent a multi-step cleaning procedure. This involved four consecutive ultrasonic treatments, each lasting 15-minute, in Extran detergent, DI water, acetone (ACE), and isopropanol (IPA), respectively. The substrates were then subjected to an additional 15-minute UV-ozone treatment to remove residual organic contaminants. Figure 3-9 illustrates the fabrication process of bifacial perovskite solar cells employing Au/MoS_2 TEs. All subsequent processing steps were conducted within an inert nitrogen atmosphere inside a glovebox, effectively minimizing potential interference from ambient moisture and oxygen.

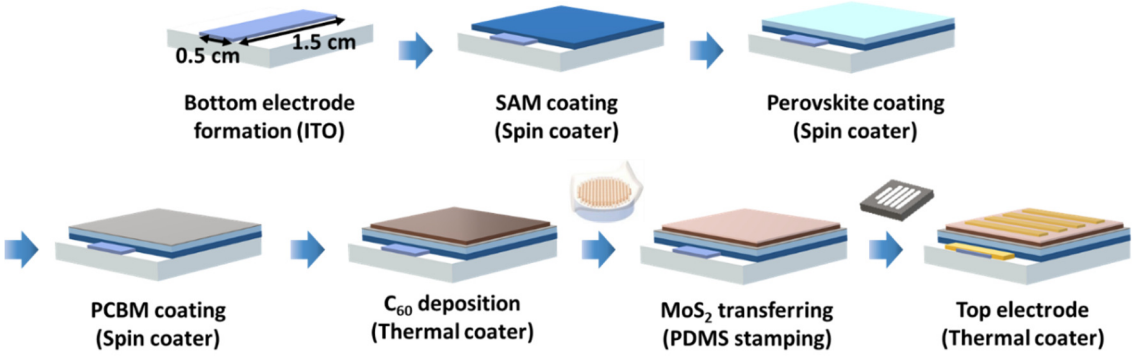

Figure 3-9 Fabrication procedure of bifacial perovskite solar cells with Au/MoS_2 TEs.

Initially, the MeO-2PACz (2-(3,6-dimethoxy-9H-carbazol-9-yl)ethyl)phosphonic acid) was spin coated onto the ITO glass substrate to serve as the hole transport layer (HTL). The MeO-2PACz stock solution was prepared by dissolving the compound in ethanol (EtOH) at a concentration of 1 mg/mL. Subsequently, a 60 μL aliquot of the

doi:10.6342/NTU202501239

solution was dispensed onto the cleaned ITO surface and spin coated at 3000 rpm for 20 seconds. The resulting films were then thermally annealed at 100 °C for 20 minutes to enhance molecular ordering and facilitate anchoring. MeO-2PACz is a highly effective self-assembled mono-layer (SAM) material, particularly well-suited for use between ITO and the perovskite layer, optimizing interfacial energy level alignment and charge transport.

The perovskite light-absorbing layer was fabricated by preparing a precursor solution consisting of 491 mg of PbI_2 (Sigma-Aldrich, 99.999%), 114 mg of $PbBr_2$ (Sigma-Aldrich, 99.999%), 170 mg of FAI (Formamidinium iodide, Sigma-Aldrich), 33.05 mg of MABr (Methylammonium bromide, Sigma-Aldrich), and 17.47 mg of CsI (Sigma-Aldrich, 5%), dissolved in a solvent mixture of 800 μL of DMF (Dimethylformamide, Sigma-Aldrich) and 200 μL of DMSO (Dimethyl sulfoxide, Sigma-Aldrich). This solution was spin coated at 2000 rpm for 2 seconds and 5000 rpm for 35 seconds, and during the process, 250 μL of ethyl acetate was dynamically introduced at 20^{th} seconds into the spin cycle to induce rapid crystallization. The coated films were then annealed at 90 °C for 10-minute to complete perovskite formation.

For electron transport layer (ETL), a PCBM ([6,6]-phenyl-C61-butyric acid methyl ester, Sigma-Aldrich) interlayer was introduced by spin coating a 20 mg/mL solution (The solvent is CB (Chlorobenzene, Sigma-Aldrich)) at 2000 rpm for 40 seconds, followed by annealing at 100 °C for 40 minutes to ensure film uniformity and proper interface formation. Subsequently, a 20 nm C_{60} layer was thermally evaporated at a rate of 0.5 nm/s within the glovebox environment.

doi:10.6342/NTU202501239

Subsequently, the mono-layer MoS_2 was transferred onto the C_{60} (Sigma-Aldrich) layer via PDMS stamping, as described in Section 3.2.1. Owing to the excellent interfacial compatibility between MoS_2 and C_{60}, no additional buffer layer was necessary to facilitate efficient charge transport. Following the MoS_2 transfer, Au films with thicknesses of 6, 8, and 10 nm were thermally evaporated onto the MoS_2 surface at a deposition rate of 0.05 nm/s. The deposition was conducted through a finger-shaped metal mask, defining top electrodes with dimensions of 14.5 mm in length and 2 mm in width.

In this way, bifacial perovskite solar cells with Au/MoS_2 TEs can be successfully fabricated. In this architecture, the PVSK active layer absorbs sunlight to generate electron-hole pairs. The photo-generated electrons are transported through the electron transport materials (PCBM and C_{60}) and subsequently extracted via the Au/MoS_2 transparent electrode. The energy level alignment of the device is illustrated in Figure 3-10. MoS_2 provides favorable energy level matching with the work function of C_{60}, facilitating efficient charge extraction. This configuration promotes effective charge separation and transport, reduces energy losses, and improves interfacial quality as well as overall device stability.

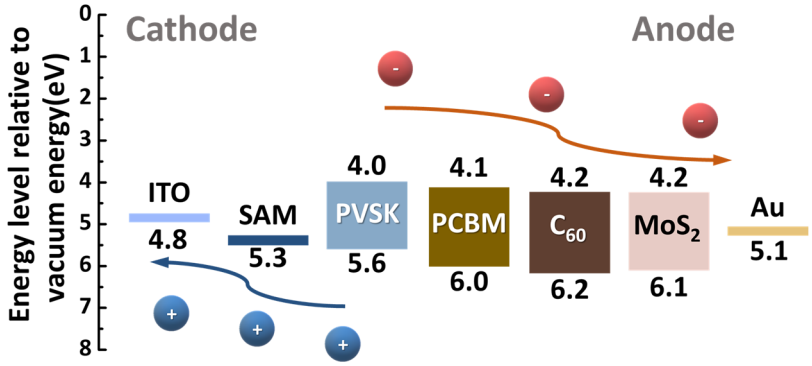

Figure 3-10 Energy level arrangement of Au/MoS_2 TE bifacial perovskite solar cells.

doi:10.6342/NTU202501239

3.3.2 Fabrication of Perovskite Solar Cells

The use of a reference device is critical for evaluating the performance of new electrode materials, as it provides a baseline for comparison. By incorporating a well-established electrode configuration, the reference device allows for the assessment of the advantages and potential improvements offered by alternative materials.

In this study, the reference mono-facial perovskite solar cell with Ag electrodes serves as a control to compare the performance of the novel Au/MoS_2 TEs, offering insights into their efficiency and effectiveness in the device. To assess the performance of transparent electrodes, 100 nm Ag electrodes were used as a substitute for the Au/MoS_2 transparent electrodes in a reference mono-facial perovskite solar cell. The fabrication process follows a similar procedure to that used for the bifacial perovskite solar cells, with one difference: after the thermal evaporation of C_{60}, the transfer of the 2D material and the deposition of a thin Au layer were omitted. Instead, only a thick Ag electrode was deposited. The Ag electrodes were fabricated using the same finger-shaped metal mask and were thermally evaporated onto the C_{60} surface at a deposition rate of 0.1 nm/s. The detailed fabrication process is shown in Figure 3-11.

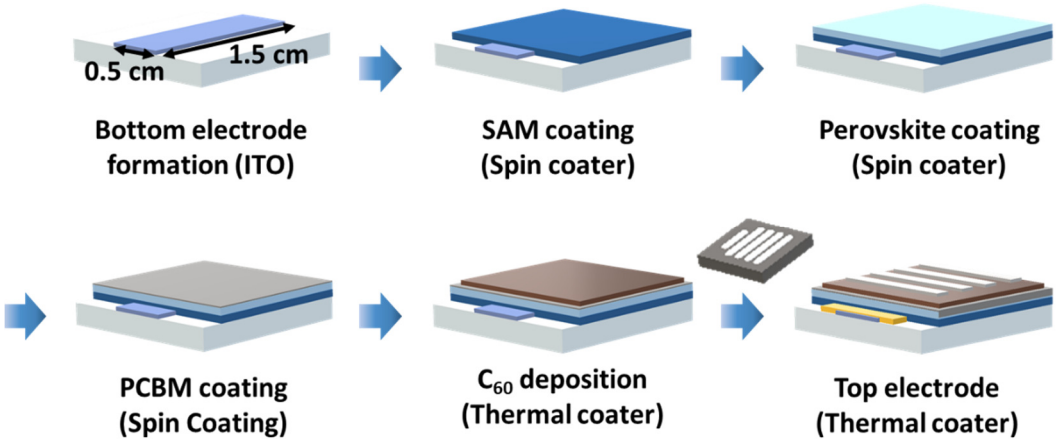

Figure 3-11 Fabrication procedure of the single-side perovskite solar cell with thick 100 nm Ag top electrodes.

doi:10.6342/NTU202501239

3.3.3 Performance Comparison of Bifacial Solar Cells with Reference Devices

According to the aforementioned experimental process, bifacial solar cells with 6, 8, and 10 nm Au/MoS_2 TEs were successfully fabricated. These bifacial solar cells offer several advantages over traditional mono-facial solar cells. Unlike conventional designs, they can collect light from both the front and back sides, enabling higher overall power generation [223]. The working principles of mono-facial and bifacial solar cells are illustrated in Figure 3-12 [223]. By capturing reflected, ambient, and scattered light from the surrounding environment or the ground, they produce more electricity using the same surface area. This makes them well-suited for high-albedo environments such as white rooftops, snowy areas, or sandy terrain, thereby improving the overall performance and cost-effectiveness of the solar energy system [224].

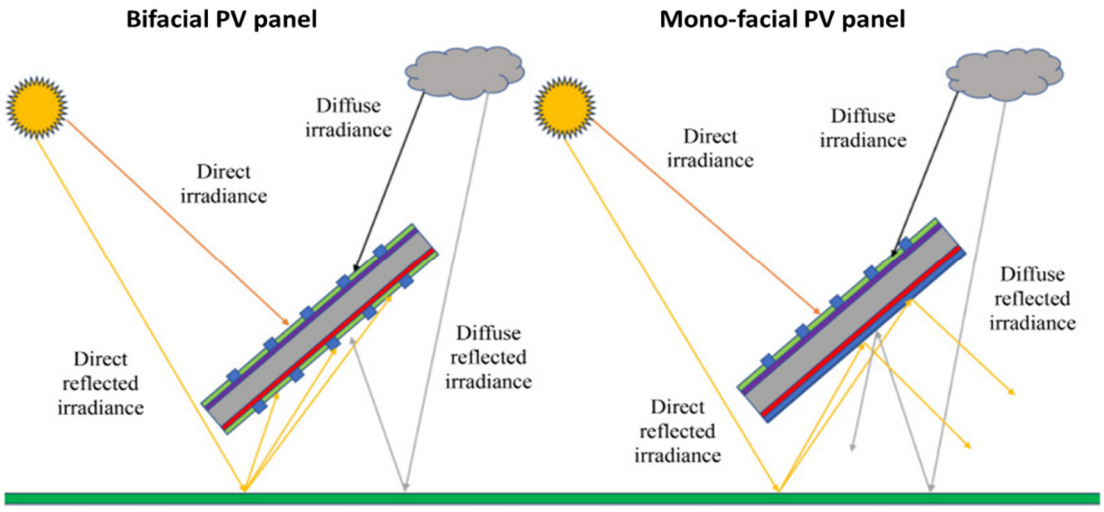

Figure 3-12 Schematic diagram of the working principle of bifacial and mono-facial photovoltaic panels [223].

doi:10.6342/NTU202501239

To evaluate the performance of PSCs using 6, 8, and 10 nm Au/MoS_2 as the top electrode, reference PSC was also fabricated with identical ITO bottom electrodes, HTLs, PVSK light absorbing layers, ETLs, and a 100 nm thick silver top electrode. A mask with a 3 mm × 2 mm opening was placed on top of each solar cell to define the illuminated area. All devices were tested under AM 1.5G illumination to assess their photovoltaic performance from both the front and back sides. The corresponding current-voltage (J-V) curves for both orientations were measured, as shown in Figure 3-13. The detailed solar cell measurement setup is described in Section 2.5.1.

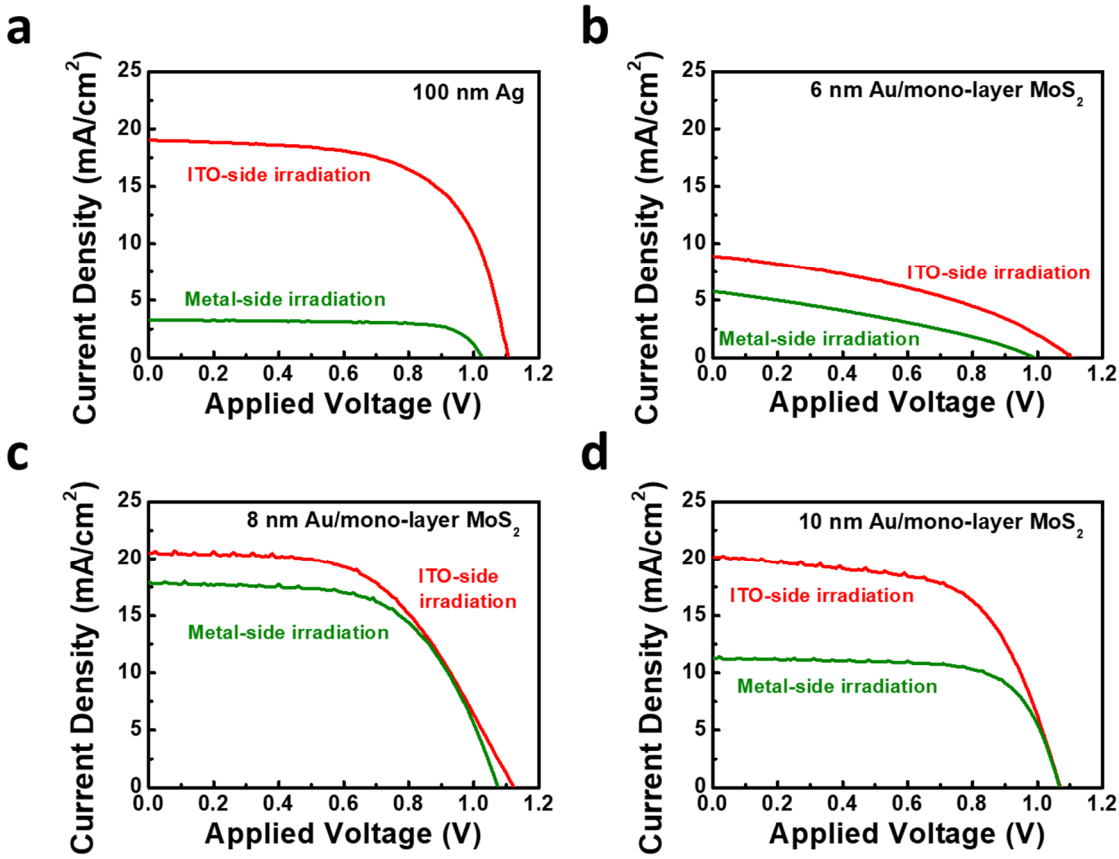

Figure 3-13 (a) J-V curve of the single-side perovskite solar cell with thick 100 nm Ag top electrodes. The bifacial solar cells with (b) 6, (c) 8, and (d) 10 nm Au electrodes deposited on the transferred mono-layer MoS_2 surfaces.

doi:10.6342/NTU202501239

To evaluate the performance of solar cells, four critical parameters are typically measured under standard illumination conditions (AM 1.5G): short-circuit current density (J_{SC}), open-circuit voltage (V_{OC}), fill factor (FF), and power conversion efficiency (PCE) [225-227]. These values provide insight into the electrical output and overall effectiveness of a solar cell in converting light into electricity.

(1) Short-circuit current density (J_{SC})

J_{SC} is the current per unit area generated by the solar cell when the external circuit is shorted (i.e., the voltage across the device is zero). It represents the maximum photocurrent the device can deliver under illumination. The unit is typically mA/cm^2.

$$J_{SC} = \frac{I_{SC}}{A} \qquad \text{(Equation } 3-1\text{)}$$

Where I_{SC} is the short-circuit current, and A is the area of the illuminated region.

(2) Open-circuit voltage (V_{OC})

V_{OC} refers to the maximum voltage a solar cell can provide when there is no external load connected (i.e., the I = 0). It depends on the material properties and the built-in potential of the p-n junction. The unit is V.

(3) Fill factor (FF)

FF is a measure of the "squareness" of the J-V curve and reflects how close the actual maximum power output is to the theoretical power output (given by $V_{OC} \times J_{SC}$). It is a dimensionless quantity, often expressed as a percentage.

$$FF = \frac{P_{MAX}}{V_{OC} \times J_{SC}} = \frac{V_{MP} \times J_{MP}}{V_{OC} \times J_{SC}} \qquad \text{(Equation } 3-2\text{)}$$

Where V_{MP} and J_{MP} are the voltage and current density at the maximum power point.

(4) Power conversion efficiency (PCE)

PCE quantifies how efficiently the solar cell converts incident light energy into

doi:10.6342/NTU202501239

electrical power. It is one of the most important parameters for comparing solar cell performance.

$$\mathrm{PCE} = \frac{\mathrm{P_{OUT}}}{\mathrm{P_{IN}}} = \frac{\mathrm{V_{OC}} \times \mathrm{J_{SC}} \times \mathrm{FF}}{\mathrm{P_{IN}}} \qquad (\text{Equation } 3-3)$$

Where P_{IN} is the power of the incident light, usually 100 mW/cm^2 under standard testing conditions.

These parameters are typically derived from the J-V characteristics of the device, and together they provide a comprehensive understanding of a solar cell's efficiency and practical applicability. Optimizing these values is essential for advancing solar energy technologies. In the context of bifacial solar cells, the bifaciality factor is a key parameter used to evaluate the contribution of rear-side illumination relative to front-side illumination [223]. Unlike conventional mono-facial solar cells, which collect light only from the front side, bifacial devices utilize additional irradiance from the rear side to generate extra current. As such, calculating this parameter provides insight into the effectiveness of the rear side in capturing incident light and converting it into electrical current.

(5) Bifaciality factor

It measures how much the rear side contributes to power generation in bifacial solar cells, helping assess overall light collection efficiency from both sides.

$$\text{Bifaciality factor } (\%) = \frac{\eta_{\mathrm{front}}}{\eta_{\mathrm{rear}}} \times 100\% \qquad (\text{Equation } 3-3)$$

Where η_{rear} and η_{front} is the efficiency measured under rear-side and front-side illumination, respectively. A higher bifaciality factor implies better rear-side performance, which is particularly beneficial in high-albedo environments where reflected or diffused light is substantial. This factor is critical in system design and energy yield simulations for bifacial photovoltaic modules.

doi:10.6342/NTU202501239

Based on the five aforementioned parameters, the photovoltaic performance of the reference PSC under front-side (ITO) and back-side (metal) illumination is evaluated. As shown in Figure 3-13 (a), when the incident light enters from the ITO side, the device exhibits a J_{SC} of approximately 21.83 mA/cm^2, a V_{OC} of around 0.97 V, resulting in a PCE of roughly 14.32%. In contrast, when illuminated from the Ag electrode side, the device exhibits a significantly reduced J_{SC} of 4.07 mA/cm^2 and a PCE of only 2.73%. This notable performance degradation is primarily attributed to the strong light absorption by the thick Ag electrode, which substantially limits photon penetration into the active layer.

Alternatively, this work developed an Au/mono-layer MoS_2 TE to replace the thick Ag top electrode without altering the fabrication process. The corresponding J-V characteristics under ITO- and metal-side illumination are shown in Figure 3-13 (b–d). Although the 6 nm Au film demonstrated high optical transmittance (Figure 3-8) and an acceptable sheet resistance of 20.35 Ω/□ (Table 3-1) when measured on glass substrates, the actual device performance was inferior compared to the reference cell. Specifically, it showed higher series resistance and lower J_{SC}, indicating poor current collection efficiency. This discrepancy is likely caused by the increased surface roughness of the perovskite layer relative to glass, which may have compromised the uniformity and conductivity of the top electrode, leading to an actual sheet resistance higher than anticipated.

A second device, fabricated using the same process with an increased Au thickness of 8 nm, is shown in Figure 3-13 (c). Under ITO-side illumination, the device achieves a V_{OC} ~ 1.12 V, J_{SC} ~ 19.92 mA/cm^2, and a PCE of ~11.36%, which closely approaches the performance of the reference device. When light enters from the metal side, the device

doi:10.6342/NTU202501239

still performs well, achieving a V_{OC} ~ 1.04 V, J_{SC} ~ 16.45 mA/cm^2, and PCE 10.18%, corresponding to a bifaciality factor of 89.6%.

Furthermore, a third device was fabricated with a 10 nm-thick Au layer to further enhance conductivity. The J-V curves for this device are shown in Figure 3-13 (d). Under front-side (ITO) illumination, the device maintains strong performance with V_{OC} ~ 1.00 V, J_{SC} ~ 21.98 mA/cm^2, and PCE ~12.27%. However, when illuminated from the rear (metal) side, J_{SC} decreases to ~12.78 mA/cm^2, leading to a reduced PCE of ~6.79%, and a bifaciality factor of 55.3%. The detailed forward (FWD) and reverse (RVS) J-V results are shown in Table 3-2.

Table 3-2 The forward and reverse J-V characteristics of four devices were measured under illumination from both sides of the solar cells.

No.	Electrode	J_{sc} (mA/cm^2)	V_{oc} (V)	Efficiency (%)
Sample 1_from ITO side	100 nm Ag	21.83 ± 1.86	0.97 ± 0.18	14.32 ± 3.13
Sample 1_form Au side	100 nm Ag	4.07 ± 0.04	0.94 ± 0.17	2.73 ± 0.55
Sample 2_from ITO side	6 nm Au/MoS_2	9.23 ± 0.36	1.11 ± 0.01	3.30 ± 0.47
Sample 2_form Au side	6 nm Au/MoS_2	7.04 ± 1.43	1.01 ± 0.08	2.30 ± 0.54
Sample 3_from ITO side	8 nm Au/MoS_2	19.92 ± 0.55	1.12 ± 0.01	11.36 ± 0.63
Sample 3_form Au side	8 nm Au/MoS_2	16.45 ± 0.33	1.04 ± 0.04	10.18 ± 0.05
Sample 4_from ITO side	10 nm Au/MoS_2	21.98 ± 1.06	1.00 ± 0.05	12.27 ± 1.48
Sample 4_form Au side	10 nm Au/MoS_2	12.78 ± 1.24	1.06 ± 0.08	6.79 ± 0.68

The above results a fundamental trade-off in device design: increasing the thickness of the Au/mono-layer MoS_2 electrode can enhance electrical conductivity, thereby reducing series resistance and potentially improving charge collection efficiency. However, this improvement comes at the cost of reduced optical transmittance through the Au/ MoS_2 electrode. As a result, the light reaching the active layer from the rear side of the bifacial PSCs is diminished, leading to a decrease in overall photocurrent

doi:10.6342/NTU202501239

generation and device performance under rear-side illumination. Therefore, careful optimization of the Au thickness is essential to balance electrical and optical properties for maximizing bifacial device efficiency.

The external quantum efficiency (EQE) spectra of the device were also measured to verify whether the addition of Au/MoS_2 transparent electrodes in bifacial solar cells affects the absorption range of the active layer. EQE measurements provide insight into the wavelength-dependent photo-response of the device, revealing how efficiently incident photons are converted into collected charge carriers at each wavelength [228]. In bifacial solar cells, comparing the EQE under front- and rear-side illumination further allows evaluation of the back electrode's optical transmittance and the contribution of rear-side photocurrent. Accordingly, Figure 3-14 (a) presents the EQE results of a PSC incorporating 8 nm Au/MoS_2 transparent electrode. When the device is illuminated from the ITO side, the highest EQE appears at around 520 nm, indicating the peak photo-response of the device. More broadly, the EQE remains above 80% within the 490-540 nm range, which corresponds to the main absorption region of the solar spectrum where photon flux is highest. This suggests that the active layer material exhibits strong light absorption and efficient carrier collection in the visible range, contributing to the overall photocurrent. The cut-off wavelength occurs near 770 nm, and based on the relation $E_g = 1240/\lambda_{cut\text{-}off}$, the energy gap of the perovskite absorber layer in this study is estimated to be approximately 1.61 eV. When the device is illuminated from the metal side, notably lower EQE values are observed in the 300-400 nm and 600-700 nm wavelength regions. This reduction aligns with the transmission characteristics of ITO and thin Au films deposited on glass substrates, as depicted in Figure 3-8. The reduced EQE in the 300-400 nm range is mainly due to absorption by the MoS_2 layer and partial reflection or

doi:10.6342/NTU202501239

absorption by the thin Au film [229]. In the 600-700 nm range, additional losses may arise from optical interference and plasmonic effects in the Au layer [222].

On the other hand, to further investigate whether the addition of MoS_2 introduces resistance in PSCs, electrochemical impedance spectroscopy (EIS) measurements were conducted. EIS is a technique used to analyze charge transport and recombination dynamics within a device by applying a small AC voltage over a defined frequency range [230]. It provides quantitative information on charge transfer resistance (R_{ct}), carrier recombination processes, series resistance, and shunt resistance at the interfaces within the solar cell. Figure 3-14 (b) shows the EIS curve of the device under metal-side illumination, measured at an applied bias of 900 mV. The device exhibits low series resistance, indicating efficient charge transfer across the device interface. This result confirms that the 8 nm Au/MoS_2 top electrode does not impede carrier mobility or significantly increase the series resistance.

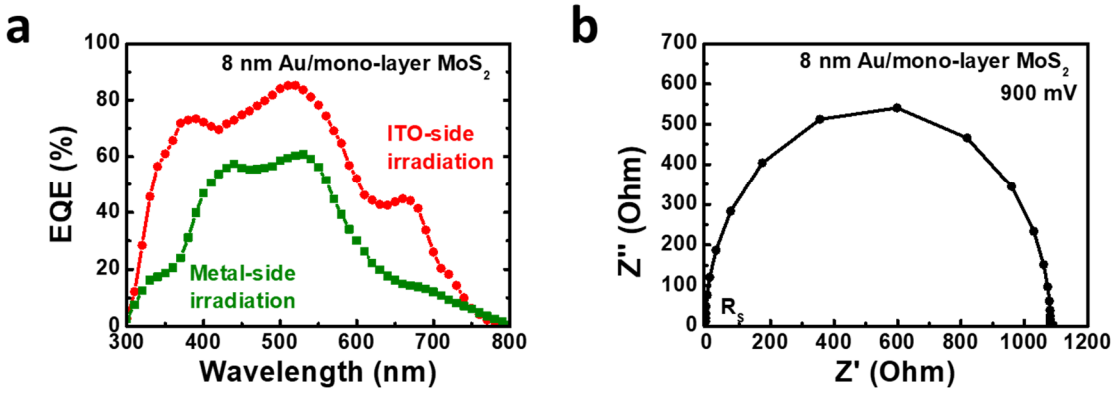

Figure 3-14 (a)The EQE and (b) EIS curve of the device with 8 nm Au/mono-layer MoS_2 TEs. The EIS curve of the device was measured at an applied voltage of 900 mV.

Another important aspect to consider is the long-term stability of the solar cell. The J-V characteristics of the same device featuring 8 nm-thick Au/MoS_2 transparent electrodes, after being stored in a glove box for six months, are shown in Figure 3-15. For

doi:10.6342/NTU202501239

comparison, the original performance of the freshly fabricated device (Figure 3-13) is also included in Figure 3-15. Detailed solar energy measurement results are presented in Table 3-3. As illustrated, only a slight reduction in short-circuit current density and power conversion efficiency is observed under illumination from both the ITO and metal sides. Despite this minimal degradation, the device still maintains a bifaciality factor of 85.6%. These findings indicate that the thin Au layer deposited on MoS_2 remains a stable and effective transparent electrode for solar cells and potentially for other optoelectronic devices involving light emission or absorption.

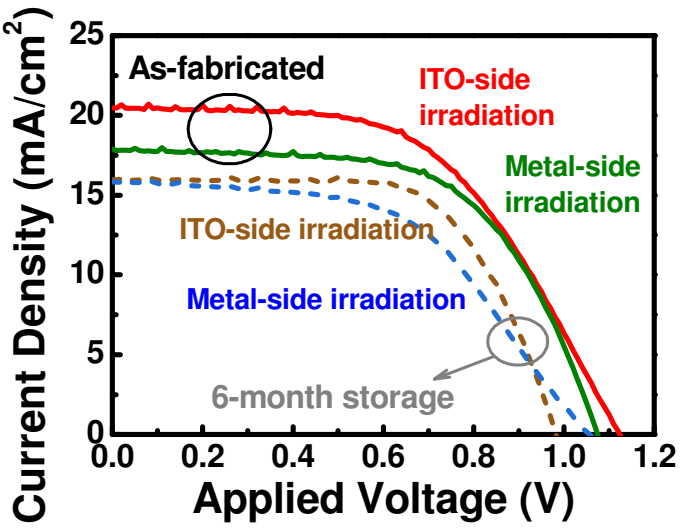

Figure 3-15 The J-V curve of the device with 8 nm Au/mono-layer MoS_2 transparent electrodes after 6-month storage in a glovebox. The J-V curve of the as-fabricated device is also shown in the figure.

Table 3-3 The J-V characteristics of the device with 8 nm Au/MoS_2 TE was measured under illumination from both sides of the solar cells after 6-month storage in a glovebox.

No.	Electrode	J_{sc} (mA/cm²)	V_{oc} (V)	PCE (%)
Sample 3_from ITO side	8 nm Au/MoS_2	20.47	1.12	12.52
Sample 3_form Au side	8 nm Au/MoS_2	17.90	1.07	11.67
Sample 5_from ITO side	8 nm Au/MoS_2 (6-month storage)	15.94	0.99	10.29
Sample 5_form Au side	8 nm Au/MoS_2 (6-month storage)	15.83	1.06	8.81

doi:10.6342/NTU202501239

3. 4 Application Potential and Future Directions

3.4.1 Potential of Different Metals as Transparent Electrodes

The ability of van der Waals epitaxial growth on MoS_2 surfaces to facilitate the formation of continuous, conductive Au thin films suggests a promising route toward developing cost-effective alternatives for transparent electrodes. To explore this possibility, a new device was fabricated by depositing an 8 nm Ag onto a mono-layer MoS_2 film transferred onto the same perovskite solar cell structure. The resulting J-V curve is presented in Figure 3-16 (a). Compared with the device using an 8 nm Au-based TE, the Ag-based device exhibits a noticeably higher series resistance, implying that the conductivity of the 8 nm Ag film is inferior. This reduction in conductivity is likely due to surface oxidation of the ultrathin Ag layer when exposed to ambient air. The decrease in conductivity may be attributed to the fact that the surface of ultrathin silver is more susceptible to oxidation than that of Au. Additionally, silver is more sensitive to sulfur and other contaminants, which may contribute to the observed high series resistance.

Consequently, when solar illumination is applied from the ITO side, the device delivers a J_{SC} of approximately 26.4 mA/cm^2. However, illumination from the Ag side yields a significantly lower J_{SC} of around 18.6 mA/cm^2. To better understand this behavior, another sample consisting of an 8 nm Ag film on transferred mono-layer MoS_2 supported by a glass substrate was prepared, and its transmission spectrum was measured, as shown in Figure 3-16 (b). For comparison, the spectrum for an 8 nm Au/MoS_2 film on glass is also included. The Ag-based sample displays roughly 10% higher optical absorption in the visible range, which likely accounts for the reduced photocurrent when the device is illuminated from the metal side.

doi:10.6342/NTU202501239

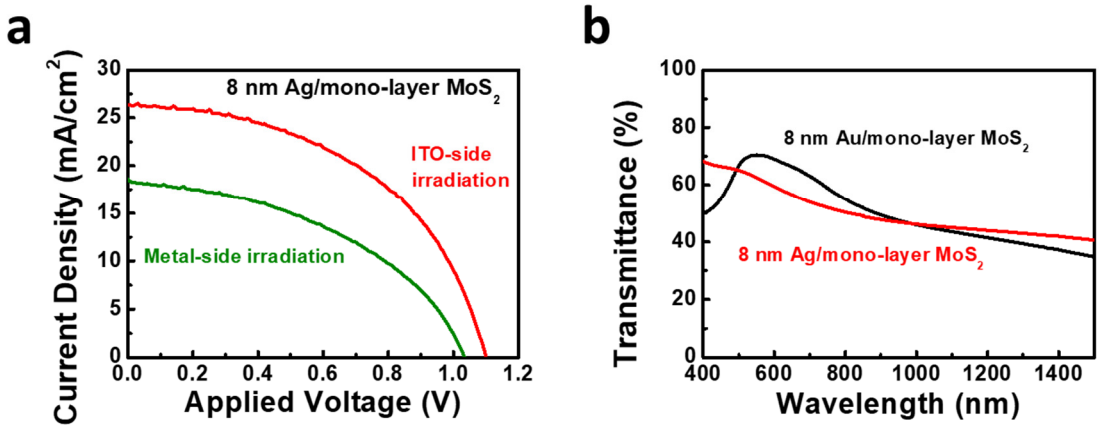

Figure 3-16 (a) The J−V curve of the device with 8 nm Ag/MoS_2 transparent electrodes. (b) The transmission spectra of 8 nm Au and Ag grown on the surface of the mono-layer MoS_2 transferred to glass substrates.

Despite this, the device still achieves a bifaciality factor of 58.9%. These findings support the notion that van der Waals epitaxial growth on MoS_2 is beneficial not only for Au but also for Ag, enabling the formation of uniform, conductive ultrathin films. To further improve the performance, especially under metal-side illumination, the application of a passivation layer to inhibit Ag oxidation could allow for thinner, more conductive Ag electrodes, ultimately enhancing bifacial solar cell efficiency.

Based on this concept, it can be seen that depositing thin metal films onto the MoS_2 surface to fabricate transparent electrodes has great potential. Still, there are multiple crucial aspects that need further investigation. MoS_2, as a typical layered 2D material with a surface free of dangling bonds, supports the van der Waals epitaxial growth of metals such as Au, Ag, and Cu [218-220]. This mechanism facilitates the formation of continuous and conductive ultrathin metal films, even at thicknesses of just a few nanometers.

doi:10.6342/NTU202501239

Nevertheless, the success of this process is influenced by multiple factors, including the metal-MoS_2 work function alignment, wettability, and interfacial charge interactions. According to reported work function data, high work function metals like Au (ψ = ~5.1), and Pd (ψ = ~5.12) are more likely to form low Schottky barriers with MoS_2 [128, 231], promoting efficient carrier injection and collection, and thus preserving solar cell charge transport. Conversely, low work function metals such as Ti (ψ = ~4.3), or Al (ψ = ~4.1) tend to form higher Schottky barriers, potentially hindering electron transport and degrading device performance.

Oxidation also presents a major challenge. Reactive metals such as Cu and Al readily oxidize in air, leading to the formation of non-conductive oxide layers at the metal–MoS_2 interface or on the metal surface. Even a few nanometers of oxide can significantly increase contact resistance and reduce optical transmittance, thereby compromising the function of the transparent electrode.

Therefore, while the integration of ultrathin metal films on MoS_2 surfaces offers promising design flexibility for transparent electrodes, its practical viability must be carefully evaluated. Parameters such as metal type, deposition conditions, and oxidation stability must be optimized to ensure reliable performance in high-efficiency optoelectronic applications.

doi:10.6342/NTU202501239

Chapter 4 Vertical and Planar 2D Material Photodetectors

✧ This chapter is adapted from content published in Advanced Materials Interfaces, vol. 12, issue 5, pp. 2400641, November 2024, with partial revisions by the author.

4.1 Opportunities and Challenges in Multi-layer 2D Material-Based Devices

4.1.1 Advantages of Multi-layer 2D Material-Based Applications

While mono-layer 2D materials have been extensively studied, multi-layer counterparts offer enhanced design flexibility owing to their tunable thickness, enabling broader applicability in real-world devices. Their increased thickness helps suppress quantum tunneling and mitigates the risk of electrical shorting, thereby enhancing their suitability for a wide range of electronic applications. For instance, few-layer 2D materials have been employed in transistors and memory devices, where the increased thickness contributes to improved electrostatic control and stability [89, 90, 232]. Second, multi-layer 2D materials exhibit superior light absorption capabilities, which have the potential to enhance photoelectric conversion efficiency—an essential factor in photovoltaic applications. Their broadband absorption and increased optical path length can improve photon harvesting, potentially leading to better device performance as advances in fabrication and interface engineering continue to address current limitations. For instance, thick WS_2 flakes have been used to fabricate vertical photovoltaic devices that demonstrate clear photovoltaic responses, although their power conversion efficiencies remain relatively low at present [164, 233].

doi:10.6342/NTU202501239

In addition to their electronic and optical benefits, multi-layer 2D materials also offer structural advantages that enhance functional versatility. The van der Waals forces between the layers in multi-layer 2D materials impart excellent thermal stability and mechanical flexibility, making them well-suited for flexible electronic devices [113, 117, 234]. Moreover, interlayer coupling in these materials can modulate band structure, affect carrier mobility, and introduce new quantum phenomena, thereby enabling novel device concepts such as spintronic applications [235]. Despite the aforementioned advantages in structural robustness, light absorption, and device integration, systematic studies on carrier transport mechanisms in multi-layer 2D materials, especially the comparison between in-plane (lateral) and out-of-plane (vertical) transport, remain limited. Unlike mono-layer systems, where carrier dynamics are primarily confined to a single plane, multi-layer 2D materials introduce interlayer interactions governed by weak van der Waals forces. These interactions result in fundamentally different transport behaviors along different crystallographic directions, with lateral transport benefiting from covalent bonding within layers, while vertical transport is hindered by low interlayer coupling and increased recombination probability. Understanding and controlling these directional transport processes is thus crucial for realizing the full potential of multi-layer 2D materials in optoelectronic applications. Given these gaps in understanding, especially in directional charge transport, this study investigates multi-layer 2D materials in two distinct device geometries, vertical photovoltaic and lateral photoconductive photodetectors, to directly compare and analyze carrier transport across and along the layers. This dual approach not only provides new insights into the anisotropic transport behavior of multi-layer TMDs but also offers practical guidelines for engineering high-performance, directionally-optimized optoelectronic devices.

doi:10.6342/NTU202501239

4.1.2 Challenges in Multi-layer 2D Material Growth

While multi-layered 2D materials offer significant potential, several challenges must be addressed to fully unlock their capabilities for device applications. Among the most pressing challenges are the controlled synthesis of large-area, uniform, and high-quality multi-layer films, as well as the resolution of interfacial issues, particularly in vertical device architectures. These factors continue to hinder the scalability and practical deployment of multi-layer 2D materials.

Various techniques have been explored for the growth of multi-layered 2D materials, yet each approach presents its own limitations [109]. For example, MBE provides exceptional precision, allowing for atomically controlled, layer-by-layer deposition of 2D materials. While this method yields high-quality films with sharp interfaces, MBE suffers from a slow growth rate, limited scalability, and high equipment costs, making it unsuitable for cost-effective, large-scale production.

method for synthesizing high-quality, large-area 2D materials due to its scalability and controllability. Typically, metal oxides such as MoO_3 or WO_3 react with chalcogen precursors like sulfur or selenium to form TMD layers on substrates [104]. While mono-layer growth is relatively well-controlled, achieving uniform multi-layer structures remains challenging. A primary limitation is the self-limiting nature of CVD [236]. After a mono-layer forms, the surface becomes chemically saturated, suppressing vertical growth and favoring lateral expansion. Consequently, extending the growth time or increasing the precursor concentration does not reliably lead to multi-layer formation, but instead directly results in a different nucleation mechanism [237]. This hinders the

doi:10.6342/NTU202501239

development of multi-layer 2D materials with well-defined electronic and optical characteristics, which are essential for advanced device applications.

PVD techniques, such as (post-deposition) sputtering followed by sulfurization, are scalable and compatible with industrial processes. Previous studies have demonstrated that multi-layer MoS_2 films can be synthesized by sulfurizing Mo layers deposited via RF sputtering [238, 239]. However, if the Mo precursor layer is too thick, planar growth behavior dominates, and the formation of Mo oxides becomes difficult to suppress. This results in the incomplete sulfurization of Mo, leaving residual oxide clusters surrounded by thin MoS_2 layers, as shown in Figure 4-1 [239]. These structural inhomogeneities degrade the film quality and limit device performance. Therefore, optimizing PVD conditions remains an essential task in achieving high-quality multi-layer 2D materials.

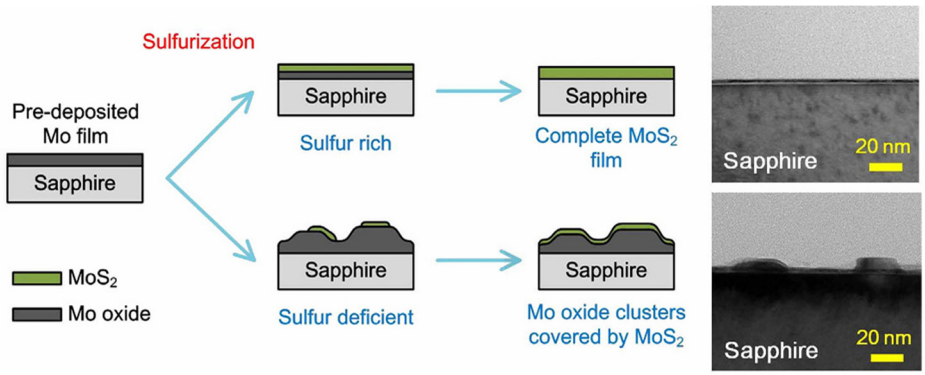

Figure 4-1 Schematic illustration of the growth evolution of MoS_2 samples synthesized under sulfur-rich and sulfur-deficient conditions [239].

In conclusion, while multi-layer 2D materials hold great promise for next-generation electronics and optoelectronics, overcoming synthesis-related challenges, particularly in achieving uniformity, scalability, and layer control, is essential. Continued efforts to develop more effective and controllable growth techniques will be pivotal in realizing the full potential of these materials in practical applications.

doi:10.6342/NTU202501239

4.2 Two-stage Growth Procedure of Multi-layer MoS_2

4.2.1 Wafer-Scale Multi-layer MoS_2 Growth

In this work, a PVD-based method for growing multi-layer MoS_2 was developed, enabling the synthesis of high-quality, wafer-scale MoS_2 films with fewer than 30 layers. This section provides a detailed description of the growth process, which consists of two main steps: (1) deposition of amorphous MoS_2 using a sputtering system (Section 2.1.2) and (2) high-temperature sulfurization (Section 2.1.4), as illustrated in Figure 4-2.

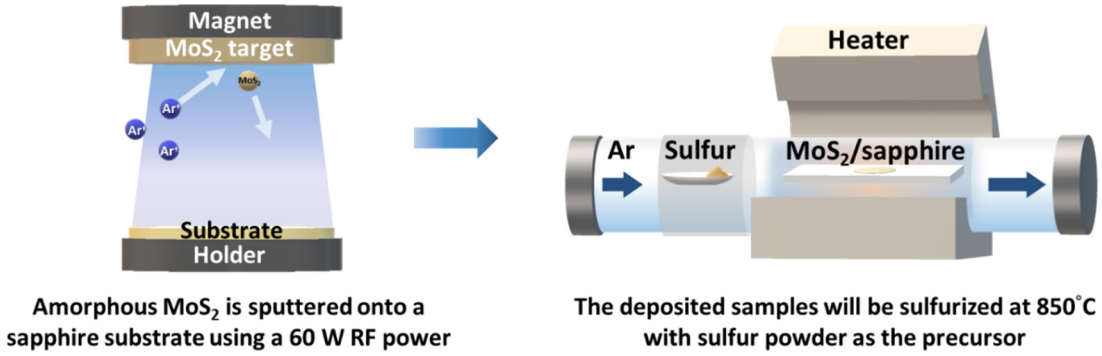

Figure 4-2 Schematic illustration of the wafer-scale multi-layer MoS_2 growth process.

(1) Deposition of amorphous MoS_2

To address the aforementioned limitations, using amorphous MoS_2, rather than metallic Mo target [239], offers a more effective strategy. The intrinsically planar structure of MoS_2 helps suppress cluster formation during high temperature processing. The method of using an RF sputtering system to pre-deposit amorphous MoS_2 is as follows: First, the main power supplies of the chiller and the RF magnetron sputtering machine are turned on, followed by activation of the mechanical pump and the diffusion pump. The diffusion pump is allowed to warm up for 40 minutes. Afterward, N_2 is introduced to break the vacuum, allowing the chamber to be opened. A 2-inch single-side polished C-plane sapphire substrate and an amorphous MoS_2 target (99.9%, Summit-Tech Resource Corp.) are then placed

doi:10.6342/NTU202501239

into the chamber. The mechanical pump is used to evacuate the chamber from atmospheric pressure to 3×10^{-2} torr. Once this pressure is reached, the mechanical pump valve is closed and the diffusion pump valve is opened to further evacuate the chamber to below 1×10^{-5} torr, ensuring a high-purity environment.

For the sputtering process, 30 sccm of Ar is introduced as the working gas, and the chamber pressure is stabilized at 5×10^{-2} torr. The RF power supply is then turned on to provide 15 W of initial power. At this stage, Ar plasma becomes visible between the target and the substrate. The power is gradually increased to a working level of 60 W, and the pressure is adjusted to 4×10^{-3} torr. A pre-sputtering step of 1 minute is performed to stabilize the power output and remove any molybdenum oxide (MoO_x) present on the target surface. Subsequently, the shutter is opened to allow uniform deposition of the MoS_2 onto the sapphire substrate. MoS_2 films were deposited for various durations, namely, 40, 80, 120, 160, and 200 seconds. After deposition, the shutter is closed, RF power output is gradually reduced to 0 W, and the Ar gas flow is stopped. Finally, the diffusion pump valve is closed, N_2 is introduced to break the vacuum, and the samples are retrieved from the chamber.

(2) High temperature sulfurization

Subsequently, the sample was transferred to a quartz tube furnace for high temperature sulfurization. The amorphous MoS_2 deposited substrate was positioned at the center of the furnace, while sulfur powder was placed in an alumina crucible within an independently controlled heating zone equipped with a heating belt. A mechanical pump evacuated the system from atmospheric pressure to 10^{-3} torr to ensure a clean environment. Ar (200 sccm) served as the carrier, and the chamber pressure was regulated at 50 torr using a pressure controller. The central zone of the

doi:10.6342/NTU202501239

furnace was ramped to 850 °C at a rate of 20 °C/min. The sulfur zone was initially preheated to 90 °C and gradually increased to 160 °C once the furnace center reached 500 °C. At this point, sulfur began to melt and evaporate, with the resulting vapor transported into the reaction zone by carrier gas. Sulfur vapor reacted with the amorphous MoS_2 sample at the center of the furnace, resulting in MoS_2 formation within 20 minutes. A longer sulfurization time than that used in Section 3.2.1 was employed to ensure complete conversion of thicker samples. Following, the system was allowed to cool naturally to room temperature. The chamber was then vented with N_2, and the sulfurized MoS_2 sample was collected.

Photographs of multi-layer MoS_2 films deposited for different durations (40, 80, 120, 160, and 200 seconds) using RF sputtering followed by low-pressure sulfurization are shown in Figure 4-3. An obvious trend was observed: the color of the samples gradually darkened with increasing deposition time, indicating a corresponding increase in film thickness. This suggests that the duration of the sputtering process plays an important role in determining the final thickness of the MoS_2 film.

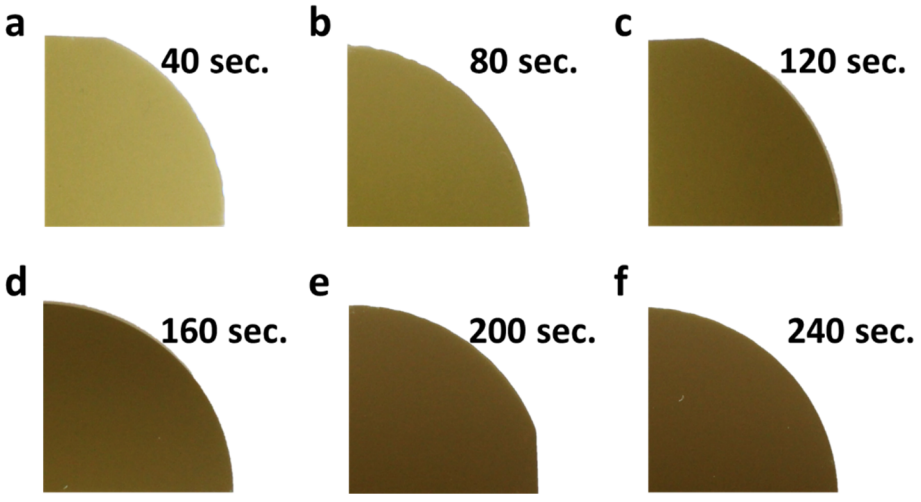

Figure 4-3 Photos of multi-layer MoS_2 films with different deposition times.

doi:10.6342/NTU202501239

Raman spectroscopy was conducted after the growth process to further evaluate both the number of MoS_2 layers and the overall material quality. As shown in Figure 4-4 (a), the characteristic E_{2g}^1 peak is located between approximately 382 cm^{-1} and 383 cm^{-1}, while the A_{1g} peak appears between 407 cm^{-1} and 408 cm^{-1}. These peak positions yield a Δk ($A_{1g} - E_{2g}^1$) value ranging from 24 cm^{-1} to 25 cm^{-1}, which gradually stabilizes around 25.2 cm^{-1} as the film becomes thicker. This trend is consistent with previously reported results in the literature, as shown in Figure 4-4 (b) [204]. The stabilization of Δk indicates that beyond a certain thickness, the Raman peak separation becomes less sensitive to further increases in the number of layers. In addition, the Raman signal intensity decreases with increasing film thickness, likely due to enhanced light absorption and scattering in thicker samples.

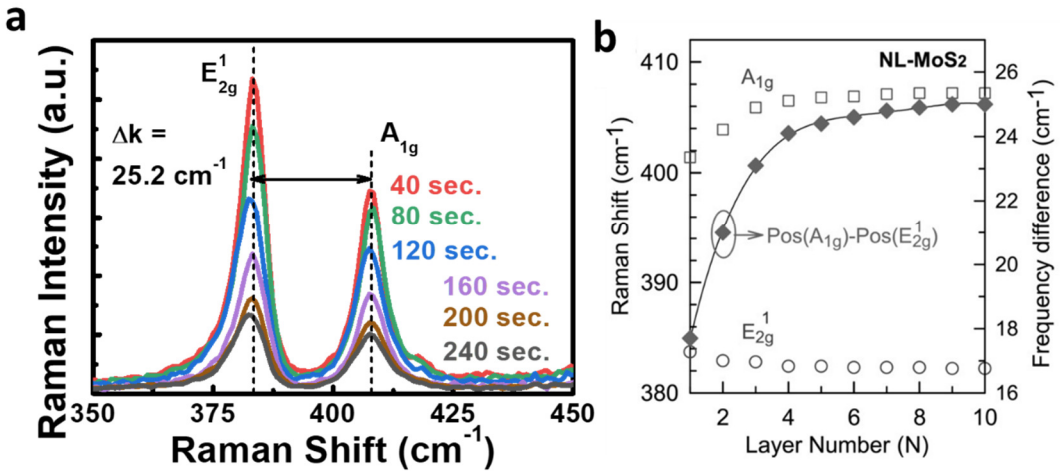

Figure 4-4 (a) Raman spectroscopy of MoS_2 at different sputtering durations. (b) Measured positions of A_{1g}, E_{2g}^1, and the corresponding Δk values for 1-10 layer MoS_2 using a 532 nm laser [204].

In summary, once the Δk value reaches a plateau, it becomes increasingly difficult to accurately assess film thickness using Raman spectroscopy alone. Therefore, the development of complementary characterization methods is needed to determine whether additional layers have formed.

doi:10.6342/NTU202501239

4.2.2 Layer Number Determination and Property Characterization of Multi-layer MoS_2

In addition to direct verification through cross-sectional HRTEM, atomic layer etching offers an alternative approach for accurately determining the number of MoS_2 layers [199, 240]. A schematic of the step-by-step ALE process is shown in Figure 4-5. By systematically repeating the etching cycles, the total number of 2D materials layers can be identified once the underlying substrate (sapphire) becomes visible, confirming complete MoS_2 removal [199, 240].

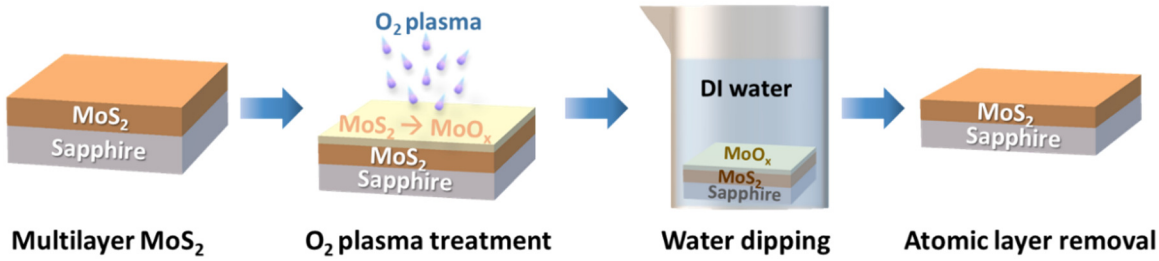

Figure 4-5 Schematic diagram of the atomic layer etching process.

The ALE of multi-layer MoS_2 was carried out using a customized low-pressure RF oxygen plasma system. Initially, the multi-layer MoS_2 sample was placed inside the chamber, which was evacuated from atmospheric pressure to 5×10^{-2} torr using a scroll pump. During the etching process, the O_2 flow rate was maintained at 30 sccm, and the chamber pressure was stabilized at 4.5×10^{-1} torr. The RF power was set to a low level of 30 W to enable precise etching control. Once the chamber pressure stabilized, the plasma power was activated, and a visible oxygen plasma glow was observed. The plasma was applied for exactly 4 seconds before being promptly turned off. The oxygen plasma selectively oxidized the topmost MoS_2 layer into MoO_x.

doi:10.6342/NTU202501239

After plasma exposure, N_2 was introduced to vent the chamber, and the sample was removed. The samples were then immersed in DI water and gently rinsed to remove the oxidized layer. This oxidation-stripping cycle was repeated until the underlying substrate was fully exposed, as illustrated in Figure 4-6. By precisely controlling the plasma duration in each cycle, one MoS_2 layer could be selectively removed, enabling accurate determination of the original film's layer number.

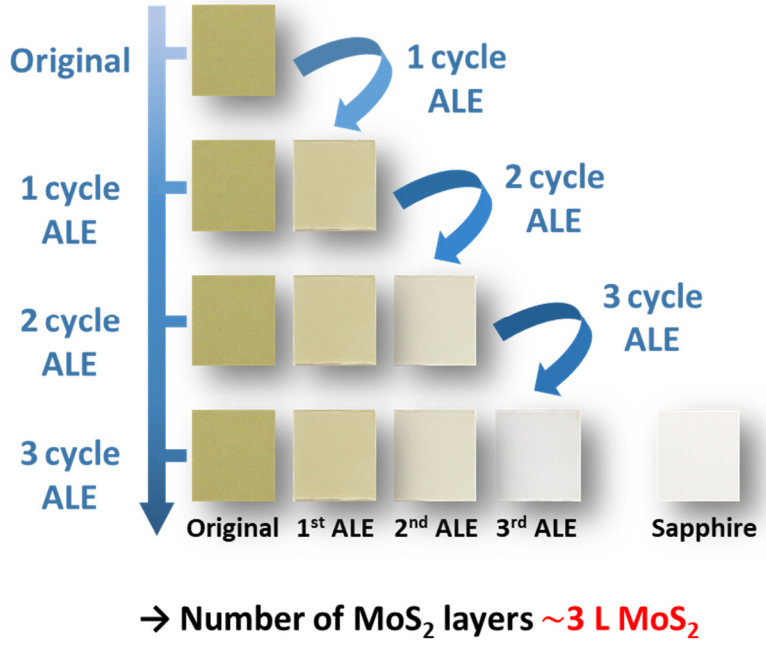

Figure 4-6 Determination of the number of oxidation-stripping cycles by colorimetry.

According to this method, the 6 samples with varying sputtering durations and gradually darkening colors, as described above, were also analyzed using ALE system. Figure 4-7 illustrate the relationship between sputtering duration and the number of MoS_2 layers. The number of layers corresponding to sputtering times of 40, 80, 120, 160, 200, and 240 seconds are 6, 14, 18, 21, 26, and 32 layers, respectively. A linear regression analysis was then performed on these data points. Based on the resulting trend line, the estimated sputtering durations required to obtain 10, 20, and 30 layers of MoS_2 are approximately 60 seconds, 145 seconds, and 225 seconds, respectively.

doi:10.6342/NTU202501239

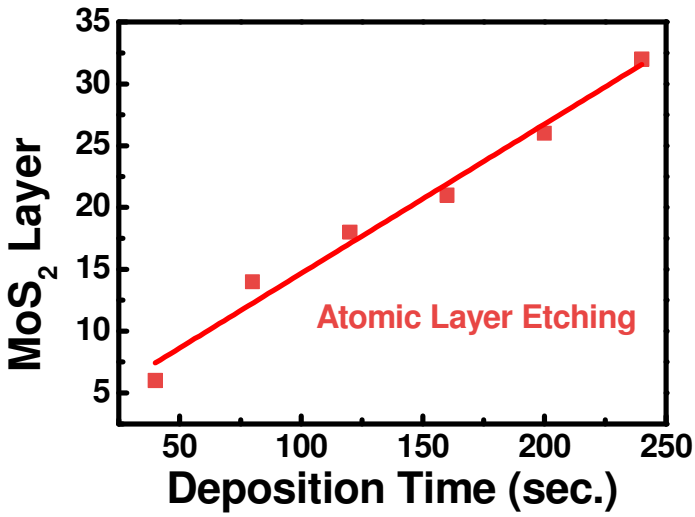

Figure 4-7 Relationship between sputtering durations and number of MoS_2 layers.

To validate the linear correlation between sputtering time and the number of MoS_2 layers, three additional samples were fabricated with sputtering durations of 60, 145, and 225 seconds, corresponding to the predicted layer numbers of 10, 20, and 30, respectively (Figure 4-8).

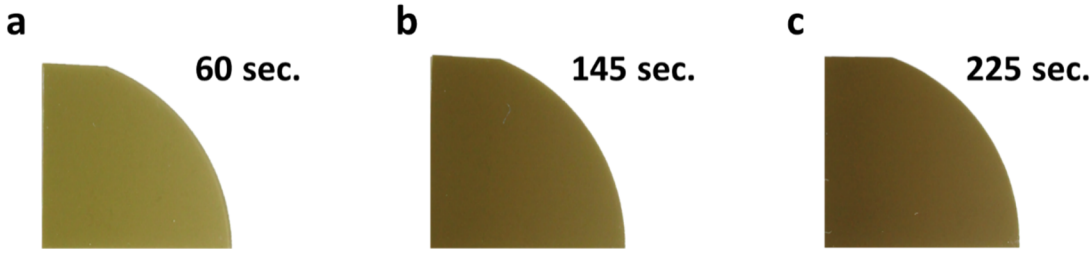

Figure 4-8 The pictures of the quarter 2-inch samples three samples with 60, 145 and 225 sputtering times.

The Raman spectra of these samples are presented in Figure 4-9. Consistent with the previous results, the films of all three samples were uniform and exhibited dark coloration. Although an increase in the number of MoS_2 layers appears to correlate with longer sputtering durations, all three samples exhibited the same Δk value of 25.2 cm^{-1}. This indicates that the films contain more than 5 layers [241]; however, the precise number of layers cannot be determined solely from Raman.

doi:10.6342/NTU202501239

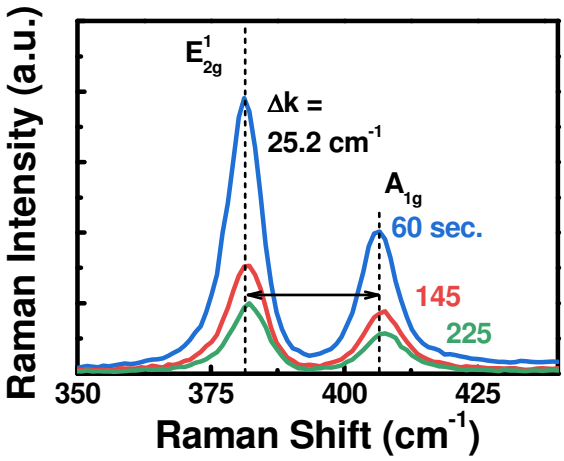

Figure 4-9 The Raman spectrum of three samples with 60, 145 and 225 sputtering times.

Therefore, cross-sectional HRTEM was conducted on the three samples to determine the number of MoS_2 layers. The corresponding images are shown in Figure 4-10. Unlike the cluster formation often observed in thick MoS_2 films grown with Mo targets [239], uniform multi-layer MoS_2 was grown on the sapphire substrates. The sputtering durations for the three samples were 60, 145, and 225 seconds, corresponding to actual layer counts of 8, 18, and 31, respectively. These results demonstrate that, although sputtering is a relatively mature technique, the use of amorphous MoS_2 targets enables wafer-scale, controllable growth of multi-layer MoS_2.

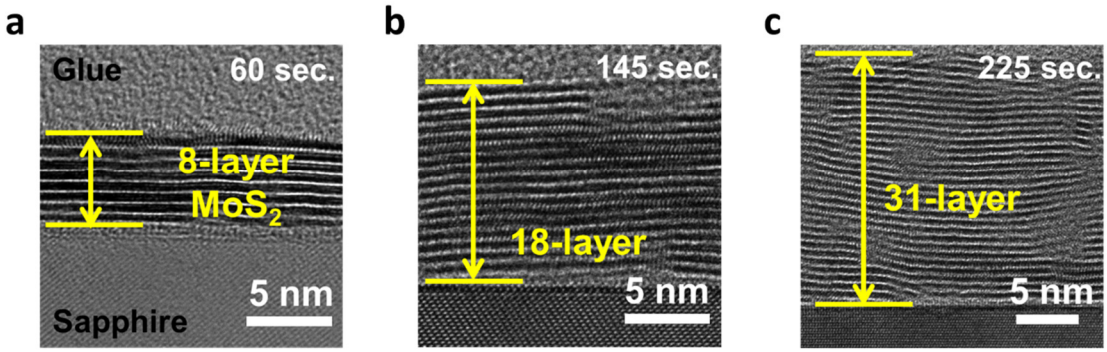

Figure 4-10 The cross-sectional HRTEM images of three samples with (a) 60, (b) 145 and (c) 225 sputtering times.

doi:10.6342/NTU202501239

The corresponding layer numbers obtained from ALE and HRTEM analyses are plotted against sputtering time in Figure 4-11. As shown, the MoS_2 layer counts from both methods differ by only one to two layers, confirming that: (a) the ALE technique provides reliable quantification of MoS_2 thickness, and (b) sputtering with a MoS_2 target yields a linear relationship between sputtering time and film thickness, enabling controlled growth of films with up to 30 layers.

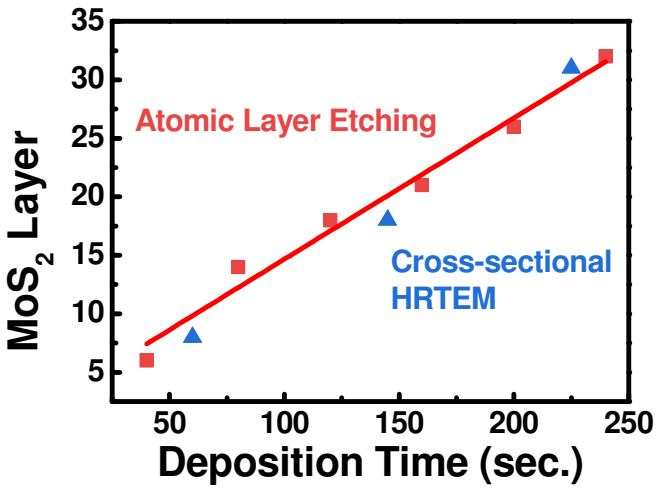

Figure 4-11 Number of MoS_2 layers in samples prepared with different sputtering durations, determined by ALE and HRTEM.

To further investigate the growth mechanism of multi-layer MoS_2, the cross-sectional HRTEM and energy-dispersive X-ray spectroscopy (EDX) elemental mapping were performed on a sample prepared with a sputtering duration of 60 seconds. The corresponding images are presented in Figure 4-12. HRTEM images taken before the sulfurization process show a uniform amorphous film on the sapphire substrate. In contrast, the HRTEM image acquired after sulfurization clearly shows a well-defined, crystalline MoS_2 film composed of 8 atomic layers, consistent with the result shown in Figure 4-10 (a). In addition, EDX elemental mapping of the amorphous film before sulfurization reveals the presence of molybdenum (Mo) and sulfur (S), with a minor

doi:10.6342/NTU202501239

signal from oxygen (O), likely originating from the substrate surface or ambient exposure. These results demonstrate that RF sputtering using a MoS_2 target produces an amorphous MoS_2 film, which crystallizes into a continuous, layered structure, rather than forming island-like domains, after high-temperature sulfurization. This confirms the feasibility of achieving wafer-scale growth of multi-layer MoS_2 with uniform thickness and structural integrity.

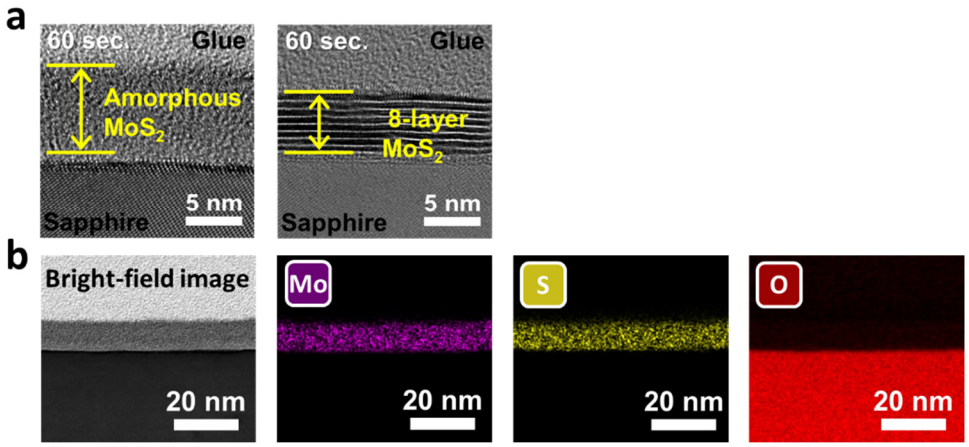

Figure 4-12 (a) The cross-sectional HRTEM images of the sample with 60 sec. sputtering time before and after the sulfurization procedure. (b) The Mo, S and O element mappings of the amorphous MoS_2 film.

To further evaluate the Mo:S composition ratio in the MoS_2 films obtained by sulfurizing the amorphous precursors, EDX elemental mapping was performed on the same sample containing an 8-layer MoS_2 structure. The cross-sectional HRTEM image, along with elemental maps for carbon (C), sulfur (S), molybdenum (Mo), oxygen (O), and aluminum (Al), is presented in Figure 4-13. As shown, strong Mo and S signals are localized within the MoS_2 layer, while the Al and O signals originate from the sapphire substrate, and C may come from surface contamination or the TEM grid. The quantified Mo:S atomic ratio is close to 1:2, indicating that the sulfurization process effectively converts the amorphous MoS_2 film into a fully sulfurized crystalline MoS_2 structure with minimal sulfur deficiency.

doi:10.6342/NTU202501239

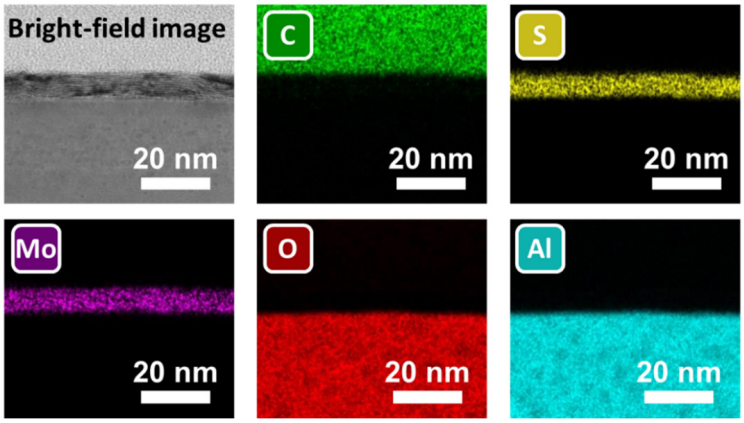

Figure 4-13 Elemental mapping of Mo, S, and O in amorphous MoS_2 thin films sputtered for 60 seconds after the sulfurization process.

To further optimize the material properties of the MoS_2 films, reduce internal recombination of photo-generated carriers, and improve the performance of subsequent photovoltaic devices, a high-temperature re-sulfurization process was performed on the previously grown 10-, 20-, and 30-layer MoS_2 samples. The procedure followed the same steps described in Section 4.2.1, with the exception that the re-sulfurization was conducted in a low-pressure sulfurization system at 950 °C for 10-minute, instead of the original 850 °C for 20 minutes. The objective of this post-treatment is to improve film crystallinity and eliminate residual defects that may have been introduced during the initial sulfurization or RF sputtering process. As shown in Figure 4-14, the Raman spectra of the MoS_2 samples before and after re-sulfurization exhibit clear spectral improvements. Specifically, the intensity of the E_{2g}^1 and A_{1g} peaks increases significantly after high-temperature treatment, while the full width at half maximum (FWHM) of the E_{2g}^1 mode becomes narrower, as illustrated in Table 4-1. Since the E_{2g}^1 vibrational mode reflects the in-plane phonon vibration of the MoS_2 lattice, its FWHM serves as a useful metric to evaluate crystallinity [242]. The observed narrowing of the FWHM indicates a reduction in lattice disorder and improvement in crystalline quality.

doi:10.6342/NTU202501239

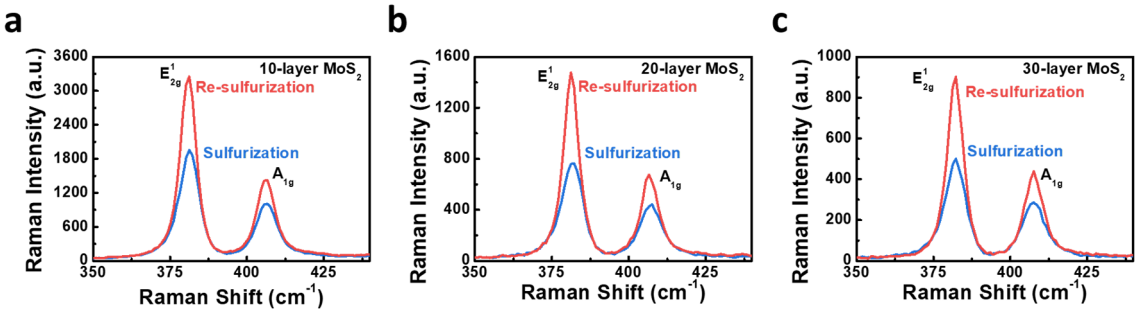

Figure 4-14 Raman spectra of the (a) 10-, (b) 20-, and (c) 30-layer MoS_2 samples before and after re-sulfurization at 950 °C for 10-minute.

Table 4-1 Detailed Raman spectra of the 10-, 20-, and 30-layer MoS_2 samples before and after re-sulfurization at 950 °C for 10-minute, including the positions of the $E_{2g}{}^1$ and A_{1g} modes, Δk value, and the FWHM.

Re-sulfurization at 950°C for 10 minutes				
	E^1_{2g}	A_{1g}	△k	FWHM
10-layer MoS_2	381.2	406.6	25.4	7.28
Re-Sulfurization of 10-layer MoS_2	381.2	406.6	25.4	5.85
20-layer MoS_2	382.2	407.6	25.4	7.72
Re-Sulfurization of 20-layer MoS_2	381.2	406.6	25.4	5.79
30-layer MoS_2	382.2	407.6	25.4	7.61
Re-Sulfurization of 30-layer MoS_2	382.2	407.6	25.4	5.97

Following, X-ray diffraction (XRD) and X-ray photoelectron spectroscopy (XPS) measurements were performed on three samples with 10-, 20-, and 30-layer MoS_2 (actual layer numbers of 8, 18, and 31, as shown in Figure 4-10). The results align with the observations from cross-sectional HRTEM images, confirming that layered MoS_2 with consistent crystal orientation can be obtained through the sulfurization of amorphous MoS_2 films.

doi:10.6342/NTU202501239

The XRD curves for the three samples are presented in Figure 4-15. Besides the peak corresponding to the sapphire substrate, the MoS_2 (002) peak (JCPDS Card No. 75-1539) is observed, consistent with the few-layer MoS_2 characteristics reported in the literature [243]. Notably, the FWHM of the (002) peak decreases with increasing MoS_2 layer numbers. While this suggests improved crystallinity, literature also indicates that such broadening can occur when transitioning from bulk to few-layer MoS_2 [244]. Thus, the layer-number-dependent layer spacing may contribute to the observed FWHM broadening [245, 246]. Further investigation of the XRD dependence on MoS_2 layer numbers is needed. However, the consistent (002) peak across all samples indicates that the same crystal plane orientation is maintained regardless of layer number.

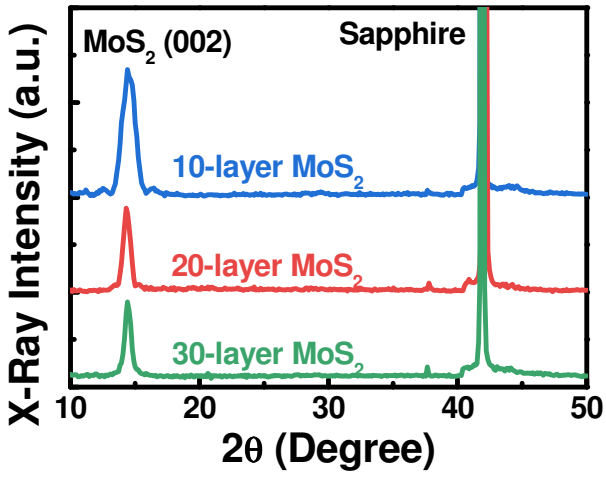

Figure 4-15 The XRD analysis of 10-, 20-, and 30- layer MoS_2 samples after re-sulfurization at 950 °C for 10-minute.

In addition, the XPS spectra for the three samples (10-, 20-, and 30-layer MoS_2) are shown in Figure 4-16. Full-spectrum XPS analysis reveals Mo 3d and S 2p signals at 231 eV and 164 eV, respectively, corresponding to MoS_2. No peaks associated with molybdenum oxides (MoO_3 or MoO_2) are observed around 530-531 eV. A minor peak at

doi:10.6342/NTU202501239

534 eV suggests the presence of organic oxygen species (C=O and C-O), likely due to surface contamination. Furthermore, detailed XPS analysis for the 20-layer MoS_2 sample is shown in Figure 4-16 (b, c). The Mo 3d spectrum displays characteristic Mo^{4+} peaks of MoS_2, with a binding energy separation of approximately 3.2 eV between the Mo $3d_{5/2}$ and Mo $3d_{3/2}$ peaks [247]. These results confirm that no detectable Mo oxide bonding is present in the sulfurized MoS_2 films. In the S 2p spectrum, the S $2p_{3/2}$ and S $2p_{1/2}$ peaks appear at 161.4 eV and 162.4 eV, respectively, with no additional peaks indicating oxidation or sulfur-related defects, as shown in Figure 4-16 (c).

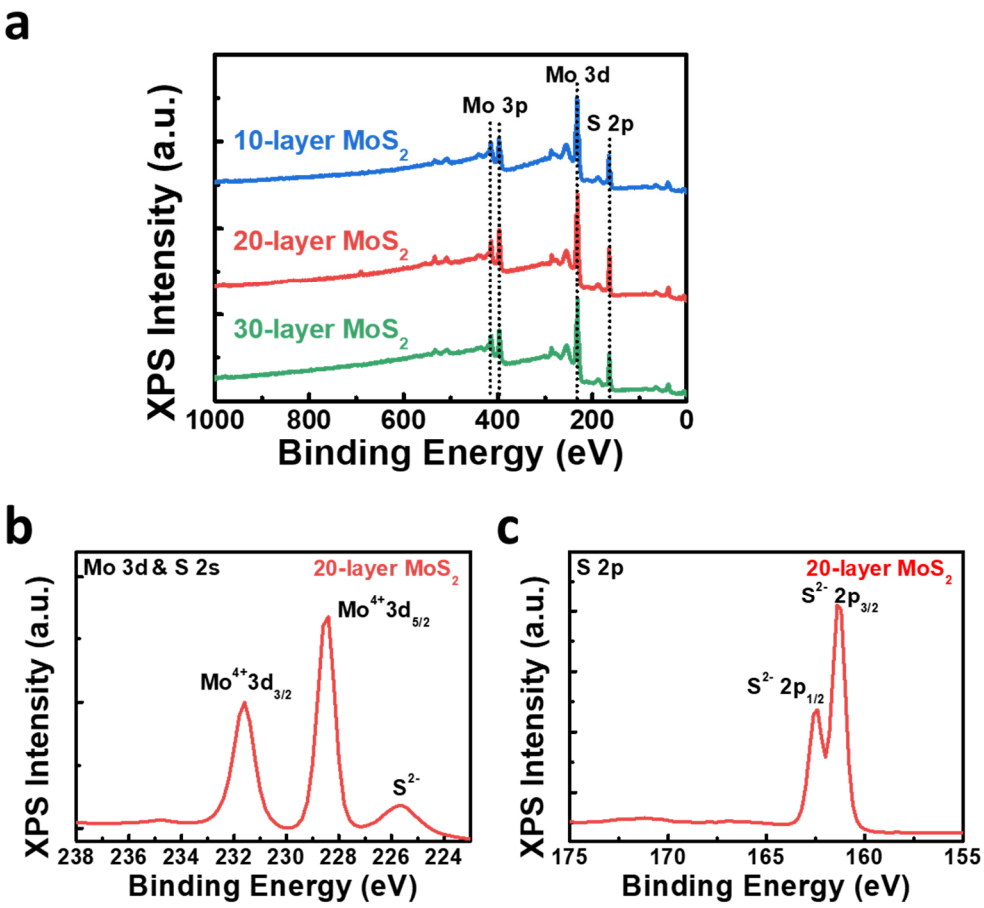

Figure 4-16 The XPS analysis of 10-, 20-, and 30- layer MoS_2 samples after re-sulfurization at 950 °C for 10-minute: (a) full scan spectrum; (b) Mo 3d, S 2s core-level spectra, and (c) S 2p spectrum of the sample with 20-layer MoS_2.

doi:10.6342/NTU202501239

4.3 Vertical Photovoltaic Photodetectors with Multi-layer MoS_2

4.3.1 Fabrication of Vertical Photodetectors

As previously stated, the objective of this chapter is to fabricate both vertical and planar devices based on multi-layer MoS_2, with the aim of analyzing charge transport mechanisms in different directions. To this end, a vertical photovoltaic device was fabricated by leveraging the excellent light absorption characteristics of multi-layer MoS_2 within a vertical architecture. The fabrication process of the device can be categorized into three main steps, as illustrated in Figure 4-17: (1) preparation of the bottom electrode, (2) transfer of the MoS_2 film, and (3) deposition of the top electrode.

Figure 4-17 The fabrication procedure of the Au/MoS_2/Al vertical device.

(1) Preparation of the bottom electrode

First, a 2-inch single-side polished c-plane sapphire substrate was cut into quarters using a diamond scribe. The substrate with a shadow mask was then placed face-down onto the sample holder of an electron beam evaporation system. The shadow mask featuring rectangular apertures with a width of 0.5 mm and a length of 1.6 mm was utilized to define the electrode regions. Al with a thickness of 30 nm was selected as the bottom electrode due to its high electrical conductivity and its natural tendency to form a thin native oxide layer on the surface. This oxide layer functions as an insulating barrier, effectively reducing the risk of short circuits in the

doi:10.6342/NTU202501239

presence of localized damage or imperfections in the overlying multi-layer MoS_2 film. High-purity Al pellets (99.999%) were loaded into the chamber, ensuring a sufficient quantity of source material for deposition. The chamber was initially evacuated from atmospheric pressure to approximately 3×10^{-2} torr using an oil rotary pump. Subsequently, a cryo pump was employed to further reduce the pressure to ~1×10^{-6} torr, thereby minimizing contamination and ensuring a high-purity deposition environment. Once the target pressure was achieved, the electron beam was engaged to heat the Al pellets to their molten state, thereby producing aluminum vapor. When the deposition rate stabilized at 1 Å/s, as monitored by a quartz crystal microbalance, the shutter was opened to initiate deposition. Al was deposited until a target thickness of 30 nm was reached. At that point, the shutter was closed to terminate the deposition process. After deposition, the cryo pump valve was closed to stop pumping, and N_2 was introduced to vent the chamber back to atmospheric pressure. The substrate was then retrieved for subsequent processing.

(2) Transfer of the MoS_2 film

To transfer the multi-layer MoS_2 films (aforementioned 10-, 20-, and 30- layer MoS_2 samples after re-sulfurization at 950 °C for 10-minute) grown on sapphire substrates onto 30 nm Al/sapphire substrates, a PMMA assisted transfer process was employed, consistent with the approach described earlier (Section 2.2.2). The process began by mounting the sample onto a spin coater using a vacuum chuck. A PMMA A4 solution was drop-cast onto the sample surface, followed by spin coating at 500 rpm for 10 seconds and then 800 rpm for 20 seconds to ensure uniform coverage. The coated sample was then baked on a hotplate at 120 °C for 5 minute to solidify the PMMA layer. After baking, the sample was cut into appropriate sizes

doi:10.6342/NTU202501239

using a utility knife. The prepared sample was then immersed in a 3 M KOH solution, allowing the solution to penetrate to the edge of the film and peel off the multi-layer MoS_2 from the sapphire substrate. The detached MoS_2/PMMA film was then transferred to DI water to thoroughly rinse off any residual KOH. Subsequently, the MoS_2/PMMA stack was transferred onto the Al-coated sapphire substrate. To improve adhesion, the sample was initially baked at 80 °C for 5 minute to eliminate surface moisture, followed by gentle mechanical pressing using a laminator and a subsequent baking step at 80 °C for 10-minute. To further improve film-substrate contact, another PMMA A4 layer was spin coated onto the transferred MoS_2 film using the same parameters. The sample was then left undisturbed for 1 hour to ensure full conformal contact. Finally, the PMMA layer was removed by immersing the sample in acetone for 20 minutes, completing the PMMA assisted transfer process of the multi-layer MoS_2 film onto the 30 nm Al/sapphire substrate.

(3) Deposition of the top electrode

As demonstrated by the results presented in Chapter 3 (Table 3-1 and Figure 3-8), a 10 nm Au deposited on MoS_2 exhibits an optical transmittance of approximately 70% within the visible spectrum, while maintaining a low sheet resistance of around 7.43 Ω/□. These properties suggest that ultrathin Au film is a promising candidate for use as a transparent top electrode in 2D material-based photovoltaic devices. Accordingly, upon completion of the transfer process, a 10 nm Au film was deposited onto the MoS_2 surface via electron beam evaporation, utilizing a shadow mask to define the electrode pattern. A shadow mask featuring rectangular apertures with a width of 0.6 mm and a length of 1.6 mm was utilized to define the electrode regions. The deposition procedure began by placing the transferred sample face-

doi:10.6342/NTU202501239

down onto the sample holder inside the electron beam evaporator. High-purity Au pellets (99.99%) were loaded into the crucible, and the system was initially evacuated using an oil rotary pump to reduce the chamber pressure from atmospheric pressure to approximately 3×10^{-2} torr. The pumping was then switched to a cryo pump, further lowering the pressure to around 1×10^{-6} torr to ensure a high-purity environment for deposition. Once the Au reached a molten state under the controlled electron beam heating, metal vapor was generated. When the deposition rate stabilized at 0.5 Å/s, the shutter was opened, and film thickness was monitored using a quartz crystal microbalance. After reaching the desired thickness of 10 nm, the shutter was closed to complete the deposition. Finally, the cryogenic pump valve was closed to stop evacuation, and the chamber was vented to atmospheric pressure with nitrogen gas before retrieving the sample.

Upon completing the aforementioned fabrication procedures, a vertical photovoltaic device featuring a simple sandwich-like architecture was successfully fabricated. The structure consists of a 30 nm Al layer serving as the bottom electrode, a multi-layer MoS_2 film functioning as the light-absorbing layer, and a 10 nm Au layer deposited as the top transparent electrode. The choice of Al and Au as the bottom and top electrodes, respectively, is not only based on their electrical and optical properties but also on their distinct work functions. Al possesses a relatively low work function (ψ = ~4.3), while Au exhibits a higher work function (ψ = ~5.1 eV). This work function difference facilitates the formation of an internal electric field across the MoS_2 layer, which drives the separation of photo-generated electron-hole pairs and promotes unidirectional carrier transport. As a result, the built-in potential generated by the asymmetric contact configuration plays an important role in enhancing the photovoltaic response of the device.

doi:10.6342/NTU202501239

4.3.2 Vertical Photodetectors with Different MoS_2 Layers

To systematically investigate the photovoltaic response characteristics of Au/MoS_2/Al vertical devices incorporating varying numbers of MoS_2 layers (after re-sulfurization at 950 °C for 10-minute) as the light-absorbing medium, a series of spectral response measurements were conducted using the experimental setup detailed in Section 2.5.3. In this configuration, the broadband illumination provided by a Xe lamp was focused onto the active region of the 2D material photovoltaic devices. The incident light, after passing through the semi-transparent top Au electrode (10 nm), irradiates the underlying MoS_2 films, which consist of 10-, 20-, and 30- layers, respectively. Figure 4-18 presents the optical microscope image of the device layout, along with a schematic representation of the illuminated area, demonstrating the spatial overlap between the focused light spot and the device's active region.

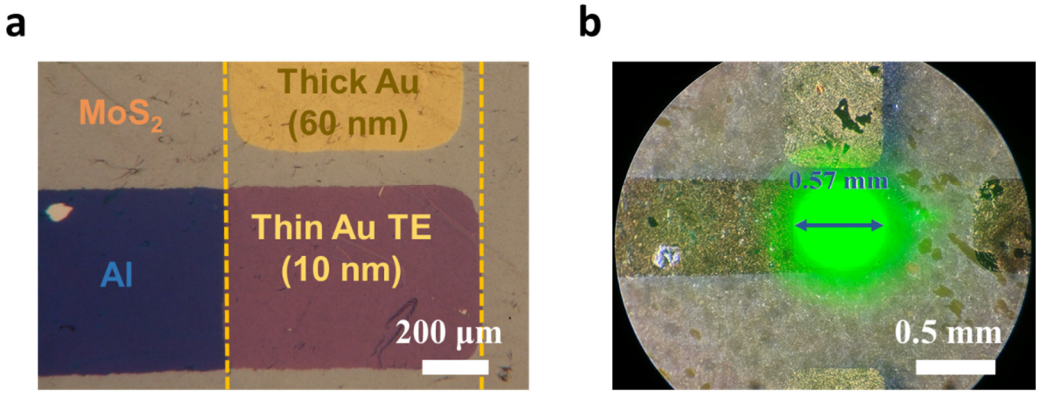

Figure 4-18 Optical microscope images showing (a) the vertical photodetector layout and (b) the illumination spot size of the xenon lamp.

To ensure precise correlation between photon energy and device photo-response, the optical power at each wavelength was calibrated using an optical power meter, as illustrated in Figure 4-19. A precision source-meter unit coupled with a lock-in amplifier

doi:10.6342/NTU202501239

was employed to measure the corresponding photocurrent signals, enabling high sensitivity and noise rejection. Spectral response measurements were carried out over the wavelength range of 450-800 nm with a step size of 10 nm. At each wavelength, the photocurrent was recorded with an integration time of 3 seconds to ensure measurement stability and repeatability. This experimental setup allows for a reliable evaluation of the photo-response characteristics of vertical 2D photovoltaic devices as a function of MoS_2 layer thickness, thereby elucidating the impact of absorber thickness on carrier generation and extraction efficiency.

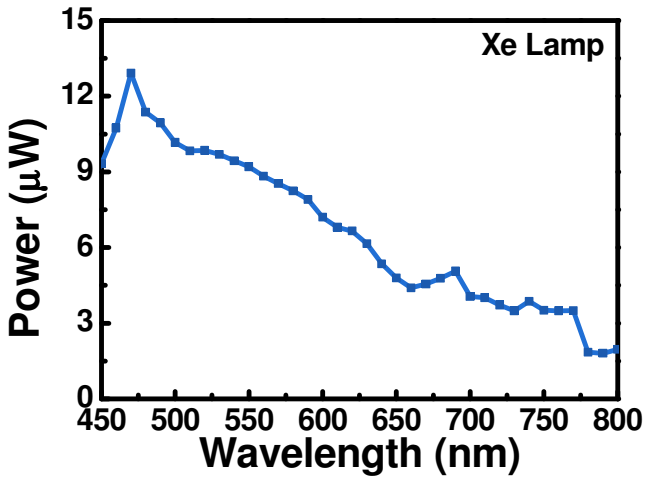

Figure 4-19 Measured optical power of the xenon lamp source at different wavelengths, calibrated using an optical power meter.

Figure 4-20 presents the corresponding photocurrent of devices with MoS_2 films of different thicknesses. As illustrated, the photocurrent varies with the wavelength of incident light and the number of MoS_2 layers, reflecting the thickness-dependent photo-response behavior. Notably, measurable photocurrents are observed even without external bias, attributed to the built-in electric field arising from the work function difference between the Al and Au electrodes, confirming the successful realization of a vertical photovoltaic effect.

doi:10.6342/NTU202501239

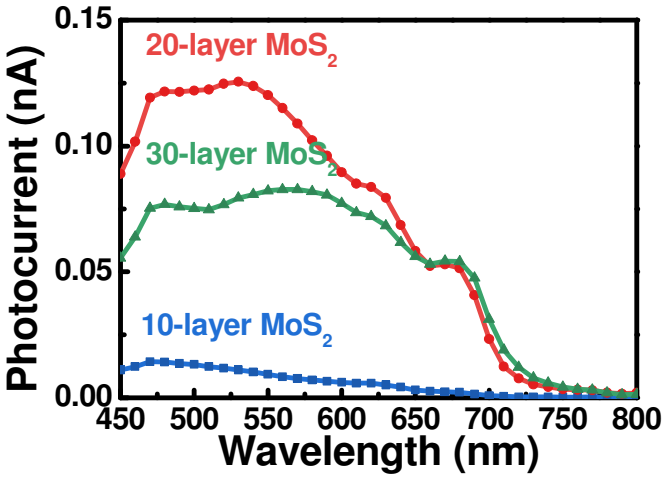

Figure 4-20 Photocurrent of vertical MoS_2 photodetectors with 10-, 20-, and 30-layer MoS_2 absorption layers under wavelength-dependent illumination. The active region of the device is 0.3 mm^2.

The measured photocurrent was subsequently converted into responsivity using Equation 4-1:

$$\text{Responsivity} = \frac{I_{ph}}{W_{light} \times \frac{A_{channel}}{A_{light}}} \qquad \text{(Equation } 4-1\text{)}$$

Where I_{ph} is the measured photocurrent, W_{light} is the incident optical power at a given wavelength, $A_{channel}$ denotes the active area of the vertical photodetector, and A_{light} represents the illuminated area on the device surface (refer to Figure 4-18 (b)). Figure 4-21 shows the extracted spectral responsivity curves. As the number of MoS_2 layers increases, the responsivity generally improves. Among the three devices evaluated (10-, 20-, and 30-layer MoS_2), the 20-layer sample exhibits the highest responsivity, with a peak value of 8.9 μA/W at 640 nm. The relatively low responsivity observed in the 10-layer device is likely attributed to insufficient optical absorption resulting from the limited thickness of the MoS_2 layer. In contrast, the reduced performance of the 30-layer device may stem from increased defect density or degraded film quality, which can impede efficient carrier transport and collection.

doi:10.6342/NTU202501239

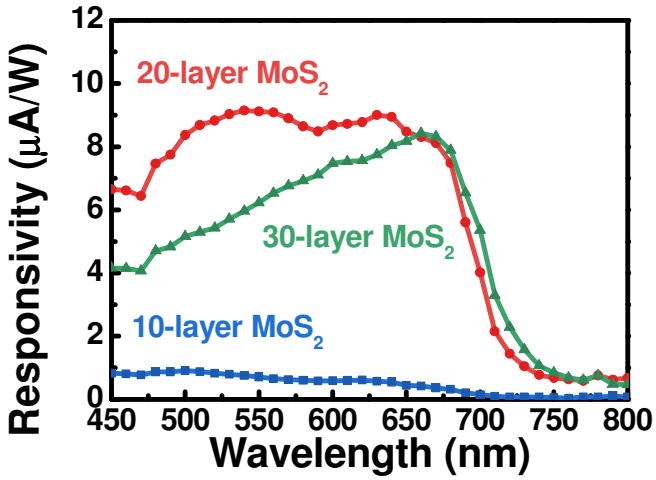

Figure 4-21 The spectral responses of vertical MoS_2 photodetectors with 10-, 20-, and 30-layer MoS_2 absorption layers under wavelength-dependent illumination. The active region of the device is 0.3 mm^2.

Another notable observation is the red-shift of the cut-off wavelength with increasing MoS_2 thickness. This behavior arises from the interplay between the optical absorption characteristics of MoS_2 and the interfacial band alignment at the metal-semiconductor junction. When the energy of incident photons exceeds the bandgap of MoS_2, corresponding to wavelengths shorter than its PL peak, electrons in the VB can be excited to the CB, generating electron-hole pairs that are subsequently separated by the built-in electric field formed by the asymmetric metal contacts. Conversely, when photon energy falls below the bandgap (longer wavelengths), carrier generation is suppressed, resulting in negligible photocurrent. According to the literature, the photoluminescence peak of mono-layer MoS_2 typically appears around 660 nm. As the layer thickness increases, the bandgap narrows, resulting in a red shift of both the PL peak and the cut-off wavelength. This phenomenon, as observed in Figure 4-21, is consistent with previous studies.

doi:10.6342/NTU202501239

4.3.3 The Role of Carrier Transport Layers

While photovoltaic responses are observed in multi-layer MoS_2 within a vertical device configuration, the responsivity values remain relatively low. Previous studies on organic devices have demonstrated that MoO_3 can serve as a carrier transport layer, thereby enhancing photocurrent generation [248]. However, due to the water solubility of MoO_3 is soluble in water (as previously mentioned), three devices incorporating 5 nm, 10 and 15 nm MoO_3 layers, deposited after 20-layer MoS_2 transfer, were fabricated. MoO_3 films were deposited using a thermal evaporation system at a rate of 0.02 nm/s. Figure 4-22 presents the photocurrent and spectral response characteristics of the fabricated devices under zero-bias conditions, illustrating the dependence of photo-response on MoO_3 layer thickness across the 450-800 nm wavelength range.

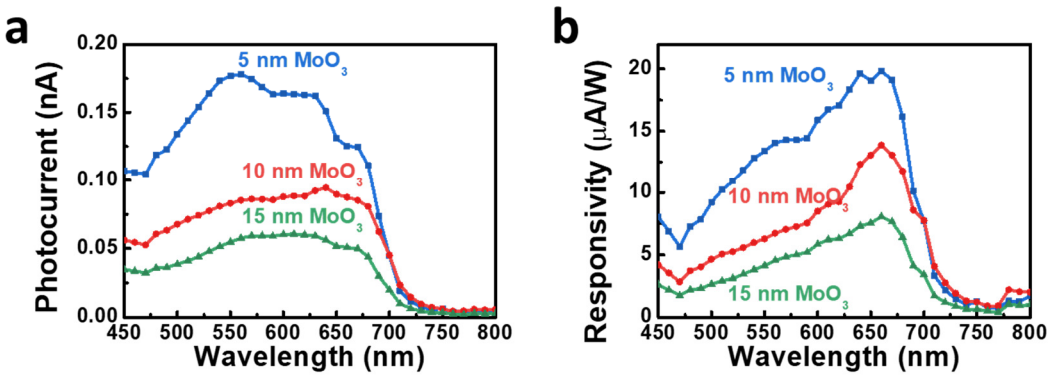

Figure 4-22 (a) The photocurrent and (b) spectral responses of the three devices with 5, 10, and 15 nm MoO_3 carrier transport layers, respectively.

Compared with the device without a MoO_3 layer (Figure 4-20), the device incorporating a 5 nm MoO_3 carrier transport layer exhibits enhanced photocurrent and spectral responsivity. Specifically, the responsivity at 660 nm increases by a factor of 2–3, demonstrating that a thin MoO_3 layer effectively facilitates hole extraction in multi-

doi:10.6342/NTU202501239

layer MoS_2 devices. However, increasing the MoO_3 thickness to 10 nm and 15 nm leads to reduced responsivity (Figure 4-23), likely due to increased series resistance and carrier blocking caused by MoO_3's wide bandgap and poor conductivity. This trend indicates the critical role of energy band alignment and thickness optimization in charge extraction for van der Waals heterostructures. While a thin MoO_3 layer can promote carrier transport and suppress interfacial recombination, excessive thickness impedes carrier mobility and reduces overall device efficiency.

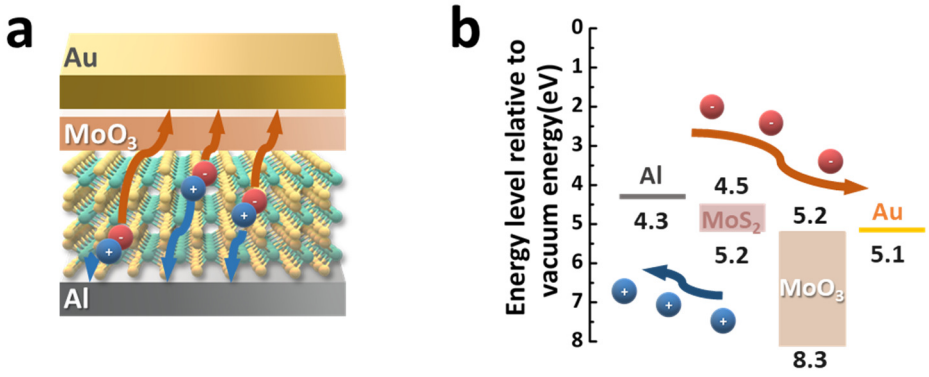

Figure 4-23 (a) Schematic illustration of vertical carrier transport in the MoO_3/MoS_2 structure, and (b) corresponding energy band diagram of the vertical photovoltaic photodetector.

The effectiveness of thin MoO_3 as a carrier transport layer for multi-layer MoS_2 suggests the difference in current flow between the lateral and vertical directions in 2D materials. In the lateral direction, atoms are bonded chemically, and current flow resembles that in conventional semiconductors. In contrast, because 2D layers are held together by van der Waals forces, vertical current flow requires carriers to hop between layers, a mechanism more akin to organic devices. Although further optimization is required, these findings demonstrate the potential of multi-layer MoS_2 for vertical photovoltaic device applications.

doi:10.6342/NTU202501239

4.3.4 Impact of Heterostructure Integration on the Performance of Photovoltaic Devices

Another approach to enhance the photo-response of vertical photovoltaic devices, a p–n junction was constructed by integrating an additional 2D material to facilitate more effective carrier separation. Specifically, a mono-layer of WS_2 was introduced as the p-type layer, forming a vertical heterostructure with the configuration: 10 nm Au/20-layer MoS_2/1-layer WS_2/30 nm Al.

The mono-layer WS_2 was procured from 2D Semiconductor Company. The film was synthesized using a plasma-enhanced CVD method. To grow the W-based TMDs, a high-purity (6N) WO_3 precursor was utilized in combination with H_2S gas. Prior to film deposition, c-plane sapphire substrates were cleaned with a piranha solution and treated with Ar plasma to ensure a contaminant-free surface. WS_2 was deposited at 830 °C, followed by rapid cooling to suppress bilayer formation and minimize nucleation site density. Additionally, NaCl was also introduced during growth to enhance material transport and promote uniform mono-layer formation.

Raman and PL spectroscopy were employed to assess the WS_2 film quality. As shown in Figure 4-24 , the Raman spectrum exhibits characteristic peaks with a separation (Δk) of 61.3 cm^{-1}, confirming the mono-layer nature of the WS_2. [249]. Additionally, the PL spectrum shows a sharp emission peak at ~620 nm, indicating high optical quality consistent with mono-layer WS_2.

Subsequently, the mono-layer WS_2 was transferred onto the 30 nm Al bottom electrode via PDMS stamping, as detailed in Section 2.2.1. A 20-layer MoS_2 film was then sequentially transferred onto the WS_2 using the procedure described in Section 4.3.1, thereby establishing a vertical p-n heterojunction. Finally, a 10 nm transparent Au top electrode was deposited to complete the device architecture.

doi:10.6342/NTU202501239

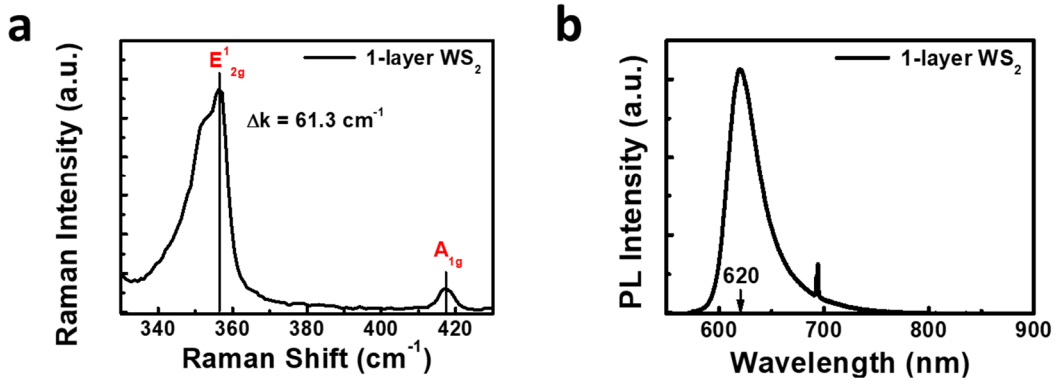

Figure 4-24 (a) Raman and (b) PL spectra of mono-layer WS_2, confirming its mono-layer nature and optical quality.

Figure 4-25 presents the photocurrent and spectral response characteristics of the device incorporating a 20-layer MoS_2/1-layer WS_2 heterojunction structure, measured under zero-bias conditions. The results demonstrate enhanced photo-response compared to the device with 10 nm Au/20-layer MoS_2/30 nm Al (Figure 4-21), indicating that the introduction of the WS_2 facilitates more efficient carrier separation through the formation of a vertical p-n junction. This enhancement likely arises from the built-in electric field at the WS_2/MoS_2 interface, generated by differences in their Fermi levels and work functions.

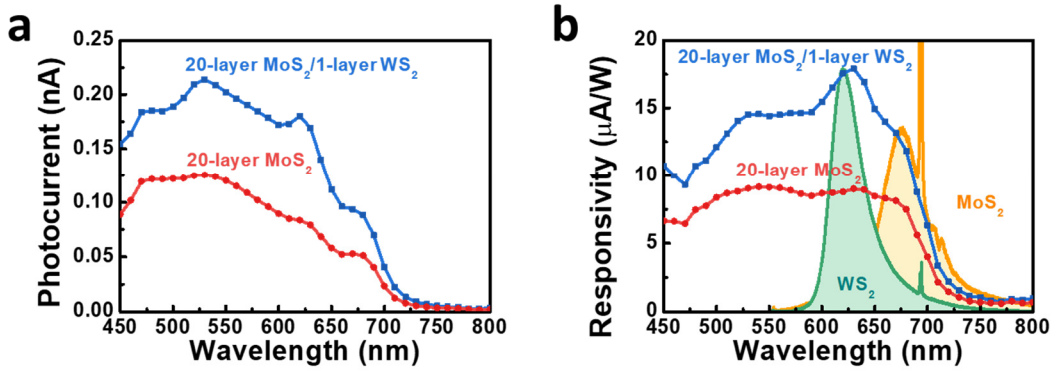

Figure 4-25 (a) Photocurrent and (b) spectral response characteristics of devices incorporating a 20-layer MoS_2/1-layer WS_2 heterojunction structure, compared with devices containing only 20-layer MoS_2.

doi:10.6342/NTU202501239

In this configuration, photo-excited holes in the MoS_2 are driven toward the WS_2 layer, while electrons are directed toward the MoS_2 side, facilitating directional charge transport across the heterojunction, as shown in Figure 4-26. Moreover, the atomically sharp interface between WS_2 and MoS_2 minimizes defect states and interface traps, contributing to improved carrier mobility and enhanced photocurrent generation.

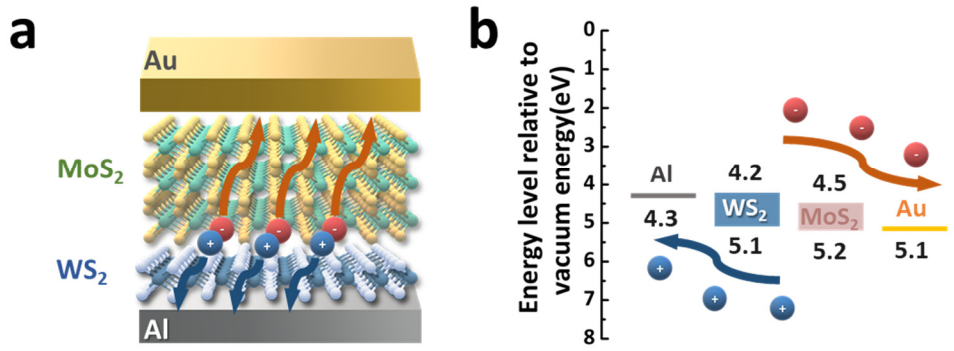

Figure 4-26 (a) Schematic illustration of vertical carrier transport in the 20-layer MoS_2/1-layer WS_2 structure, and (b) corresponding energy band diagram of the vertical photovoltaic photodetector.

In summary, this work presents two promising strategies to overcome the confinement of vertical transport in multi-layer MoS_2 devices: (1) the use of MoO_3 as an effective carrier transport layer, and (2) the enhancement of charge dynamics through the built-in electric field of the vertical p-n heterostructure. While the performance of vertical devices still requires further optimization, these results suggest the potential for utilizing multi-layer 2D materials in vertical photovoltaic applications.

doi:10.6342/NTU202501239

4.4 Planar Photoconductive Photodetectors with Multi-layer MoS_2

4.4.1 Fabrication of Planar Photodetectors

This chapter aims to fabricate both vertical and planar device configurations based on multi-layer MoS_2 to investigate charge transport mechanisms along both in-plane and out-of-plane directions. To this end, a planar photoconductive device was realized through the construction of a MoS_2/graphene heterostructure.

MoS_2, a representative member of the TMD family, possesses a layer-dependent bandgap, making it well-suited for optoelectronic applications [36]. Its ability to undergo optical excitation enables the generation of photocurrent under illumination. However, despite these promising optical properties, MoS_2 suffers from relatively low intrinsic carrier mobility, which limits its charge transport and extraction efficiency in the lateral direction. In contrast, graphene exhibits exceptional electrical conductivity and high carrier mobility, making it an ideal charge transport medium.

To leverage the complementary properties of these two materials, a planar heterostructure photodetector was fabricated by integrating MoS_2 as the light-absorbing layer and graphene as the carrier transport layer. In this configuration, MoS_2 absorbs incident photons to generate electron–hole pairs, while the underlying graphene enables rapid and efficient extraction of the photo-generated carriers, thereby enhancing the photo-response and improving the overall device performance. The fabrication process, as illustrated in Figure 4-27: (1) growth and transfer of graphene, (2) definition of source and drain electrodes, (3) definition of the channel region, (4) electrical property analysis of the graphene bottom-gate transistor, and (5) transfer of MoS_2 film.

doi:10.6342/NTU202501239

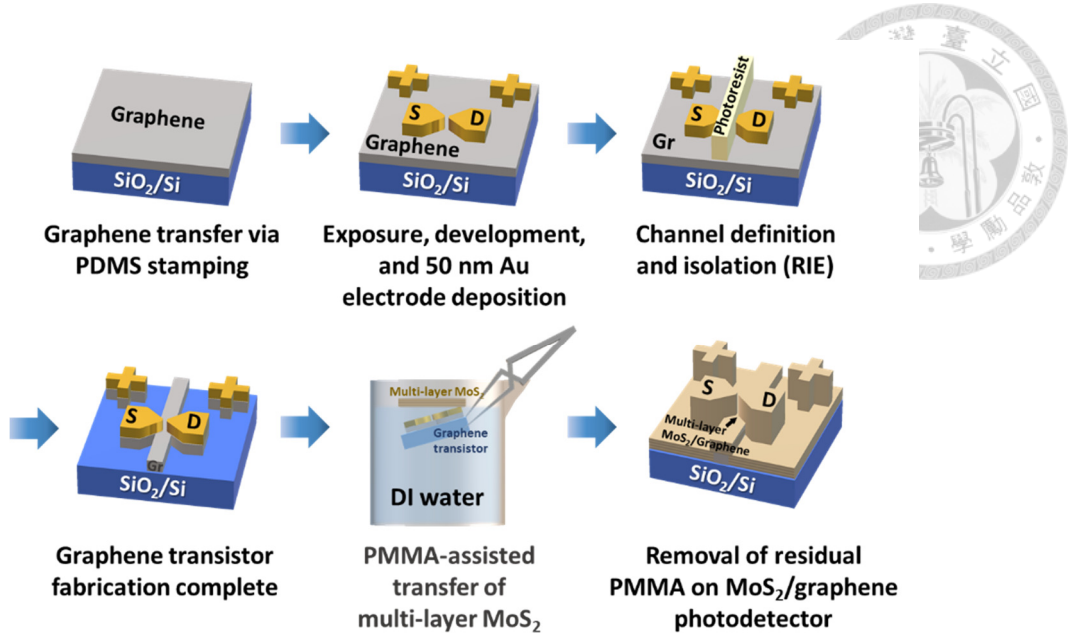

Figure 4-27 Fabrication procedure of the MoS_2/graphene photodetector.

(1) Growth and transfer of graphene

As mentioned in Section 2.1.1, graphene synthesis can be achieved by utilizing a metal substrate as a catalytic medium to promote the decomposition of hydrocarbon precursors. In this work, copper foil was employed as the catalytic substrate for graphene growth. Initially, copper foil was cut into square segments (1.5×1.5 cm^2) and carefully placed on a quartz stage, which was subsequently inserted into the furnace. The system was then evacuated from atmospheric pressure to ~13 mtorr using a mechanical pump. Following, Ar was introduced at a controlled flow rate of 10 sccm to serve as the carrier gas, while the internal pressure was stabilized at 330 mtorr via a butterfly valve. The furnace was subsequently heated to the growth temperature of 1030 °C at a rate of 20 °C/min. After reaching the target temperature, an annealing step was performed for one hour to eliminate surface contaminants from the copper substrate. Following annealing, H_2 (7 sccm) and C_2H_6 (15 sccm) were introduced as precursor gases, and the chamber pressure was regulated to 660 mtorr. The graphene growth process was then carried out under

doi:10.6342/NTU202501239

these conditions for 30 minutes. After the growth process was completed, the C_2H_6 flow was stopped, and the substrate was rapidly transferred to a cooler zone in the furnace to enable fast cooling for approximately 15-minute. Finally, all process gases were shut off, the chamber was evacuated to its base pressure, and N_2 was introduced to break the vacuum prior to retrieving the synthesized graphene sample. Figure 4-28 shows the graphene growth setup and the synthesized graphene film.

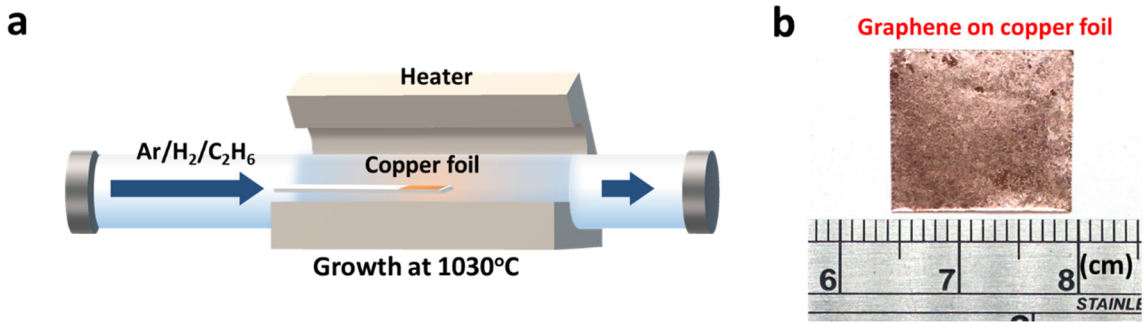

Figure 4-28 Schematic of the (a) graphene growth system and (b) photograph of the graphene film synthesized on a copper substrate under the specified conditions.

Raman spectroscopy was performed to evaluate the layer number and material quality after sample growth. Figure 4-29 shows the Raman spectrum of the sample transferred to the SiO_2/Si substrate using the PDMS transfer technique (As illustrated in Section 2.2.1). The G peak at 1585.8 cm^{-1} corresponds to the in-plane vibration of sp^2 carbon atoms, while the 2D peak at 2675.6 cm^{-1} reflects the electronic structure of graphene [250]. The sharp and symmetric 2D peak, with an intensity about twice that of the G peak, further confirms the presence of mono-layer graphene. The D peak at 1341.4 cm^{-1} is attributed to defects. A low D/G intensity ratio (~0.15) indicates that the graphene is of high quality with minimal defects. These results verify the successful transfer of high-quality mono-layer graphene onto the SiO_2/Si substrate.

doi:10.6342/NTU202501239

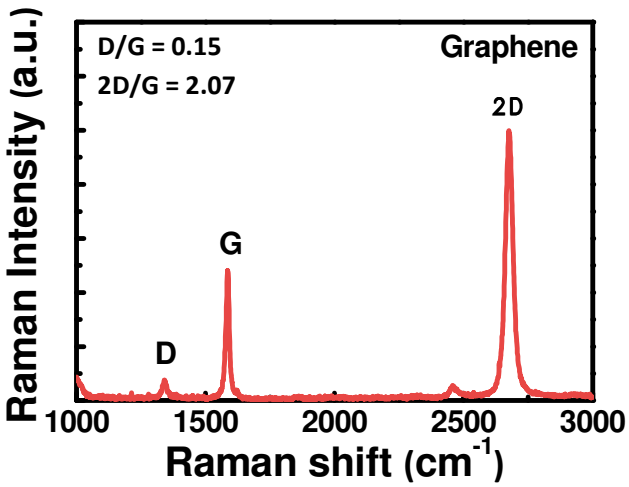

Figure 4-29 Raman spectrum of graphene transferred using the PDMS stamp-assisted method, confirming characteristic G and 2D bands indicative of mono-layer graphene.

(2) Definition of source and drain electrodes

After removing the residual PDMS from the graphene surface (As illustrated in Section 2.2.1), the source and drain electrodes are patterned through the following steps: The sample was first mounted onto the spin coater using a vacuum pump, and HMDS (Hexamethyldisilazane) was applied dropwise using a pipette. The sample was then coated with HMDS at 1000 rpm for 10 seconds, followed by 3000 rpm for 30 seconds, enhancing the adhesion of the photoresist. After the HMDS coating, a negative photoresist (DNR-L300) was applied in the same manner, followed by baking on a hotplate at 100°C for 2 minutes to cure the photoresist. A mask with the designed pattern was aligned on the sample, and exposure was performed for 60 seconds. After exposure, the sample was baked at 100°C for 1 minute and developed in a 2.38% TMAH (Tetramethyl ammonium hydroxide) solution for 19 seconds to define the electrode areas. Au was then deposited onto the sample using an electron beam evaporator at a rate of 1.0 Å/s to a thickness of 50 nm, serving as the contact

doi:10.6342/NTU202501239

electrodes. After deposition, the sample was immersed in acetone for 15-minute to remove the photoresist and excess gold, leaving the Au only in the defined areas.

(3) Definition of the channel region

The sample was remounted on the spin coater using a vacuum pump, and HMDS was dispensed via pipette and spin-coated at 500 rpm for 10 s, followed by 3000 rpm for 20 s to ensure uniform surface treatment. After the HMDS coating, a positive photoresist (AZ-5214E) is applied in the same manner, and the sample is baked on a hotplate at 120°C for 2 minutes to cure the photoresist. Next, the sample is aligned with the mask using the optical microscope in the mask aligner. The exposure time is set to 51 seconds, after which the positive photoresist is developed with AZ-300MIF developer for 2 minutes to define the channel region, forming a protective layer. Subsequently, the sample is etched using a RIE system, with CF_4 plasma used to etch away the film outside the channel region. The etching parameters are RF power at 90 W, CF_4 flow rate at 30 sccm, chamber pressure at 1.3 Pa, and etching time of 60 seconds. After etching, the sample is immersed in acetone for 15-minute to remove the photoresist. This completes the channel definition, and an optical microscope image of the bottom-gate transistor is shown in Figure 4-30.

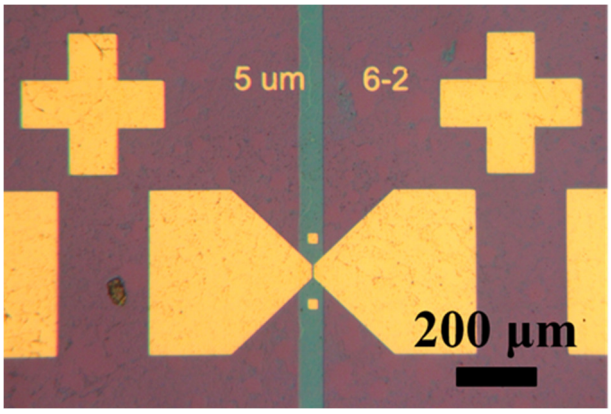

Figure 4-30 Optical microscope image of the fabricated graphene bottom-gate transistor.

doi:10.6342/NTU202501239

(4) Electrical property analysis of the graphene bottom-gate transistor

After fabricating the graphene transistor, electrical measurements were performed using a Keysight B2912B source/measure units system. The measurement conditions were set with a gate-to-source voltage (V_{GS}) range of -50 V to 50 V, while the drain-to-source voltage (V_{DS}) was fixed at 0.5 V. The field-effect mobility (μ_{FET}) was calculated using the transistor mobility formula (Equation 4-2).

$$\mu_{FET} = \frac{1}{V_{DS}} \frac{t}{\varepsilon} \frac{L}{W} \frac{d I_D}{d V_G} \qquad \text{(Equation } 4-2\text{)}$$

Where, t denotes the oxide thickness, which is 300 nm SiO_2, and ε represents the dielectric permittivity, approximately 3.45×10^{-13} F/cm. The channel length (L) and width (W) were 5 μm and 25 μm, respectively.

Figure 4-31 presents the electrical characteristics of the graphene transistor. The I_D–V_D curve in Figure 4-31 (a) exhibits a symmetric current range of -2 to 2 mA, with graphene as the channel material. The I_D–V_G curve displaying ambipolar behavior of graphene, with a maximum drain current of 2.23 mA at V_G = -50 V. Despite its high conductivity, the lack of a bandgap results in a low on/off ratio [53]. The extracted hole and electron mobilities are 1080 and 422 $cm^2/V\cdot s$, respectively.

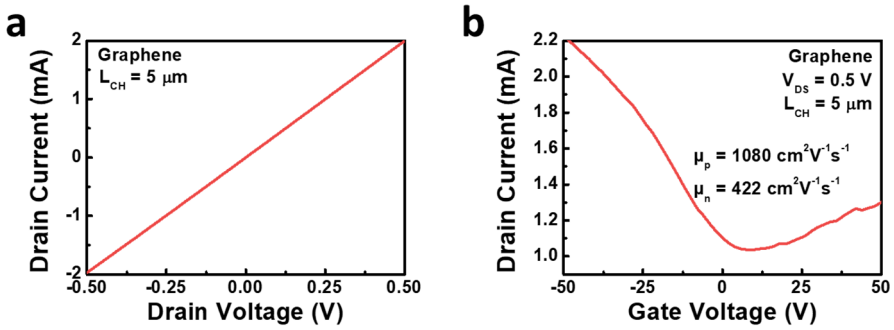

Figure 4-31 The transfer curve of a graphene transistor at V_{DS} = 0.5 V.

doi:10.6342/NTU202501239

(5) Transfer of MoS_2 film.

After the fabrication of the graphene bottom-gate transistor, a MoS_2 film is employed as the light absorption layer to enable photodetection at specific wavelengths. Here, planar photodetectors based on MoS_2 films of three different thicknesses—mono-layer, 10 layers, and 20 layers MoS_2—were fabricated. Devices incorporating 30-layer MoS_2 were excluded from the comparison due to the relatively low material quality observed. The MoS_2 films were synthesized using the optimized growth techniques described in the previous sections. Specifically, the mono-layer MoS_2 was synthesized by pre-depositing MoO_3 via ALD system, followed by a sulfurization process, as detailed in Section 3.2.1. In contrast, the 10-layer and 20-layer MoS_2 films were fabricated through the sputter deposition of amorphous MoS_2, followed by sulfurization, as described in Section 4.2.1. To further enhance crystallinity and overall material quality, these thicker films were subsequently subjected to a re-sulfurization treatment at 950 °C for 10-minute, as outlined in Section 4.2.2. The Raman spectra of the three MoS_2 films with different thicknesses are presented in Figure 4-32, and the results are consistent with those reported in the previous section.

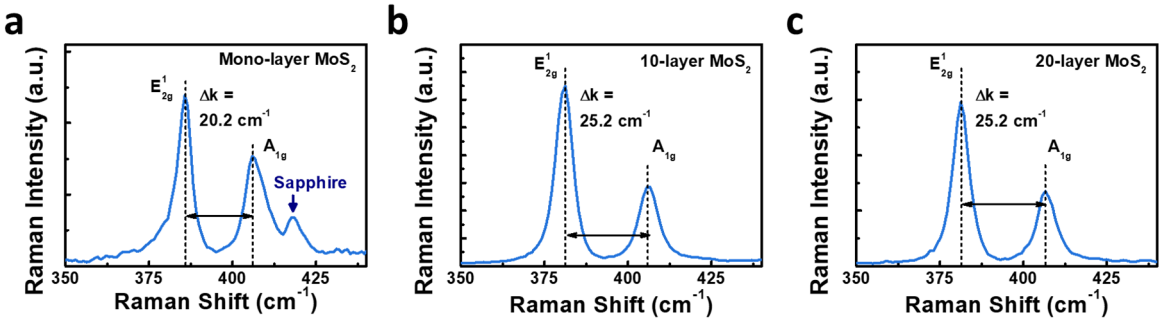

Figure 4-32 Raman spectra of (a) 1-layer MoS_2 grown by ALD, .10-, and 20-layer MoS_2 films deposited via the sputtering system.

doi:10.6342/NTU202501239

The MoS_2 is subsequently transferred onto the graphene channel region, forming a heterostructure that leverages the high carrier mobility of graphene and the strong light absorption characteristics of MoS_2. To preserve optimal material properties, the mono-layer MoS_2 was transferred onto the graphene channel using the PDMS stamping technique, which effectively minimizes contamination and mechanical damage. In contrast, multi-layer MoS_2, due to stronger interlayer interactions and adhesion forces, could not be transferred using PDMS [199]. Instead, a PMMA-assisted transfer method was used to ensure reliable detachment and maintain film integrity. The schematic diagrams of the two transfer methods, along with optical microscope images of the fabricated devices, are shown in Figure 4-33.

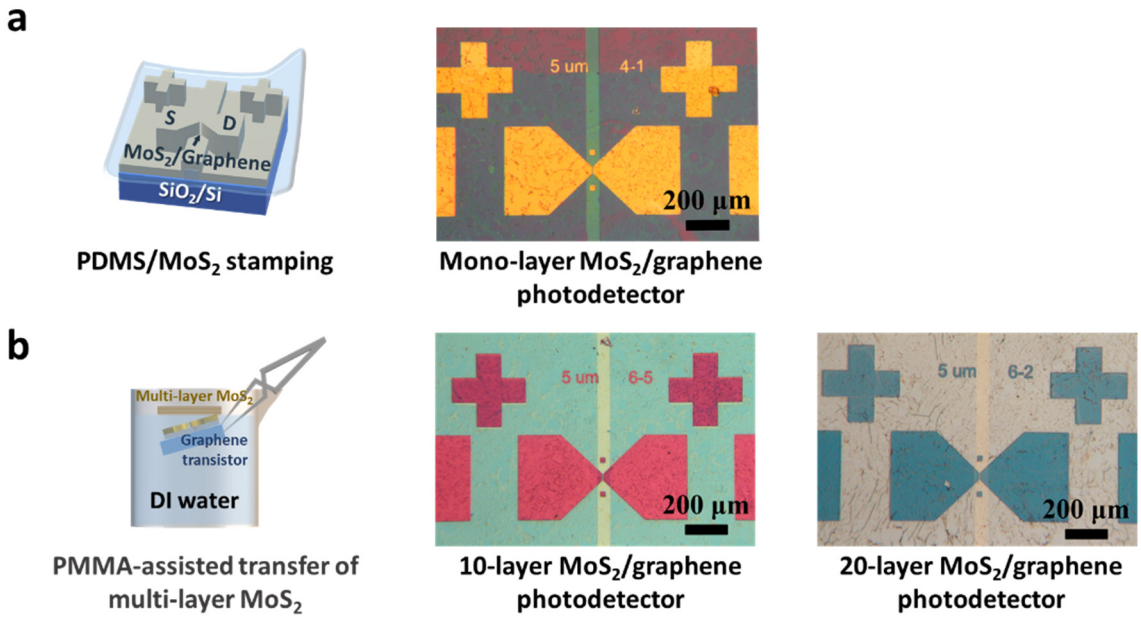

Figure 4-33 Schematic diagrams of (a) PDMS stamping transfer for mono-layer MoS_2 and (b) PMMA-assisted transfer for multi-layer MoS_2. The corresponding optical microscope images of the fabricated devices after each transfer process are also shown in the figure.

doi:10.6342/NTU202501239

✧ The transfer process for mono-layer MoS_2:

The mono-layer MoS_2 was separated using the PDMS stamping transfer technique as described in Section 2.2.1. To separate the MoS_2 from the sapphire substrate, a PDMS sheet was first cut to the desired size and carefully adhered to the MoS_2 film, ensuring strong attachment. The PDMS/MoS_2 stack was then immersed in 3M KOH solution, which gradually penetrated the film edges and facilitated delamination of MoS_2 from the sapphire. Once sufficient separation was achieved, tweezers were used to gently lift off the MoS_2, leaving it attached to the PDMS. The PDMS/MoS_2 film was then thoroughly rinsed with DI water to remove any residual KOH, followed by drying on a hot plate at 80 °C for 5 minute to eliminate moisture. The dried MoS_2 film was then aligned and placed onto the graphene transistor. A second thermal treatment at 80 °C for 5 minute was performed to enhance adhesion. Finally, the PDMS layer was carefully peeled off using tweezers, completing the transfer process.

✧ The transfer process for multi-layer MoS_2:

To transfer the multi-layer MoS_2 films (aforementioned 10-, and 20- layer MoS_2 samples after re-sulfurization at 950 °C for 10-minute) grown on sapphire substrates onto graphene transistor, a PMMA assisted transfer process was employed, consistent with the approach described earlier (Section 2.2.2). The process began by mounting the sample onto a spin coater using a vacuum chuck. A PMMA A4 solution was drop-cast onto the sample surface, followed by spin coating at 500 rpm for 10 seconds and then 800 rpm for 20 seconds to ensure uniform coverage. The coated sample was then baked on a hotplate at 120 °C for 5 minute to solidify the

doi:10.6342/NTU202501239

PMMA layer. After baking, the sample was cut into appropriate sizes. The prepared sample was then immersed in a 3 M KOH solution, allowing the solution to penetrate to the edge of the film and peel off the multi-layer MoS_2 from the sapphire substrate. The detached MoS_2/PMMA film was then transferred to DI water to thoroughly rinse off any residual KOH. Subsequently, the MoS_2/PMMA stack was transferred onto the graphene transistor. To improve adhesion, the sample was initially baked at 80 °C for 5 minute to eliminate surface moisture, followed by gentle mechanical pressing using a laminator and a subsequent baking step at 80 °C for 10-minute. To further improve film-substrate contact, another PMMA A4 layer was spin coated onto the transferred MoS_2 film using the same parameters. The sample was then left undisturbed for 1 hour to ensure full conformal contact. Finally, the PMMA layer was removed by immersing the sample in acetone for 20 minutes, completing the PMMA assisted transfer process of the multi-layer MoS_2 film onto graphene transistor.

doi:10.6342/NTU202501239

4.4.2 Fabrication of Reference Planar Photodetectors

The fabrication process of the MoS_2 bottom-gate transistor closely follows the previously described steps, as illustrated in Figure 4-34:

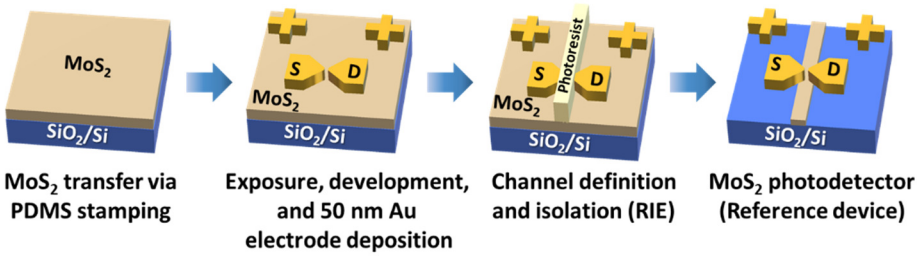

Figure 4-34 Fabrication procedure of the MoS_2 bottom-gate transistor.

(1) Growth and transfer of MoS_2

The mono-layer MoS_2 was synthesized via ALD of MoO_3 followed by sulfurization, and transferred using the PDMS stamping method, as detailed in Section 3.2.1. The film was delaminated from the sapphire substrate with KOH, aligned onto a SiO_2/Si substrate, and thermally treated at 80 °C to enhance adhesion before peeling off the PDMS.

(2) Definition of source and drain electrodes

After PDMS residue removal, source and drain electrodes were patterned by spin-coating HMDS and negative photoresist, followed by photolithography and development using TMAH. 50 nm Au electrodes were then deposited by e-beam evaporation and defined via a lift-off process in acetone.

(3) Definition of the channel region

The sample underwent HMDS and AZ-5214E photoresist coating, followed by exposure and development to define the channel region. CF_4-based RIE was then used for etching, and the photoresist was removed with acetone, completing the channel patterning process.

doi:10.6342/NTU202501239

4.4.3 The Influence of Channel Lengths to Device Performance

To systematically investigate the photo-response characteristics of planar photodetectors, a series of spectral response measurements were conducted using the experimental setup detailed in Section 2.5.3. In this configuration, the broadband illumination provided by a Xe lamp was focused onto the active region of the 2D material photodetectors. The incident light irradiates the MoS_2 films, which consist of 1-, 10-, and 20-layers, respectively. Figure 4-35 presents the optical microscope image of the device layout, along with a schematic representation of the illuminated area, demonstrating the spatial overlap between the focused light spot and the device's active region.

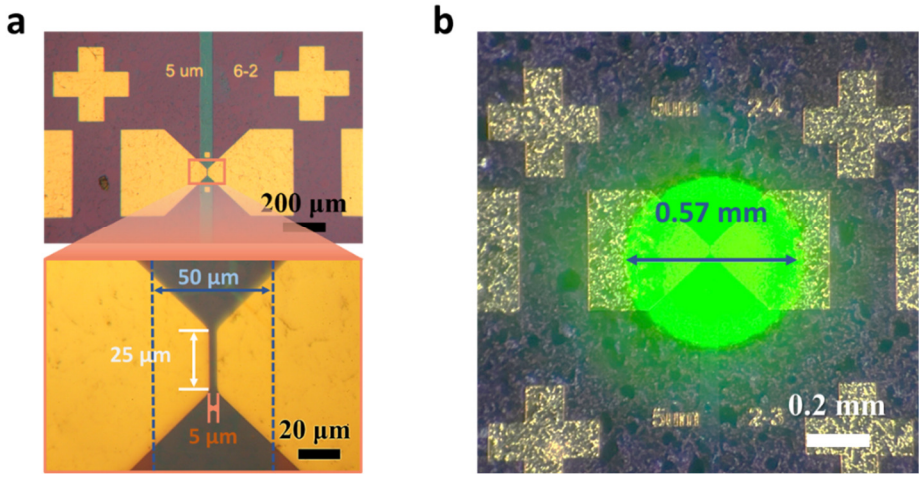

Figure 4-35 Optical microscope images showing (a) the planar photodetector layout and (b) the illumination spot size of the xenon lamp.

As shown in Figure 4-19, the optical power at each wavelength was calibrated using a power meter to ensure accurate correlation with the device's photo-response. Based on Equation 4-1, the responsivity of the device can be determined by taking into account the effective illuminated area of the device and the spot size of the incident light. Photocurrent measurements were conducted over the wavelength range of 500-800 nm using a precision source meter in conjunction with a lock-in amplifier. To ensure signal stability,

doi:10.6342/NTU202501239

an integration time of 3 seconds was applied. The frequency of the optical chopper was varied between 5 Hz and 30 Hz in order to investigate the frequency dependence of the photo-response.

Subsequently, the planar photodetector was characterized under illumination with light sources of varying wavelengths. As described in Section 4.4.1, mono-layer MoS_2/mono-layer graphene heterostructure photodetectors with a channel width of 25 μm and length of 5 μm were fabricated. The corresponding photocurrent and spectral response under an applied bias of 0.5 V are shown in Figure 4-36 (a, b). For comparison, a reference photodetector consisting of standalone mono-layer MoS_2, without the graphene layer, was also fabricated (Section 4.4.2). Its photocurrent and spectral response, measured under the same bias condition, are presented in Figure 4-36 (c, d).

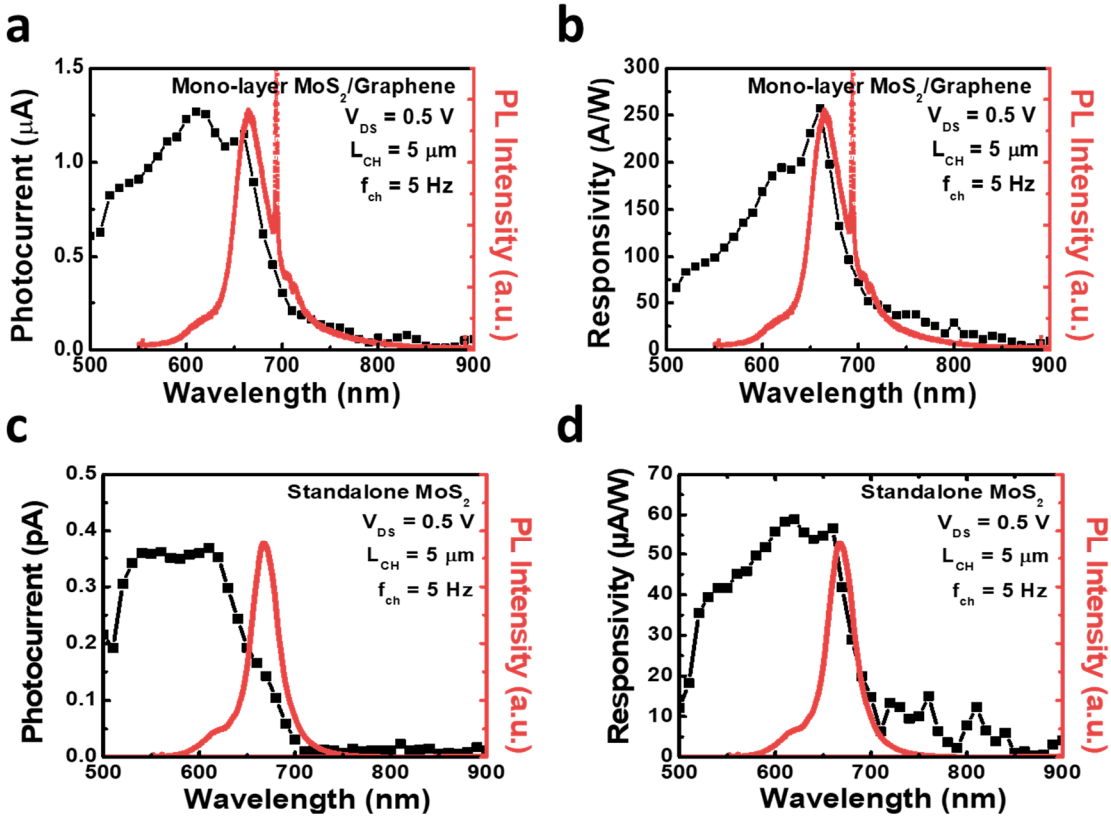

Figure 4-36 (a) Photocurrent and (b) spectral response of MoS_2/graphene photodetector, and (c) (d) corresponding data for standalone mono-layer MoS_2 device.

doi:10.6342/NTU202501239

As shown in the figures, both devices exhibit clear photo-responses that correspond with the absorption characteristics of mono-layer MoS_2, confirming its effectiveness as a light-absorbing layer despite its atomically thin thickness. The observed cutoff wavelength near 670 nm is consistent with the intrinsic bandgap of mono-layer MoS_2 [251]. Notably, the MoS_2/graphene heterostructure device demonstrates a responsivity enhancement of more than six orders of magnitude compared to the standalone MoS_2 device. A peak responsivity of 257.2 A/W is recorded at a wavelength of 660 nm under a 0.5 V bias.

Assuming comparable optical absorption in both devices due to the identical MoS_2 thickness, the difference in photo-response can be primarily attributed to the strategic separation of the light absorption layer (MoS_2) and the carrier transport layer (graphene). The superior electrical properties of graphene enable fast carrier transport, reducing the transit time and thereby significantly increasing the photoconductive gain, as described by Equation 4-3.

$$G = \frac{\tau_{lifetime}}{\tau_{transit}} \qquad \text{(Equation } 4-3\text{)}$$

where $\tau_{lifetime}$ is the carrier lifetime in the absorption layer, and $\tau_{transit}$ is the carrier transit time in the transport layer. In the standalone MoS_2 device, both are governed by MoS_2. In contrast, the heterostructure device benefits from $\tau_{lifetime}$ being determined by MoS_2, and $\tau_{transit}$ by the highly conductive graphene. The high gain observed in the MoS_2/graphene device indicates that carrier transit is faster in graphene than in MoS_2. This reduced transit time, combined with the relatively long carrier lifetime in MoS_2, results in substantial photoconductive gain. Additionally, the low contact resistance at the MoS_2/graphene interface enables efficient carrier transfer, further enhancing responsivity [252].

doi:10.6342/NTU202501239

Based on the measured responsivity of the mono-layer MoS_2/graphene photodetector shown in Figure 4-36, the quantum efficiency (QE) can be estimated using Equation 4-4:

$$\mathrm{QE} = \frac{\mathrm{R} \cdot \mathrm{h} \cdot \mathrm{c}}{q \cdot \lambda} \qquad \text{(Equation } 4-4\text{)}$$

where R is the responsivity (A/W), λ is the wavelength of incident light, h is Planck's constant, c is the speed of light, and q is the elementary charge. Under an applied drain-source voltage (V_{DS}) of 0.5 V and a chopper frequency of 5 Hz, the device exhibits a peak QE of 483 at 660 nm. This high quantum efficiency indicates that the incorporation of graphene enhances carrier transport within the channel. These results suggest that, even under relatively low bias conditions, the presence of graphene substantially reduces carrier transit time, thereby enabling higher responsivity in devices with identical mono-layer MoS_2 absorption layers.

To gain deeper insight into how photocurrent correlates with carrier transit time in the graphene channel, four additional devices composed of mono-layer MoS_2 and mono-layer graphene were fabricated, each with distinct channel lengths of 2.5, 10, 20, and 40 μm. The fabrication method follows the same procedure as the 5 μm channel device illustrated in Section 4.4.1. Figure 4-37 displays the photocurrent and spectral response at an applied bias of 0.5 V for all five devices with channel lengths of 2.5, 5, 10, 20, and 40 μm. Compared to the 5 μm channel device, the 2.5 μm channel version exhibits an even higher responsivity of 680.6 A/W at 660 nm. While the overall shape of the spectral response remains consistent across devices, the responsivity decreases noticeably with increasing channel length, as shown in Figure 4-37 (b).

doi:10.6342/NTU202501239

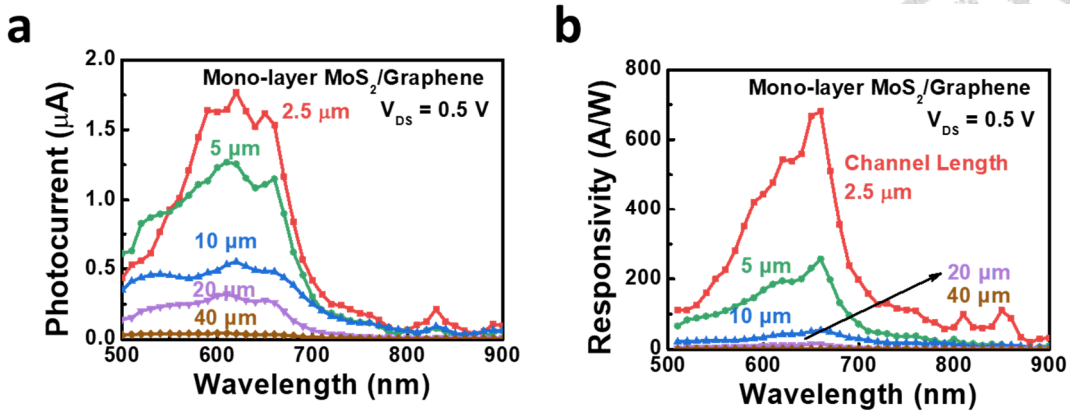

Figure 4-37 (a) Photocurrent and (b) spectral response of the mono-layer MoS_2/mono-layer graphene photodetectors with channel lengths of 2.5, 5, 10, 20, and 40 μm.

The responsivity demonstrates a nonlinear dependence on the channel length. The corresponding responsivity values, as a function of channel length, are presented in Figure 4-38 (a), obtained under a constant bias voltage of 0.5 V and an illumination wavelength of 620 nm. For comparison, the associated photocurrent measurements are shown in Figure 4-38 (b). As shown in the figures, both responsivity and photocurrent decrease exponentially with increasing channel length. This trend aligns with previous reports that graphene ribbon resistance scales exponentially in the ballistic transport regime [253], suggesting ballistic carrier transport in the graphene channel. The nonlinear reduction in carrier transit time with shorter channels contributes to the enhanced responsivity.

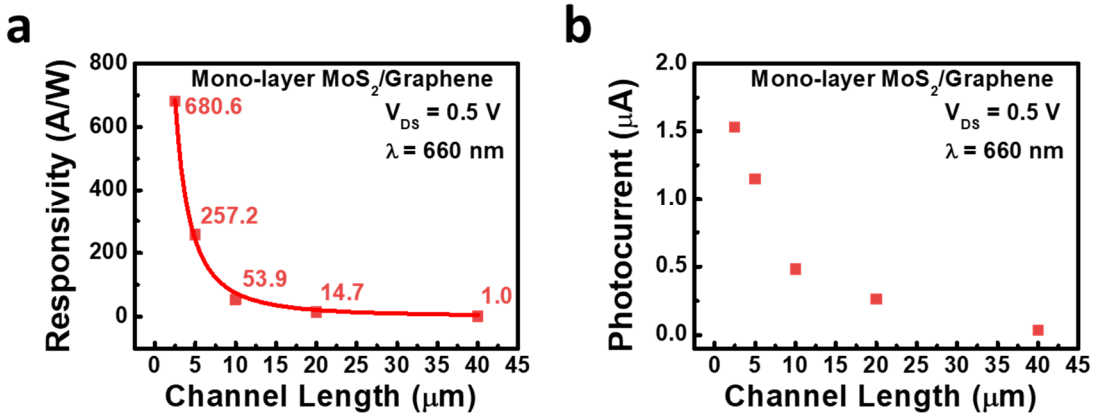

Figure 4-38 (a) Responsivity and (b) photocurrent values at 660 nm under 0.5 V for MoS_2/graphene photodetectors with channel lengths of 2.5, 5, 10, 20 and 40 μm.

doi:10.6342/NTU202501239

In addition to the influence of channel length, this work also investigates the responsivity of MoS_2/graphene photodetectors under varying chopper frequencies (5 Hz and 30 Hz), using devices with channel lengths of 5 μm and 40 μm, as shown in Figure 4-39. For the photodetector with a 5 μm channel, a responsivity of 257.2 A/W is observed under 5 Hz modulation. However, when the chopper frequency is increased to 30 Hz, the responsivity drops to 101.4 A/W, indicating a decrease in photocurrent with increasing modulation frequency (Figure 4-39 (a)). This suggests that the device may not be capable of following rapidly modulated optical signals, implying a limited temporal response. In contrast, the photodetector with a 40 μm channel exhibits consistently low responsivity values of approximately 1 A/W at both 5 Hz and 30 Hz (Figure 4-39 (b)). This behavior implies that the device's temporal response is sufficiently slow that further increases in modulation frequency do not significantly affect its photocurrent, indicating that it can effectively follow fast-switching light signals without additional responsivity loss.

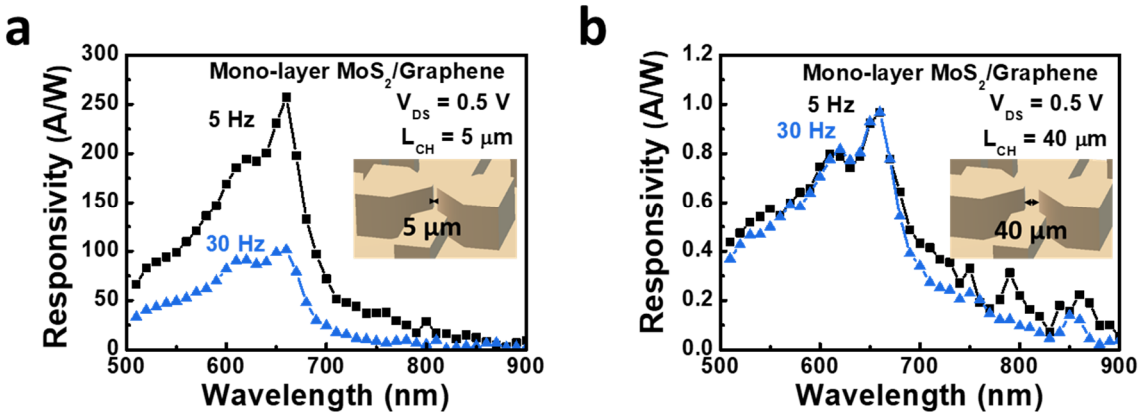

Figure 4-39 Responsivity of the mono-layer MoS_2/mono-layer graphene photodetectors with channel lengths of (a) 5 μm., and (b) 40 μm. under different chopper frequencies (5, 30 Hz). A schematic illustration of the device architecture is also provided.

doi:10.6342/NTU202501239

In addition to responsivity, response time is another critical performance parameter for photodetectors. To assess the temporal behavior of mono-layer MoS_2/graphene lateral photodetectors, time-resolved measurements were carried out under a bias voltage of 0.5 V and a chopper frequency of 5 Hz, using incident light with a wavelength of 550 nm. The illumination was directed onto the active regions of two devices with channel lengths of 5 μm and 40 μm, respectively. The corresponding time-domain photocurrent responses are shown in Figure 4-40.

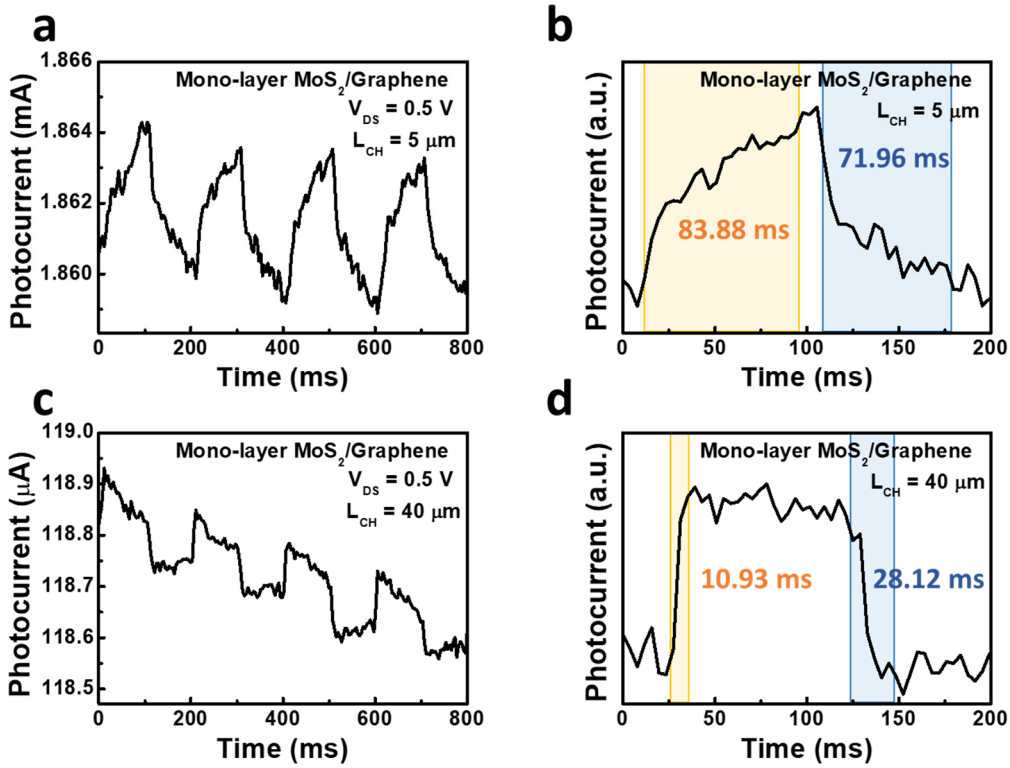

Figure 4-40 Time-resolved photo-response of mono-layer MoS_2/graphene photodetectors with channel lengths of (a, b) 5 μm and (c, d) 40 μm. Panels (a, c) show the photocurrent signals after normalization, and (b, d) present the magnified views for detailed analysis.

The two photodetectors with different channel lengths exhibit markedly distinct temporal photocurrent waveforms. In the case of the device with a 5 μm channel length, the signal deviates from an ideal square waveform, indicating a sluggish photo-response. The measured rise and fall times are 83.88 ms and 71.96 ms, respectively. Although this

doi:10.6342/NTU202501239

device demonstrates a high responsivity, the prolonged response time suggests limitations in charge replenishment dynamics. For the MoS_2/graphene photodetector with a 40 μm channel length, the photocurrent waveform closely resembles an ideal square wave, indicating a fast photo-response. The measured rise and fall times are 10.93 ms and 28.12 ms, respectively.

As shown in Figure 4-41 (a), the slow temporal response of the 5 μm-channel device is due to the limited rate of carrier replenishment in the MoS_2 layer. Due to graphene's much higher conductivity, current primarily flows through the graphene. Upon illumination, photo-excited electrons transfer to the graphene, leaving holes in MoS_2. The short transit time in graphene leads to photoconductive gain and high responsivity. However, the limited electron reservoir in mono-layer MoS_2 causes hole accumulation, which eventually hinders efficient electron transfer, slowing the rise time. After the light is turned off, additional time is needed for electrons to return and restore equilibrium, prolonging the fall time. For the 40 μm-channel device, the weaker photocurrent suggests fewer photo-excited carriers. With fewer electrons transferred to graphene and fewer holes in MoS_2, charge equilibrium is restored more quickly, resulting in a shorter response time, as shown in Figure 4-41 (b). Further studies are required to clarify the carrier dynamics at the MoS_2/graphene interface, particularly recombination within MoS_2 layer.

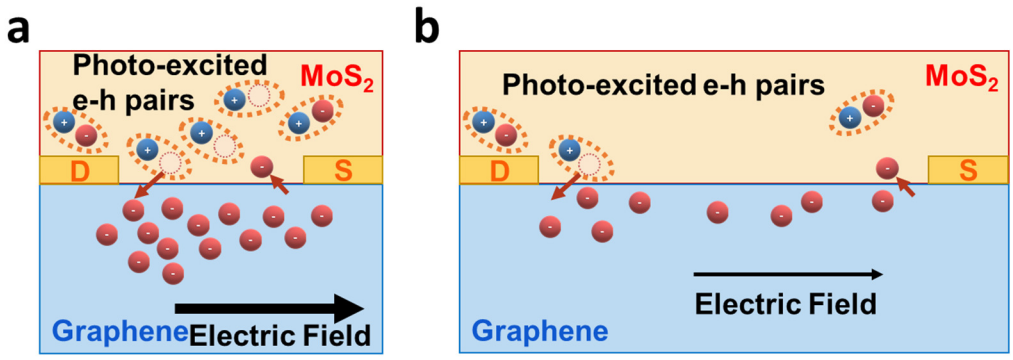

Figure 4-41 Schematic illustration of the operating mechanism in mono-layer MoS_2/graphene photodetectors with channel lengths of (a) 5 μm and (b) 40 μm.

doi:10.6342/NTU202501239

4.4.4 Comparison of Planar Photodetectors with Single- and Multi-Layer MoS_2 Light Absorption Layers

To simultaneously achieve high responsivity and fast temporal response in MoS_2/graphene photodetectors, this study investigates strategies to enhance electron storage capacity within the MoS_2 layer. Increasing the number of MoS_2 layers emerges as an effective approach, as it facilitates faster charge neutrality and reduces response time without compromising responsivity. Devices incorporating 1-, 10-, and 20-layer MoS_2 as the absorption layer, all with mono-layer graphene channels (25 μm width, 5 μm length), were fabricated as described in Section 4.4.1. Their performance was evaluated under illumination with varying wavelengths.

Figure 4-42 presents the photocurrent and spectral responses of the three devices at a V_{DS} of 0.5 V. At a chopper frequency of 5 Hz and a wavelength of 660 nm, the devices with 1-, 10-, and 20-layer MoS_2 exhibited responsivities of 257.2, 576.0, and 471.1 A/W, respectively, corresponding to quantum efficiencies of 483, 1082, and 885. The 10-layer device showed the best performance, attributed to its enhanced light absorption, which increases the generation of electron-hole pairs. Moreover, multi-layer MoS_2 offers longer carrier lifetimes [254], supporting repeated circulation of carriers within the graphene channel and thereby enhancing the photoconductive gain. The thicker MoS_2 also passivates the graphene, shielding it from environmental fluctuations and helping maintain electrical stability [255]. However, the 20-layer device showed a slight decline in responsivity, likely due to reduced crystallinity in thicker films. Higher defect densities, like grain boundaries, increase scattering and recombination, limiting mobility and charge transport despite greater absorption. A red-shift in the photo-response spectrum with increasing MoS_2 thickness reflects its bandgap transition from a direct 1.8 eV to an indirect ~1.2 eV [36], extending sensitivity into the near-infrared. The frequency response

doi:10.6342/NTU202501239

of the devices was further evaluated at a chopper frequency of 30 Hz. The 10- and 20-layer MoS_2 devices exhibited responsivity values similar to those measured at 5 Hz, indicating stable and fast carrier dynamics. In contrast, the mono-layer MoS_2 device showed a noticeable drop in responsivity at 30 Hz, suggesting slower carrier response times and limited ability to follow rapid modulation.

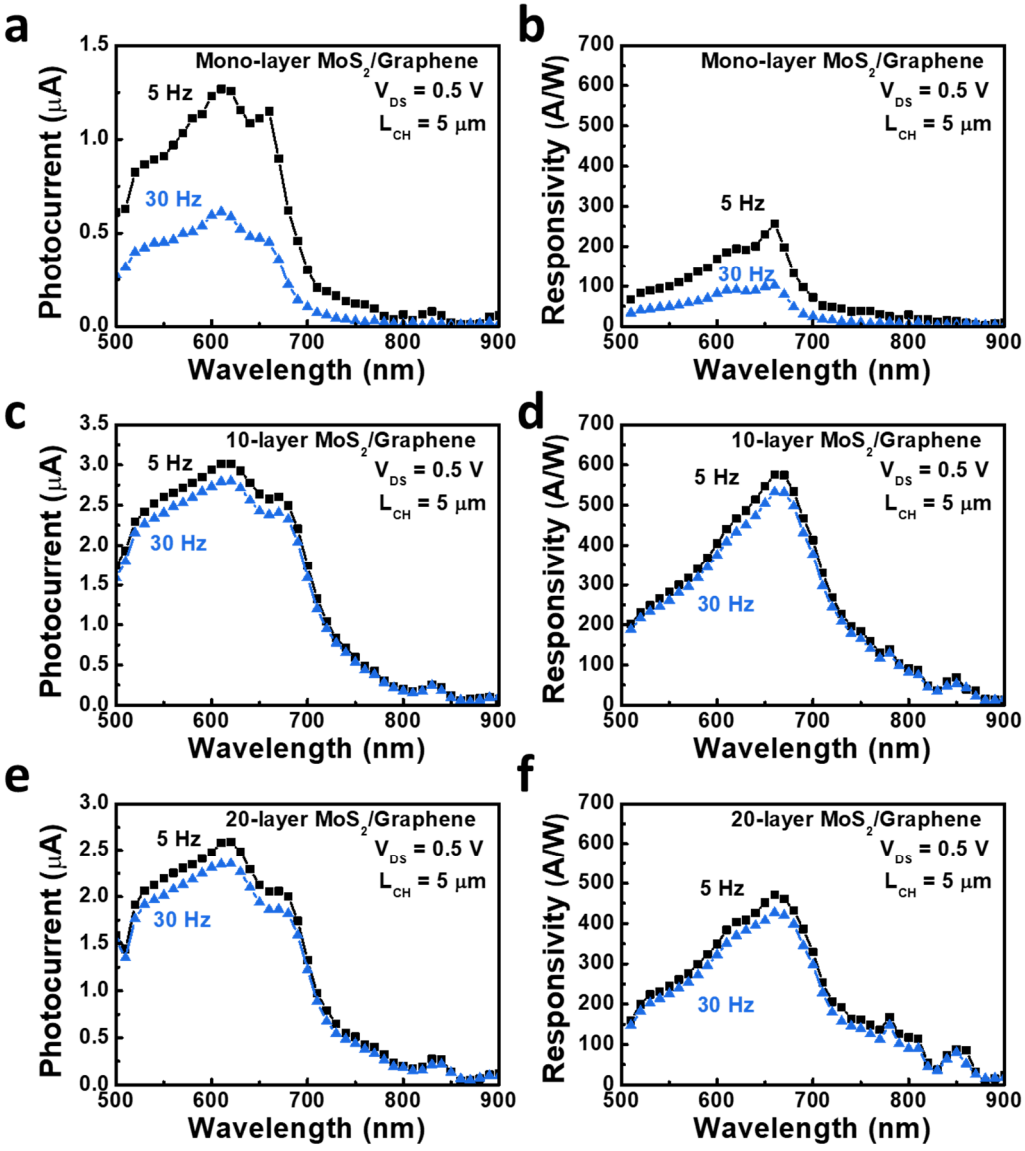

Figure 4-42 Photocurrent and spectral responses of three devices with 1-, 10-, and 20-layer MoS_2 absorption layers at 5 Hz and 30 Hz chopping frequencies.

doi:10.6342/NTU202501239

To further analyze temporal behavior, time-resolved measurements were conducted at 550 nm under 0.5 V and a 5 Hz chopper frequency. As shown in Figure 4-43, the 10- and 20-layer devices exhibited near square-wave photocurrent profiles, with rise/fall times of 7.02/8.22 ms and 21.87/31.25 ms, respectively. By comparison, the mono-layer device showed slower dynamics, with rise and fall times of 83.88 ms and 71.96 ms.

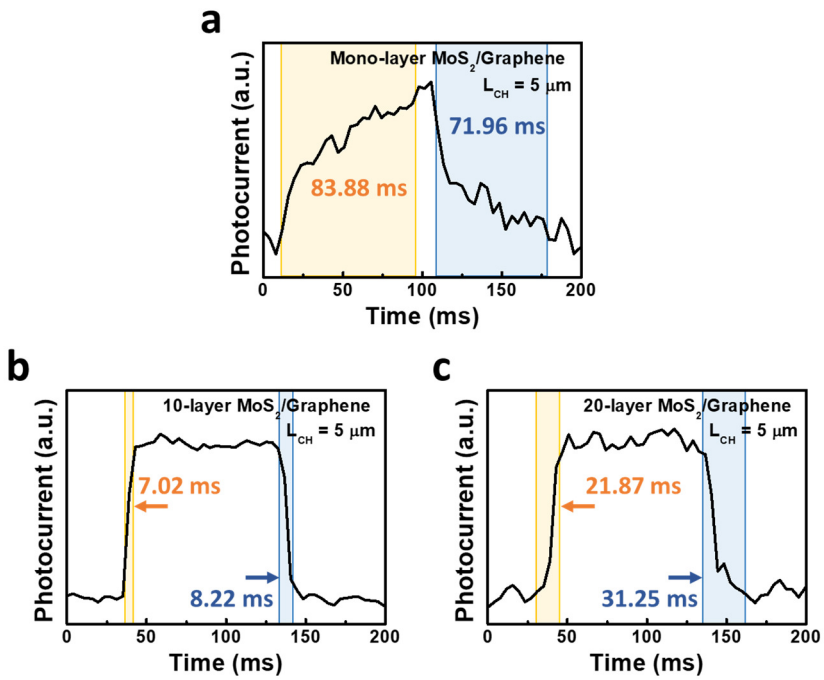

Figure 4-43 The time-dependent currents for three devices with 1-, 10-, and 20-layer MoS_2 absorption layers were measured with an optical chopper frequency of 5 Hz, an irradiation wavelength of 550 nm, and an applied voltage of 0.5 V.

In summary, multi-layer MoS_2 exhibits strong potential for lateral optoelectronic applications, especially photodetectors demanding both high responsivity and rapid temporal response. Increasing the number of MoS_2 layers enhances device performance through improved optical absorption, efficient carrier extraction, and extended carrier lifetimes. These longer lifetimes facilitate carrier replenishment and mitigate hole accumulation (Figure 4-41), thereby reducing response times and ensuring stable operation across modulation frequencies. Such properties position multi-layer MoS_2 as a compelling platform for high-performance photodetection in planar device architectures.

doi:10.6342/NTU202501239

4.5 Application Potential and Future Directions

4.5.1 Performance Optimization of Vertical Photovoltaic Devices Based on 2D Materials

This work fabricated photovoltaic devices based on multi-layer MoS_2 and explored two main strategies to enhance the performance of vertical architectures: the introduction of additional carrier transport layers and the construction of van der Waals heterostructures. While both approaches showed promising improvements, the overall power conversion efficiency of these vertical devices remains limited.

To better understand this performance bottleneck, it is essential to consider the intrinsic challenges associated with vertical transport in layered materials. Vertical charge transport in 2D materials is inherently more challenging than in-plane transport. While multi-layer structures enhance light absorption and offer tunable properties, their vertical conductivity is often limited by material quality. The reduced performance of vertical photovoltaic devices is mainly due to the use of sputtering followed by sulfurization. Although this method enables growth of MoS_2 films up to 30 layers, it typically results in small grains and numerous grain boundaries. As thickness increases, vertical transport is increasingly hindered by scattering and recombination, leading to lower device efficiency. In addition, the interface between the 2D materials and the metal electrodes requires further optimization. Due to the use of PMMA-assisted transfer techniques, polymer residues may remain at the interfaces, leading to the formation of trap states that hinder efficient charge extraction and increase series resistance. These interfacial issues, combined with bulk recombination losses, underscore the importance of high-quality multi-layer material synthesis and clean, scalable transfer methods in advancing the performance of 2D-based photovoltaic devices.

doi:10.6342/NTU202501239

To maximize light absorption while minimizing recombination losses and enhancing charge collection efficiency, further developments in both material quality and transfer technology are needed. Beyond material and interface engineering, integrating 2D semiconductors with high-efficiency photovoltaic platforms such as perovskite solar cells offers a promising route to enhance vertical device performance. Van der Waals stacking enables lattice-mismatch-free integration, combining the broadband absorption and tunable bandgaps of 2D materials with the strong light harvesting and efficient charge separation of perovskites. This hybrid approach could overcome limitations inherent to each material class and facilitate the development of tandem or semi-transparent architectures with improved efficiency. Moreover, the mechanical flexibility and ultrathin nature of 2D materials align well with the lightweight and solution-processable characteristics of perovskites, making such systems well-suited for flexible and wearable energy applications. Nevertheless, challenges such as interlayer band alignment, environmental stability, and large-area uniformity must be addressed to realize practical, scalable devices.

In summary, optimizing 2D-based vertical photovoltaic devices requires a multifaceted strategy involving material quality, interfacial engineering, and smart integration with complementary systems. Hybrid architectures leveraging the strengths of 2D materials and perovskites represent a compelling direction for high-performance, ultrathin, and flexible solar technologies.

doi:10.6342/NTU202501239

4.5.2 Performance Optimization of Planar Photoconductive Devices Based on 2D Materials

A planar photodetector based on a 10-layer MoS_2/graphene heterostructure exhibited high responsivity and fast response time, demonstrating the strong potential of multi-layer 2D materials for lateral device configurations. Unlike vertical architectures, which often suffer from recombination losses during carrier transport, lateral devices offer more direct pathways and practical application potential.

Photodetectors typically face a trade-off between high responsivity and fast response. While avalanche photodetectors offer high gain via carrier multiplication, they require high voltages and suffer from increased noise, limiting their suitability for low-power or scalable applications [256, 257]. In contrast, the lateral MoS_2/graphene photodetectors presented in this work show that ballistic carrier transport within the graphene channel could serve as a promising mechanism to simultaneously achieve high gain and rapid response. To further improve performance, several strategies can be considered:

First, both graphene and MoS_2 in this study were assembled via transfer processes. Although optimized, a more fundamental improvement lies in fabricating devices directly on as-grown 2D films synthesized on the target substrate. This approach avoids transfer-induced defects, residues, and misalignments that compromise interface quality and electrical performance.

Second, a dual-channel graphene architecture can be employed to accelerate carrier extraction. By introducing two parallel graphene channels, the carrier collection efficiency can be significantly improved without relying solely on extending carrier

doi:10.6342/NTU202501239

lifetime within the MoS_2 layer. This configuration alleviates the intrinsic gain-speed trade-off observed in single-channel devices.

Combining these two concepts, a dual-channel photodetector was fabricated by growing mono-layer MoS_2 directly on a sapphire substrate, followed by sequential graphene transfers to construct the dual-channel structure, as shown in Figure 4-44 (a). Compared to the single-channel device in Figure 4-36, this design achieved a substantial improvement in responsivity. Under identical channel dimensions (25 μm width, 5 μm length) and a drain-source voltage of 0.5 V, the spectral response in Figure 4-44 (b) reveals a notable enhancement. At 660 nm, the responsivity increased from 257.2 A/W to a record-high 3003.7 A/W.

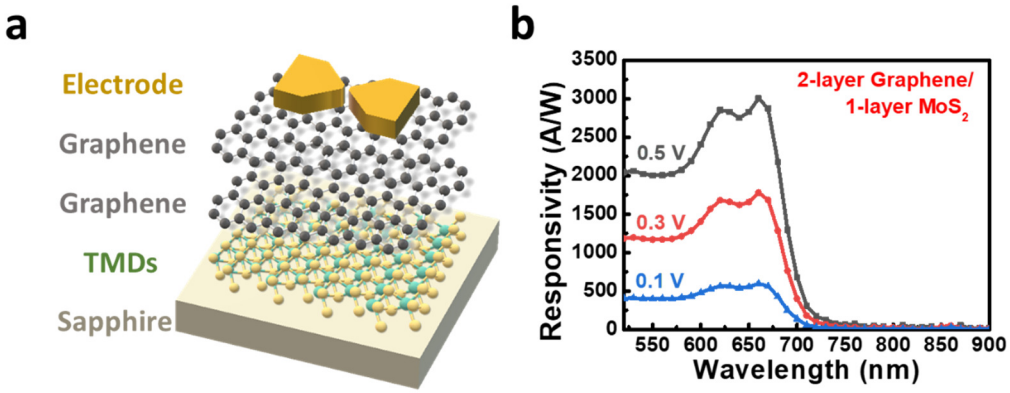

Figure 4-44 (a) Schematic of the dual-channel planar photodetector structure. (b) Spectral responsivity of the corresponding 2-layer graphene/MoS_2 photodetector.

In summary, using as-grown substrates and dual graphene channel designs can effectively address performance bottlenecks in MoS_2/graphene photodetectors, offering a promising route to high-performance 2D optoelectronic devices. And Chapter 5 further extends this concept to multi-band and flexible photodetectors based on the same design methodology.

doi:10.6342/NTU202501239

Chapter 5 High-Responsivity and Wavelength-Tunable Flexible Photodetectors Based on 2D Material Heterostructures

5.1 Development and Challenges of Multi-Band or Flexible Photodetectors

5.1.1 Challenges and Bottlenecks of Multi-Band Photodetectors

Photodetection is central to optoelectronics, supporting a wide range of applications from communications to sensing. Photodetectors convert light into electrical signals and are increasingly utilized across spectral regions from UV to IR [258]. To meet specific application needs, these devices require carefully tailored materials and fabrication techniques suited to their target wavelength. In the visible spectrum, silicon remains the dominant material due to its low cost, mature processing infrastructure, and scalability [259, 260]. However, its performance is limited by relatively low responsivity (~1 A/W) [261], and mechanical rigidity, factors that restrict its use in low-light or flexible applications. For infrared detection, narrow-bandgap III-V semiconductors such as GaSb, InAs, and InSb offer superior light absorption and carrier mobility [262]. Nevertheless, they are hindered by growth-induced defects and require low temperature operation to suppress thermal noise. Although performance can be improved through advanced designs like superlattices and interface engineering [263], these approaches often involve expensive, precision-dependent fabrication techniques such as MBE, posing challenges for mass production.

doi:10.6342/NTU202501239

In contrast, semiconducting2D materials, including MoS_2, WS_2, WSe_2, and black phosphorus, offer unique advantages. Their layer-dependent bandgaps span from deep ultraviolet (e.g., h-BN) to mid-infrared (e.g., black phosphorus), enabling wavelength-specific or broadband light absorption by selecting appropriate materials or heterostructures [28, 35]. In addition, their atomically thin nature allows for ultimate electrostatic control, which is beneficial for suppressing dark current and enabling ultralow-power operation [85].

Moreover, van der Waals heterostructures constructed from 2D materials allow precise control of band alignment without the constraints of lattice matching, unlike traditional III-V systems. Type-II band alignments formed through vdW stacking enable efficient charge separation and prolonged carrier lifetimes, which are critical for achieving high photoconductive gain [264]. These heterostructures can also be engineered to exhibit photogating effects, quantum confinement, or built-in asymmetries, allowing for novel functionalities such as self-powered operation or polarization sensitivity [85].

When integrated with graphene or metallic 2D layers, these semiconductors benefit from high carrier mobility and excellent conductivity, enabling ballistic transport and reducing carrier transit time [80, 265]. This addresses one of the primary challenges of traditional photodetectors—the trade-off between responsivity and speed. In addition, the intrinsically flexible nature of 2D materials makes them uniquely suited for wearable, or foldable optoelectronic platforms, opening new application domains beyond rigid silicon-based systems. Overall, these advantages position 2D materials as a promising alternative for advanced photodetectors. With continued progress in material engineering, device architecture design, and integration strategies, 2D-based photodetectors are well-positioned to meet the demands of next-generation optoelectronic applications.

doi:10.6342/NTU202501239

5.1.2 Challenges and Bottlenecks of Flexible Photodetectors

Flexible photodetectors have attracted wide attention in recent years for their potential in wearable electronics, biomedical sensors, and foldable optoelectronic devices. Unlike conventional rigid photodetectors, flexible counterparts must maintain stable performance under mechanical deformation such as bending, stretching, and twisting. This requires mechanically compliant materials and fabrication techniques that preserve optoelectronic functionality.

Traditional approaches to achieving flexibility often rely on organic semiconductors or quantum dots on flexible substrates, each offering distinct advantages and limitations [181, 266]. Organic photodetectors provide excellent mechanical flexibility, low-temperature processing, and compatibility with large-area solution printing [181]. Their tunable absorption spectra make them attractive for wearable applications. However, they often suffer from low carrier mobility, limited bandwidth, and poor ambient stability, which hinder sensitivity and long-term operation. Quantum dots, such as PbS and perovskite nanocrystals, have shown promising broadband absorption and high responsivity on flexible substrates [266]. Yet, the toxicity of heavy-metal QDs and the environmental sensitivity of perovskites raise concerns about safety and scalability.

In contrast, 2D materials offer a range of unique advantages, including atomic-scale thickness, intrinsic mechanical flexibility, and clean van der Waals interfaces that enable integration without lattice matching. Photodetectors based on these materials exhibit outstanding optoelectronic performance, as shown in the previous chapter, with responsivities reaching ~10^2–10^3 A/W across the visible to near-infrared spectrum—comparable to, or even exceeding, those of organic and quantum dot-based devices. Furthermore, optimized device architectures have demonstrated response times on the millisecond scale, indicating their potential for high-speed operation.

doi:10.6342/NTU202501239

Beyond their device performance, 2D materials also exhibit excellent mechanical adaptability. They can conform to curved or deformable surfaces while retaining high optical absorption, elevated carrier mobility, and tunable bandgaps. Their mechanical robustness and chemical stability ensure reliable operation under bending or stretching [82, 113]. Additionally, strain engineering in these materials enables real-time modulation of their optical and electronic properties in response to mechanical deformation, paving the way for adaptive, strain-sensitive photodetectors—a feature rarely achievable in conventional material systems [267]. It is anticipated that similar fabrication approaches could be employed to develop flexible photodetectors operating across various wavelength ranges, further broadening the potential applications of 2D material-based optoelectronics.

Although 2D materials offer clear advantages, incorporating them into flexible photodetectors still presents several technical hurdles. Producing large-area, uniform films without defects remains a demanding task. In addition, transferring these layers onto flexible substrates without introducing cracks, wrinkles, or contamination requires precise process control. Maintaining low contact resistance and stable electrical behavior under repeated bending is also necessary to ensure reliable device operation. Moreover, to protect against environmental effects, flexible passivation layers that provide both mechanical robustness and adequate barrier properties must be developed to support long-term performance.

Nevertheless, with ongoing progress in material synthesis, transfer techniques, and device integration, photodetectors based on 2D materials are emerging as strong candidates for intelligent and conformable optoelectronic systems. Their unique combination of broadband photo-response, high carrier mobility, and mechanical flexibility makes them particularly suited for flexible photodetection applications.

doi:10.6342/NTU202501239

5.2 Fabrication and Analysis of Multi-Band Photodetectors

5.2.1 Fabrication of Multi-Band Photodetectors

The realization of high-performance multi-band and flexible photodetectors relies on the prior development and systematic optimization of multi-band detection architectures, which serve as the essential foundation for their successful implementation. As discussed in Chapter 4, the material quality and the extent of transfer processing are closely linked to the resulting responsivity. Therefore, in this chapter, high-crystallinity mono-layer TMDs (WS_2, MoS_2, and WSe_2) synthesized via CVD are employed as the light absorption layer without transfer. These are integrated with a graphene transport layer to fabricate photodetectors, aiming to investigate whether the resulting photo-response spectra exhibit multi-band characteristics depending on the choice of TMD material. The corresponding device fabrication process involves three main steps, as illustrated in Figure 5-1: (1) TMD synthesis, (2) graphene growth and transfer, and (3) definition of source and drain electrodes.

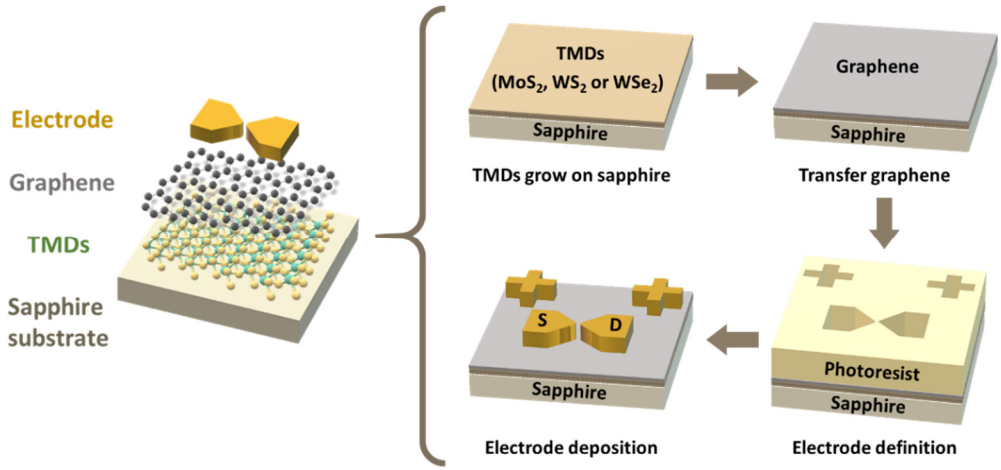

Figure 5-1 Schematic illustration of the fabrication process for TMDs/graphene photodetectors on sapphire substrates. The TMD light absorption layers include WS_2, MoS_2, and WSe_2.

doi:10.6342/NTU202501239

(1) Synthesis of TMDs

Mono-layer WS_2, MoS_2, and WSe_2 samples used in this study were sourced from 2D Semiconductor Company and synthesized via a plasma-assisted CVD process. High-purity (6N) WO_3 and MoO_3 precursors were employed, along with H_2S and H_2Se gases, to facilitate the growth of Mo- and W-based TMDs. Prior to deposition, c-plane sapphire substrates were thoroughly cleaned using a piranha solution, followed by argon plasma treatment to ensure a pristine surface condition.

The CVD growth was performed at 690 °C for MoS_2 and 830 °C for WS_2 and WSe_2. Following deposition, a rapid cooling process was applied to minimize bilayer formation and reduce the density of nucleation sites. Additionally, NaCl was introduced during growth to facilitate the formation of uniform, high-quality mono-layer films.

The Raman spectra of CVD-grown WS_2, MoS_2, and WSe_2 on sapphire substrates are presented in Figure 5-2. The observed Raman mode separations, 61.3 cm^{-1} for WS_2 and 19.3 cm^{-1} for MoS_2, confirm the formation of mono-layer films [249, 268-271]. For WSe_2, the distinct $E_{2g}{}^1$ and A_{1g} modes further validate the mono-layer nature of the sample [271].

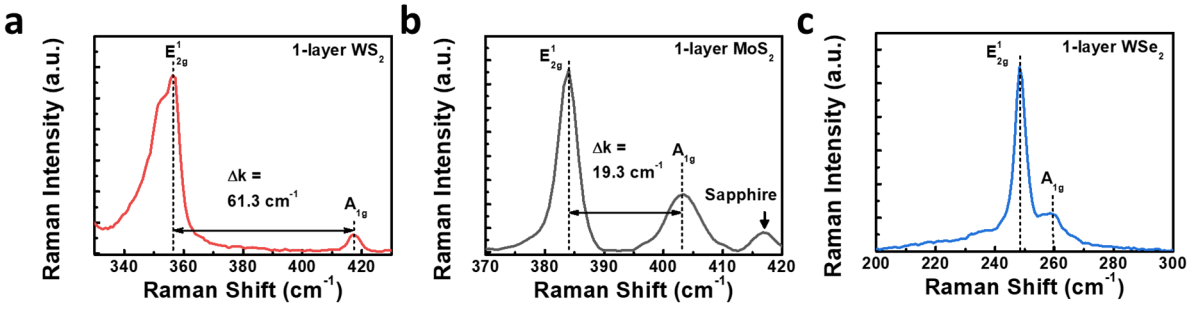

Figure 5-2 Raman spectra of mono-layer (a) WS_2, (b) MoS_2, and (c) WSe_2 grown on sapphire substrates, confirming their characteristic vibrational modes and mono-layer thickness.

doi:10.6342/NTU202501239

(2) Growth and transfer of graphene

Graphene was synthesized using copper foil (1.5 × 1.5 cm^2) as the catalytic substrate. The foil was placed on a quartz stage and inserted into a furnace. The chamber was evacuated to ~13 mtorr, followed by Ar gas introduction at 10 sccm to stabilize pressure at 330 mtorr. The furnace was heated to 1030 °C at a rate of 20 °C/min. An annealing step was performed for 1 hour to remove surface contaminants. Graphene growth was initiated by introducing H_2 (7 sccm) and C_2H_6 (15 sccm) at 660 mtorr, and maintained for 30 minutes. After growth, the C_2H_6 flow was stopped and the sample was rapidly cooled for 15-minute under continued H_2/Ar flow. Finally, all gases were shut off, the system was evacuated, and N_2 was introduced to release the vacuum before retrieving the graphene sample.

Graphene transfer was performed using PDMS stamping method. First, PDMS was laminated onto the graphene film, and the stack was immersed in a 1 M $Fe(NO_3)_3$ solution to etch away the copper substrate. After rinsing and drying, the PDMS/graphene film was aligned and transferred onto the target substrate (TMDs on sapphire substrate), followed by heat treatment at 120 °C for 1.5 hours to improve adhesion. Finally, the PDMS layer was peeled off, completing the transfer process, as illustrated in Section 2.2.1.

(3) Definition of source and drain electrodes

After removing PDMS residues, source and drain electrodes were fabricated by first spin-coating HMDS and a negative photoresist, followed by photolithographic patterning and development using TMAH. Subsequently, 50 nm of Au was deposited using e-beam evaporation, and the electrode patterns were defined through a lift-off process in acetone.

doi:10.6342/NTU202501239

5.2.2 Evaluating the Performance of Multi-Band Photodetectors

To investigate the photo-response characteristics of planar-type multi-band photodetectors, spectral response measurements were performed using the experimental setup described in Section 2.5.3. In this configuration, broadband illumination from a Xe lamp was focused onto the active region (graphene/TMDs) of the 2D material photodetectors. Figure 5-3 presents the optical microscope image of the device layout, along with a schematic representation of the illuminated area, demonstrating the spatial overlap between the focused light spot and the device's active region.

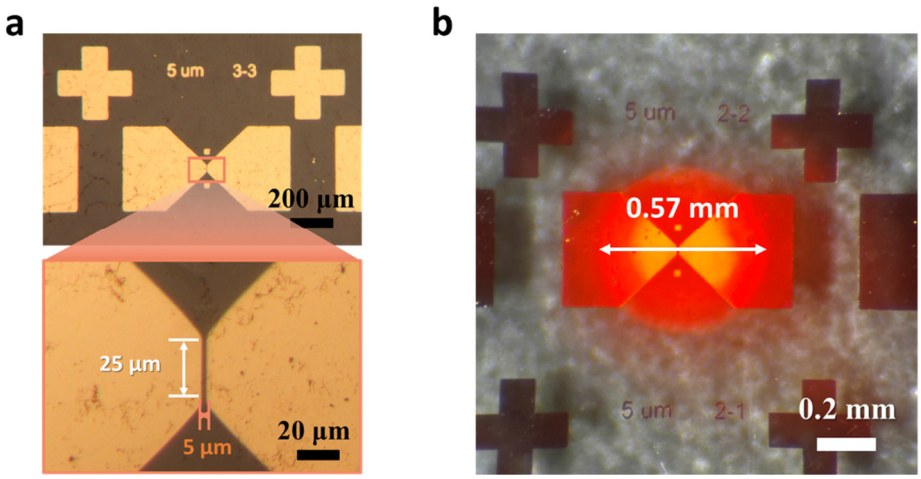

Figure 5-3 Optical microscope images showing (a) the planar-type multi-band photodetector layout and (b) the illumination spot size of the xenon lamp.

The optical power at each wavelength was calibrated using a power meter to ensure accurate correlation with the device's photo-response (Figure 4-19). Photocurrent measurements were conducted over the wavelength range of 500-1000 nm using a precision source meter in conjunction with a lock-in amplifier. To ensure signal stability, an integration time of 3 seconds was applied. The frequency of the optical chopper was varied between 5 Hz and 30 Hz in order to investigate the frequency dependence of the photo-response.

Following, the performance of the planar photodetector was characterized under

doi:10.6342/NTU202501239

illumination with light sources of varying wavelengths. As described in Section 5.2.1, mono-layer graphene/mono-layer TMDs (WS_2, MoS_2, and WSe_2) heterostructure photodetectors with channel dimensions of 25 μm (width) and 5 μm (length) were fabricated. Their corresponding spectral responses under applied biases of 0.1, 0.3, and 0.5 V are presented in Figure 5-4 (a-c). For comparison, the responsivity of the three devices under an applied bias of 0.5 V are presented in Figure 5-4 (d), illustrating the distinct response wavelengths corresponding to each light-absorbing material. The observed response wavelengths, approximately 630 nm for WS_2, 660 nm for MoS_2, and 750 nm for WSe_2, closely match the photoluminescence peaks of the as-grown TMDs (620 nm, 676 nm, and 756 nm, respectively), as shown in Figure 5-5, confirming their effectiveness as active light-absorbing layers.

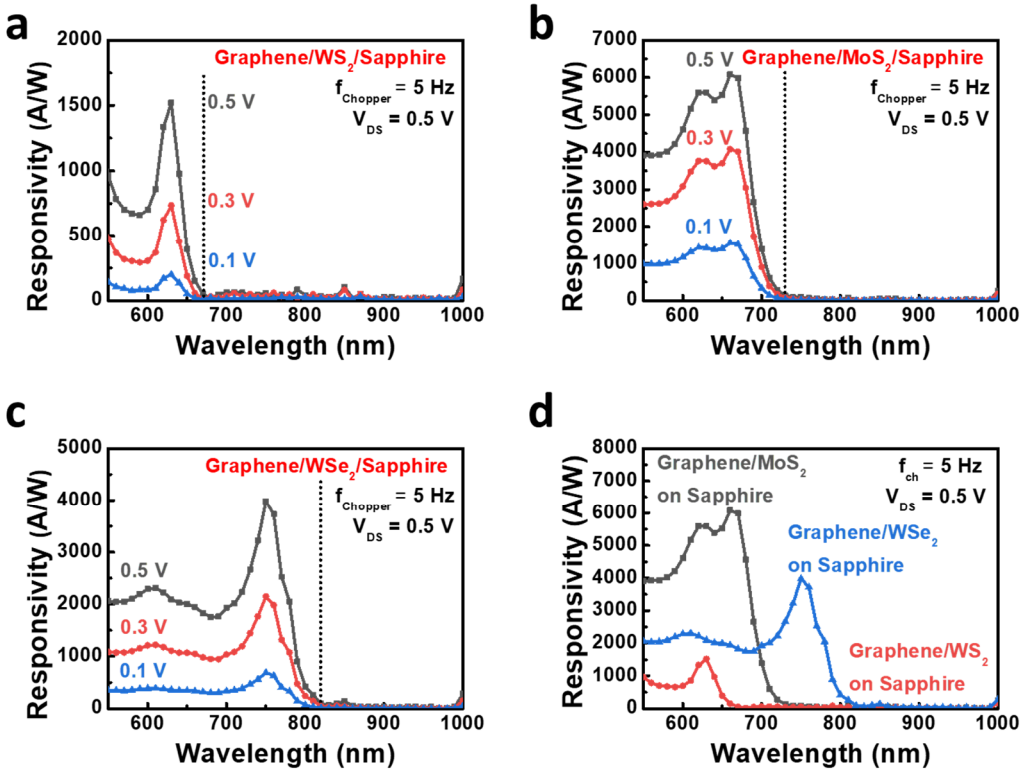

Figure 5-4 The spectral response curves of (a) graphene/WS_2, (b) graphene/MoS_2, and (c) graphene/WSe_2 photodetectors on sapphire substrate under applied voltage of 0.1, 0.3, and 0.5 V. (d) Comparison of the cut-off wavelengths of the three devices at 0.5 V.

doi:10.6342/NTU202501239

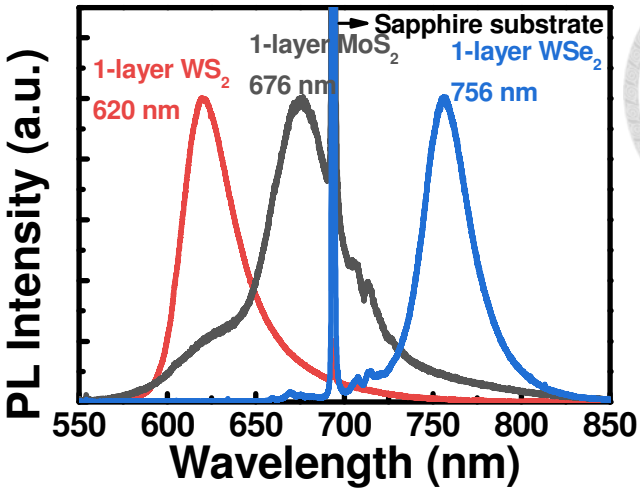

Figure 5-5 Photoluminescence spectra of mono-layer WS_2, MoS_2, and WSe_2.

Notably, all devices exhibited high responsivity values exceeding 10^3 A/W under an applied bias of 0.5 V, with responsivities of 1521.9 A/W for WS_2 (at 630 nm), 6077.9 A/W for MoS_2 (at 660 nm), and 3977.8 A/W for WSe_2 (at 750 nm). These high responsivities directly contribute to enhanced signal detection performance, which can be further evaluated using the detectivity (D*). Detectivity is a fundamental figure of merit for photodetectors, representing the device's ability to sense weak optical signals in the presence of background noise. It is defined as the inverse of the noise-equivalent power (NEP), normalized by the square root of the detector area (A) and the measurement bandwidth (Δf), as expressed by the Equation 5-1:

$$\text{Detectivity} = \frac{\sqrt{A\Delta f}}{NEP} \qquad (\text{Equation } 5-1)$$

Alternatively, for photoconductive detectors dominated by shot noise, detectivity can be expressed in terms of responsivity (R) and dark current (I_d), as shown in Equation 5-2:

$$\text{Detectivity} = \frac{R}{\sqrt{2qI_d}} \qquad (\text{Equation } 5-2)$$

Where R is the responsivity in A/W, q is the elementary charge (1.602×10^{-19} C), I_d is the dark current in amperes.

doi:10.6342/NTU202501239

As shown in Figure 5-6, the corresponding detectivity values were 6.9×10^{10} (WS_2), 17.6×10^{10} (MoS_2), and 9.2×10^{10} Jones (WSe_2), further confirming the high performance of the graphene-based heterostructures. These results suggest that the dominant photocurrent mechanism arises primarily from the high photoconductive gain enabled by the graphene transport layer, rather than from the intrinsic properties of the individual TMD light absorption layer.

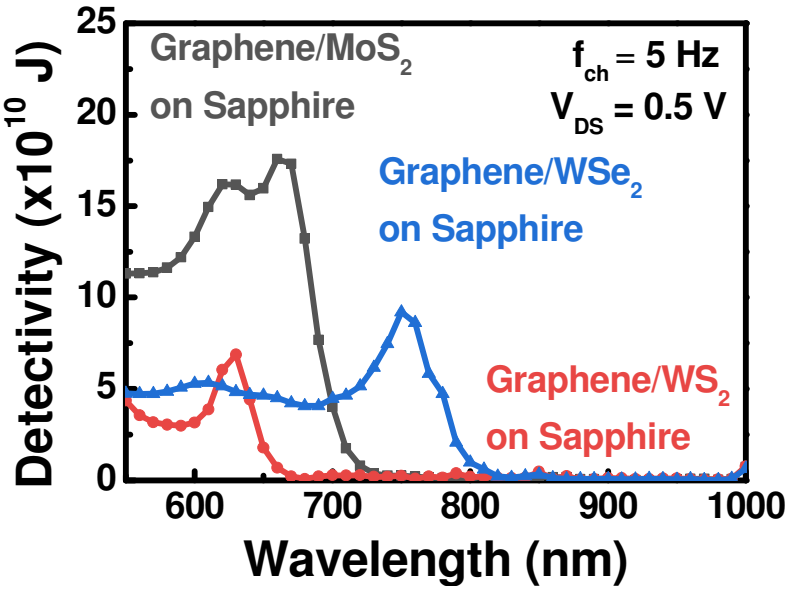

Figure 5-6 Detectivity of graphene/WS_2, graphene/MoS_2, and graphene/WSe_2 photodetectors fabricated on sapphire substrates under an applied bias of 0.5 V.

A schematic illustration of the device operation mechanism is provided in Figure 5-7. When illuminated, photo-generated electrons within the TMD layer transfer to the graphene layer under the applied bias, leaving holes behind. The resulting hole accumulation in the TMD induces electrostatic gating, attracting additional electrons into the graphene and modulating its carrier concentration. Given the high carrier mobility of graphene, even a small change in carrier density leads to a significant current variation, producing the observed high responsivity.

doi:10.6342/NTU202501239

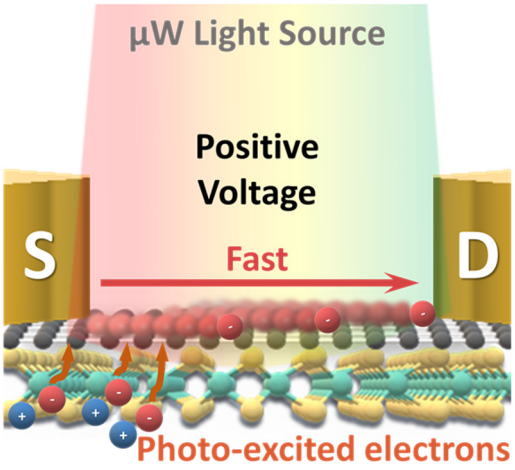

Figure 5-7 A schematic diagram depicting the operation mechanism of the graphene/TMD heterostructure photodetectors.

However, while the electron extraction–hole accumulation–carrier modulation process enhances device responsivity, it inherently imposes a limitation on temporal response. To better understand this trade-off, responsivity was measured not only at a 5 Hz chopping frequency but also at 30 Hz. Figure 5-8 presents the measurement results for the graphene/WS_2, graphene/MoS_2, and graphene/WSe_2 photodetectors. For the graphene/WS_2 device, a responsivity of 1521.9 A/W was recorded at 630 nm under 5 Hz modulation. However, as the chopping frequency increased to 30 Hz, the responsivity at the same wavelength decreased significantly to 703.7 A/W, indicating a frequency-dependent drop in photocurrent (Figure 5-8 (a)). Similarly, the graphene/MoS_2 device showed a responsivity of 6077.9 A/W at 660 nm under 5 Hz, which decreased to 2315.5 A/W at 30 Hz (Figure 5-8 (b)). For the graphene/WSe_2 photodetector, the responsivity declined from 3977.8 A/W at 750 nm under 5 Hz to 1834.6 A/W at 30 Hz (Figure 5-8 (c)). These reductions in responsivity with increasing modulation frequency suggest that the devices cannot efficiently follow rapidly modulated optical signals, indicating limited temporal response.

To further confirm the dynamic characteristics, transient photocurrent measurements

doi:10.6342/NTU202501239

were conducted at each device's peak response wavelength under a 0.5 V bias, with a 5 Hz chopping frequency, as shown in Figure 5-8 (d). All devices exhibited rise and fall times exceeding 50 ms, consistent with previously reported graphene/TMD heterostructures [272-275]. This behavior is attributed to the intrinsic carrier dynamics: upon illumination, holes accumulate in the TMD layer while electrons are extracted into graphene. When the light is turned off, the rapid transport of carriers in graphene allows only a limited number of electrons to recombine with trapped holes in the TMD. This imbalance delays the return to equilibrium, thus extending the fall time and limiting the device's speed.

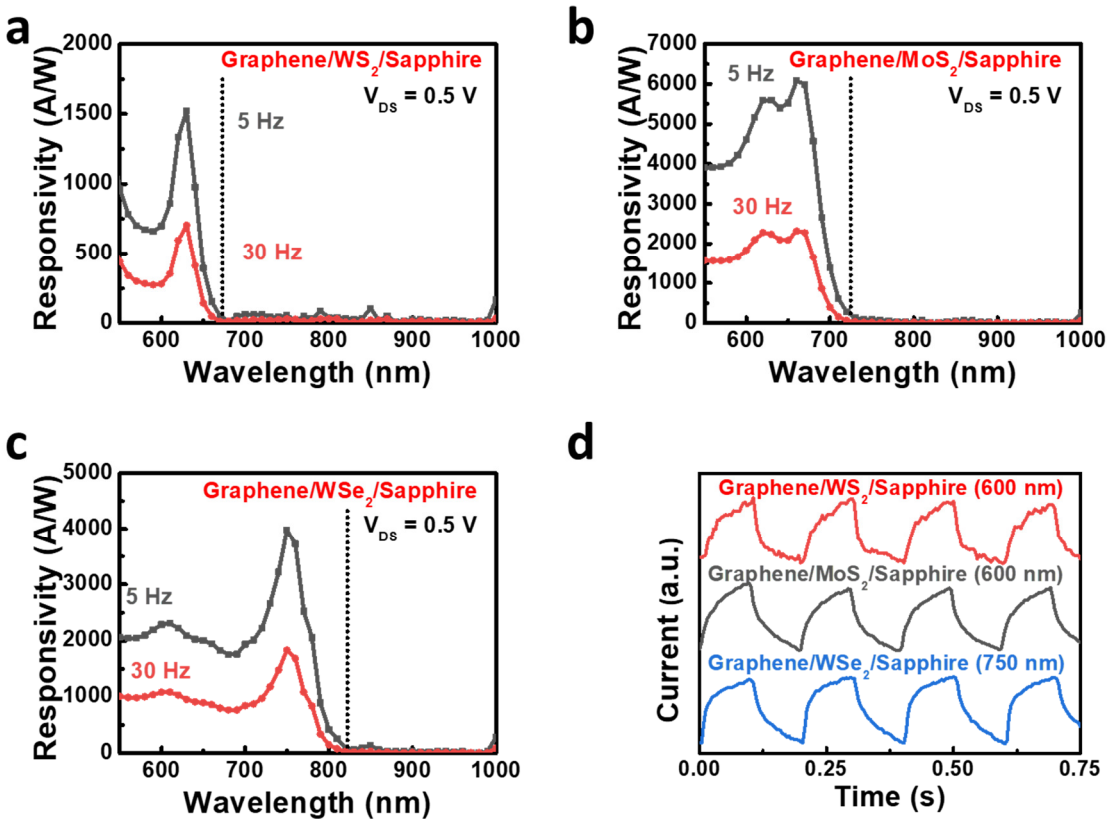

Figure 5-8 Responsivity of (a) graphene/WS_2, (b) graphene/MoS_2, and (c) graphene/WSe_2 photodetectors on sapphire substrates measured under different optical chopper frequencies (5, 30 Hz). (d) Transient photocurrent responses at 0.5 V bias and 5 Hz, with excitation wavelengths of 600 nm (WS_2, MoS_2) and 750 nm (WSe_2).

doi:10.6342/NTU202501239

5.3 Fabrication and Analysis of Flexible Photodetectors

5.3.1 Fabrication of Flexible Photodetectors

As discussed above, the 2D material-based photodetectors developed in this study demonstrate exceptionally high responsivity (>10^3 A/W) on rigid sapphire substrates. Although the temporal response is relatively slow, this performance characteristic remains promising for flexible optoelectronic applications. The elevated responsivity enables reliable operation under low-light conditions or low-power environments, while the current response time is still adequate for many practical uses, particularly in scenarios where real-time imaging or ultra-fast switching is not required. Having established the feasibility of multi-band photodetection using various TMDs as light absorption layers, this study further proposes transferring the same heterostructures onto flexible substrates to assess their potential for integration into flexible photonic systems. The device fabrication procedure consists of three stages, as depicted in Figure 5-9: (1) synthesis and transfer of TMD materials, (2) growth and transfer of graphene, and (3) patterning of source and drain electrodes.

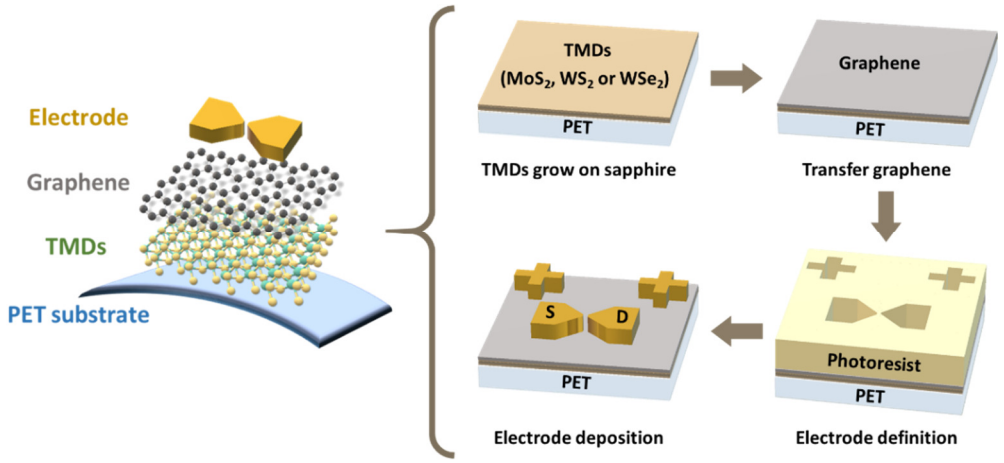

Figure 5-9 Schematic illustration of the fabrication process for TMDs/graphene photodetectors on PET substrates. The TMD light absorption layers include WS_2, MoS_2, and WSe_2.

doi:10.6342/NTU202501239

(1) Synthesis and transfer of TMD materials:

The mono-layer WS_2 MoS_2, and WSe_2 films used in this study were procured from 2D Semiconductor and synthesized using the same method described in Section 5.2.1. Due to the use of flexible polyethylene terephthalate (PET) instead of the sapphire substrate employed during TMD growth, an additional transfer step was required. These mono-layer films were transferred from sapphire substrates to PET substrates using a PDMS stamping technique, as detailed in Section 2.2.1. PDMS was adhered to the WS_2 MoS_2, or WSe_2 film and immersed in a 3M KOH solution to facilitate delamination. After sufficient separation, the PDMS/TMD stack was rinsed, dried, and aligned onto the PET substrate. A second heating step was applied to enhance adhesion, and the PDMS layer was then removed. Photographs of the three samples after transfer are shown in Figure 5-10. To minimize bending during subsequent processing, the PET substrate was first affixed to a sapphire substrate.

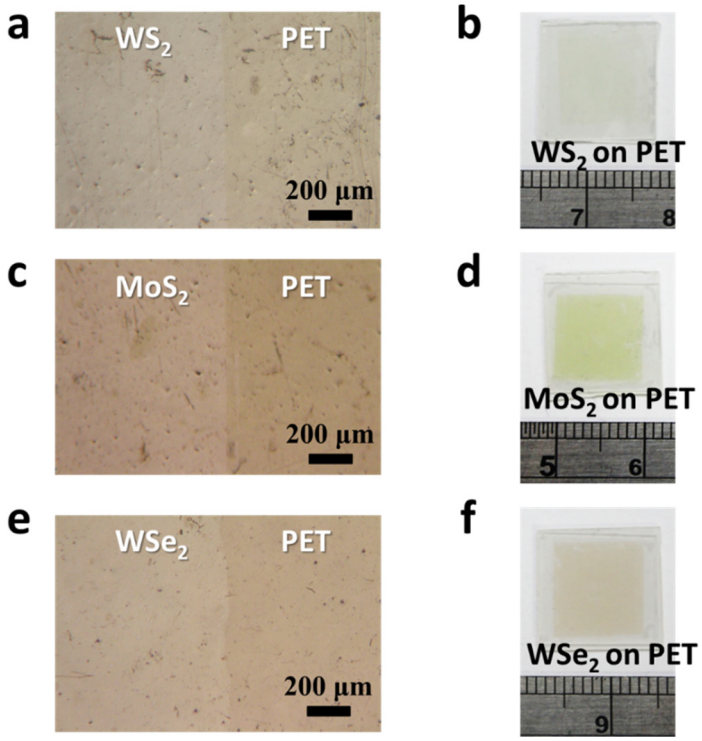

Figure 5-10 Optical microscope images and photographs of (a, b) WS_2, (c, d) MoS_2, and (e, f) WSe_2transferred onto PET substrates.

doi:10.6342/NTU202501239

(2) Growth and transfer of graphene

Graphene was synthesized using copper foil (1.5 × 1.5 cm^2) as the catalytic substrate. The foil was placed on a quartz stage and inserted into a furnace , where the chamber was evacuated to ~13 mtorr. Ar gas was introduced at 10 sccm to stabilize pressure at 330 mtorr. The furnace was heated to 1030 °C at a rate of 20 °C/min, and annealed for 1 hour to remove surface contaminants. Graphene growth was initiated by introducing H_2 (7 sccm) and C_2H_6 (15 sccm) at 660 mtorr for 30 minutes. After growth, the C_2H_6 flow was stopped and the sample was rapidly cooled for 15-minute under H_2/Ar flow. Finally, all gases were shut off, the system evacuated, and N_2 was introduced to release the vacuum.

Graphene transfer was performed using the PDMS stamping method. PDMS was first laminated onto graphene, and the stack was immersed in 1 M $Fe(NO_3)_3$ to etch the copper substrate. After rinsing and drying, the PDMS/graphene film was aligned and transferred onto the target substrate (TMDs on PET), followed by thermal treatment at 120 °C for 1.5 hours to enhance adhesion. Finally, the PDMS layer was peeled off, completing the process, as shown in Section 2.2.1.

(3) Definition of source and drain electrodes

To define the source and drain electrodes, residual PDMS was removed, followed by spin-coating a thin layer of HMDS and negative photoresist. Photolithographic patterning and TMAH development were then performed. Gold (50 nm) was deposited via e-beam evaporation, and the electrode structures were formed through a lift-off process in acetone. The use of a plastic substrate enables flexible device fabrication, but the limited thermal and chemical tolerance of PET imposes constraints. To preserve device integrity, tight control over processing temperature and solvent exposure was required.

doi:10.6342/NTU202501239

5.3.2 Evaluating the Performance of Flexible Photodetectors

Figure 5-11 presents the electrical characteristics of the graphene/WS_2, graphene/MoS_2, and graphene/WSe_2 photodetectors. The three I_D-V_D curves exhibit similar and symmetric current ranges from -1 to 1 mA, with graphene as the channel material. This similarity arises because the electrical transport is predominantly governed by the graphene layer, which serves as the main conducting channel in all devices. Although the TMD layers differ in composition and optical properties, they function primarily as photon absorbers and do not directly participate in lateral current conduction. As a result, in the absence of illumination, the carrier transport behavior is largely determined by the graphene-electrode interfaces and the intrinsic properties of the graphene itself, leading to nearly identical I_D-V_D characteristics across the three heterostructure configurations.

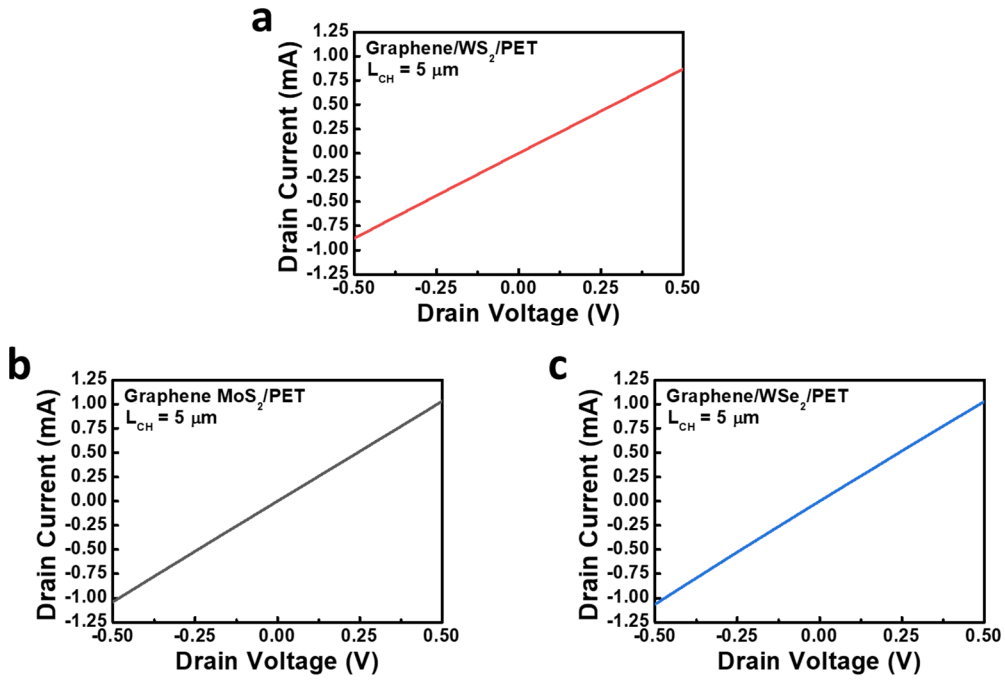

Figure 5-11 The I_D–V_D curves of (a) graphene/WS_2, (b) graphene/MoS_2, and (c) graphene/WSe_2 photodetectors on PET substrates.

doi:10.6342/NTU202501239

To investigate the photo-response characteristics of flexible planar-type multi-band photodetectors, spectral response measurements were performed using the experimental setup described in Section 2.5.3. In this configuration, broadband illumination from a Xe lamp was focused onto the active region (graphene/TMDs) of the 2D material photodetectors. Figure 5-12 presents the optical microscope image of the device layout, along with a schematic representation of the illuminated area, demonstrating the spatial overlap between the focused light spot and the device's active region.

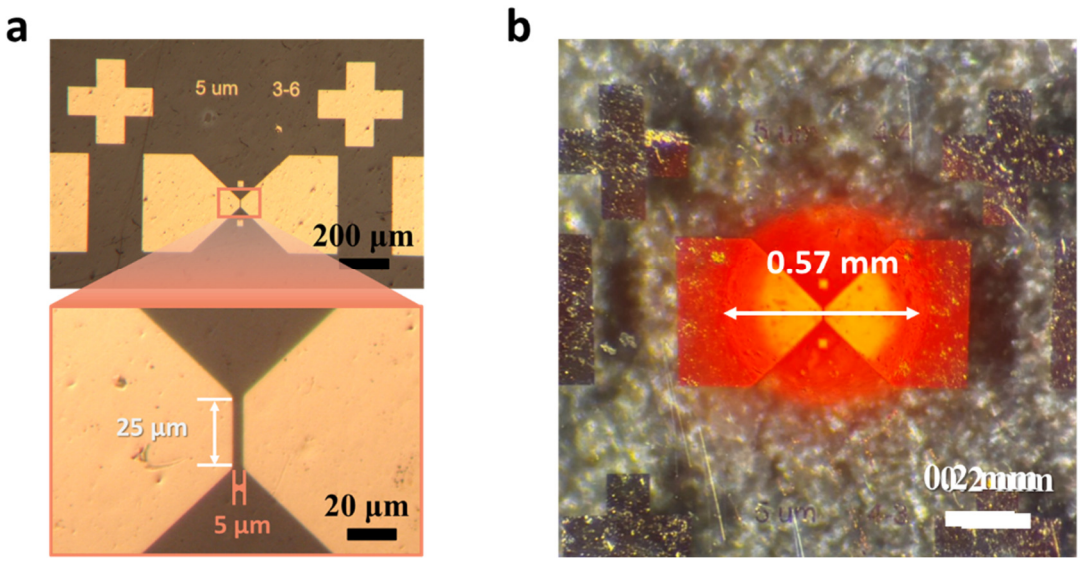

Figure 5-12 Optical microscope images showing (a) the flexible planar-type multi-band photodetector layout and (b) the illumination spot size of the xenon lamp.

The optical power at each wavelength was calibrated using a power meter to ensure accurate correlation with the device's photo-response (Figure 4-19). Photocurrent measurements were conducted over the wavelength range of 500-1000 nm using a precision source meter in conjunction with a lock-in amplifier. To ensure signal stability, an integration time of 3 seconds was applied. The frequency of the optical chopper was varied between 5 Hz and 30 Hz in order to investigate the frequency dependence of the photo-response.

The performance of the flexible photodetectors was systematically evaluated under

doi:10.6342/NTU202501239

illumination with varying wavelengths. As detailed in Section 5.3.1, mono-layer graphene/mono-layer TMD (WS_2, MoS_2, and WSe_2) heterostructure devices with channel dimensions of 25 μm × 5 μm were fabricated. Their corresponding photocurrent and spectral responses under applied biases of 0.1, 0.3, and 0.5 V are presented in Figure 5-13 (a-f). All devices maintained high responsivity, with slight decreases compared to sapphire-based counterparts. Specifically, at 0.5 V, the graphene/WS_2, graphene/MoS_2, and graphene/WSe_2 devices achieved responsivities of 472.0 A/W (at 630 nm), 1331.9 A/W (at 660 nm), and 713.8 A/W (at 750 nm), respectively. The performance degradation is primarily attributed to imperfections introduced during the additional transfer process onto flexible substrates, such as interfacial defects, wrinkles, or surface roughness. Despite these challenges, the devices retained relatively high responsivity, indicating the robustness and reliability of the heterostructure architecture.

For comparison, Figure 5-14 (a) summarizes the responsivity of the three devices under a fixed bias of 0.5 V. The observed peak response wavelengths (~640 nm for WS_2, ~660 nm for MoS_2, and ~750 nm for WSe_2) closely match the photoluminescence emission peaks of the as-grown TMDs (620 nm, 676 nm, and 756 nm, respectively; see Figure 5-5), validating their effectiveness as active light-absorbing layers.

Based on the measured responsivity and the standard responsivity-to-quantum efficiency relationship (Equation 4-4), the estimated QE values at 0.5 V were 925.7 for WS_2, 2502.4 for MoS_2, and 1180.0 for WSe_2. Correspondingly, the detectivity values were calculated to be 3.2×10^{10} Jones for WS_2, 8.2×10^{10} Jones for MoS_2, and 4.4×10^{10} Jones for WSe_2, as shown in Figure 5-14 (b). These values indicate strong capability for detecting weak optical signals under low-noise conditions. These values reflect the strong ability of the devices to detect weak optical signals under low-noise conditions.

doi:10.6342/NTU202501239

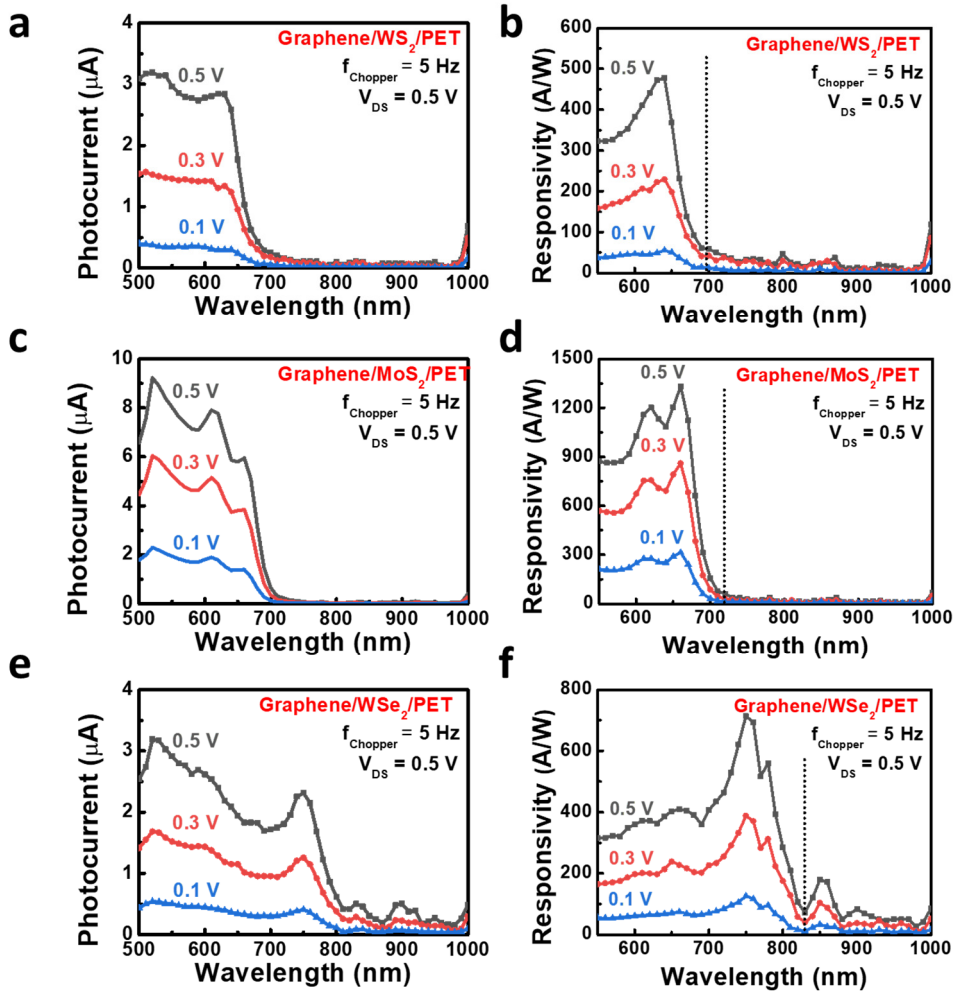

Figure 5-13 Photocurrent (a, c, e) and spectral response (b, d, f) curves of graphene/WS_2, graphene/MoS_2, and graphene/WSe_2 photodetectors on PET substrates under applied voltages of 0.1, 0.3, and 0.5 V.

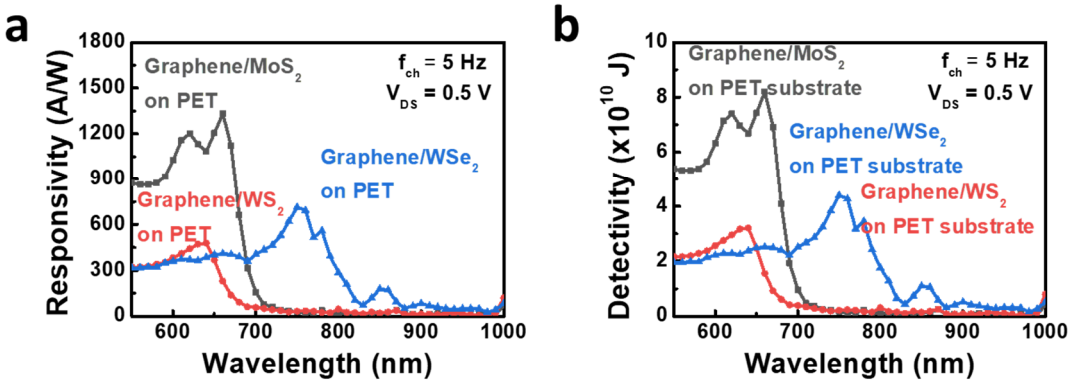

Figure 5-14 Responsivity and detectivity of graphene/WS_2, graphene/MoS_2, and graphene/WSe_2 photodetectors on PET substrates under an applied bias of 0.5 V.

doi:10.6342/NTU202501239

The mono-layer graphene/TMD photodetectors on PET substrates maintained high responsivity and detectivity, indicating that the intrinsic optical properties of the TMDs remained intact after transfer process. To further evaluate their temporal performance, the devices were measured under modulated light at different chopping frequencies. As shown in Figure 5-15, increasing the chopping frequency from 5 Hz to 30 Hz led to a noticeable decrease in responsivity at the same excitation wavelength. For the graphene/WS_2 device, a responsivity of 477.8 A/W was recorded at 640 nm under 5 Hz modulation. However, as the chopping frequency increased to 30 Hz, the responsivity at the same wavelength decreased to 306.6 A/W, indicating a frequency-dependent drop in photocurrent (Figure 5-14 (a)). Similarly, the graphene/MoS_2 device showed a responsivity of 1331.9 A/W at 660 nm under 5 Hz, which decreased to 646.2A/W at 30 Hz (Figure 5-14 (b)). For the graphene/WSe_2 photodetector, the responsivity declined from 713.4 A/W at 750 nm under 5 Hz to 490.2 A/W at 30 Hz (Figure 5-14 (c)).

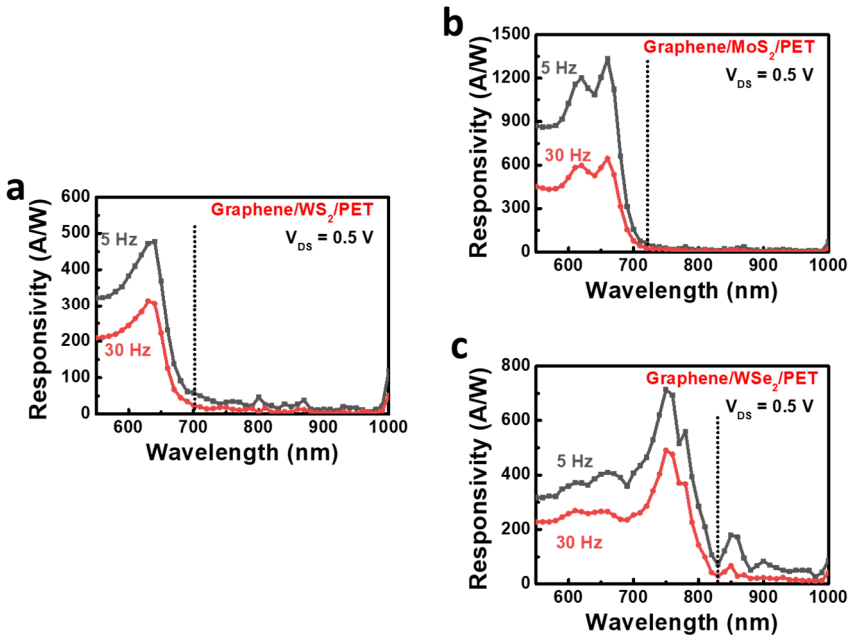

Figure 5-15 Responsivity of (a) graphene/WS_2, (b) graphene/MoS_2, and (c) graphene/WSe_2 photodetectors on PET substrates measured under different optical chopper frequencies (5, 30 Hz).

doi:10.6342/NTU202501239

To further investigate the dynamic response, time-resolved photocurrent measurements were conducted, as shown in Figure 5-16. The incident wavelengths were 600 nm for WS_2 and MoS_2 devices, and 750 nm for the WSe_2 device. All devices exhibited rise and fall times similar to those on sapphire substrates, approximately 50 ms. The relatively slow response is attributed to the limited electron replenishment in mono-layer TMDs due to their low charge storage capacity under dynamic illumination. Notably, the graphene/WSe_2 device exhibited a slightly shorter rise time, possibly due to strain relaxation following the transfer process. These results confirm that the flexible graphene/TMD photodetectors fabricated on PET substrates exhibit acceptable response times, while their relatively high responsivity renders them well-suited for flexible optoelectronic applications operating in low-light or low-power environments.

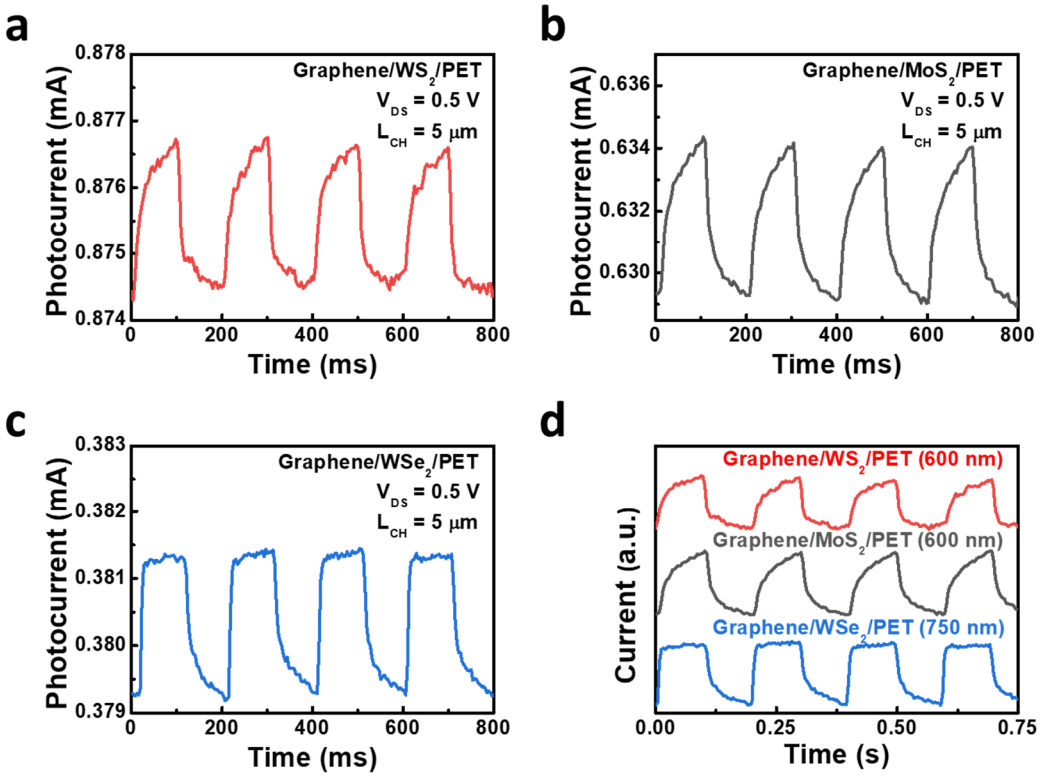

Figure 5-16 Transient photocurrents at 0.5 V for (a) graphene/WS_2 and (b) graphene/MoS_2 at 600 nm, and (c) graphene/WSe_2 at 750 nm. (d) Response time comparison of the three photodetectors at a chopping frequency of 5 Hz.

doi:10.6342/NTU202501239

Since the devices are fabricated using wafer-scale 2D materials, multiple photodetectors can be integrated on a single flexible PET substrate, which offers excellent bendability and suitability for flexible electronic applications. As illustrated in Figure 5-17 (a), a hand-hold PET substrate embedded with 2D material photodetectors demonstrates the device's physical flexibility. Although dynamic electrical measurements under continuous bending were not performed, the devices were fixed onto stages with various curvature radii to simulate mechanical deformation in practical scenarios, as shown in Figure 5-17 (b).

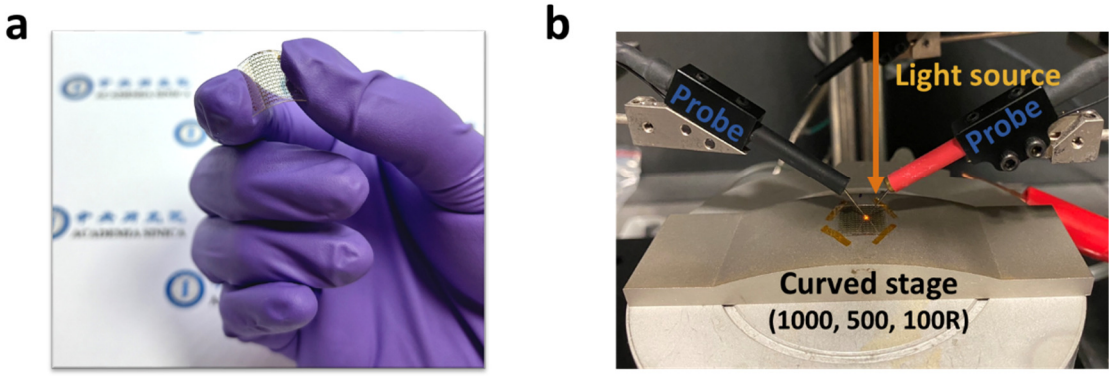

Figure 5-17 (a) The picture of the hand-hold PET substrate with numerous photodetectors. (b) The system setup for the device performances under different bending conditions.

Given that the curvature radius of a typical commercial curved display is 4000R to 1000R, this study covers more severe bending conditions including curvature radii of 1000, 500, and 100 mm (i.e., 1000 R, 500 R, and 100 R). The spectral responses curves of the flexible graphene/WS_2, graphene/MoS_2, and graphene/WSe_2 photodetectors fabricated on PET substrates under different curvatures 1000R, 500R, and 100R are shown in Figure 5-18. While Figure 5-19 indicates the changes in responsivity at the highest response wavelengths for each device under different bending curvatures.

doi:10.6342/NTU202501239

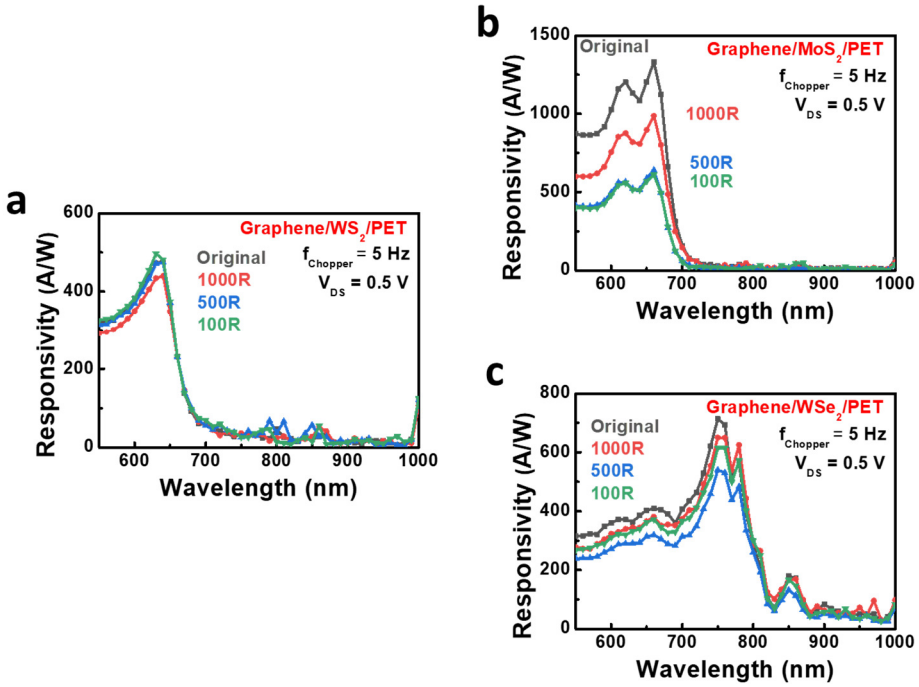

Figure 5-18 The spectral response curves of the (a) graphene/WS_2, (b) graphene/MoS_2, and (c) graphene/WSe_2 photodetectors on PET substrate under unbent, 1000R, 500R and 100R banding conditions.

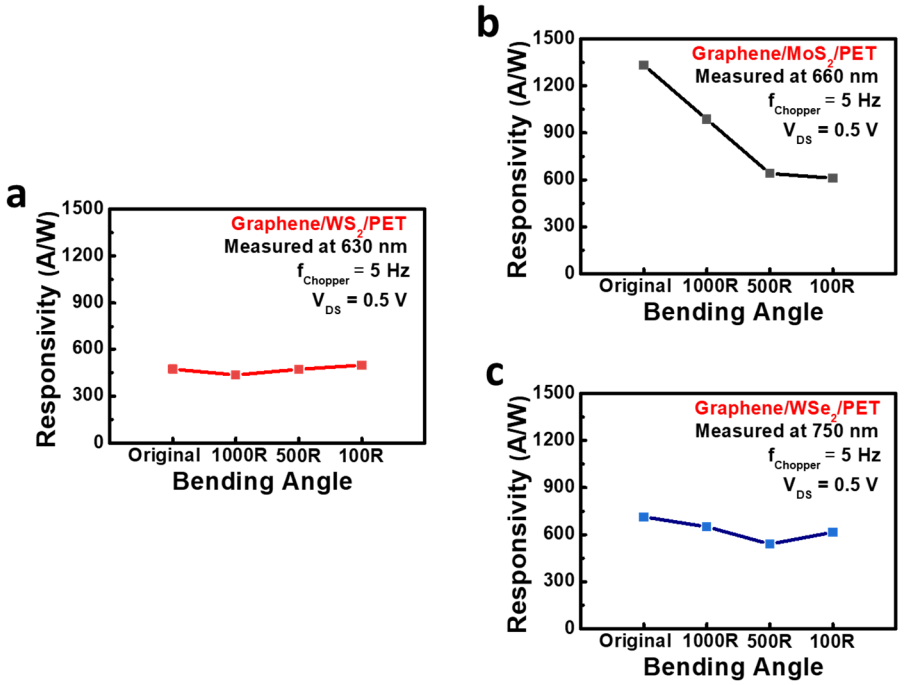

Figure 5-19 The responsivity value of the (a) WS_2 device at 630 nm, (b) MoS_2 device at 660 nm, and (c) WSe_2 device at 750 nm were measured to assess the performance of the devices under various bending conditions.

doi:10.6342/NTU202501239

The results reveal that the responsivity of the WS_2 and WSe_2 devices exhibits minimal degradation across all bending conditions. Specifically, for the WS_2 device, the responsivity at 630 nm remains stable, with values of 434.0, 471.0, and 496.9 A/W under bending radii of 1000R, 500R, and 100R, respectively. Similarly, the WSe_2 device demonstrates responsivity values of 650.2, 540.2, and 614.8 A/W at 750 nm under the same bending conditions. In contrast, the MoS_2 device exhibits a significant decline in performance under increasing curvature. The responsivity at 660 nm decreases from 986.8 A/W at 1000R to 640.4 A/W at 500R, and 610.8 A/W at 100R

The MoS_2 device initially exhibits high responsivity, but its performance drops significantly upon bending, which can be attributed to the surface roughness of the light-absorbing TMD layer. As shown in the $1 \times 1\ \mu m^2$ AFM images in Figure 5-20 (a-c), the as-grown TMD films on sapphire substrates exhibit root-mean-square (RMS) roughness values of 1.85 nm for WS_2, 2.09 nm for WSe_2, and 0.49 nm for MoS_2. While WS_2 and WSe_2 films display relatively rougher surfaces, the MoS_2 film shows a flatter and more uniform morphology.

Under mechanical stress, flatter films may undergo localized delamination due to stronger adhesion to the PET substrate, potentially disrupting carrier transport pathways and leading to reduced device responsivity, as illustrated in Figure 5-20 (d-f). Furthermore, the flatter morphology may reflect larger crystal domains, which are more susceptible to stress-induced lattice distortions. These observations indicated that both surface morphology and mechanical adaptability of 2D materials play important roles in determining the performance and structural stability of flexible photodetectors.

doi:10.6342/NTU202501239

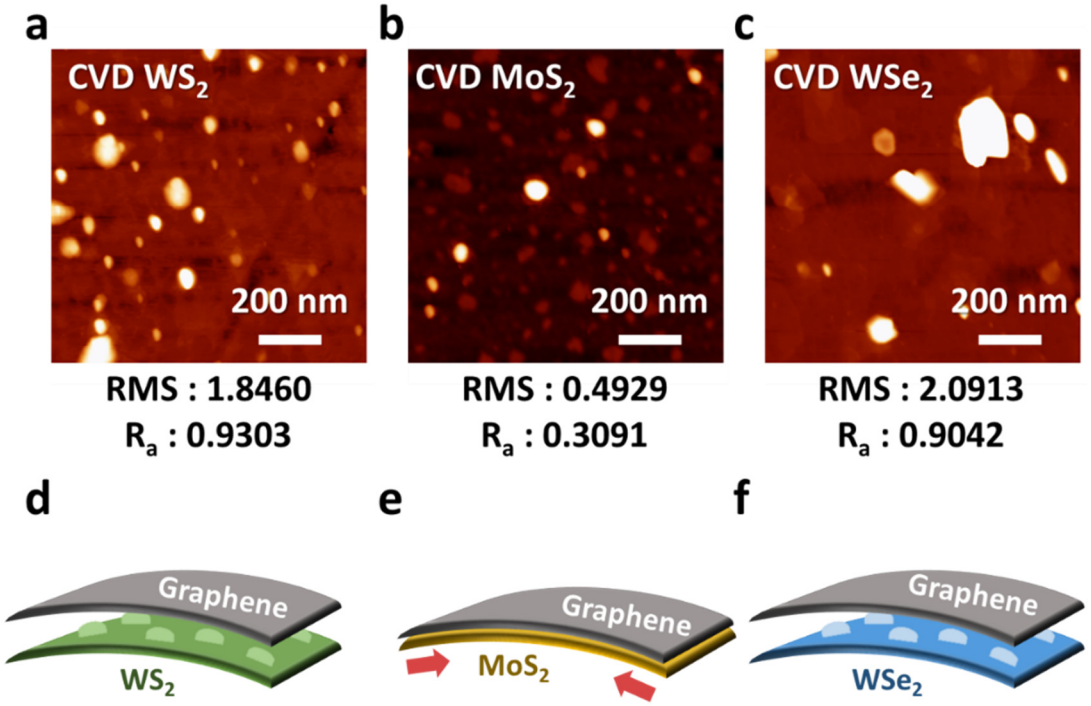

Figure 5-20 The 1 × 1 μm^2 AFM images of the as-grown TMD films (WS_2, MoS_2 and WSe_2) on sapphire substrates.

To evaluate the long-term stability of 2D material-based devices, their spectral responses were re-measured three months after initial fabrication. As shown in Figure 5-21 (a), the spectral responsivity of the flexible 2D material-based photodetectors remained stable under ambient conditions after three months of storage. Specifically, the WS_2 device retained a responsivity of 474.8 A/W at 640 nm compared to its initial value of 477.8 A/W, the MoS_2 device maintained 831.7 A/W at 660 nm compared to its original 1331.9 A/W, and the WSe_2 device preserved 611.5 A/W at 750 nm relative to its initial 713.4 A/W. These results confirm the long-term environmental stability of the devices, with minimal degradation caused by atmospheric exposure or prolonged storage.

In contrast, the performance under mechanical bending was also examined using a bending radius of 100R, as shown in Figure 5-21 (b). Under this condition, the WS_2-based device showed a reduction in responsivity to 226.2 A/W at 640 nm. The MoS_2-based

doi:10.6342/NTU202501239

device exhibited a more substantial drop, with its responsivity at 660 nm decreasing to 390.5 A/W. Remarkably, the WSe_2-based device still maintained a high responsivity of 536.5 A/W at 750 nm, indicating superior mechanical robustness under curvature stress.

Although all three devices maintained high responsivity levels (> 200 A/W) even after prolonged ambient storage and mechanical deformation, WSe_2-based devices demonstrated the least performance degradation under bending, demostrating their potential for reliable operation in flexible and wearable optoelectronic systems. Further investigation is required to fully elucidate the underlying mechanisms responsible for the observed differences in mechanical resilience. Nonetheless, the results collectively underscore the promising long-term operational stability and mechanical adaptability of 2D-material-based flexible photodetectors.

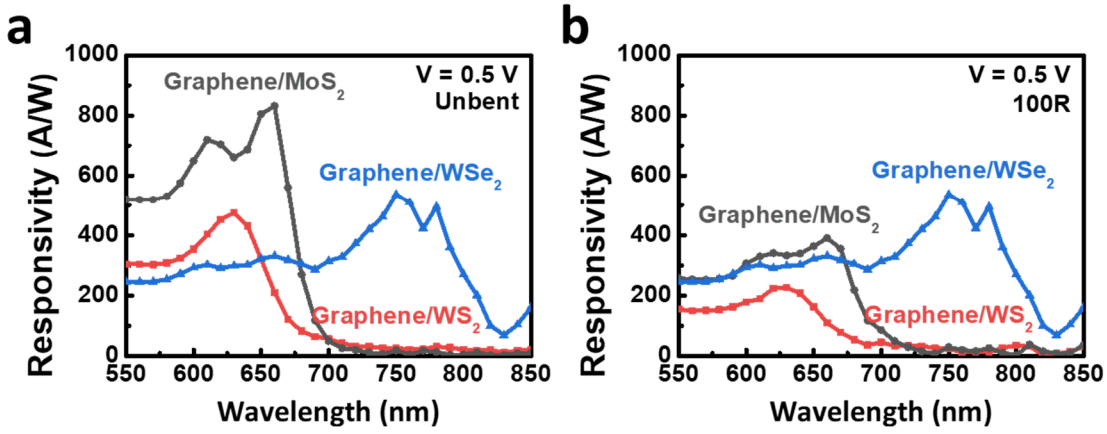

Figure 5-21 Spectral responsivity curves of graphene/TMD photodetectors on PET substrates measured after three months of ambient storage, under (a) unbent and (b) bent (100R) conditions.

doi:10.6342/NTU202501239

5.4 Application Potential and Future Directions

5.4.1 Broadening the Detection Spectrum of Photodetectors Using Diverse 2D Absorbing Layers

Flexible photodetectors based on 2D materials have demonstrated remarkable optical tunability, mechanical flexibility, and compatibility with transparent substrates. Devices composed of mono-layer graphene combined with a single transition metal dichalcogenide absorber exhibit high responsivity and excellent long-term environmental stability. However, the detection bandwidth of such devices remains fundamentally limited by the fixed bandgap of the individual TMD layer. To realize 2D material-based photodetectors with broader spectral response and enhanced carrier extraction efficiency, the incorporation of additional light-absorbing layers with complementary optical properties presents a promising strategy.

One promising design concept involves vertically stacking two TMD layers with distinct bandgaps on either side of a central graphene layer. For example, forming a MoS_2/graphene/WSe_2 heterostructure. In this configuration, MoS_2 and WSe_2 serve as complementary light-absorbing materials, enabling broadband photon absorption spanning from the visible to the near-infrared region. The graphene interlayer, characterized by its high carrier mobility and zero bandgap, functions as an efficient charge transport channel, facilitating the extraction of photo-generated carriers from both TMD layers. Furthermore, the inherent asymmetry in the band alignment of MoS_2 and WSe_2 may give rise to a built-in vertical electric field across the heterostructure, which can enhance charge separation and suppress carrier recombination, thereby improving overall device performance.

doi:10.6342/NTU202501239

From a materials perspective, this stacked design is compatible with established 2D material synthesis and transfer techniques. Both MoS_2 and WSe_2 can be grown by CVD system and transferred with minimal interface contamination via PDMS stamping. In addition, previous experimental results show that graphene maintains excellent electrical conductivity and mechanical stability regardless of whether it is in the upper or lower layer. These characteristics suggest that the proposed MoS_2/graphene/WSe_2 heterostructure is not only conceptually feasible but also manufacturable using current 2D material processing methods.

Furthermore, the structure should maintain mechanical flexibility and be compatible with flexible substrates like PET. The performance under bending conditions is expected to be either maintained or even improved, owing to the symmetrical mechanical support provided by the dual absorber layers.

In summary, the proposed tri-layer heterostructure offers a promising direction for future research in 2D material-based photodetectors. By combining spectral broadening with potentially enhanced carrier dynamics and mechanical resilience, this design addresses key limitations of current single-absorber devices. While further experimental validation and theoretical modeling are necessary to explore interfacial effects, charge transfer mechanisms, and overall device performance, the concept presents a strong foundation for advancing flexible optoelectronic applications.

doi:10.6342/NTU202501239

Chapter 6 Conclusion

In this study, 2D materials were integrated into various optical applications. In Chapter 3, it was demonstrated that ultrathin Au films deposited on mono-layer MoS_2 can serve as high-conductivity transparent electrodes, enabled by a unique van der Waals epitaxial growth mechanism. These transparent electrodes were further applied in perovskite solar cells, where an 8 nm Au layer was deposited on transferred mono-layer MoS_2, replacing the conventional thick Ag electrode. This approach achieved a high bifaciality of 89.6% in the resulting bifacial perovskite solar cells, indicating the practicality of 2D-material-assisted transparent metal electrodes. This is attributed to the solution-free transfer process of mono-layer MoS_2, room-temperature metal deposition, and the excellent optical transmittance of thin Au films. The EQE and EIS measurements confirmed that the MoS_2/Au interface did not introduce significant optical losses or series resistance that would otherwise deteriorate device performance. These results underscore the potential of 2D material based transparent electrodes in advancing photovoltaic technologies.

In Chapter 4, multi-layer MoS_2 films were synthesized via sulfurization of amorphous MoS_2 at 850 °C, forming wafer-scale, uniform MoS_2 films up to 30 layers. These films were utilized in both vertical photovoltaic and lateral photoconductive devices to further investigate carrier transition behaviors in different orientations. In vertical architectures, a simple Au/MoS_2/Al sandwiched structure enabled the observation of photovoltaic response due to the work function difference between the top (Au) and bottom (Al) electrodes. The introduction of MoO_3 as a carrier transport layer or the formation of WS_2-based heterostructures further enhanced the photovoltaic performance.

doi:10.6342/NTU202501239

In lateral devices, a separation strategy using MoS_2 as the light absorption layer and graphene as the carrier transport layer resulted in a MoS_2/graphene photodetector with high responsivity. Ballistic transport photocurrent was observed due to the high carrier mobility of the graphene layer. However, due to the limited number of electrons in a single layer of MoS_2, extraction of photo-excited electrons causes holes to accumulate in the absorbing layer, resulting in slower reaction times. By employing multi-layer MoS_2 with greater electron storage capacity, this issue was mitigated. A device with 10-layer MoS_2 achieved a significantly reduced response time (< 10 ms) while maintaining a high responsivity of 576.0 A/W.

Lastly, the performance of lateral heterojunction photodetectors was further optimized using graphene as a transport layer and different transition metal dichalcogenides (TMDs: WS_2, MoS_2, and WSe_2) as light absorption layers, enabling wavelength-selective photodetection on sapphire substrates. Due to the short carrier transport time in graphene, hole accumulation in the TMD layer modulated the graphene's conductivity, resulting in high responsivities of 1521.9 A/W (WS_2 at 630 nm), 6077.9 A/W (MoS_2 at 660 nm), and 3977.8 A/W (WSe_2 at 750 nm). These devices also demonstrated high detectivities of 6.9, 17.6, and 9.2×10^{10} Jones, respectively. Following a similar film transfer and fabrication process, mono-layer graphene/TMD photodetectors were successfully fabricated on flexible PET substrates. High responsivities in the range of 10^2-10^3 A/W were still observed. Although the graphene/MoS_2 device showed relatively larger responsivity degradation, the comparable performance retained by graphene/WS_2 and graphene/WSe_2 devices suggested that the ultrathin nature of 2D materials is advantageous for flexible device integration. The bandgap tunability of 2D semiconductors also enables customizable spectral selectivity, indicating their promising

doi:10.6342/NTU202501239

applications not only in conventional electronics but also in low-light photodetection scenarios.

In conclusion, this work comprehensively demonstrates the multi-functionality of 2D materials in next-generation optoelectronic platforms, spanning transparent electrodes, efficient photovoltaic junctions, and wavelength-selective flexible photodetectors. The scalable synthesis, mechanical adaptability, and electronic versatility of these materials collectively reveal their significance in driving forward both rigid and flexible photonic technologies.

doi:10.6342/NTU202501239

Reference

[1] Wallace, Philip Richard. "The band theory of graphite." *Physical review* 71.9 (1947): 622.

[2] Novoselov, Kostya S., et al. "Electric field effect in atomically thin carbon films." *Science* 306.5696 (2004): 666-669.

[3] Novoselov, Kostya S., et al. "Two-dimensional atomic crystals." *Proceedings of the National Academy of Sciences* 102.30 (2005): 10451-10453.

[4] Nakano, Hideyuki, et al. "Soft synthesis of single-crystal silicon mono-layer sheets." *Angewandte Chemie International Edition* 45.38 (2006): 6303-6306.

[5] Pacile, Daniela, et al. "The two-dimensional phase of boron nitride: Few-atomic-layer sheets and suspended membranes." *Applied Physics Letters* 92.13 (2008).

[6] Terrones, Mauricio, et al. "Pure and doped boron nitride nanotubes." *Materials today* 10.5 (2007): 30-38.

[7] Bourlinos, Athanasios B., et al. "Liquid-phase exfoliation of graphite towards solubilized graphenes." *Small* 5.16 (2009): 1841-1845.

[8] Coleman, Jonathan N., et al. "Two-dimensional nanosheets produced by liquid exfoliation of layered materials." *Science* 331.6017 (2011): 568-571.

[9] Cunningham, Graeme, et al. "Solvent exfoliation of transition metal dichalcogenides: dispersibility of exfoliated nanosheets varies only weakly between compounds." *ACS nano* 6.4 (2012): 3468-3480.

[10] Zeng, Zhiyuan, et al. "Single-layer semiconducting nanosheets: high-yield preparation and device fabrication." *Angewandte Chemie-International Edition* 50.47 (2011): 11093-11097.

doi:10.6342/NTU202501239

[11] Zhao, Weijie, et al. "Evolution of electronic structure in atomically thin sheets of WS_2 and WSe_2." *ACS nano* 7.1 (2013): 791-797.

[12] Fang, Hui, et al. "High-performance single layered WSe_2 p-FETs with chemically doped contacts." *Nano letters* 12.7 (2012): 3788-3792.

[13] Bianco, Elisabeth, et al. "Stability and exfoliation of germanane: a germanium graphane analogue." *ACS nano* 7.5 (2013): 4414-4421.

[14] Mashtalir, Olha, et al. "Intercalation and delamination of layered carbides and carbonitrides." *Nature communications* 4.1 (2013): 1716.

[15] Liu, Han, et al. "Phosphorene: an unexplored 2D semiconductor with a high hole mobility." *ACS nano* 8.4 (2014): 4033-4041.

[16] Li, Likai, et al. "Black phosphorus field-effect transistors." *Nature nanotechnology* 9.5 (2014): 372-377.

[17] Jiang, Y. C., et al. "Raman fingerprint for semi-metal WTe_2 evolving from bulk to mono-layer." *Scientific reports* 6.1 (2016): 19624.

[18] Ares, Pablo, et al. "Mechanical isolation of highly stable antimonene under ambient conditions." *arXiv preprint arXiv:1608.06859* (2016).

[19] Mañas-Valero, Samuel, et al. "Raman spectra of ZrS_2 and $ZrSe_2$ from bulk to atomically thin layers." *Applied Sciences* 6.9 (2016): 264.

[20] Huang, Bevin, et al. "Layer-dependent ferromagnetism in a van der Waals crystal down to the mono-layer limit." *Nature* 546.7657 (2017): 270-273.

[21] Ranjan, Pranay, et al. "Freestanding borophene and its hybrids." *Advanced Materials* 31.27 (2019): 1900353.

[22] Huang, Yuan, et al. "Universal mechanical exfoliation of large-area 2D crystals." *Nature communications* 11.1 (2020): 2453.

doi:10.6342/NTU202501239

[23] Su, Sheng-Kai, et al. "Layered semiconducting 2D materials for future transistor applications." *Small Structures* 2.5 (2021): 2000103.

[24] Liu, Yuan, et al. "Promises and prospects of two-dimensional transistors." *Nature* 591.7848 (2021): 43-53.

[25] Iannaccone, Giuseppe, et al. "Quantum engineering of transistors based on 2D materials heterostructures." *Nature nanotechnology*13.3 (2018): 183-191.

[26] Long, Mingsheng, et al. "Progress, challenges, and opportunities for 2D material based photodetectors." *Advanced Functional Materials* 29.19 (2019): 1803807.

[27] Dong, Tao, et al."Flexible photodetector based on 2D materials: processing, architectures, and applications."*Advanced Materials Interfaces* 7.4 (2020): 1901657.

[28] Qiu, Qinxi, et al. "Photodetectors of 2D materials from ultraviolet to terahertz waves." *Advanced Materials* 33.15 (2021): 2008126.

[29] Withers, Freddie, et al. "Light-emitting diodes by band-structure engineering in van der Waals heterostructures." *Nature materials* 14.3 (2015): 301-306.

[30] Ricciardulli, Antonio Gaetano, et al. "Solution-processable 2D materials applied in light-emitting diodes and solar cells." *Advanced Materials Technologies* 5.8 (2020): 1900972.

[31] Sheng, Yuewen, et al. "High-performance WS_2 mono-layer light-emitting tunneling devices using 2D materials grown by chemical vapor deposition." *ACS nano* 13.4 (2019): 4530-4537.

[32] Britnell, Liam, et al. "Strong light-matter interactions in heterostructures of atomically thin films." *Science* 340.6138 (2013): 1311-1314.

[33] Palummo, Maurizia, Marco Bernardi, and Jeffrey C. Grossman. "Exciton radiative lifetimes in two-dimensional transition metal dichalcogenides." *Nano letters* 15.5 (2015): 2794-2800.

doi:10.6342/NTU202501239

[34] Li, Qiang, et al. "Engineering optical absorption in graphene and other 2D materials: advances and applications." *Advanced Optical Materials* 7.20 (2019): 1900595.

[35] Gupta, Sunny, et al. "In pursuit of 2D materials for maximum optical response." *ACS nano* 12.11 (2018): 10880-10889.

[36] Conley, Hiram J., et al. "Bandgap engineering of strained mono-layer and bilayer MoS_2." *Nano letters* 13.8 (2013): 3626-3630.

[37] Li, Xinming, et al. "Graphene-on-silicon Schottky junction solar cells." *Advanced Materials (Weinheim)* 22 (2010).

[38] He, Yu-Ming, et al. "Single quantum emitters in mono-layer semiconductors." *Nature nanotechnology* 10.6 (2015): 497-502.

[39] Goossens, Stijn, et al. "Broadband image sensor array based on graphene–CMOS integration." *Nature Photonics* 11.6 (2017): 366-371.

[40] Mennel, Lukas, et al. "Ultrafast machine vision with 2D material neural network image sensors." *Nature* 579.7797 (2020): 62-66.

[41] Shin, Jiho, et al. "Vertical full-colour micro-LEDs via 2D materials-based layer transfer." *Nature* 614.7946 (2023): 81-87.

[42] Wang, Chong, et al. "The optical properties and plasmonics of anisotropic 2D materials." *Advanced Optical Materials* 8.5 (2020): 1900996.

[43] Arezoomandan, Sara, et al. "Tunable terahertz metamaterials employing layered 2-D materials beyond graphene." *IEEE Journal of Selected Topics in Quantum Electronics* 23.1 (2016): 188-194.

[44] Sun, Zhipei, Amos Martinez, and Feng Wang. "Optical modulators with 2D layered materials." *Nature Photonics* 10.4 (2016): 227-238.

[45] Zhou, Linlin, et al. "Nonlinear optical characterization of 2D materials." *Nanomaterials* 10.11 (2020): 2263.

doi:10.6342/NTU202501239

[46] Mounet, Nicolas, et al. "Two-dimensional materials from high-throughput computational exfoliation of experimentally known compounds." *Nature nanotechnology* 13.3 (2018): 246-252.

[47] Kang, Jiahao, et al. "Graphene and beyond-graphene 2D crystals for next-generation green electronics." *Micro-and Nanotechnology Sensors, Systems, and Applications VI*. Vol. 9083. SPIE, 2014.

[48] Wang, Hong, et al. "High-quality mono-layer superconductor $NbSe_2$ grown by chemical vapour deposition." *Nature communications* 8.1 (2017): 394.

[49] Li, Lu, et al. "Coexistence of magnetic order and two-dimensional superconductivity at $LaAlO_3/SrTiO_3$ interfaces." *Nature physics* 7.10 (2011): 762-766.

[50] Island, Joshua O., et al. "Titanium trisulfide (TiS_3): a 2D semiconductor with quasi-1D optical and electronic properties." *Scientific reports* 6.1 (2016): 22214.

[51] Sipos, Balazs, et al. "From Mott state to superconductivity in 1T-TaS_2." *Nature materials* 7.12 (2008): 960-965.

[52] Kim, Kinam, et al. "A role for graphene in silicon-based semiconductor devices." *Nature* 479.7373 (2011): 338-344.

[53] Martin, Jens, et al. "Observation of electron–hole puddles in graphene using a scanning single-electron transistor." *Nature physics* 4.2 (2008): 144-148.

[54] Zhu, Yu, et al. "Rational design of hybrid graphene films for high-performance transparent electrodes." *ACS nano* 5.8 (2011): 6472-6479.

[55] Liu, Chang-Hua, et al. "Graphene photodetectors with ultra-broadband and high responsivity at room temperature." *Nature nanotechnology* 9.4 (2014): 273-278.

[56] Wang, Ze-gao, et al. "Flexible graphene-based electroluminescent devices." *ACS nano* 5.9 (2011): 7149-7154.

doi:10.6342/NTU202501239

[57] Si, Chen, Jian Zhou, and Zhimei Sun. "Half-metallic ferromagnetism and surface functionalization-induced metal–insulator transition in graphene-like two-dimensional Cr_2C crystals." *ACS applied materials & interfaces* 7.31 (2015): 17510-17515.

[58] Žutić, Igor, Jaroslav Fabian, and S. Das Sarma. "Spintronics: Fundamentals and applications." *Reviews of modern physics* 76.2 (2004): 323.

[59] Ashton, Michael, et al. "Two-dimensional intrinsic half-metals with large spin gaps." *Nano Letters* 17.9 (2017): 5251-5257.

[60] Lemme, Max C., et al. "2D materials for future heterogeneous electronics." *Nature communications* 13.1 (2022): 1392.

[61] Hong, Seokmo, et al. "Ultralow-dielectric-constant amorphous boron nitride." *Nature* 582.7813 (2020): 511-514.

[62] Petrone, Nicholas, et al. "Flexible 2D FETs using hBN dielectrics." *2015 IEEE International Electron Devices Meeting (IEDM)*. IEEE, 2015.

[63] Zhuang, Pingping, et al. "Nonpolar resistive switching of multi-layer-hBN-based memories." *Advanced Electronic Materials* 6.1 (2020): 1900979.

[64] Im, HoHyun, et al. "Capacitance–voltage characteristics of Pt/hBN/WSe_2 metal–insulator–semiconductor capacitor doped by charge-transfer process." *Applied Physics Letters* 120.2 (2022).

[65] Midtvedt, Daniel, Caio H. Lewenkopf, and Alexander Croy. "Strain–displacement relations for strain engineering in single-layer 2d materials." *2D Materials* 3.1 (2016): 011005.

[66] Yang, Gao, et al. "Structure of graphene and its disorders: a review." *Science and technology of advanced materials* 19.1 (2018): 613-648.

doi:10.6342/NTU202501239

[67] Ekuma, C. E., V. Dobrosavljević, and D. Gunlycke. "First-principles-based method for electron localization: application to mono-layer hexagonal boron nitride." *Physical Review Letters* 118.10 (2017): 106404.

[68] Mortezaei Nobahari, Mohammad. "Electro-optical properties of strained mono-layer boron phosphide." *Scientific Reports* 13.1 (2023): 9849.

[69] Qin, Rui, et al. "Uniaxial strain-induced mechanical and electronic property modulation of silicene." *Nanoscale research letters* 9 (2014): 1-7.

[70] Ren, Ceng-Ceng, et al. "Tunable electronic and topological properties of germanene by functional group modification." *Nanomaterials* 8.3 (2018): 145.

[71] Lu, Pengfei, et al. "Quasiparticle and optical properties of strained stanene and stanane." *Scientific reports* 7.1 (2017): 3912.

[72] Dien, Vo Khuong, et al. "Electronic and optical properties of graphene, silicene, germanene, and their semi-hydrogenated systems." *RSC advances* 12.54 (2022): 34851-34865.

[73] Li, ShaoRong, et al. "First-principle study on the photoelectric properties of mono-layer h-BN under different strain types." *Journal of Molecular Modeling* 30.2 (2024): 56.

[74] Vu, Tuan V., et al. "Structural, elastic, and electronic properties of chemically functionalized boron phosphide mono-layer." *RSC advances* 11.15 (2021): 8552-8558.

[75] Xu, Yong, et al. "Large-gap quantum spin Hall insulators in tin films." *Physical review letters* 111.13 (2013): 136804.

[76] Gablech, Imrich, et al. "Monoelemental 2D materials-based field effect transistors for sensing and biosensing: phosphorene, antimonene, arsenene, silicene, and

doi:10.6342/NTU202501239

germanene go beyond graphene." *TrAC Trends in Analytical Chemistry* 105 (2018): 251-262.

[77] Miró, Pere, Martha Audiffred, and Thomas Heine. "An atlas of two-dimensional materials." *Chemical Society Reviews* 43.18 (2014): 6537-6554.

[78] D'Olimpio, Gianluca, et al. "Enhanced electrocatalytic activity in GaSe and InSe nanosheets: the role of surface oxides." *Advanced Functional Materials* 30.43 (2020): 2005466.

[79] Sarkar, Abdus Salam, et al. "Liquid exfoliation of electronic grade ultrathin tin (II) sulfide (SnS) with intriguing optical response." *npj 2D Materials and Applications* 4.1 (2020): 1.

[80] Gao, Anyuan, et al. "Observation of ballistic avalanche phenomena in nanoscale vertical InSe/BP heterostructures." *Nature nanotechnology* 14.3 (2019): 217-222.

[81] Hu, Yi, et al. "2D arsenene and arsenic materials: Fundamental properties, preparation, and applications." *Small* 18.9 (2022): 2104556.

[82] Geim, Andre K., and Irina V. Grigorieva. "Van der Waals heterostructures." *Nature* 499.7459 (2013): 419-425.

[83] Chaves, A., et al. "Bandgap engineering of two-dimensional semiconductor materials." *npj 2D Materials and Applications* 4.1 (2020): 29.

[84] Novoselov, K. S, et al. "2D materials and van der Waals heterostructures." *Science* 353.6298 (2016): aac9439.

[85] Liang, Shi-Jun, et al. "Van der Waals heterostructures for high-performance device applications: challenges and opportunities." *Advanced Materials* 32.27 (2020): 1903800.

[86] Frisenda, Riccardo, et al. "Atomically thin p–n junctions based on two-dimensional materials." *Chemical Society Reviews* 47.9 (2018): 3339-3358.

doi:10.6342/NTU202501239

[87] Huang, Xiaohe, et al. "2D semiconductors for specific electronic applications: from device to system." *npj 2D Materials and Applications* 6.1 (2022): 51.

[88] Duong, Dinh Loc, et al. "van der Waals layered materials: opportunities and challenges." *ACS nano* 11.12 (2017): 11803-11830.

[89] Tsai, Po-Cheng, et al. "Persistent charge storage and memory operation of top-gate transistors solely based on two-dimensional molybdenum disulfide." *Nanotechnology* 34.30 (2023): 305701.

[90] Chang, Che-Jia, et al. "Molybdenum Disulfide Transistors Bearing All-2D-Material Interfaces: Device Performance Optimization and Influences of Interfaces and Passivation Layers." *ACS Applied Electronic Materials* 5.11 (2023): 6384-6391.

[91] Kwon, Junyoung, et al. "Thickness-dependent Schottky barrier height of MoS_2 field-effect transistors." *Nanoscale* 9.18 (2017): 6151-6157.

[92] Zou, Taoyu, et al. "Two-dimensional tunneling memtransistor with thin-film heterostructure for low-power logic-in-memory complementary metal-oxide semiconductor." *ACS nano* 18.21 (2024): 13849-13857.

[93] Castellanos-Gomez, Andres, et al. "Spatially resolved optical absorption spectroscopy of single-and few-layer MoS_2 by hyperspectral imaging." *Nanotechnology* 27.11 (2016): 115705.

[94] Liu, Kai, et al. "Elastic properties of chemical-vapor-deposited mono-layer MoS_2, WS_2, and their bilayer heterostructures." *Nano letters* 14.9 (2014): 5097-5103.

[95] Shin, Gwang Hyuk, et al. "Ultrasensitive phototransistor based on WSe_2–MoS_2 van der Waals heterojunction." *Nano letters* 20.8 (2020): 5741-5748.

[96] Dhanabalan, Sathish Chander, et al. "Present perspectives of broadband photodetectors based on nanobelts, nanoribbons, nanosheets and the emerging 2D materials." *Nanoscale* 8.12 (2016): 6410-6434.

doi:10.6342/NTU202501239

[97] Velusamy, Dhinesh Babu, et al. "Flexible transition metal dichalcogenide nanosheets for band-selective photodetection." *Nature communications* 6.1 (2015): 8063.

[98] Bhuyan, Md Sajibul Alam, et al. "Synthesis of graphene." *International Nano Letters* 6.2 (2016): 65-83.

[99] Zaretski, Aliaksandr V., et al. "Metal-assisted exfoliation (MAE): green, roll-to-roll compatible method for transferring graphene to flexible substrates." *Nanotechnology* 26.4 (2015): 045301.

[100] Tao, Junguang, et al. "Growth of wafer-scale MoS_2 mono-layer by magnetron sputtering." *Nanoscale* 7.6 (2015): 2497-2503.

[101] Orofeo, Carlo M., et al. "Scalable synthesis of layer-controlled WS_2 and MoS_2 sheets by sulfurization of thin metal films." *Applied Physics Letters* 105.8 (2014).

[102] Johansson, Fredrik OL, et al. "Minimizing sputter-induced damage during deposition of WS_2 onto graphene." *Applied Physics Letters* 110.9 (2017).

[103] Yang, Pengfei, et al. "Batch production of 6-inch uniform mono-layer molybdenum disulfide catalyzed by sodium in glass." *Nature communications* 9.1 (2018): 979.

[104] Cai, Zhengyang, et al. "Chemical vapor deposition growth and applications of two-dimensional materials and their heterostructures." *Chemical reviews* 118.13 (2018): 6091-6133.

[105] Li, Na, et al. "Atomic layer deposition of Al_2O_3 directly on 2D materials for high-performance electronics." *Advanced Materials Interfaces* 6.10 (2019): 1802055.

[106] Mattinen, Miika, Markku Leskelä, and Mikko Ritala. "Atomic layer deposition of 2D metal dichalcogenides for electronics, catalysis, energy storage, and beyond." *Advanced Materials Interfaces* 8.6 (2021): 2001677.

doi:10.6342/NTU202501239

[107] Kim, Hyun Gu, and Han-Bo-Ram Lee. "Atomic layer deposition on 2D materials." *Chemistry of Materials* 29.9 (2017): 3809-3826.

[108] Fu, Deyi, et al. "Molecular beam epitaxy of highly crystalline mono-layer molybdenum disulfide on hexagonal boron nitride." *Journal of the American Chemical Society* 139.27 (2017): 9392-9400.

[109] Cao, Wei, et al. "2-D layered materials for next-generation electronics: Opportunities and challenges." *IEEE Transactions on Electron Devices* 65.10 (2018): 4109-4121.

[110] Curry, John F., et al. "Impact of microstructure on MoS_2 oxidation and friction." *ACS applied materials & interfaces* 9.33 (2017): 28019-28026.

[111] Yasaei, Poya, et al. "Stable and selective humidity sensing using stacked black phosphorus flakes." *ACS nano* 9.10 (2015): 9898-9905.

[112] Li, Qiang, et al. "Recent advances in oxidation and degradation mechanisms of ultrathin 2D materials under ambient conditions and their passivation strategies." *Journal of Materials Chemistry A* 7.9 (2019): 4291-4312.

[113] Wang, Guorui, et al. "Recent advances in the mechanics of 2D materials." *International Journal of Extreme Manufacturing* 5.3 (2023): 032002.

[114] Cui, Teng, et al. "Fatigue of graphene." *Nature materials* 19.4 (2020): 405-411.

[115] Liu, Ping, Qing-Xiang Pei, and Yong-Wei Zhang. "Low-cycle fatigue failure of MoS_2 mono-layer." *Extreme Mechanics Letters* 58 (2023): 101942.

[116] Wang, Xuewen, Yinghui Sun, and Kai Liu. "Chemical and structural stability of 2D layered materials." *2D Materials* 6.4 (2019): 042001.

[117] Nan, Hai Yan, et al. "The thermal stability of graphene in air investigated by Raman spectroscopy." *Journal of Raman Spectroscopy* 44.7 (2013): 1018-1021.

doi:10.6342/NTU202501239

[118] Wang, Xuewen, et al. "Substrate modified thermal stability of mono-and few-layer MoS_2." *Nanoscale* 10.7 (2018): 3540-3546.

[119] Wu, Sanfeng, et al. "Mono-layer semiconductor nanocavity lasers with ultralow thresholds." *Nature* 520.7545 (2015): 69-72.

[120] Yao, Baicheng, et al. "Gate-tunable frequency combs in graphene–nitride microresonators." *Nature* 558.7710 (2018): 410-414.

[121] Lee, Seung Hoon, et al. "Switching terahertz waves with gate-controlled active graphene metamaterials." *Nature materials* 11.11 (2012): 936-941.

[122] Vicarelli, L., et al. "Graphene field-effect transistors as room-temperature terahertz detectors." *Nature materials* 11.10 (2012): 865-871.

[123] Noori, Yasir J., et al. "Photonic crystals for enhanced light extraction from 2D materials." *ACS Photonics* 3.12 (2016): 2515-2520.

[124] Gonzalez Marin, Juan Francisco, et al. "MoS2 photodetectors integrated with photonic circuits." *npj 2D Materials and Applications* 3.1 (2019): 14.

[125] Watson, Adam J., et al. "Transfer of large scale two-dimensional semiconductors: challenges and developments." *2D Materials* 8.3 (2021): 032001.

[126] Shen, Pin-Chun, et al. "Ultralow contact resistance between semimetal and mono-layer semiconductors." *Nature* 593.7858 (2021): 211-217.

[127] Chen, Kuan-Chao, et al. "Multi-layer elemental 2D materials: antimonene, germanene and stanene grown directly on molybdenum disulfides." *Semiconductor Science and Technology* 34.10 (2019): 105020.

[128] Chang, Che-Jia, et al. "High-performance transistors with polycrystalline 2D material channels: The influence of gold electrode crystallinity and the layer number of molybdenum disulfide channels." *Applied Surface Science* 693 (2025): 162795.

doi:10.6342/NTU202501239

[129] Yuan, Jintao, et al. "Mono-layer WS_2 nanosheets passivated with HfO2 for enhanced photodetectors." *ACS Applied Nano Materials* 6.6 (2023): 4594-4601.

[130] Cho, Ah-Jin, and Jang-Yeon Kwon. "Hexagonal boron nitride for surface passivation of two-dimensional van der Waals heterojunction solar cells." *ACS Applied Materials & Interfaces* 11.43 (2019): 39765-39771.

[131] Mercado, Elisha, et al. "Passivation of layered gallium telluride by double encapsulation with graphene." *ACS omega* 4.19 (2019): 18002-18010.

[132] Rowell, Michael W., and Michael D. McGehee. "Transparent electrode requirements for thin film solar cell modules." *Energy & Environmental Science* 4.1 (2011): 131-134.

[133] Park, Helen Hejin. "Transparent electrode techniques for semitransparent and tandem perovskite solar cells." *Electronic Materials Letters* 17 (2021): 18-32.

[134] Ali, Ahmad Hadi, Zainuriah Hassan, and Ahmad Shuhaimi. "Enhancement of optical transmittance and electrical resistivity of post-annealed ITO thin films RF sputtered on Si." *Applied Surface Science* 443 (2018): 544-547.

[135] Meng, Li-jian, and M. P. Dos Santos. "Properties of indium tin oxide films prepared by rf reactive magnetron sputtering at different substrate temperature." *Thin solid films* 322.1-2 (1998): 56-62.

[136] Kamioka, T., et al. "Analysis of interface workfunction and process-induced damage of reactive-plasma-deposited ITO/SiO_2/Si stack." *AIP Advances* 7.9 (2017).

[137] Yu, Shihui, et al. "Preparation and investigation of nano-thick FTO/Ag/FTO multi-layer transparent electrodes with high figure of merit." *Scientific reports* 6.1 (2016): 20399.

[138] Theuring, Martin, et al. "AZO-Ag-AZO transparent electrode for amorphous

doi:10.6342/NTU202501239

silicon solar cells." *Thin solid films* 558 (2014): 294-297.

[139] Li, Xinming, et al. "Anomalous behaviors of graphene transparent conductors in graphene–silicon heterojunction solar cells." *Advanced Energy Materials* 3.8 (2013): 1029-1034.

[140] Hecht, David S., Liangbing Hu, and Glen Irvin. "Emerging transparent electrodes based on thin films of carbon nanotubes, graphene, and metallic nanostructures." *Advanced materials* 23.13 (2011): 1482-1513.

[141] Lu, Xi, Yaokang Zhang, and Zijian Zheng. "Metal-based flexible transparent electrodes: challenges and recent advances." *Advanced Electronic Materials* 7.5 (2021): 2001121.

[142] Zhang, Yaokang, et al. "Solution-processed transparent electrodes for emerging thin-film solar cells." *Chemical reviews* 120.4 (2020): 2049-2122.

[143] Chen, Yang, et al. "“Reinforced concrete”-like flexible transparent electrode for organic solar cells with high efficiency and mechanical robustness." *Science China Chemistry* 65.6 (2022): 1164-1172.

[144] Nair, Rahul Raveendran, et al. "Fine structure constant defines visual transparency of graphene." *Science* 320.5881 (2008): 1308-1308.

[145] Koh, Wee Shing, et al. "The potential of graphene as an ITO replacement in organic solar cells: An optical perspective." *IEEE Journal of Selected topics in quantum electronics* 20.1 (2013): 36-42.

[146] Suk, Ji Won, et al. "Transfer of CVD-grown mono-layer graphene onto arbitrary substrates." *ACS nano* 5.9 (2011): 6916-6924.

doi:10.6342/NTU202501239

[147] Chen, Hsuan-An, et al. "Type-II superlattice infrared photodetectors with graphene transparent electrodes." *IEEE Photonics Technology Letters* 29.19 (2017): 1691-1694.

[148] You, Peng, et al. "Efficient semitransparent perovskite solar cells with graphene electrodes." *Advanced Materials* 27.24 (2015): 3632-3638.

[149] Bae, Sukang, et al. "Roll-to-roll production of 30-inch graphene films for transparent electrodes." *Nature nanotechnology* 5.8 (2010): 574-578.

[150] Lim, Yi Rang, et al. "Roll-to-Roll production of layer-controlled molybdenum disulfide: a platform for 2D semiconductor-based industrial applications." *Advanced Materials* 30.5 (2018): 1705270.

[151] Wang, Rui, et al. "Prospects for metal halide perovskite-based tandem solar cells." *Nature Photonics* 15.6 (2021): 411-425.

[152] Okil, M., et al. "From crystalline to low-cost silicon-based solar cells: A review." *Silicon* 14.5 (2022): 1895-1911.

[153] Ferekides, C. S., et al. "CdTe thin film solar cells: device and technology issues." *Solar energy* 77.6 (2004): 823-830.

[154] Mufti, Nandang, et al. "Review of CIGS-based solar cells manufacturing by structural engineering." *Solar energy* 207 (2020): 1146-1157.

[155] Hanmandlu, Chintam, et al. "3D nanographene precursor suppress interfacial recombination in PEDOT: PSS based perovskite solar cells." *Nano Energy* 107 (2023): 108136.

doi:10.6342/NTU202501239

[156] Muñoz-García, Ana Belén, et al. "Dye-sensitized solar cells strike back." *Chemical Society Reviews* 50.22 (2021): 12450-12550.

[157] Jošt, Marko, et al. "Monolithic perovskite tandem solar cells: a review of the present status and advanced characterization methods toward 30% efficiency." *Advanced Energy Materials* 10.26 (2020): 1904102.

[158] Das, Sonali, et al. "The role of graphene and other 2D materials in solar photovoltaics." *Advanced Materials* 31.1 (2019): 1802722.

[159] Al-Ashouri, Amran, et al. "Monolithic perovskite/silicon tandem solar cell with> 29% efficiency by enhanced hole extraction." *Science* 370.6522 (2020): 1300-1309.

[160] Maragliano, Carlo, Ahmed Zayan, and Marco Stefancich. "Three-dimensional point-focus spectral splitting solar concentrator system." *International Journal of Optics and Applications* 4.4A (2014): 6-11.

[161] Dimroth, Frank, et al. "Four-junction wafer-bonded concentrator solar cells." *IEEE Journal of Photovoltaics* 6.1 (2015): 343-349.

[162] Green, M. A. et al., Solar Cell Efficiency Tables (version 62). National Renewable Energy Laboratory (NREL), Golden, CO (United States), (2023).

[163] Bellini, Emiliano. "KAUST claims 33.7% efficiency for perovskite/silicon tandem solar cell." *Zugriff am* (2023): 06-16.

[164] Went, Cora M., et al. "A new metal transfer process for van der Waals contacts to vertical Schottky-junction transition metal dichalcogenide photovoltaics." *Science*

doi:10.6342/NTU202501239

Advances 5.12 (2019): eaax6061.

[165] Bernardi, Marco, Maurizia Palummo, and Jeffrey C. Grossman. "Extraordinary sunlight absorption and one nanometer thick photovoltaics using two-dimensional mono-layer materials." *Nano letters* 13.8 (2013): 3664-3670.

[166] Tsai, Meng-Lin, et al. "Mono-layer MoS_2 heterojunction solar cells." *ACS nano* 8.8 (2014): 8317-8322.

[167] Huo, Nengjie, et al. "Novel and enhanced optoelectronic performances of multi-layer MoS_2–WS_2 heterostructure transistors." *Advanced Functional Materials* 24.44 (2014): 7025-7031.

[168] Deng, Yexin, et al. "Black phosphorus–mono-layer MoS_2 van der Waals heterojunction p–n diode." *ACS nano* 8.8 (2014): 8292-8299.

[169] Flöry, Nikolaus, et al. "A WSe_2/$MoSe_2$ heterostructure photovoltaic device." *Applied Physics Letters* 107.12 (2015).

[170] Wang, Feng, et al. "Tunable GaTe-MoS_2 van der Waals p–n junctions with novel optoelectronic performance." *Nano letters* 15.11 (2015): 7558-7566.

[171] Pezeshki, Atiye, et al. "Electric and photovoltaic behavior of a few-layer α-$MoTe_2$/MoS_2 dichalcogenide heterojunction." *Advanced Materials* 28.16 (2016): 3216-3222.

[172] Song, Yi, et al. "Role of interfacial oxide in high-efficiency graphene–silicon Schottky barrier solar cells." *Nano letters* 15.3 (2015): 2104-2110.

[173] Dai, Ruina, et al. "Metal–organic-compound-modified MoS_2 with enhanced solubility for high-performance perovskite solar cells." *ChemSusChem* 10.14 (2017):

doi:10.6342/NTU202501239

2869-2874.

[174] Pospischil, Andreas, et al. "CMOS-compatible graphene photodetector covering all optical communication bands." *Nature Photonics* 7.11 (2013): 892-896.

[175] Du, Pengfei, et al. "Single-photon detection approach for autonomous vehicles sensing." *IEEE Transactions on Vehicular Technology* 69.6 (2020): 6067-6078.

[176] Polat, Emre O., et al. "Flexible graphene photodetectors for wearable fitness monitoring." *Science advances* 5.9 (2019): eaaw7846.

[177] Saleem, Muhammad Imran, Aung Ko Ko Kyaw, and Jaehyun Hur. "Infrared Photodetectors: Recent Advances and Challenges Toward Innovation for Image Sensing Applications." *Advanced Optical Materials* 12.33 (2024): 2401625.

[178] Liu, Chaoyue, et al. "Silicon/2D-material photodetectors: from near-infrared to mid-infrared." *Light: Science & Applications* 10.1 (2021): 123.

[179] Nayak, Pabitra K., et al. "Photovoltaic solar cell technologies: analysing the state of the art." *Nature Reviews Materials* 4.4 (2019): 269-285.

[180] Yang, Wei, et al. "Silicon-compatible photodetectors: trends to monolithically integrate photosensors with chip technology." *Advanced Functional Materials* 29.18 (2019): 1808182.

[181] Chow, Philip CY, and Takao Someya. "Organic photodetectors for next-generation wearable electronics." *Advanced Materials* 32.15 (2020): 1902045.

[182] Fang, Hehai, and Weida Hu. "Photogating in low dimensional photodetectors." *Advanced science* 4.12 (2017): 1700323.

[183] Lu, Xiaowei, et al. "Progress of photodetectors based on the photothermoelectric effect." *Advanced Materials* 31.50 (2019): 1902044.

doi:10.6342/NTU202501239

[184] Taha, Bakr Ahmed, et al. "Plasmonic-enabled nanostructures for designing the next generation of silicon photodetectors: trends, engineering and opportunities." *Surfaces and Interfaces* (2024): 104334.

[185] Chen, Guanyu, et al. "High-Speed Photodetectors on Silicon Photonics Platform for Optical Interconnect." *Laser & Photonics Reviews* 16.12 (2022): 2200117.

[186] Guo, Ruiqi, et al. "Advances in colloidal quantum dot-based photodetectors." *Journal of Materials Chemistry C* 10.19 (2022): 7404-7422.

[187] Zhou, Wenjia, et al. "Solution-processed upconversion photodetectors based on quantum dots." *Nature Electronics* 3.5 (2020): 251-258.

[188] Yang, Ming, Hongxi Zhou, and Jun Wang. "Topological insulators photodetectors: Preparation, advances and application challenges." *Materials Today Communications* 33 (2022): 104190.

[189] Wu, Kewen, et al. "Research progress on topological material-based photodetectors." *Materials Advances* 4.21 (2023): 5018-5032.

[190] Zhang, Jiaxin, et al. "Recent advances and prospects for GaN-based hybrid type ultraviolet photodetector." *Semiconductor Science and Technology* (2024).

[191] Ahmadi, Mahshid, Ting Wu, and Bin Hu. "A review on organic–inorganic halide perovskite photodetectors: device engineering and fundamental physics." *Advanced Materials* 29.41 (2017): 1605242.

[192] Choi, Soo Ho, et al. "Large-scale synthesis of graphene and other 2D materials

doi:10.6342/NTU202501239

towards industrialization." *Nature Communications* 13.1 (2022): 1484.

[193] Pham, Phuong V., et al. "2D heterostructures for ubiquitous electronics and optoelectronics: principles, opportunities, and challenges." *Chemical reviews* 122.6 (2022): 6514-6613.

[194] Lee, Wi Hyoung, et al. "Simultaneous transfer and doping of CVD-grown graphene by fluoropolymer for transparent conductive films on plastic." *ACS Nano* 6.2 (2012): 1284-1290.

[195] Kang, Sumin, et al. "Role of crack deflection on rate dependent mechanical transfer of multi-layer graphene and its application to transparent electrodes." *ACS Applied Nano Materials* 2.4 (2019): 1980-1985.

[196] Wang, Yu, et al. "Electrochemical delamination of CVD-grown graphene film: toward the recyclable use of copper catalyst." *ACS nano* 5.12 (2011): 9927-9933.

[197] Gorantla, Sandeep, et al. "A universal transfer route for graphene." *Nanoscale* 6.2 (2014): 889-896.

[198] Jung, Wonsuk, et al. "Ultraconformal contact transfer of mono-layer graphene on metal to various substrates." *Advanced Materials (Deerfield Beach, Fla.)* 26.37 (2014): 6394-6400.

[199] Chen, Kuan-Chao, et al. "The atomic layer etching of molybdenum disulfides using low-power oxygen plasma." *Semiconductor Science and Technology* 34.4 (2019): 045007.

[200] Raman, Chandrasekhara Venkata. "A new radiation." *Indian Journal of physics*

doi:10.6342/NTU202501239

2 (1928): 387-398.

[201] Oklopčić, Antonija, Christopher M. Hirata, and Kevin Heng. "Raman scattering by molecular hydrogen and nitrogen in exoplanetary atmospheres." *The Astrophysical Journal* 832.1 (2016): 30.

[202] Hwang, Dusun, et al. "Novel auto-correction method in a fiber-optic distributed-temperature sensor using reflected anti-Stokes Raman scattering." *Optics express* 18.10 (2010): 9747-9754.

[203] Ottaviano, L., et al. "Mechanical exfoliation and layer number identification of MoS_2 revisited." *2D Materials* 4.4 (2017): 045013.

[204] Li, Xiao-Li, et al. "Layer-number dependent optical properties of 2D materials and their application for thickness determination." *Advanced Functional Materials* 27.19 (2017): 1604468.

[205] Aoki, Takeshi. "Photoluminescence spectroscopy." *Characterization of Materials* (2002): 1-12.

[206] Binnig, Gerd, Calvin F. Quate, and Ch Gerber. "Atomic force microscope." *Physical review letters* 56.9 (1986): 930.

[207] Rana, Md Sohel, Hemanshu Roy Pota, and Ian R. Petersen. "Improvement in the imaging performance of atomic force microscopy: A survey." *IEEE Transactions on Automation Science and Engineering* 14.2 (2016): 1265-1285.

[208] Qian, Wen-yuan. "First Electron Microscope Is Constructed." (1931).

[209] Williams, David B., et al. *The transmission electron microscope*. Springer Us,

doi:10.6342/NTU202501239

2009.

[210] Weckhuysen, Bert M. "Ultraviolet-visible spectroscopy." (2004): 255-270.

[211] Schroder, Dieter K. *Semiconductor material and device characterization*. John Wiley & Sons, 2015.

[212] Valdes, Leopoldo B. "Resistivity measurements on germanium for transistors." *Proceedings of the IRE* 42.2 (2007): 420-427.

[213] Chelly, Avraham, et al. "Broad review of four-point probe correction factors: Enhanced analytical model using advanced numerical and experimental cross-examination." *Results in Physics* 48 (2023): 106445.

[214] Sennett, R. S., and G. D. Scott. "The structure of evaporated metal films and their optical properties." *Journal of the Optical Society of America* 40.4 (1950): 203-211.

[215] Fahland, M., P. Karlsson, and C. Charton. "Low resisitivity transparent electrodes for displays on polymer substrates." *Thin Solid Films* 392.2 (2001): 334-337.

[216] Yun, Jungheum. "Ultrathin metal films for transparent electrodes of flexible optoelectronic devices." *Advanced Functional Materials* 27.18 (2017): 1606641.

[217] Zhang, Cheng, et al. "Thin-metal-film-based transparent conductors: Material preparation, optical design, and device applications." *Advanced Optical Materials* 9.3 (2021): 2001298.

[218] Zhang, Yu-Wei, et al. "Highly conductive nanometer-thick gold films grown on

doi:10.6342/NTU202501239

molybdenum disulfide surfaces for interconnect applications." *Scientific reports* 10.1 (2020): 14463.

[219] Chang, Che-Jia, et al. "Layered graphene growth directly on sapphire substrates for applications." *ACS omega* 7.15 (2022): 13128-13133.

[220] Liu, Yu-Wei, et al. "Nanometer-thick copper films with low resistivity grown on 2D material surfaces." *Scientific reports* 12.1 (2022): 1823.

[221] Chen, Kuan-Chao, et al. "Van der Waals Epitaxy of Large-Area and Single-Crystalline Gold Films on MoS_2 for Low-Contact-Resistance 2D–3D Interfaces." *ACS Applied Nano Materials* 3.3 (2020): 2997-3003.

[222] Al-Kuhaili, M. F. "Enhancement of plasmonic transmittance of porous gold thin films via gold/metal oxide bi-layers for solar energy-saving applications." *Solar Energy* 181 (2019): 456-463.

[223] Garrod, Aydan, and Aritra Ghosh. "A review of bifacial solar photovoltaic applications." *Frontiers in Energy* 17.6 (2023): 704-726.

[224] Kumar, Prashant, Gyanendra Shankar, and Basudev Pradhan. "Recent progress in bifacial perovskite solar cells." *Applied Physics A* 129.1 (2023): 63.

[225] Agrawal, Anupam, et al. "Advancements, frontiers and analysis of metal oxide semiconductor, dye, electrolyte and counter electrode of dye sensitized solar cell." *Solar Energy* 233 (2022): 378-407.

[226] Bartesaghi, Davide, et al. "Competition between recombination and extraction of free charges determines the fill factor of organic solar cells." *Nature*

doi:10.6342/NTU202501239

communications 6.1 (2015): 7083.

[227] Bernardi, Marco, and Jeffrey C. Grossman. "Computer calculations across time and length scales in photovoltaic solar cells." *Energy & Environmental Science* 9.7 (2016): 2197-2218.

[228] Armin, Ardalan, et al. "Quantum efficiency of organic solar cells: electro-optical cavity considerations." *ACS Photonics* 1.3 (2014): 173-181.

[229] Hashemi, Mahdieh, Narges Ansari, and Mahsa Vazayefi. "MoS_2-based absorbers with whole visible spectrum coverage and high efficiency." *Scientific reports* 12.1 (2022): 6313.

[230] Lazanas, Alexandros Ch, and Mamas I. Prodromidis. "Electrochemical impedance spectroscopy─ a tutorial." *ACS measurement science au* 3.3 (2023): 162-193.

[231] Akkanen, Suvi-Tuuli Marianne, Henry Alexander Fernandez, and Zhipei Sun. "Optical modification of 2D materials: Methods and applications." *Advanced Materials* 34.19 (2022): 2110152.

[232] Chen, Hsuan-An, et al. "Scalable MoS_2/graphene heterostructures grown epitaxially on sapphire substrates for phototransistor applications." *Semiconductor Science and Technology* 33.2 (2018): 025007.

[233] Nguyen, Anh Thi, et al. "High-Performance and Lithography-Free Au/WS_2/Ag Vertical Schottky Junction Solar Cells." *Advanced Materials Interfaces* 10.15 (2023): 2300031.

doi:10.6342/NTU202501239

[234] Yoon, Jongwon, et al. "Highly flexible and transparent multi-layer MoS_2 transistors with graphene electrodes." *Small* 9.19 (2013): 3295-3300.

[235] Qiu, Weicheng, et al. "Thickness-controlled growth of multi-layer graphene on Ni (111) using an approximate equilibrium segregation method for applications in spintronic devices." *ACS Applied Nano Materials* 6.6 (2023): 4236-4242.

[236] Liu, H. F., Swee Liang Wong, and D. Z. Chi. "CVD growth of MoS_2-based two-dimensional materials." *Chemical Vapor Deposition* 21.10-11-12 (2015): 241-259.

[237] Zhou, Dong, et al. "Unveiling the growth mechanism of MoS_2 with chemical vapor deposition: from two-dimensional planar nucleation to self-seeding nucleation." *Crystal Growth & Design* 18.2 (2018): 1012-1019.

[238] Wu, Chong-Rong, et al. "Establishment of 2D crystal heterostructures by sulfurization of sequential transition metal depositions: preparation, characterization, and selective growth." *Nano letters* 16.11 (2016): 7093-7097.

[239] Wu, Chong-Rong, et al. "The growth mechanism of transition metal dichalcogenides by using sulfurization of pre-deposited transition metals and the 2D crystal heterostructure establishment." *Scientific reports* 7.1 (2017): 42146.

[240] Chen, Kuan-Chao, et al. "Atomic layer etchings of transition metal dichalcogenides with post healing procedures: equivalent selective etching of 2D crystal heterostructures." *2D Materials* 4.3 (2017): 034001.

[241] Lee, Changgu, et al. "Anomalous lattice vibrations of single-and few-layer MoS_2." *ACS nano* 4.5 (2010): 2695-2700.

doi:10.6342/NTU202501239

[242] Xu, Xiangming, et al. "High-performance mono-layer MoS_2 films at the wafer scale by two-step growth." *Advanced Functional Materials* 29.32 (2019): 1901070.

[243] Sathiyan, S., et al. "Evolution of the Polarizing Effect of MoS_2." *IEEE Photonics Journal* 7.6 (2015): 1-10.

[244] Dong, Huina, et al. "High-yield preparation and electrochemical properties of few-layer MoS_2 nanosheets by exfoliating natural molybdenite powders directly via a coupled ultrasonication-milling process." *Nanoscale research letters* 11 (2016): 1-14.

[245] Jeong, Yesul, et al. "Structural characterization and transistor properties of thickness-controllable MoS_2 thin films." *Journal of Materials Science* 54 (2019): 7758-7767.

[246] Bang, Gyeong Sook, et al. "Effective liquid-phase exfoliation and sodium ion battery application of MoS_2 nanosheets." *ACS applied materials & interfaces* 6.10 (2014): 7084-7089.

[247] Wang, H. W., P. Skeldon, and G. E. Thompson. "XPS studies of formation from ammonium tetrathiomolybdate solutions." *Surface and Coatings Technology* 91.3 (1997): 200-207.

[248] Avigad, Eytan, and Lioz Etgar. "Studying the effect of MoO_3 in hole-conductor-free perovskite solar cells." *ACS Energy Letters* 3.9 (2018): 2240-2245.

[249] McCreary, Kathleen M., et al. "The effect of preparation conditions on Raman and photoluminescence of mono-layer WS_2." *Scientific reports* 6.1 (2016): 35154.

doi:10.6342/NTU202501239

[250] Ferrari, Andrea C., and Denis M. Basko. "Raman spectroscopy as a versatile tool for studying the properties of graphene." *Nature nanotechnology* 8.4 (2013): 235-246.

[251] Tsai, Po-Cheng, et al. "The influence of contact metals on epitaxially grown molybdenum disulfide for electrical and optical device applications." *Nanotechnology* 33.50 (2022): 505205.

[252] Tsai, Po-Cheng, et al. "Charge Storage of Isolated Mono-layer Molybdenum Disulfide in Epitaxially Grown MoS_2/Graphene Heterostructures for Memory Device Applications." *ACS Applied Materials & Interfaces* 13.38 (2021): 45864-45869.

[253] Baringhaus, Jens, et al. "Exceptional ballistic transport in epitaxial graphene nanoribbons." *Nature* 506.7488 (2014): 349-354.

[254] Wang, Haining, Changjian Zhang, and Farhan Rana. "Surface recombination limited lifetimes of photoexcited carriers in few-layer transition metal dichalcogenide MoS_2." *Nano letters* 15.12 (2015): 8204-8210.

[255] Tsai, Po-Cheng, et al. "In-plane gate graphene transistor with epitaxially grown molybdenum disulfide passivation layers." *Scientific reports* 13.1 (2023): 9197.

[256] Hossain, Md Mottaleb, et al. "Low-noise speed-optimized large area CMOS avalanche photodetector for visible light communication." *Journal of Lightwave Technology* 35.11 (2017): 2315-2324.

[257] Yi, Xin, et al. "Extremely low excess noise and high sensitivity $AlAs_{0.56}Sb_{0.44}$ avalanche photodiodes." *Nature Photonics* 13.10 (2019): 683-686.

doi:10.6342/NTU202501239

[258] Wu, Dan, et al. "Recent progress of narrowband perovskite photodetectors: fundamental physics and strategies." *Advanced Devices & Instrumentation* 4 (2023): 0006.

[259] Dyck, Rudolph H., and Gene P. Weckler. "Integrated arrays of silicon photodetectors for image sensing." *IEEE Transactions on Electron Devices* 15.4 (1968): 196-201.

[260] Casalino, Maurizio, et al. "Near-infrared sub-bandgap all-silicon photodetectors: state of the art and perspectives." *Sensors* 10.12 (2010): 10571-10600.

[261] Li, Chao, et al. "Record-breaking-high-responsivity silicon photodetector at infrared 1.31 and 1.55 μm by argon doping technique." *IEEE Transactions on Electron Devices* 70.5 (2023): 2364-2369.

[262] Niu, Shouzhu, et al. "Brief review of epitaxy and emission properties of GaSb and related semiconductors." *Crystals* 7.11 (2017): 337.

[263] Plis, Elena A. "InAs/GaSb Type-II Superlattice Detectors." *Advances in Electronics* 2014.1 (2014): 246769.

[264] Wu, Enping, et al. "In situ fabrication of 2D WS_2/Si type-II heterojunction for self-powered broadband photodetector with response up to mid-infrared." *ACS photonics* 6.2 (2019): 565-572.

[265] Martyniuk, Piotr, et al. "Infrared avalanche photodiodes from bulk to 2D materials." *Light: Science & Applications* 12.1 (2023): 212.

doi:10.6342/NTU202501239

[266] Ren, Zhenwei, et al. "Bilayer PbS quantum dots for high-performance photodetectors." *Advanced materials* 29.33 (2017): 1702055.

[267] Du, Junli, et al. "Strain engineering in 2D material-based flexible optoelectronics." *Small Methods* 5.1 (2021): 2000919.

[268] Liu, Jun, et al. "Reduction in thermal conductivity of mono-layer MoS_2 by large mechanical strains for efficient thermal management." *Scientific Reports* 15.1 (2025): 1976.

[269] Lu, Ang-Yu, et al. "Unraveling the Correlation between Raman and Photoluminescence in Mono-layer MoS_2 through Machine-Learning Models." *Advanced Materials* 34.34 (2022): 2202911.

[270] Shi, Wei, et al. "Raman and photoluminescence spectra of two-dimensional nanocrystallites of mono-layer WS_2 and WSe_2." *2D Materials* 3.2 (2016): 025016.

[271] Li, Hai, et al. "Preparation and applications of mechanically exfoliated single-layer and multi-layer MoS_2 and WSe_2 nanosheets." *Accounts of chemical research* 47.4 (2014): 1067-1075.

[272] Deng, Wenjie, et al. "High detectivity from a lateral graphene–MoS_2 Schottky photodetector grown by chemical vapor deposition." *Advanced Electronic Materials* 4.9 (2018): 1800069.

[273] Zhang, Wenjing, et al. "Ultrahigh-gain photodetectors based on atomically thin graphene-MoS_2 heterostructures." *Scientific reports* 4.1 (2014): 3826.

doi:10.6342/NTU202501239

[274] Xu, Hua, et al. "High responsivity and gate tunable graphene-MoS_2 hybrid phototransistor." *Small* 10.11 (2014): 2300-2306.

[275] Roy, Kallol, et al. "Graphene–MoS_2 hybrid structures for multifunctional photoresponsive memory devices." *Nature nanotechnology* 8.11 (2013): 826-830.

doi:10.6342/NTU202501239

Publication List

Journal Articles

1. **Yu-Han Huang**, Chintam Hanmandlu, Abhishek Kumar, Chao-Hsin Wu, Chih-Wei Chu, and Shih-Yen Lin, "Bifacial Perovskite Solar Cells with Gold Transparent Electrodes Grown on Molybdenum Disulfide Surfaces", ACS Appl. Energy Mater., vol. 7, issue 14, pp. 5698-5705, June 2024.
2. **Yu-Han Huang**, Zhi-Wei Chen, Chao-Hsin Wu, Po-Tsung Lee, and Shih-Yen Lin, "Layer Number Controllable Molybdenum Disulfide Film Growth and Its Applications in Vertical and Planar Photodetectors", Adv. Mater. Interfaces, vol. 12, issue 5, pp. 2400641 November 2024.
3. **Yu-Han Huang**, Cheng-Yu Chen, Yi-Tien Chiang, Chao-Hsin Wu, Shoou-Jinn Chang, and Shih-Yen Lin, "Two-Dimensional Material Photodetectors: High Responsivities and Short Response Times of Graphene/Multi-layer MoS_2 Heterostructures", ACS Appl. Electron. Mater., vol. 7, issue 9, pp. 3947-3954, April 2025.
4. **Yu-Han Huang**, Cheng-Yu Chen, Chun-Yuan Huang, Chao-Hsin Wu, and Shih-Yen Lin, "Flexible 2D Material Hetero-structure Photodetectors with High Responsivities, Tunable Wavelengths and Short Response Times", ACS Applied Materials & Interfaces, under review.

Conference papers

1. **Yu-Han Huang**, Hanmandlu Chintam, Chao-Hsin Wu, Chih-Wei Chu, and Shih-Yen Lin, "Highly Conductive Nanometer Gold Films Grown on MoS_2 surfaces for Transparent Electrode Applications of Perovskite Solar Cells", Graphene Week 2023, Gothenburg, Sweden (2023/9/4-2023/9/8, poster).
2. **Yu-Han Huang**, Hanmandlu Chintam, Chao-Hsin Wu, Chih-Wei Chu, and Shih-Yen Lin, "Bifacial Perovskite Solar Cells with Gold Transparent Electrodes Grown on Molybdenum Disulfide", OPTIC 2023, Tainan, Taiwan (2023/12/1-2023/12/3, oral).
3. Zhi-Wei Chen, **Yu-Han Huang**, Po-Tsung Lee and Shih-Yen Lin, "Thick Molybdenum Disulfide Film Growth and Photovoltaic Responses of Vertical 2D Material Devices", OPTIC 2023, Tainan, Taiwan (2023/12/1-2023/12/3, oral).
4. **Yu-Han Huang**, Po-Cheng Tsai, Dun-Jei Zhang, Chao-Hsin Wu, and Shih-Yen Lin, "2D Material Heterostructures for High Responsivity Photo-transistors in Lateral

doi:10.6342/NTU202501239

Device Architecture", SSDM 2024, Himeji, Japan (2024/9/1-2024/9/4, oral).

5. **Yu-Han Huang**, Zhi-Wei Chen, Chao-Hsin Wu, Po-Tsung Lee and Shih-Yen Lin, "Wafer-scale and Layer Number Controllable Molybdenum Disulfide Films for Light Sensing Devices", OPTIC 2024, Taipei, Taiwan (2024/11/27-2024/11/29, oral, Best Student Paper Award).
6. Cheng-Yu Chen, **Yu-Han Huang**, Chao-Hsin Wu and Shih-Yen Lin, "Separate Light Absorption and Carrier Transport in Avalanche 2D Material Photodetectors Using Graphene/Multi-layer MoS_2 Heterostructures", OPTIC 2024, Taipei, Taiwan (2024/11/27-2024/11/29, oral with student award candidate).
7. Hao-Yu Wang, **Yu-Han Huang**, Po-Tsung Lee and Shih-Yen Lin, "Sequential Transferring and Epitaxially Grown Bi-layer MoS_2 Films for Electronic Device Applications", OPTIC 2024, Taipei, Taiwan (2024/11/27-2024/11/29, poster).
8. **Yu-Han Huang**, Chao-Hsin Wu and and Shih-Yen Lin, "Wafer-scale and Multi-Layer Molybdenum Disulfide Film Growth with Layer Number Controllability up to 30 and Its Application in Photodetectors with Short Response Times", Photonics West 2025, San Francisco, California, US (2025/1/25-2025/1/30, oral with student travel grant).

Awards

1. Junior Scientist Award (RCAS 2023): Silver Medal, Yu-Han Huang (黃郁涵)
2. Junior Scientist Award (RCAS 2024): Gold Medal, Yu-Han Huang (黃郁涵)
3. 2024 未來科技獎 (技術團隊: 林時彥, 李柏璁, 黃俊元, 呂宥蓉, 張哲嘉, 黃郁涵)
4. OPTIC 2024 Best Student Paper Award: Yu-Han Huang (黃郁涵)
5. TOSIA 2025 科技論文獎優勝 (黃郁涵)

doi:10.6342/NTU202501239